University of Hamburg
Faculty of Chemistry

Investigating Nanostructured Materials by Multi-modal in situ X-ray Methods

Dissertation
zur Erlangung des Doktorgrades
an der Fakultät für Mathematik,
Informatik und Naturwissenschaften
Fachbereich Chemie
der Universität Hamburg

vorlegt von
Davide Derelli

Hamburg
2024

Gutachter/innen der Dissertation: Prof. Dr. Dorota Koziej
Prof. Dr. Tobias Beck

Zusammensetzung der Prüfungskommission: Prof. Dr. Dorota Koziej
Prof. Dr. Alf Mews
Prof. Dr. Carmen Herrmann

Vorsitzende der Prüfungskommission: Prof. Dr. Dorota Koziej

Datum der Disputation: 07.06.2024

The present dissertation was carried out at the Center for Hybrid Nanostructures (CHyN), Institute of Nanostructure ad Solid State Physics, Department of Physics, University of Hamburg between September 2019 and April 2024.

To Giuseppe and Simone.

List of Publications

- **Davide Derelli***, Francesco Caddeo*, Kilian Frank, Kilian Krötzsch, Patrick Ewerhardt, Marco Krüger, Sophie Medicus, Lars Klemeyer, Marvin Skiba, Charlotte Ruhmlieb, Olof Gutowski, Ann-Christin Dippel, Wolfgang J. Parak, Bert Nickel, and Dorota Koziej,
  "Photodegradation of $CuBi_2O_4$ Films Evidenced by Fast Formation of Metallic Bi using Operando Surface-sensitive X-ray Scattering",
  Angewandte Chemie International Edition, 62, e202307948 (2023)
  DOI: 10.1002/anie.202307948

- **Davide Derelli***, Kilian Frank*, Lukas Grote, Federica Mancini, Ann-Christin Dippel, Olof Gutowski, Bert Nickel, and Dorota Koziej,
  "Direct Synthesis of CuPd Icosahedra Supercrystals Studied by In Situ X-Ray Scattering",
  Small, 2311714 (2024)
  DOI: 10.1002/smll.202311714

* *indicates equal contribution*

Table of Content

List of Publications VII

Table of Content IX

List of Abbreviations XV

Abstract XVII

Zusammenfassung XIX

1 Introduction 1

1.1 Objective of the thesis 3

1.2 Structure of the thesis 4

2 Theoretical background and state of the knowledge 7

2.1 Growth of nanoparticles in solution 7

2.1.1 The classical nucleation theory 7

2.1.2 Non-classical nucleation pathways 10

2.1.3 The synthesis of Pd, Cu and alloyed CuPd nanocrystals in oleylamine 12

2.1.4 The direct synthesis of supercrystals 14

2.2 Fundamentals of photo-electrochemical hydrogen production 16

2.2.1 The electronic structure of semiconductors 17

2.2.2 The semiconductor-liquid junction 18

2.2.3 The PEC cell 19

2.2.4 Diagnostic measurements for PEC electrodes 20

2.2.5 The photocorrosion of PEC-active films 21

2.3 X-ray based methods to the structural characterization of nanomaterials 24

2.3.1 X-ray Scattering 24

2.3.2 The atomic pair distribution function 27

2.3.2.1 Rapid acquisition of PDF data 28

2.3.2.2 Modeling the PDF 31

2.3.3 Small-angle X-ray scattering 34

2.3.4 X-ray diffraction 37

2.3.5 X-ray absorption spectroscopy 39

2.3.5.1 XANES and HERFD-XANES 40

2.3.5.2 EXAFS 42

2.3.6 X-ray refraction and reflection from interfaces 43

2.3.7 Toward operando scattering studies on PEC-active films 48

3 Materials and methods 49

3.1 Chemicals 49

3.2 Synthesis of metallic nanoparticles 50

3.2.1 Synthesis of Pd and Cu nanocrystals 50

3.2.2 Synthesis and assembly of CuPd icosahedra 50

3.3 Fabrication of thin films 51

3.3.1 Cleaning of the FTO substrates 51

3.3.2 Fabrication of Fe_2O_3 films 51

3.3.3 Fabrication of Ti_2O films 52

3.3.4 Fabrication of $CuBi_2O_4$ films 52

3.4 Analytical methods 52

3.4.1 PXRD 52

3.4.2 In-house SAXS 53

3.4.3 FTIR 53

3.4.4 UV-vis 53

3.4.5 SEM 53

3.4.6 TEM 53

3.4.7 HRTEM 54

3.4.8 SAED 54

3.4.9 EDX 54

3.4.10 ICP-MS 54

3.4.11 PEC characterization 55

3.5 Sample environment for in situ/operando measurements 55

3.5.1 SHINES reactor 55

3.5.2 SCOPE cell 56

3.5.3 LED illumination setup 57

3.6 Synchrotron-based characterization methods 57

3.6.1 Simultaneous TS and SAXS 57

3.6.2 High-energy X-ray scattering in grazing incidence 58

3.6.3 QEXAFS 60

3.6.4 HERFD-XANES 60

3.6.5 XANES 60

3.7 Data processing and analysis 61

3.7.1 Processing of the TS-PDF data 61

3.7.1.1 Refinement by AC approximation 61

3.7.1.2 Refinement by discrete atomistic models 62

3.7.1.3 Refinement by discrete atomistic models and Monte Carlo optimization algorithm 63

3.7.1.4 Correction of aberration for total scattering data from thin films 64

3.7.2 Processing of the SAXS data 64

3.7.2.1 Analysis of in situ Pd data 65

3.7.2.2 Analysis of in situ Cu data 65

3.7.2.3 Analysis of CuPd crystals and supercrystals 65

3.7.2.4 Analysis of the GISAXS data 67

3.7.3 Processing of the QEXAFS data 67

3.7.3.1 MCR-ALS analysis 67

3.7.3.2 Fit of the EXAFS profiles 68

3.7.4 Processing of the HERFD-XANES data 68

3.7.5 Processing of the XANES data 69

3.8 Calculation of the pairwise interaction potential of CuPd nanocrystals . . 69

4 Results and discussions **71**

4.1 Technical and methodological advancements towards multi-modal X-ray scattering measurements 71
4.1.1 The simultaneous SAXS and PDF acquisition 72
4.1.1.1 Joining SAXS and TS data 72
4.1.2 SHINES reactor for nanoparticle synthesis 74
4.1.3 High-energy X-ray scattering in grazing incidence 76
4.1.3.1 Technical requirements 76
4.1.3.2 Surface sensitivity studies 77
4.1.3.3 Effect of the data-aberration correction algorithm 80
4.1.4 SCOPE cell for operando measurements on PEC films 82
4.1.4.1 Background contribution to the Total Scattering signal . 84
4.1.4.2 PEC properties probed within SCOPE 85
4.1.5 Supporting information 87
4.2 Elucidating the formation mechanisms of Pd and Cu metallic nanocrystals 90
4.2.1 Synthesis and ex situ characterization of Pd and Cu nanocrystals 90
4.2.2 The formation of Pd nanocrystals studied in situ 93
4.2.3 Overview on the formation of Cu nanocrystals by in situ PDF . . 100
4.2.4 Chemical transformations prior to Cu nanocrystal nucleation . . . 102
4.2.5 Structural rearrangement to Cu nanocrystals 106
4.2.6 Supporting information 109
4.3 Revealing the nucleation and self-assembly of alloyed CuPd icosahedra . 125
4.3.1 Overview of the simultaneous PDF/SAXS data during the synthesis of CuPd nanocrystals 126
4.3.2 Chemical transformations affecting Cu and Pd precursors 128
4.3.3 Atomic structure of the inorganic CuPd nanocrystal cores 130
4.3.4 Revealing the nucleation of CuPd nanocrystals during synthesis . 133
4.3.5 The directed self-assembly of CuPd icosahedra 135
4.3.6 Mechanism of the supercrystal formation 137
4.3.7 Supporting information 141
4.4 Elucidating the photodegradation of $CuBi_2O_4$ films by operando surface-sensitive X-ray scattering 160

4.4.1 Morphological and photo-electrochemical characterization of $CuBi_2O_4$ electrodes . . . 160
4.4.2 Ex situ characterization of the photocorrosion of $CuBi_2O_4$ electrodes 163
4.4.3 Operando high energy X-ray scattering studies during chronoamperometry . . . 166
4.4.4 Overview of the photocorrosion mechanisms affecting $CuBi_2O_4$ electrodes . . . 169
4.4.5 Supporting information . . . 172

5 Summary and perspective 177

Bibliography 183

Appendix 211

Acknowledgments 217

Declaration of Oath 221

List of Abbreviations

AC	attenuated crystal
ADP	atomic displacement parameters
acac	acetylacetonate
CA	chronoamperometry
CE	counter electrode
COD	crystallographic open database
DSE	Debye scattering equation
EC	electrochemistry or electrochemical
EDX	energy-dispersive X-ray spectroscopy
EXAFS	extended X-ray absorption fine structure
fcc	face-centered cubic
fwhm	full width at half maximum
FT	Fourier transform
FTIR	Fourier-transform infrared spectroscopy
FTO	fluorine-dopped tin oxide
GISAXS	grazing incidence small-angle X-ray scattering
HER	hydrogen evolution reaction
HERFD	high energy-resolution fluorescence-detected
HRTEM	high-resolution transmission electron microscopy
ICP-MS	inductively coupled plasma mass spectrometry
ICSD	inorganic crystal structure database
LCA	linear-combination analysis
LED	light-emitting diode
LSV	linear sweep voltametry

MCR-ALS	multivariate curve resolution by alternating least squares
OAc	oleic acid
OAm	oleylamine
OCP	open circuit potential
OER	oxygen evolution reaction
PDF	pair distribution function
PEC	photo-electrochemistry or photo-electrochemical
PEEK	polyether ether ketone
PXRD	powder X-ray diffraction
QEXAFS	quick scanning extended X-ray absorption fine structure
RE	reference electrode
RHE	reversible hydrogen electrode
ROI	region of interest
Rw	weighted residual error
SAED	selected area electron diffraction
SAXS	small-angle X-ray scattering
SCOPE	scattering cell for operando photo-electrochemistry
SEM	scanning electron microscope
SHINES	stirring and heating in situ cell for nanoparticle synthesis
TEM	transmission electron microscopy
TS	(X-ray) total scattering
WE	working electrode
XANES	X-ray absorption near-edge structure
XAS	X-ray absorption spectroscopy
XRD	X-ray diffraction

Abstract

Understanding the structural transformations affecting nanomaterials is essential to rationally improve their properties and functionalities. Despite recent advances in several X-ray investigation routines, the transformation phenomena affecting nanomaterials entail structural modifications on several length scales that cannot be covered by a single analytical method. In this thesis, we establish a multi-modal X-ray scattering setup to collect structural information spanning from fractions of Å to hundreds of nanometers via simultaneous acquisition of small-angle X-ray scattering (SAXS) and X-ray total scattering (TS). We then apply the method to investigate the model syntheses of Pd, Cu, and CuPd nanocrystals in solution, and to further elucidate the degradation of photoelectrochemical (PEC) $CuBi_2O_4$ thin films during operation.

We reveal that a Pd(II)-amino initial complex directly converts into Pd nanocrystals without formation of intermediates, in agreement with the classical nucleation model. We employ the pair-distribution function (PDF) analysis of the in situ TS signal and complementary in situ X-ray absorption spectroscopy (XAS) during the synthesis of Cu nanocrystals to reveal a multi-step conversion of an initial Cu(II)-amino complex into a partially reduced Cu(I) organometallic intermediate prior to the nucleation of polycrystalline Cu_2O seeds. We further demonstrate via PDF and SAXS that individual Cu_2O seeds fuse together to form larger Cu_2O nanocrystals, which slowly convert into metallic Cu. We thus show that the synthesis of Cu nanocrystals follows a complex non-classical crystallization pathway.

Both in situ XAS and PDF suggest that alloyed CuPd nanocrystals form via preliminary formation of Pd-rich seeds, which promote the direct reduction of the Cu(I)-amino intermediate into the metallic form without formation of the Cu_2O phase. PDF analysis further indicates that the CuPd nanocrystals nucleate and grow as multi-twinned icosahedra. Furthermore, SAXS data reveals that the as-formed CuPd icosahedra assemble within the reaction medium into large face-centered cubic (fcc) supercrystals due to the entropic forces arising by the ordering of the solvent molecules into lamellae.

We reveal by both PDF and SAXS that the fast decrease in the performances of $CuBi_2O_4$ electrodes correlates directly with the formation of a metallic Bi phase. We also identify additional degradation phenomena, such as the emergence of metallic Cu and the dissolution of the electrode in contact with the electrolyte, which further affect the $CuBi_2O_4$ thin film activity and morphology. Overall, our study shows that the multimodal acquisition of PDF, SAXS, and XAS significantly enhances our understanding on the transformation mechanisms affecting nanomaterials and poses the methodological basis to investigate the fabrication and operation of a wide range of nanostructured materials.

Zusammenfassung

Das Verständnis der strukturellen Veränderungen von Nanomaterialien ist von entscheidender Bedeutung für die Verbesserung ihrer Eigenschaften und Funktionalitäten. Trotz der jüngsten Fortschritte in verschiedenen Röntgenmethoden können strukturelle Veränderungen auf mehreren Längenskalen nicht mit einer einzigen analytischen Methode erfasst werden. In dieser Arbeit etablieren wir einen multimodalen Röntgenstreuungsaufbau, um strukturelle Informationen von Bruchteilen von Å bis zu Hunderten Nanometern durch das simultane Messen von Röntgenkleinwinkelstreuung (Small Angle X-ray Scattering, SAXS) und Röntgentotalstreuung (Total Scattering, TS) zu erhalten. Wir verwenden den multimodalen Ansatz, um die Synthese von Pd-, Cu- und CuPd-Nanokristallen in Lösung sowie die Zersetzung von photoelektrochemischen (PEC) $CuBi_2O_4$-Dünnschichten in-situ bzw. operando zu untersuchen.

Wir zeigen, dass ein initialer Pd(II)-Aminkomplex direkt, ohne Zwischenprodukt, in Pd-Nanokristalle umwandelt wird. Wir nutzen die Paarverteilungsfunktion (Pair Distribution Function, PDF) des TS-Signals mit komplementärer Röntgenabsorptionsspektroskopie (X-ray Absorption Spectroscopy, XAS), um die mehrstufige Umwandlung eines initialen Cu(II)-Aminkomplexes in eine teilweise reduzierte Cu(I)-Aminspezies vor der Nukleationskeimbildung von polykristallinen Cu_2O-Keimen aufzuzeigen. Des Weiteren demonstrieren wir mittels PDF und SAXS, dass einzelne Cu_2O-Keime miteinander verschmelzen und größere Cu_2O-Nanokristalle bilden, die sich langsam in metallisches Cu umwandeln. Folglich zeigen wir, dass die Synthese von Cu-Nanokristallen einem komplexen, nicht-klassischen Kristallisationsweg folgt.

Sowohl die in-situ XAS- als auch die in-situ PDF-Analyse deuten darauf hin, dass sich legierte CuPd-Nanokristalle durch die vorherige Bildung von Pd-reichen Keimen bilden, die die direkte Reduktion des Cu(I)-Amin-Zwischenprodukts in die metallische Form

ohne Bildung der Cu_2O-Phase fördern. Die PDF-Analyse deutet außerdem darauf hin, dass die Nanokristalle als mehrfach verzwillingte Ikosaeder keimen und wachsen. Darüber hinaus zeigen SAXS-Daten, dass sich die gebildeten CuPd-Ikosaeder im Reaktionsmedium aufgrund der entropischen Kräfte durch die Anordnung der Lösungsmittelmoleküle in Lamellen, zu großen kubisch flächenzentrierten Superkristallen zusammensetzen.

Wir zeigen mit PDF sowie mit SAXS, dass der schnelle Leistungsabfall von $CuBi_2O_4$-Elektroden direkt mit der Bildung einer metallischen Bi-Phase korreliert. Wir identifizieren zusätzliche Degradationsphänomene, wie die Entstehung von metallischem Cu und die Auflösung der Elektrode im Kontakt mit dem Elektrolyten, welche die $CuBi_2O_4$-Dünnschichtaktivität und Morphologie weiter beeinträchtigen. Insgesamt zeigt unsere Studie, dass die multimodale Erfassung von PDF, SAXS und XAS unser Verständnis der Umwandlungsmechanismen von Nanomaterialien erheblich verbessert. Unser Ansatz stellt die methodische Grundlage für die Untersuchung der Herstellung sowie der Funktionsweise eines breiten Spektrums von nanostrukturierten Materialien.

Chapter 1

Introduction

The development of new technologies ultimately relies on our ability to produce materials with advanced properties. The term *nanomaterials* encompasses diverse materials, including nanoparticles, nanocomposites, and nanostructured films, which possess structural features within the range 1 to 100 nm on at least one dimension. Owing to their high surface-to-volume ratio and electrical confinement effects at the nanoscale, nanomaterials typically exhibit distinct physical, chemical, mechanical, and optical properties compared to their bulk counterparts.[1–4] These unique characteristics render nanomaterials crucial in a myriad of applications.[5–8] For instance, Copper (Cu), Palladium (Pd) and Copper-Palladium (CuPd) nanoparticles display remarkable catalytic properties.[9–16] However, a poor understanding of the formation mechanism of these nanomaterials limits our capacity in synthesizing tailored nanoparticles for specific catalytic purposes.

In the realm of sustainable energy production, photo-electrochemical (PEC) thin films offer the potential to directly convert solar energy into hydrogen gas (H_2), which is then stored and utilized on demand as a sustainable fuel with a potential net-zero CO_2 emissions.[17–19] However, the degradation of PEC materials under operation currently hinders their application in effective water splitting devices.[20,21]

The rational design of nanomaterials with superior quality heavily relies on our ability to discern structural features at the relevant length scales. Since their discovery in 1895, X-rays have become a fundamental tool to probe the structure of materials, owing to the high penetration depth and the small wavelength of the X-ray radiation. Although the formation of sharp peaks by X-ray diffraction (XRD) permits to fully retrieve the

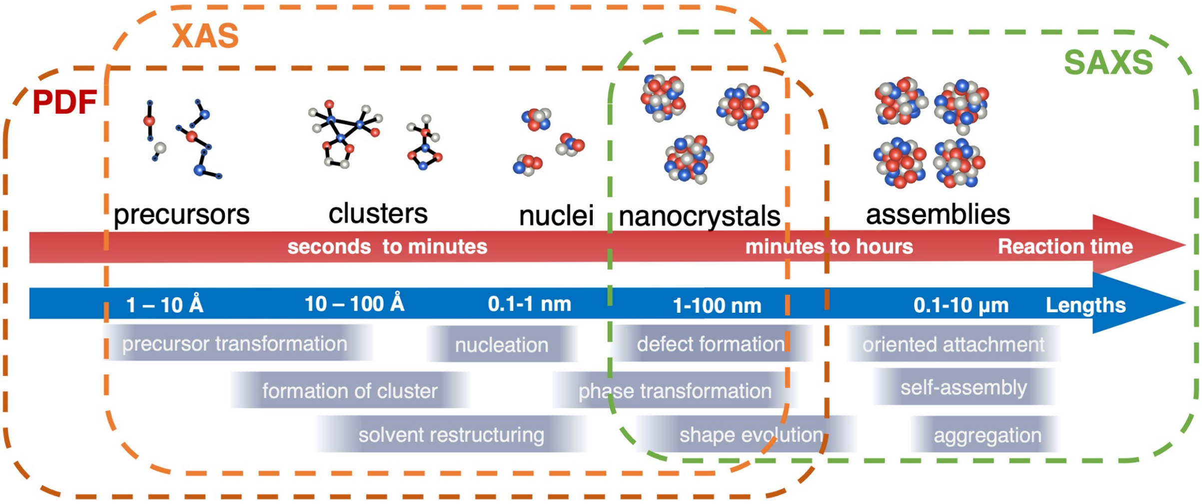

Figure 1.1: The complementary in situ techniques to study the nanoparticle formation. While PDF and XAS reveal structural and chemical transformations at early and intermediate nucleation stages, SAXS provides complementary information over the nanostructures forming at intermediate and late stages of the synthesis. The combined use of these three techniques thus provides a complete scrutiny of the nanoparticle nucleation pathways over multiple time and length scales.

atomic arrangement of bulk crystalline materials, the XRD measurement results in broad and weak diffraction peaks in the case of nanostructured materials. As a result, the amount of structural information that can be extracted from a standard XRD experiment decreases.[22,23] The measurement of X-ray total scattering (TS) and its Fourier transformation into the atomic pair distribution function (PDF) is a practical approach to overcome such limitation and effectively probe the local structure of both nanocrystalline or amorphous materials with atomic resolution. Nevertheless, the PDF does not provide information over the overall morphology of the nanomaterial and is not element sensitive. To obtain a comprehensive survey of structural transformations occurring at the nanoscale, the use of complementary X-ray techniques alongside PDF analysis is therefore imperative.

Figure 1.1 schematically illustrates the structural transformations leading to the formation of nanocrystals and nanocrystal assemblies. During the process, complex phenomena unfolds, compromising phase conversion, shape evolution, and hierarchical assembly. These phenomena span over multiple time and length scales and thus cannot be captured by a single X-ray technique.[24] X-ray absorption spectroscopy (XAS) provides insights into the local chemical environment surrounding selected elements and can be combined with PDF analysis to determine structural and chemical transformations at early and intermediate stages of the synthesis. Additionally, small-angle X-ray scattering (SAXS) provides morphological information limited to intermediate and larger length scales. The complementary use of these three techniques thus holds potential for a complete scrutiny of the multi-faceted processes driving the formation of nanomaterials. However, PDF, XAS, and SAXS are usually performed independently and there is currently no systematic approach for integrating these techniques into a unified experimental setup.

1.1 Objective of the thesis

The scope of this thesis is to develop a multi-modal experimental approach to determine the structure of nanomaterials in situ. After laying the necessary technical and methodological foundations, we validate our method by investigating two different classes of transformations, namely the synthesis of nanocrystals and nanocrystal assemblies in solution and the degradation of PEC-active thin films, as illustrated in **Figure 1.2**.

Both TS-PDF and SAXS can be performed by using high-energy X-rays and thus integrated into a single experimental setup for the simultaneous acquisition. We will design an in situ reactor which is compatible with X-ray scattering and X-ray spectroscopy measurements to investigate the synthesis of nanocrystals with high reproducibility via both methods. We will first investigate the synthesis of monometallic Pd and Cu nanocrystals, and then expand our scope to the direct synthesis of CuPd hierarchical structures.

We will develop a second sample environment for the simultaneous measurement of TS-PDF and SAXS on PEC-active thin films under operation. We will collect high-energy X-ray scattering signal in grazing incidence geometry to determine structural information limited to the thin film surface, and then apply our method to elucidate the fast degradation mechanisms affecting $CuBi_2O_4$ electrode performances.

Overall, our study poses the technical and methodological foundation for investigating nanocrystal synthesis and photoactive thin film operation both in situ and operando. It further highlights the benefits of our multi-modal investigation approach to unveil complex transformations affecting model nanostructured materials at relevant time and length scales.

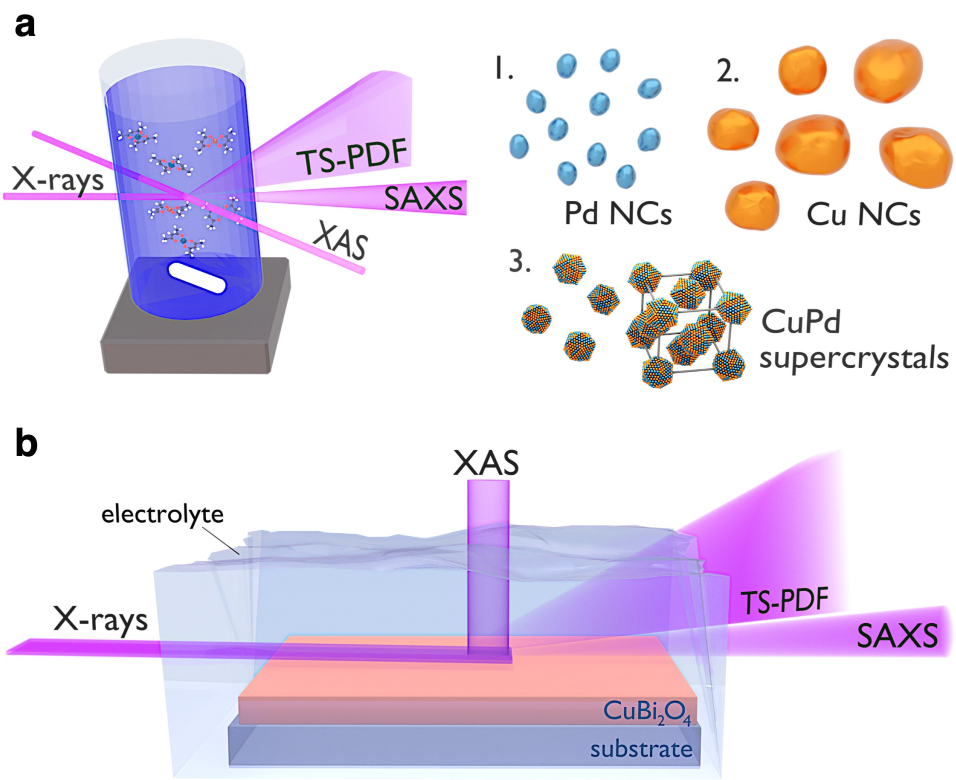

Figure 1.2: Schematic illustration of the objectives of this thesis. **a**) A multi-modal experimental approach is applied to determine the formation of nanocrystals in solution. In situ TS-PDF, SAXS, and XAS are measured to investigate the synthetic pathways to Pd (**1**) and Cu (**2**) nanocrystals, as well as to CuPd supercrystals (**3**). **b**) Operando TS-PDF and SAXS are carried out to determine the degradation mechanisms of a PEC-active $CuBi_2O_4$ thin film under operation in an electrolyte solution. The data are further complemented with ex situ XAS.

1.2 Structure of the thesis

After this introduction, in **Chapter 2**, we delve into the relevant theoretical background and current state of knowledge pertinent to the present thesis. In **Section 2.1**, we examine the formation of nanoparticles in solution, exploring classical nucleation theory as well as potential non-classical nucleation pathways. We additionally discuss the synthesis of Pd, Cu, and CuPd nanocrystals in solution, along with the direct synthesis of nanocrystal superlattices through one-pot synthesis and assembly of individual nanocrystals. Moving to **Section 2.2**, we provide fundamental insights into the PEC hydrogen production and explore the degradation of PEC electrodes during operation. In **Section 2.3**, we provide an overview of the X-ray based methods utilized in this thesis for investigating nanomaterials, with a particular emphasis on PDF analysis. Furthermore, we highlight recent advancements in surface-sensitive PDF measurement on thin films.

In **Chapter 3** we illustrate the materials and methods used throughout this thesis, with a particular focus on synchrotron-based acquisition routine and data treatment.

Chapter 4 presents the scientific results of the thesis. In **Section 4.1** we demonstrate the simultaneous acquisition of in situ SAXS and TS-PDF. We show how the combined use of two large-area X-ray detectors enables to measure structural and morphological information continuously from atomic to nanometer length scales. Furthermore, we demonstrate how grazing incidence measurements permits to probe the surface of smooth thin film sample. We further present two distinct sample environments, tailored for both in situ and operando investigations of nanoparticle synthesis and PEC film activity, respectively. Through this section we thus establish the essential technical and methodological knowledge to explore dynamic processes affecting both nanoparticle dispersions and thin film samples.

In **Section 4.2** we apply our multi-modal X-ray techniques to the model syntheses of monometallic Pd and Cu nanocrystals. We find that while Pd nanocrystals nucleate and grow according to the classical nucleation theory, Cu nanocrystals form via a non-classical, multi-step process. We demonstrate that the complementary use of XAS, PDF, and SAXS is crucial for a correct interpretation of the data.

In **Section 4.3** we utilize PDF and XAS to determine the reduction pathways to CuPd nanocrystals and further employ simultaneous PDF and SAXS to reveal the one pot nucleation and assembly of CuPd icosahedra. We find that the presence of a Pd precursor largely accelerates the reduction kinetics of a Cu(I) organo-metallic intermediate species. We further find that ordering of oleylamine and oleic acid solvent molecules plays a crucial role in the assembly of CuPd icosahedra, which is primarily driven by entropic forces.

In **Section 4.4** we apply our multi-modal TS-PDF and SAXS acquisition setup to the operando measurement of PEC-active $CuBi_2O_4$ thin films. Here,the high time resolution and enhanced surface sensitivity of the X-ray scattering measurement permits to correlate the fast decrease in the PEC performances of the $CuBi_2O_4$ electrode with the simultaneous formation of a reduced Bi phase. We further perform additional ex situ X-rays characterization measurements to reveal several degradation mechanisms that were previously unknown to affect the operation of $CuBi_2O_4$ materials.

Chapter 5 summarizes the scientific results of this thesis and provides an outlook for potential future research directions.

All results presented in this thesis were acquired in collaboration with fellow scientists. My specific contribution to each study is delineated in the preliminary remarks of the corresponding Result and Discussion section.

A conclusive comment on the use of the term *we* throughout this thesis: in chapters explaining the theoretical background and state of the knowledge, *we* refers to both the reader and the author of the thesis and is used to guide the reader through the text. In chapters presenting the results of individual research studies, *we* means all authors of the respective work.

Chapter 2

Theoretical background and state of the knowledge

2.1 Growth of nanoparticles in solution

2.1.1 The classical nucleation theory

The physical and chemical properties of the nanoparticles fundamentally depend upon their size, composition, and morphology. Understanding the nanoparticles' formation and achieving synthetic control over their final structure is therefore essential to produce suited nanomaterials for specific functional applications. The classical nucleation theory permits to rationalize the emergence of a nanoparticle in a supersaturated solution by addition of individual atoms, ions or molecules. According to the theory, the crystallization of the nanoparticles initiates from small stable nuclei which form in solution when the concentration of the active species for the nucleation, usually referred to as *monomers*, exceeds a certain critical level.[25–28] The nucleus can form either via homogeneous nucleation due to random collisions of the monomer, or via heterogeneous nucleation, i.e., by interaction between the monomer and a foreign seed.

The Gibbs free energy of a spherical nucleus with radius r is expressed as:

$$\Delta G(r) = \frac{4}{3}\pi r^3 \Delta G_V + 4\pi r^2 \gamma \tag{2.1}$$

where ΔG_V is the free energy per unit volume of the crystal and γ is the surface free

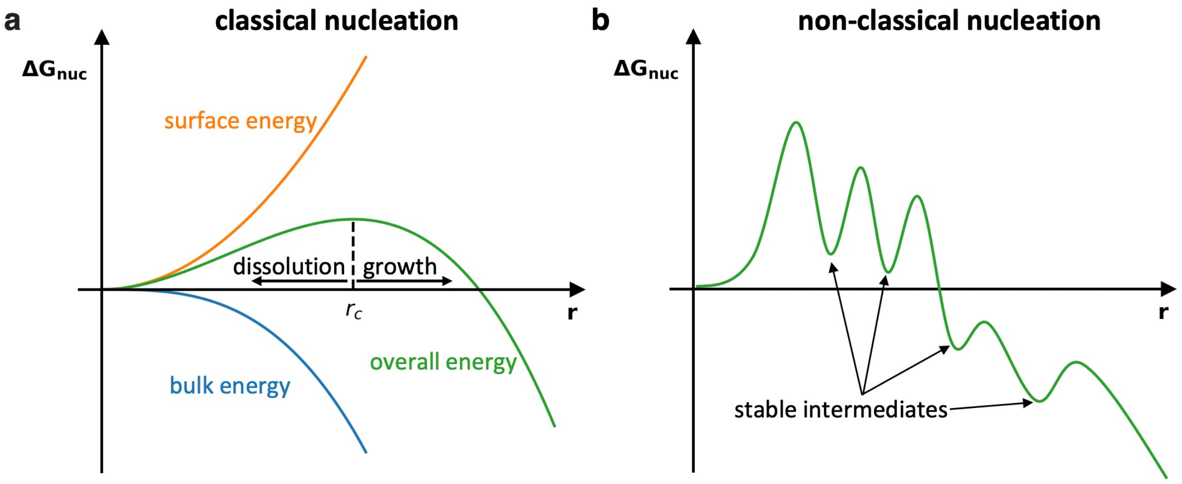

Figure 2.1: Plot of the Gibbs free energy for the classical and non-classical nucleation pathways. In **a** r_c indicates the critical radius, above which nuclei are stable upon dissolution. In **b**, the non-classical nucleation pathways encompass the formation of stable intermediates corresponding to local minima in the energy profile. Adapted from[30].

energy per unit area.[29] Equation 2.1 denotes a balance between the decrease in energy due to the formation of chemical bonds in the bulk of the nanoparticles and its increase due to the unfavourable formation of a solid-liquid interface. For small radii, the destabilizing surface energy dominates and the nucleus re-dissolves in solution. Conversely, nuclei of larger radii than a critical radius r_c are stable upon dissolution and further grow. The dependence of the free energy upon the particle radius is illustrated in **Figure 2.1**.

In the classical nucleation theory, the level of supersaturation S is the key parameter controlling the nucleation and growth of the nanoparticles. Here, S is defined as the ratio $[M]/[M]_0$ between the monomer concentration in solution and its equilibrium concentration with the solid. In **Figure 2.2**, LaMer diagram illustrates changes in the supersaturation profile during the nanoparticle synthesis.[25] Three different stages can be identified during the process. At the beginning of the synthesis, the nanoparticle precursor converts into the active monomer, which accumulates in solution. When the monomer concentration raises above a critical supersaturation level S_c, homogeneous nucleation unfolds. During the process, monomer species are consumed and the supersaturation level drops below S_c. At this stage, further nucleation is inhibited and existing nuclei grow upon addition of the remaining monomer in solution.

LaMer diagram represents a highly simplified description of the nanoparticle nucle-

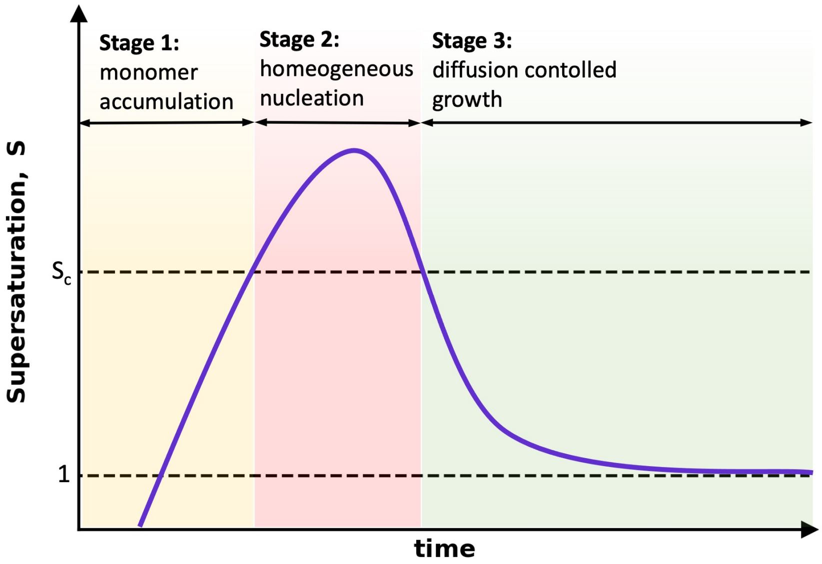

Figure 2.2: LaMer diagram. S_c indicates the critical supersaturation, while at $S = 1$ the monomer concentration in solution is in equilibrium with the nanoparticle. Adapted from[25].

ation. Nevertheless, it turns out providing a useful model to rationalize the size distribution of nanoparticles obtained through numerous synthetic routes.[31–33] For instance, the theory predicts that when nucleation stage is infinitely short, all nanoparticle nuclei form simultaneously during the synthesis and the growth process spans over the same amount of time for all seeds. In turn, the final collection of nanoparticles is expected to be very homogeneous in size. The underlining strategy is applied in two common synthetic methods: the hot-injection and the heat-up methods.[34] In the former, a stock solution containing reactive precursor is rapidly injected into a hot mixture containing surfactants.[35,36] Due to the high temperatures and the high local supersaturation level, the nanoparticle nucleation commences immediately and is incredibly fast. During formation, the surfactants bind to the nanoparticle surface and thus prevent nanoparticle aggregation.

The heat-up method is fundamentally different from the hot injection.[37,38] Here, a precursor solution is first prepared at low temperature. Then, the mixture is heated to high temperature, at which the nanoparticles form.[39,40] If the heating ramp is sufficiently fast, the temperature of the mixture quickly increases above the activation temperature for the reaction and a burst in the nucleation unfolds.[37,41] However, monodispersed nanoparticles can also be synthetised via heat-up method by use of relatively slow temperature ramps.[39,42,43] These studies suggest that auto-catalytic reactions which are not included in the classical model can also dominate the kinetics of nanoparticle nucleation, as also shown by numerical simulations.[44]

2.1.2 Non-classical nucleation pathways

The classical nucleation theory describes the growth of nanoparticles solely by addition of individual atoms, ions or molecules into the nucleus. However, nanoparticles with complex geometry, polycrystalline materials, and organic-inorganic hybrid structures are routinely synthesised. Electron microscopy and X-ray investigations further evidence the existence of synthetic pathways which are not predicted by the classical model.

In non-classical pathways, particle nucleation occurs via a multi-step process which leads to amorphous intermediates such as droplets, complexes, clusters and oligomers.[24,45] Such intermediates are moderately stable upon dissolution and decrease the overall energetic barrier to the formation of stable solids, as shown in **Figure 2.1b**.[46–49] Pre-nucleation clusters can evolve to the final nanoparticles through different routes, some of which are schematically illustrated in **Figure 2.3**. Once primary, stable nanoparticles are formed, further growth to single crystalline nanoparticles (**Figure 2.3a**) is possible in agreement with the classical nucleation theory, i.e. through addition of the monomer. Differently, primary particles could also assemble into aggregates displaying a common crystallographic orientation, referred to as mesoscale assemblies, **Figure 2.3b**, which can further fuse together to single-crystalline particles via e.g. oriented attachment.[50–52] Primary particles stabilised with organic ligands can also self-assemble on a common crystallographic orientation, forming a mesocrystal (**Figure 2.3c**).[53–55] Therefore, in mesocrystals individual particles are separated by a layer of organic species. Once these species detach from the particle surface, conversion of the mesocrystal into a mesoscale assembly takes place.[52] Pre-nucleation clusters can also follow a separate pathway which leads to the formation of an intermediate dense liquid droplet (**Figure 2.3d**) or amorphous phase e.g. via aggregation of individual clusters or oligomers.[56–58] Such intermediates further evolve through aggregation and crystallization steps, resulting in polycrystals with complex shapes.

The schematic synthetic pathways shown in **Figure 2.3** are simplified. For instance, the emergence of unoriented nanoparticle assemblies and the formation of polycrys-

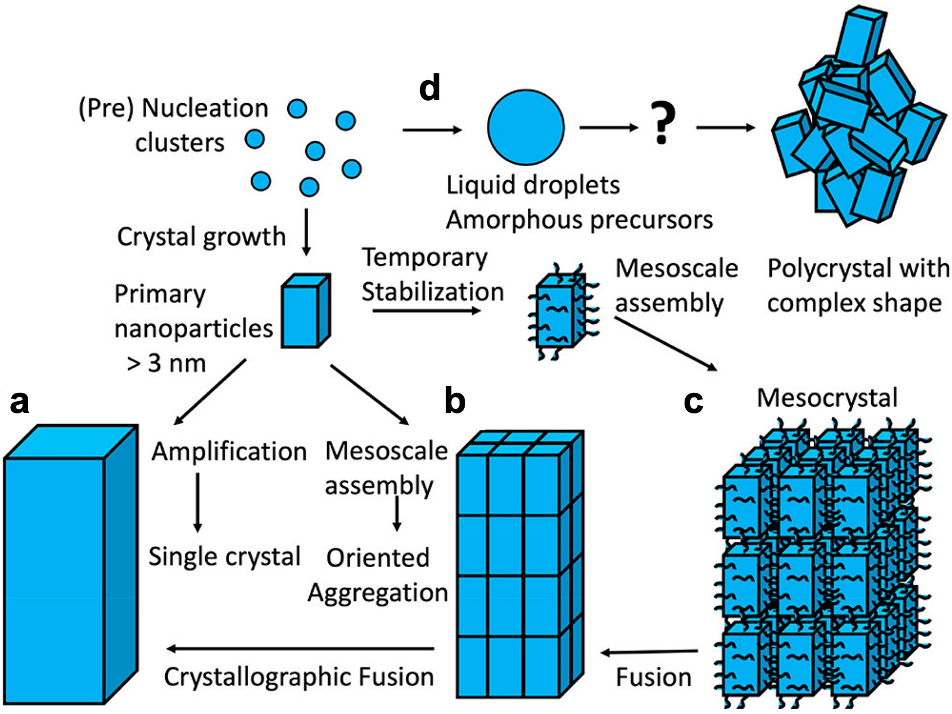

Figure 2.3: Schematic illustration of non-classical crystallization pathways. **a**) Classical nucleation results in single crystal formation. **b**) Oriented aggregation of un-stabilised primary particles produces mesoscale assemblies. **c**) Primary particles stabilised by organic surfactants self-assemble into mesocrystals. **d**) Pre-nucleation clusters evolve into the formation of a liquid droplet or amorphous precursors before nucleation of a polycrystal particle with complex shape. Adapted with permission from[24] Copyright 2019, American Chemical Society.

talline materials by unoriented aggregation of primary crystalline particles have also been observed.[59,60] Moreover, combinations of the presented pathways are also possible. In fact, a generalised model of particle nucleation does not exist. Conversely, the complexity of the involved processes imposes a shift in paradigm, from a "one model fits all" approach to a chemistry-based understanding of the nucleation and crystallization phenomena.[49,61] To this goal, X-ray methods constitute an effective tool to determine the chemical and structural modifications leading to the formation of the nanoparticle product.

In the following section, we delve into the current state of knowledge regarding the colloidal synthesis of Pd, Cu, and CuPd nanocrystals in oleylamine. Our understanding of the synthetic mechanisms behind these metallic nanocrystals primarily stems from simple ex situ observations of the final nanoparticle product. Thus, obtaining a precise description of the precursor conversion pathway into the nanocrystalline products remains largely elusive.

2.1.3 The synthesis of Pd, Cu and alloyed CuPd nanocrystals in oleylamine

Oleylamine constitutes a very versatile reagent to the colloidal synthesis of a wide range of nanosized materials due to its ability to act as a solvent, a surfactant, and a mild reducing agent at the same time.[40,62–64] For instance, Cu nanoparticles are readily synthesized by simply heating a oleylamine solution of copper acetylacetonate ($Cu(acac)_2$) precursor.[65] However, the reaction mechanisms leading the metal precursors to convert into the metallic nanocrystals are not yet completely known.

In the synthesis of Cu and Pd nanocrystals, stronger reducing agents are often combined with oleylamine to enhance the overall reducing strength of the reaction medium. Such reducing agents include boranes,[66] formaldeyde,[67] H_2,[68,69], CO.[70,71], and alcohols.[72,73] For instance, Mazumder and Sun obtain even growth rates to monodispersed 4.5 nm Pd nanocrystals after addition of a borane tributhylamine (BTB) complex to a mixture of palladium acetylacetonate ($Pd(acac)_2$) and oleylamine.[66] Differently, the use of oleylamine alone as reducing agent resulted in polydispersed nanocrystals, presumably due to multinucleation events taking place during the precursor reduction.

Different capping agents are commonly added to oleylamine to direct the synthesis of nanocrystals of selected size and shapes. The combined use of oleic acid and oleylamine has been largely explored in the synthesis of Cu and Pd nanocrystals.[68,71–77] Since oleic acid and oleylamine present distinct binding modes for different crystalline facets based on the material, tuning their concentration and relative ratio provides a mean of control over the nanocrystal final shape and size. For instance, Watt et al. obtained the thermodynamically favoured Pd polyhedra by using H_2 gas in oleylamine as reducing agent at room temperature. However, when oleic acid is introduced in a 1:1 ratio with oleylamine, highly branched nanoparticles form.[68,74] By adding a small amount of oleic acid to the oleylamine solvent, Yin et al. directed the synthesis of dish-like palladium nanostructures after reduction of $Pd(acac)_2$ via bubbling of CO.[71]

Controlling the reaction temperature and the relative ratio of the oleylamine and oleic acid capping ligands in the presence of 1,2-hexadecanediol reducing agent allowed Mott et al. to tune the shape of 5 to 25 nm copper nanoparticles from sphere to rods and cubes.[73] By inspection of the synthesis product via electron microscopy, they observed subtle cluster features in the nanoparticles which hinted to the coalescence of smaller particles during the synthesis. However, they could not provide any direct prove of the suggested mechanism. Devaraj et al. showed that stable Cu nanocrystals are obtained when oleic acid and oleylamine are jointly used during synthesis, while employing oleylamine alone resulted in nanocrystals that readily oxidize in air to form Cu-Cu_2O core-shell structures.[76] During these synthetic schemes, the removal of water from the reaction mixture was critical to produce pure Cu nanocrystals. In fact, the presence of water is known to promote the formation of Cu_2O and CuO.[76,78,79] Pesesse et al. showed that the reduction of copper acetate ($Cu(OAc)_2$) precursor in oleylamine results in mixed Cu and Cu_2O nanocrystals due to the production of water via condensation reaction between the acetate group and oleylamine.[79] However, the mechanism by which both Cu and Cu_2O form during the synthesis is not yet known.

Incorporating both Cu and Pd atoms within the same crystalline lattice through colloidal synthesis holds significant interest due to the improved (electro-)catalytic properties of the resulting nanocrystals, which were attributed to synergistic effects between the Cu and Pd metal centers. As a result, CuPd nanocrystals are increasingly employed across a broad spectrum of catalytic processes, including carbon dioxide reduction,[15,80–82] alcohol oxidation,[83,84] and carbon-carbon coupling.[85,86] In addition to their composition, the catalytic properties of CuPd nanocrystals heavily depend on their degree of crystallinity and on their crystalline phase. CuPd materials exhibit either a disordered face-centered cubic (fcc) alloy lattice (space group Fm-3m), where each lattice site is randomly occupied by a Cu or a Pd atom, or a ordered intermetallic lattice, such as the CsCl-type CuPd phase (Pm-3m) or the tetragonal Cu_3Pd phase (P4/mmm). Many synthetic routes in oleylamine to both alloyed[86–89] and intermetallic[89–91] CuPd phases are reported. Moreover, alloyed CuPd nanocrystals with the appropriate Cu:Pd composition are routinely converted into the intermetallic form upon annealing at high temperature.[92–94] However, the formation mechanism of alloyed CuPd oleylamine is still controversial. For instance, Mathiasen et. al suggest that Cu nucleates first, based on the first observation via in situ PDF of a copper-rich Cu_3Pd intermetallic phase after nucleation.[91] Conversely, Marakatti et al. speculate that Pd nucleates first, while Cu^{2+} converts slowly to Cu due to the poor reducing power of oleylamine.[89]

Investigations by multi-modal in situ X-ray methods, as proposed in this thesis, provide the opportunity to expand our knowledge over the formation of Cu, Pd, and CuPd nanocrystals by providing novel insights into the chemical and structural transformations affecting both the metal precursors and small nuclei in the presence of oleylamine and oleic acid.

2.1.4 The direct synthesis of supercrystals

The production of hierarchically structured materials is driving many recent advances in the fields of photonics,[95,96] electronics,[97,98] catalysis,[99,100] sensing[101], and nanomedicine[102–104]. The self-assembly of nanocrystals into crystalline lattices constitutes a promising bottom-up route to such metamaterials, as it permits to tune the emergent functional properties of the outcoming supercrystals via engineering of the individual building blocks.[105–110]

The most common strategies to produce assemblies of nanocrystals are slow solvent evaporation and gradual nanocrystal destabilization, e.g. via addition of an anti-solvent.[109] In both processes, a careful choice of the experimental conditions, such as time, temperature, starting nanocrystal concentration, solvent, and nature and concentration of the surfactants, is essential to deliver supercrystals of the desired symmetry, with large domain sizes, and few defects.[111–115] Moreover, the use of monodispersed nanocrystals is often a prerequisite to the formation of the superlattices.[116–118] When synthetic routes deliver polydispersed collection of nanocrystals, size-selected precipitation,[35,119] chromatography techniques,[120] and digestive ripening[121] can be used to narrow their size distribution.

The nanocrystal synthesis and their self-assembly into supercrystals are commonly performed as separate processes. After synthesis, the nanocrystals generally undergo several purification routines, sometimes followed by an additional surface functionalization step, before the assembly routine is performed. Only few recent reports demonstrate the direct conversion of molecular precursors into supercrystals via a one-pot strategy.[122–126] In these studies, the formation of the ordered superstructures is primarily ascribed to the attractive van der Waals forces affecting the nanocrystal cores, balanced by the steric repulsion of the organic surface ligands.[127] For instance, Wu et al. show that Pd, Fe, and

PbTe nanocrystals assemble during synthesis only after growth to diameters of sufficient size, as under these conditions the core-core attraction overcomes the steric repulsion due to presence of surface ligands.[123] Yet, the dynamical processes governing the concerted nanocrystal synthesis and supercrystal formation remain underexplored. For instance, the role of the solvent molecules and ligand shells[128] and the existence of intermediate states due to potential non-classical crystallization pathways[108] for the supercrystals are still largely unknown.

SAXS represents an outstanding tool to probe self-assembly processes in situ due to its compatibility with complex reaction environment, its sensitivity to the emergence of periodic nanocrystal arrangements, and its ability to provide statistically robust information by probing large collection of nanocrystals simultaneously.[129] in situ SAXS provided remarkable insights in the self-assembly at the interface[130,131] and from bulk dispersions during solvent evaporation[132,133] and nanocrystal destabilization[134,135]. In fact, all reported cases of direct synthesis of supercrystals employed in situ SAXS to provide evidence of the supercrystal formation.[122–126] However, SAXS signal doesn't detect the atomic arrangement of individual nanocrystals, with the result that structural changes at the atomic scale preliminary or concurrent to the self-assembly process might remain unnoticed. By simultaneous acquisition of SAXS and TS-PDF, we get the opportunity to close this gap and to reveal the complete process of the direct conversion of chemical precursors into supercrystals across several length scales.

2.2 Fundamentals of photo-electrochemical hydrogen production

In a photo-electrochemical (PEC) cell, solar energy is harvested and directly utilized to produce hydrogen from water. The semiconducting electrode represents the key component of the PEC device and is responsible for the absorption of the incident light, which in turn generates electron-hole pairs within the semiconductor. Electrons and holes are subsequently spatially separated due to a built-in electrical potential within the semiconductor and independently driven to the semiconductor-electrolyte interface, where either the reduction or the oxidation of water molecules takes place.

The hydrogen evolution reaction (HER), the oxygen evolution reaction (OER), as well as the overall water splitting reaction can be written as:

$$\begin{array}{lll} \text{water reduction (HER):} & 4H^+ + 4e^- \rightleftharpoons 2H_2 & E^0_{red} = +0.0\ V \\ \text{water oxidation (OER):} & 2H_2O + 4h^+ \rightleftharpoons 4H^+ + O_2 & E^0_{ox} = +1.23\ V \\ \text{water splitting:} & 2H_2O \rightleftharpoons 2H_2 + O_2 & E^0_{ws} = +1.23\ V \end{array}$$

Here, E^0 refers to the standard electrochemical potentials. To split water molecules into H_2 and O_2 it is thus necessary to overcome a considerable electrochemical potential difference ΔE^0 of 1.23 V, meaning that the water splitting reaction is thermodynamically uphill.

This chapter will provide the reader some basic theoretical knowledge over the PEC production of hydrogen. After reviewing the electronic structure of semiconductors, it describes the origin of the built-in electric field which induces the electron and holes to separate at the semiconductor/liquid junction. It further illustrates the operation of the PEC cell under illumination and then provides an overview of selected diagnostic measurements for PEC-active semiconductors. These sections are based upon the excellent review from Lewis et al.,[136] as well as a textbook chapter from van der Krol.[37] Finally, the chapter provides an overview of the current state of the knowledge on the photocorrosion of PEC-active electrodes, including $CuBi_2O_4$.

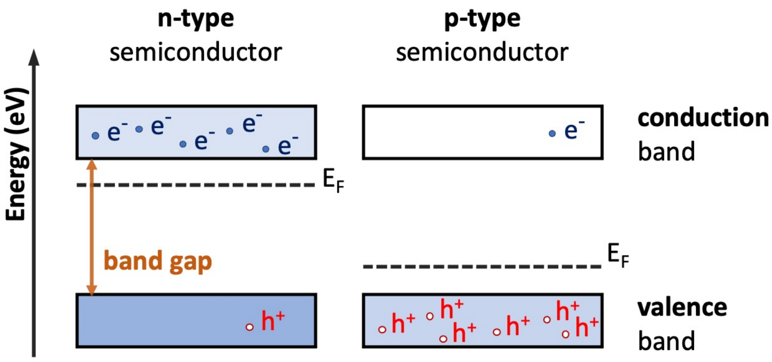

Figure 2.4: Schematic representation of the band structure for n-type and p-type semiconductors. In the scheme, the electrons and holes produced by thermal excitation are also shown. E_F indicates the energy of the Fermi level. Adapted from[136].

2.2.1 The electronic structure of semiconductors

The interaction of the atomic orbitals in a 3 dimensional solid determines the formation of electronic bands, which consist of a large number of orbitals tightly packed together in a limited energy interval. In semiconductors, we refer to the highest occupied electronic band as the *valence band* and to the lowest unoccupied band as the *conduction band*. The energy difference between the top of the valence band and the bottom of the conduction band defines the *band gap*, which is typically in the range of 0.3 to 3.5 eV. The band gap establishes the minimum photon energy required for the semiconductor to absorb light.

Upon thermal excitation or photo-absorption, a fraction of the electrons is promoted from the valence to the conduction band, determining the appearance of charge carriers in terms of electrons in the conduction bands and holes (i.e. electron vacancies) in the valence band. The mobility and concentration of the charge carriers dictate the electrical conductivity properties of semiconductors. The semiconductor conductivity is enhanced by the presence of defects or dopants, which increases the number of electron or holes charge carriers. A semiconductor where electrons constitute the majority carriers is called *n-type semiconductors*. When the majority carriers are holes the semiconductor is *p-type*.

Figure 2.4 schematically illustrates the energy diagram for n- and p-type semiconductors. Here, we further indicate the energy of the Fermi level E_F, which defines the electro-chemical potential of the semiconductor. The Fermi level lies between the valence and conduction band and is positioned closer to the conduction or valence band depending on whether the semiconductor is n-type or rather p-type.

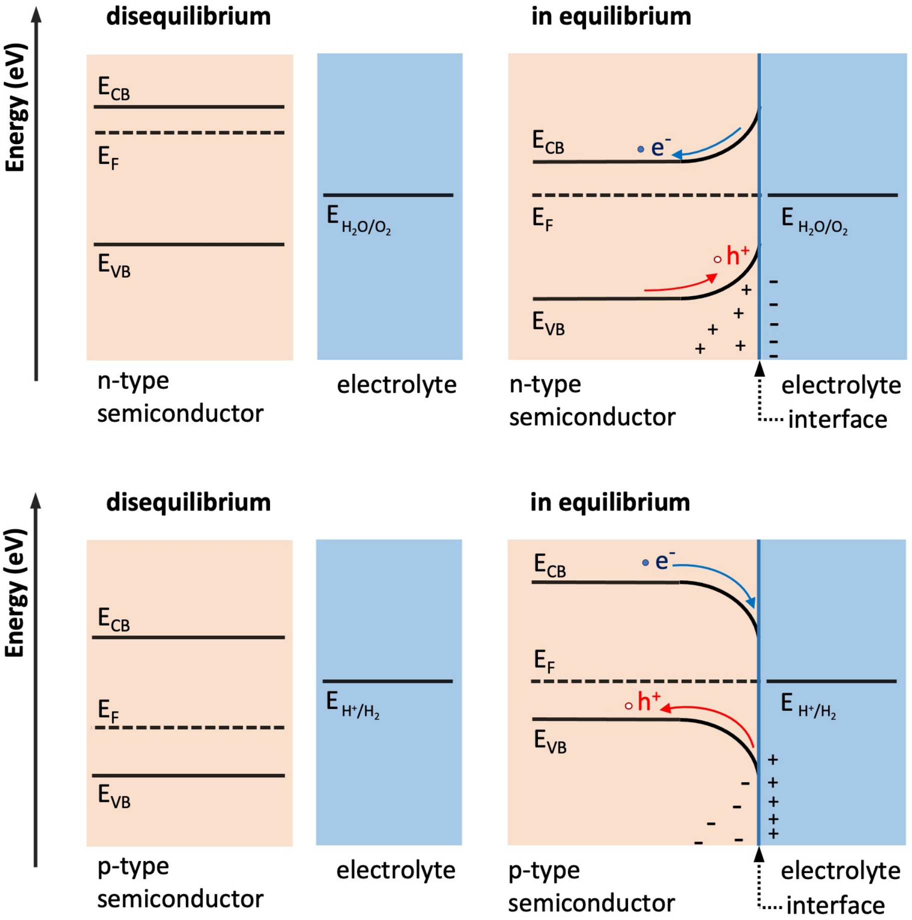

Figure 2.5: Band diagram for a n-type (*top*) and a p-type (*bottom*) semiconductor before and after reaching equilibrium with a liquid phase. For illustrative purposes, the movement of the (few) electrons and holes generated by thermal excitation is also shown. Adapted from[136].

2.2.2 The semiconductor-liquid junction

When a semiconductor comes into contact with an electrolyte, electrical charges transfer at the semiconductor-electrolyte interface due to the gap in electrochemical potential between the two media.

Figure 2.5 illustrates the band energy of the semiconductor before and after the charge transfer. In n-type semiconductors, the Fermi level typically lies above the redox potential of the electrolyte, prompting electrons to move from the solid to the liquid phase. Conversely, p-type semiconductors generally accept electrons from the liquid. At equilibrium, the Fermi level of the semiconductor aligns with the redox potential of the liquid and no net flow of charges takes place. Unshielded electrical charges on the liquid side of the semiconductor-electrolyte interface create a built-in electrical potential in the

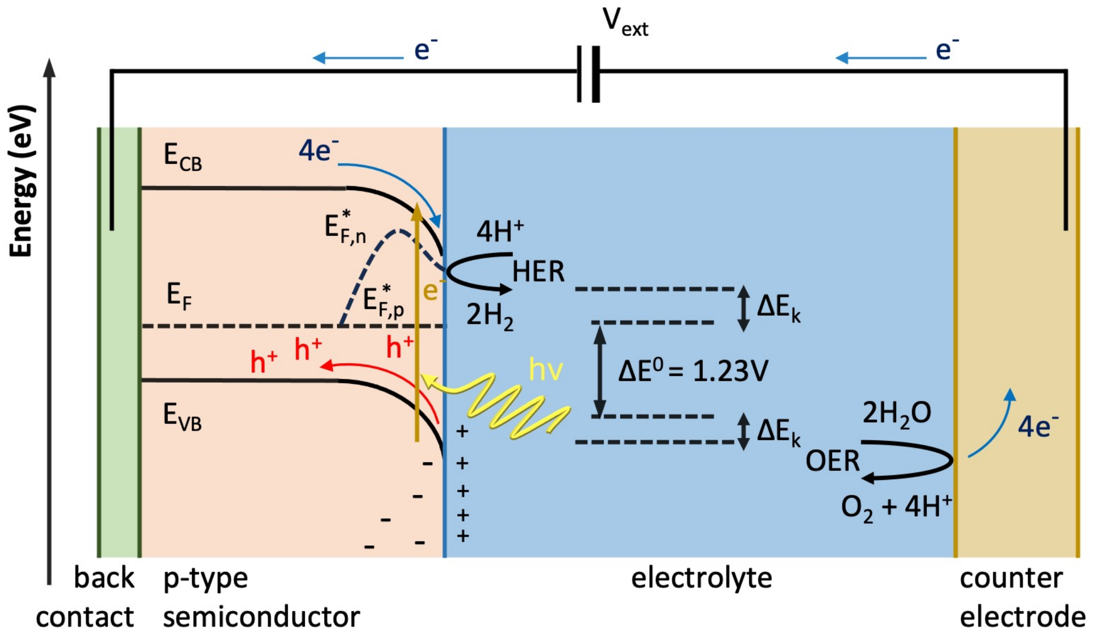

Figure 2.6: Schematic representation of a PEC cell embedding a p-type semiconductor as working electrode and a metal as counter electrode. Adapted from[137]

.

semiconducting material, causing the valence and conduction bands of n-type (p-type) semiconductors to bend upwards (downwards). The application of an external bias to the semiconductor further allows to experimentally tune the steepness of the band bending.

Due to the bending of the electronic bands, charge carriers separate and the minority carriers move toward the solid-liquid interface, where they can react with water to produce either H_2 or O_2. However, in the absence of illumination the concentration of minority carriers is low and conversion of water is inhibited. In the next section we shall see how the light absorption properties of a semiconductor embedded in a PEC cell can effectively increase the number of minority carriers, thereby facilitating the water splitting reaction.

2.2.3 The PEC cell

Figure 2.6 offers a scheme of a PEC cell embedding a p-type semiconductor. Here, the semiconductor constitutes the *working electrode* (WE), while a metal catalyst act as *counter electrode* (CE). Alternatively, the counter electrode could also be constituted by a semiconductor material. In that case, the resulting cell is named a *PEC tandem cell*.

Upon illumination, excitons, i.e. electron-hole pairs, are generated at the working electrode. Due to the electric potential close to the electrode surface, electrons separate from the holes and moves to the liquid interface, where they react with the water molecules to perform the HER. Simultaneously, the holes are extracted through the back side of the semiconductor and sent to the counter electrode to perform the complementary OER. Under illumination, the electrochemical potential of the semiconductor and the liquid is no longer in equilibrium, and the single E_F level splits into two *pseudo-Fermi levels* ($E^*_{F,p}$ and $E^*_{F,n}$), as shown in **Figure 2.6**. The energy difference between the pseudo-Fermi levels defines the *internal photovoltage* V_{ph}, which must be larger than the ΔE^0 of the water splitting reaction due to kinetic effects. Experimentally, the value of V_{ph} can be tuned by application of an external bias.

In addition to the absolute value of V_{ph}, a good alignment of the pseudo-Fermi levels with the redox potential for water reduction and oxidation is also crucial for effectively split water molecules. The chemical potential of the Fermi level is generally determined by use of a *reference electrode* (RE).

2.2.4 Diagnostic measurements for PEC electrodes

Several methods exist to determine the PEC properties of semiconductors.[138] Here, we restrict ourselves to a brief introduction for only few selected diagnostic measurements, as we will encounter them in the later chapters of this thesis.

Open circuit potential (OCP)

An OCP measurement is aimed in determining the value of V_{ph} for a semiconductor. The survey is performed in the absence of external bias and without electrical current flow between the working and the counter electrodes. Under these conditions, the potential difference between the semiconductor and the reference electrode is measured both under light illumination and in dark. The difference between the two values determines V_{ph}. Generally, V_{ph} is a function of the illumination intensity unless a sufficiently intense radiation is used. In that case, the value of V_{ph} saturates and the measured internal photovoltage correspond to the flat band potential for the material.[138]

Linear sweep voltametry (LSV)

In a LSV, the working electrode is electrically connected to the counter electrode and the electrical current is measured as a function of an applied external potential measured vs. the reference electrode. Under illumination, an LSV measurement permits to monitor the photo-electrochemical activity of the electrode. Due to the absorption of light, electron-hole pairs forms and a current flow is observed at higher (absolute) applied external potentials than a certain threshold, known as the *photocurrent onset potential*.

An LSV measurement in dark provides complementary information over the electrochemical activity of the electrode. In this measurement, the electrical current appears at a higher (absolute) onset potential compared to the light conditions and often stems from side corrosion processes. The maximum value of electrical current measured within a potential range where no dark currents are observed is therefore commonly considered as the maximum photo-electrochemical current achievable for a given semiconductor.[138]

Chronoamperometry (CA)

A CA provides information about the long-term stability of a PEC-active semiconductor. During the measurement, a constant external potential is applied between the working electrode and the counter electrode, and the electrical current is monitored as a function of time under either continuous or chopped light illumination. A decrease in the measured electrical current typically stems from a decrease in the electrode activity and generally indicates the occurrence of chemical or morphological degradation phenomena affecting the electrode.

2.2.5 The photocorrosion of PEC-active films

The rapid photocorrosion phenomena affecting most semiconductors during operation currently significantly hinders the widespread use of PEC water splitting devices in real-world applications.[20,21,138] Common degradation pathways include the dissolution of the photo-absorbing material into the electrolyte, phase transformations due to the reduction/oxidation of the metallic species under applied bias and/or illumination, loss of the semiconductor layer from the electrode surface, and the morphological restructuring of the electrode surface. Such complex degradation mechanisms cause a decline in the PEC performances. For example, Cu_2O photocathodes reduce to the inactive metallic Cu phase and concurrently oxidize to release Cu^{2+} ions into the electrolyte.[139] $BiVO_4$ photoanodes dissolve into stoichiometric Bi and V species leading to a progressively reduced thickness of the photo-absorbing layer,[140] while the surface of metal nitride electrodes passivates due to the formation of a metal oxide layer, which prevents the efficient charge transport at the semiconductor-electrolyte interface.[141–143]

$CuBi_2O_4$ has recently emerged as a promising PEC material due to its favorable electronic properties, namely a suitable band gap of 1.6–1.8 eV,[144] p-type conductivity, and a very cathodic onset potential of ca. 1 V vs. RHE (Reversible Hydrogen Electrode).[145] However, the achievable photocurrents from bare $CuBi_2O_4$ electrodes are limited by the poor charge carrier mobility and the short carrier diffusion length, and decay rapidly in steady-state conditions while at the same time no hydrogen is produced, thus indicating that the measured photoactivity likely restricts to a photocorrosion process.[146] A recent report suggests that $CuBi_2O_4$ electrodes degrade similarly to Cu_2O during operation, i.e. via consumption of the photogenerated electrons to the reduction of the Cu^{2+} cations to either Cu^{+} or Cu^{0}.[146] However, this hypothesis lacks experimental evidence.

In situ and operando investigations can provide systematic insights into the photocorrosion phenomena by monitoring the PEC material under relevant time scales and operating conditions, i.e. under applied bias and illumination. So far, ambient pressure X-ray photoelectron spectroscopy (APXPS), inductively coupled plasma mass spectroscopy (ICP-MS) and in situ UV-Vis spectroscopy have been used to assess the photocorrosion mechanism of Cu_2O, WO_3, $BiVO_4$ and n-GaP photoelectrodes under realistic working conditions.[147–150] However, these methods are limited to the determination of the local atomic environment or to the concentration of atomic species in solution. Conversely, X-ray scattering techniques, including TS-PDF and SAXS, are sensitive to morphological and structural changes ranging from the atomic up to nanometer length scales. Thus, they enable to probe local atomic structures, as well as the restructuring of the electrode surface, and the formation of new phases. Despite this potential, operando X-ray scattering investigations are currently limited to a few electrochemical studies,[151,152] and the technique has not yet be applied to monitor the surface of photoactive films in a PEC cell. The operando measurement of both TS-PDF and SAXS thus holds promise to provide novel insights into the degradation phenomena which hinders the performances of PEC-active electrodes.

2.3 X-ray based methods to the structural characterization of nanomaterials

X-rays serve as fundamental tools for the chemical and structural analysis of materials. Essentially, X-rays are electromagnetic waves with wavelengths between 10^{-8} and 10^{-10} m. Their short wavelength gives rise to unique properties crucial for material analysis. Firstly, their long penetration length enables to probe bulk materials, allowing researchers to explore their internal structure non-destructively. Secondly, their high photon energy facilitates the excitation of electrons tightly bound to the atomic nuclei and thus provide information about the electronic configuration of the absorbing atom. Lastly, their short wavelength, comparable to inter-atomic distances in matter, enables self-interference phenomena for scattering events occurring at the atomic positions, thereby permitting to determine the atomic configuration of the irradiated sample.

In this chapter, we provide a general outline relative to the main analytical tools to the structural characterization of nanomaterials by the use of X-ray radiation. The discussion is based on the excellent textbooks from Als-Nielsen and McMorrow[153], and Egami and Billinge[154]. Readers who seek a more comprehensive treatment of the methods below are referred to the mentioned material.

2.3.1 X-ray Scattering

An X-ray wave travelling through a medium determines the presence of alternating electric field (E) which causes the electrons in the medium to oscillate. In turn, the accelerated electrons produce an electron-magnetic wave which propagates in all directions perpendicular to the electron oscillating direction, effectively scattering the incoming radiation.

For unbound or weakly bound electrons, the oscillating motion happens at the same frequency as for the incoming X-rays. This process is elastic and is named *Thomson scattering*. Due to elastic scattering, the direction of the incoming wavevector changes, but its modulus is preserved.

Figure 2.7 schematically illustrates an X-ray scattering measurement performed in transmission geometry and with use of an area detector. Since both the X-ray source and

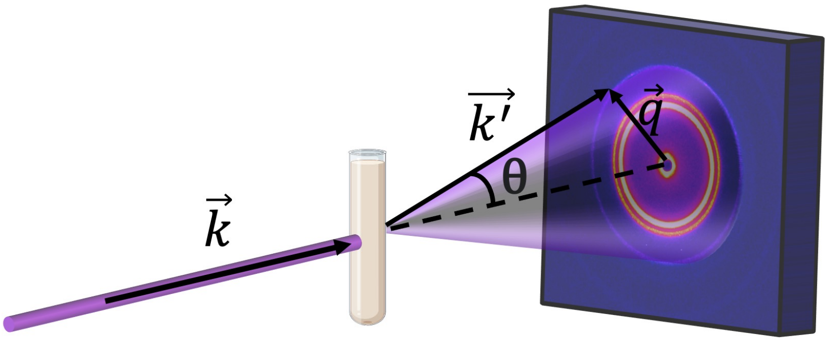

Figure 2.7: Scheme of an X-ray scattering experiment on an isotropic sample. An X-ray beam hits the sample and the resulting scattering cone is measured by means of an X-ray area detector. The incoming and scattered wawevectors $\vec{k}$ and $\vec{k'}$ and the wavevector transfer $\vec{q}$ relative to one of the represented diffraction rings are additionally shown.

the detector are far from the scattering point, the *far-field limit* applies and the incident and scattered X-rays can be considered as planar wave. The difference between the incoming $\mathbf{k}$ and the outcoming $\mathbf{k}'$ wavevectors defines the wavevector transfer $\mathbf{q} = \mathbf{k} - \mathbf{k}'$, and the modulus of q relates to the scattering angle as:

$$|\mathbf{q}| = 2k\ sin(\theta) = \frac{4\pi}{\lambda} sin(\theta) \tag{2.2}$$

In our approach, we utilize the *kinematic approximation* and disregard multiple scattering events. This assumption remains valid for scattering experiments conducted on materials with short-range order or powders, as these samples typically exhibit small scattering cross-sections and limited coherent lengths.

The scattering amplitude $A(\mathbf{q})$ generated by a an electron cloud results from the integration of the electron density $\rho(\mathbf{r})$:

$$A(\mathbf{q}) = -r_0 \int \rho(\mathbf{r}) e^{i\mathbf{q}\cdot\mathbf{r}} dv_r \tag{2.3}$$

Here, r_0 is the Thomson scattering length and v_r is the total volume of the scattering medium. The term $e^{i\mathbf{q}\cdot\mathbf{r}}$ accounts for the phase shift between wavevectors scattered at a distance $\mathbf{r}$ and with wavevector transfer $\mathbf{q}$.

In an X-ray scattering measurement, the quantity experimentally accessible is the scattering intensity $I(\mathbf{q})$, which is the square of the amplitude function:

$$I(\mathbf{q}) = \frac{|A(\mathbf{q})|^2}{r_0^2} = \int \rho(\mathbf{r})\rho(\mathbf{r}')e^{i\mathbf{q}\cdot(\mathbf{r}'-\mathbf{r})}dv_r dv_{r'} \tag{2.4}$$

where $I(\mathbf{q})$ is now conventionally formulated in units of r_0. According to (2.4), the scattering intensity corresponds to the Fourier transform of the autocorrelation function of the electron density. The total electron density of the scattering medium can be further expressed as the sum of the electron density surrounding individual atoms, by use of the atomic form factor $f^0(\mathbf{q})$

$$f^0(\mathbf{q}) = \int_{atom} \rho(\mathbf{r})e^{i\mathbf{q}\cdot\mathbf{r}}dv_r \tag{2.5}$$

For forward scattering, $\mathbf{q} = |\mathbf{q}| = 0$ and $f^0(\mathbf{q})$ equals the atomic number Z, while its value approaches 0 for $\mathbf{q} \to 0$. The exact value of the atomic form factor as a function of $\mathbf{q}$ depends on the shape of the atomic orbitals and is tabulated for each element.

Equation (2.4) can be re-written by replacing the integral with the sum over all atom pairs:

$$I(\mathbf{q}) = \sum_i \sum_j f_i^0(\mathbf{q}) f_j^{0*}(\mathbf{q}) e^{i\mathbf{q}\cdot(\mathbf{r}_i - \mathbf{r}_j)} \tag{2.6}$$

In an X-ray scattering experiment conducted over liquids, nanostructured dispersions or powders, the X-rays interact with a collection of atomic groups which are randomly distributed. Therefore, only the modulus of $\mathbf{q}$ is effectively probed during the measurement, while the direction of $\mathbf{q}$ is isotropic. Eq. (2.6) can then be rewritten after averaging the phase factor $e^{i\mathbf{q}\cdot\mathbf{r}}$ over all orientations as:

$$I(q) = \sum_i \sum_j f_i^0(q) f_j^{0*}(q) \frac{sin(q\ r_{ij})}{q\ r_{ij}} \tag{2.7}$$

Eq. 2.7 is known as the Debye Scattering Equation (DSE). The espression for the *normalised structure factor* $S(q)$ is obtained after dividing the scattering intensity by the number of scatterers and the squared of the averaged atomic scattering amplitude:

$$S(q) = \frac{I(q)}{N\langle f(q)\rangle^2} = 1 + \frac{1}{N\langle f(q)\rangle^2} \sum_{i \neq j} f_i^0(q) f_j^{0*}(q) \frac{sin(q\ r_{ij})}{q\ r_{ij}} \tag{2.8}$$

We note that $S(q)$ approaches unity when $q \to 0$. Finally, $S(q)$ can be reformulated as the *reduced total scattering structure function* $F(q)$, given by:

$$F(q) = q(S(q) - 1) = \frac{1}{N\langle f(q)\rangle^2} \sum_{i \neq j} f_i^0(q) f_j^{0*}(q) \frac{sin(q\ r_{ij})}{r_{ij}} \tag{2.9}$$

As the atomic form factor approaches 0 at high-q, multiplying $S(q)$ by q amplifies the contribution of high-angle scattering data in $F(q)$. Although the high-q region of the scattering pattern is typically disregarded in traditional Bragg diffraction analysis, it becomes essential when performing structural analysis in real space through the atomic pair distribution function.

2.3.2 The atomic pair distribution function

In this section, we provide the analytical expression and an intuitive interpretation of the reduced atomic pair distribution function (PDF, $G(r)$).

We first introduce the radial distribution function $R(r)$, which is defined as

$$R(r) = 4\pi r^2 \rho(r) \tag{2.10}$$

and is closely related to the PDF. Here, $\rho = N/V$ is the atomic density, and $4\pi r^2$ describes the size of the spherical shell at a distance r. $R(r)$ therefore measures the number of atoms positioned at a given distance r from the origin.

Alternatively, we can express $R(r)$ as the histogram of the scattering amplitudes for all the atom-pair distances in the collection, averaged over the mean scattering amplitude of the constituent atoms:

$$R(r) = \frac{1}{N} \sum_i \sum_{j \neq i} \frac{f_i(q) f_j^*(q)}{\langle f(q)\rangle^2} \delta(r - r_{ij}) \tag{2.11}$$

where δ are Dirac functions.

$G(r)$ relates to $R(r)$ as:

$$G(r) = \frac{R(r)}{r} - 4\pi r \rho_0 \gamma_0(r) \tag{2.12}$$

where ρ_0 is the averaged atomic density of the material and $\gamma_0(r)$ is a characteristic shape function for the scattering object. The PDF thus intuitively defines the scaled probability of finding two atoms at a distance r in a material. This interpretation is schematically illustrated in **Figure 2.8** Due to its ability to probe the local atomic environment, PDF analysis proves especially valuable when investigating the atomic structure of short-range ordered or amorphous materials.

Experimentally, $G(r)$ is obtained after calculating the sine Fourier transform of $F(q)$ in the accessible range of q:

$$G(r) = \frac{2}{\pi} \int_{q_{min}}^{q_{max}} F(q) sin(qr) dq \tag{2.13}$$

The experiments is appropriately referred to as *X-ray total scattering* (TS) since the diffuse scattering intensity at high-q is also collected together with the X-ray diffraction peaks. Egami and Billinge have provided analytical expressions for the normalization and correction of the experimental $I(q)$ data prior to Fourier transform calculation.[154] However, comparable values of $G(r)$ are attained using a simplified approach, based on the use of an *ad hoc* correction algorithm. In this study, we prefer this method, which is integrated into the software package *PDFGetX3*.[155]

By performing the Fourier transformation over a limited range in q, some artefacts generate in the experimental $G(r)$ due to the convolution of the ideal $G(r)$ with a step function initiating at q_{max}. Such artefacts take the form of terminating ripples which oscillate with a period of $\approx 2\pi/q_{max}$. Moreover, the truncation of the scattering signal at low angle determines the presence of the second term in Eq. 2.12, which produces a negative slope in the baseline at low-r. The rigorous derivation of the latter effect is shown by Farrow et al.[156]

2.3.2.1 Rapid acquisition of PDF data

A key experimental requirement to achieve high-resolution PDF data is the measurement of the scattering intensities up to high values of the scattering vector q. However, scattering patterns tend to be less defined and more noisy at high-q due to the decrease in the amplitude of the X-ray atomic form factors. In a typical in-house setup, consisting of an X-ray anode and a point detector, this issue is circumvented by greatly increasing the acquisition time to improve the signal-to-noise ratio at wider scattering angles. How-

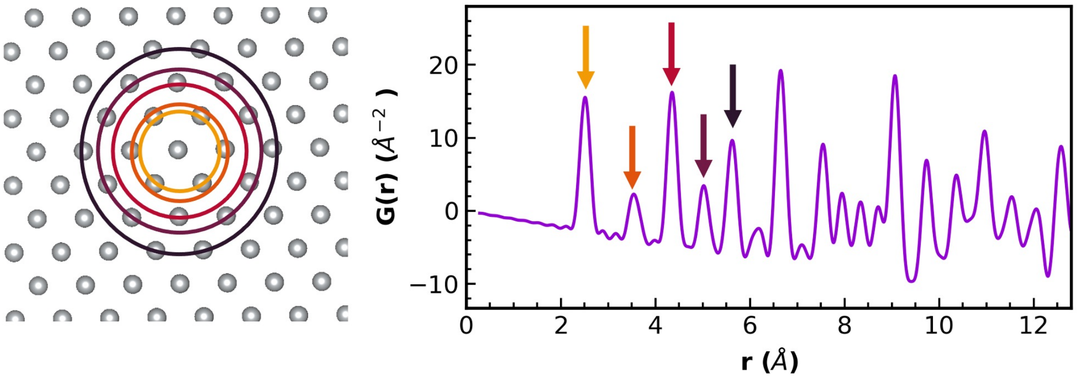

Figure 2.8: Illustration of the physical interpretation of the atomic pair distribution function. Each peak in the PDF corresponds to the normalized probability of finding an atom in a shell of radius r from an other atom, which is located in the origin.

ever, these measurements are very slow and typically take up to several hours even for crystalline samples.

At the synchrotron, the rapid acquisition of the pair distribution function is obtained by combining the high-flux radiation to the use of an image-plate (IP) detector.[157] The detector is usually positioned to intersect the direct beam at its center or alternatively at one corner, and improved statistics at high-q are obtained by the increasing number of pixels at longer radial distances from the beam point of normal incidence (PONI). The sample-to-detector distance (SDD) is then adjusted so to measure the scattering signal up to 25-30 $Å^{-1}$. By increasing the SDD, higher values of q_{max} are collected at the expense of a reduced q-resolution due to the finite pixel size. High-energy X-ray radiation with energy above 50 keV is typically employed to reduce the geometrical amplitude of the scattering cone.

Measurements of a standard allows to precisely calibrate the geometry of the experiment, i.e. the relative position and orientation of the sample and the detector. Since IP detectors cannot discriminate on the energy of the detected radiation, the measured signal is the sum of elastic scattering, unelastic (Compton) scattering and fluorescence. Most of these contributions are corrected prior to the PDF extraction.[154,155,158,159]

Figure 2.9 shows the data reduction stages to obtain the PDF starting from the azimuthally integrated total scattering data. The first step consists in the removal of the background scattering signal generated by all experimental components but the sample

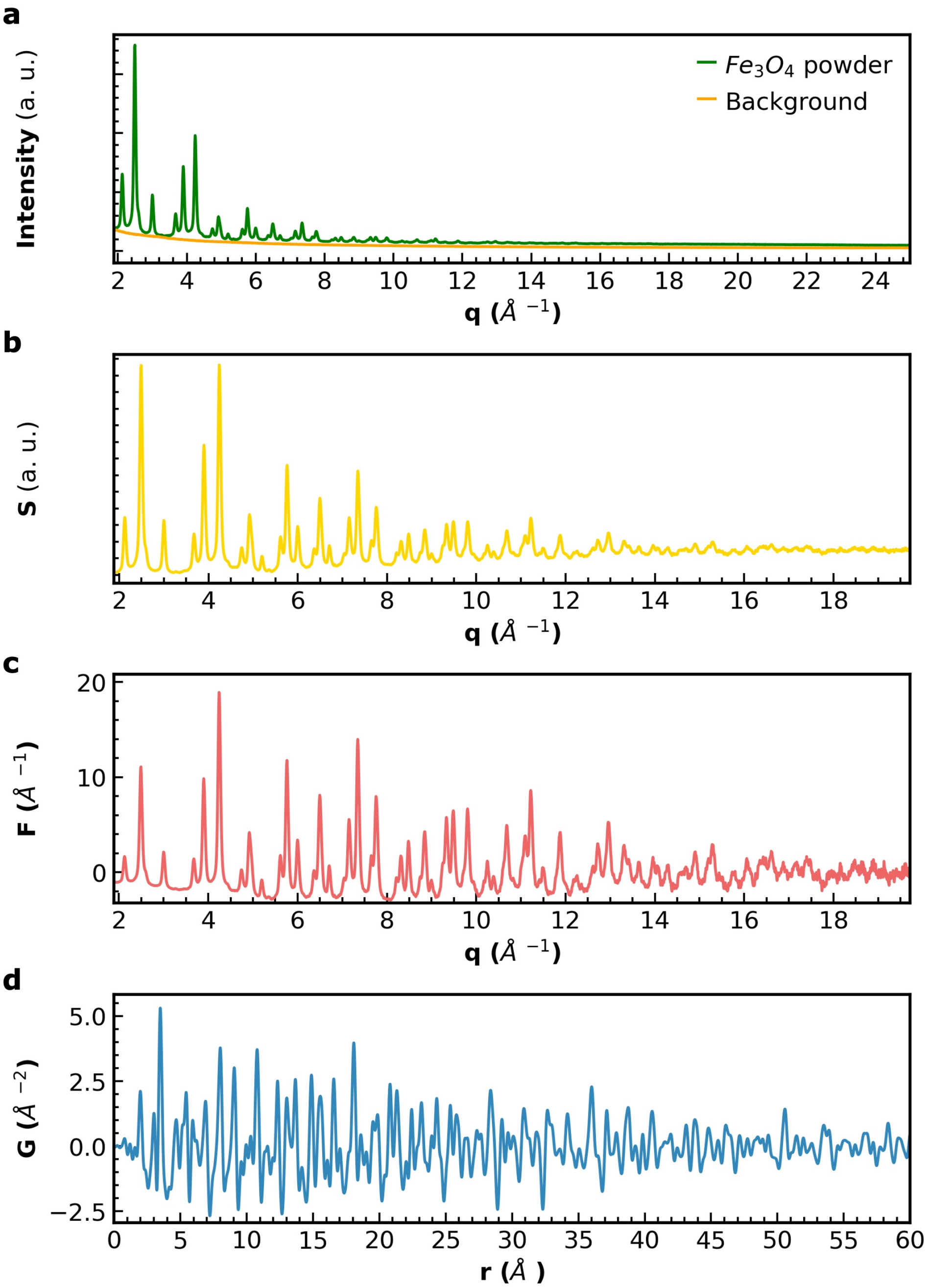

Figure 2.9: Data processing steps applied to a Fe_3O_4 crystalline powder measured in a 1 mm polyamide capillary. **a**) Plot of the total scattering intensity from the sample measurement $I(q)$ and the scaled background intensity. The latter is dominated by the signal from the capillary as well as by air scattering. **b**) Plot of the total scattering structure factor $S(q)$. **c**) Plot of the reduced structure factor $F(q)$. **d**) Plot of the pair distribution function $G(r)$

of interest. Air scattering and scattering from the sample container all contribute to the background. In this work, we determine the background signal by performing a separate X-ray scattering measurement in the exact same conditions as for the main experiment in the absence of the sample. For in situ runs, we performe time-resolved measurements of the scattering signal generated by the heated solvent mixture in the absence of the nanoparticle precursors. We then remove the background contribution from the total in situ scattering signal by use of a scale factor, which we select either manually or by using an automated routine to deliver a background-subtracted intensity pattern which approaches 0 at high-q.

The resulting intensities are then converted into the total scattering structure factor $S(q)$ and further to the reduced structure factor $F(q)$. As the signal-to-noise ratio becomes unfavorable at high-q, it is necessary to introduce a q_{max} parameter to limit the q-range of the data before Fourier transforming $F(q)$ into $G(r)$. Selection of an appropriate value of q_{max} must be performed carefully, as noise removal via decreasing of the selected q_{max} value comes at the expense of a lower resolution in r of the outcoming $G(r)$.

2.3.2.2 Modeling the PDF

The PDF provides a survey of the interatomic distances in a given material. Due to its intuitive nature, even a qualitative inspection of the experimental PDF provides valuable insights into the atomic structure of the sample. Apart from the presence of the terminating ripples, the peak positions in the PDF directly reflect the interatomic distances in direct space. In the interpretation of the in situ measurements, the formation or consumption of chemical compounds can be directly inferred after observing an increase or decrease in the PDF intensity and their characteristic bond distances. Moreover, the intensity of the PDF peaks correlates with the number of atomic pairs involved in a specific interatomic distance, and the peaks are more intense when heavier elements are involved in the atomic pair. Finally, the peak width determines the distribution of the atomic distances in the atom-atom pair, and directly correlates with the atomic thermal vibrations.

In addition to these qualitative observations, more detailed structural information are extracted after comparison of the experimental PDF data with simulated data generated from a model structure. In this work, modeling of the PDF is performed either within the attenuated crystal (AC) approximation or by use of discrete atomistic models and of the DSE. These two approaches are outlined in the next paragraphs.

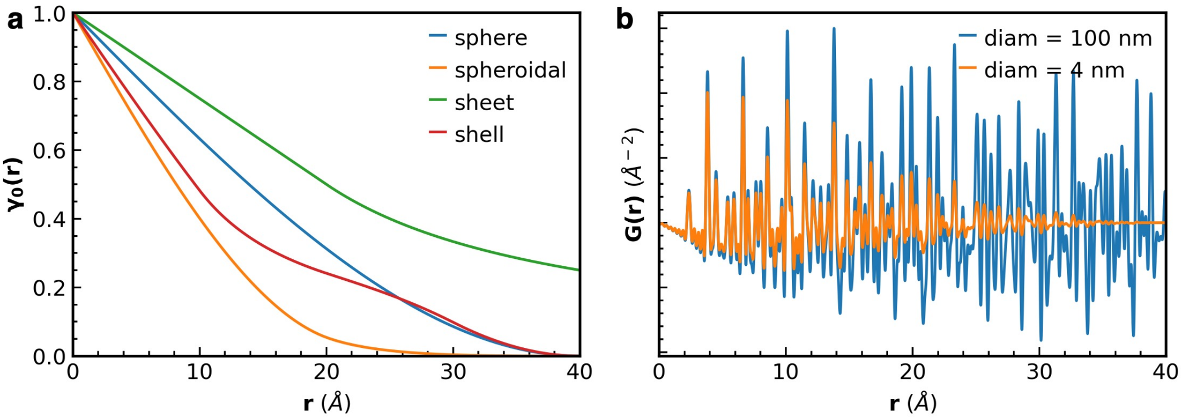

Figure 2.10: Modelling of the PDF by the AC approximation. **a**) The characteristic dampening function $\gamma_0(r)$ profiles for selected shapes of the crystalline domain. The plot includes a sphere (spherical diameter = 40 Å), a spheroidal (axial and equatorial sizes = 40 and 20 Å, respectively), a 20 Å thick sheet, and a shell with internal and external diameter of 20 and 40 Å. **b**) Comparison of the simulated PDF profiles for a spherical CeO_2 crystalline domain with a diameter of 100 and 4 nm, respectively. The different sizes in the model affect the intensity of the simulated PDF peaks, but not their position and shape.

Modelling by the AC approximation We employed the AC approximation to model the PDF of nanocrystalline materials. This method utilizes a small box approach, where a single crystallographic unit cell is replicated based on the lattice symmetry using periodic boundary conditions. The resulting PDF is then convoluted with a characteristic dampening function, $\gamma_0(r)$, to account for the finite size and unique shape of coherent crystalline domains. In this work, we model the PDF via AC approximation by use of the *PDFGenerator* class implemented in *Diffpy-CMI* python package.[160]

Figure 2.10 shows the $\gamma_0(r)$ profiles for selected shapes and further showcases the effect of convoluting the simulated PDF of CeO_2 with $\gamma_0(r)$ functions for spheres of different sizes. The AC approximation serves as the direct-space analogue of the Rietveld refinement in reciprocal space.[161]

We calculated the PDF in direct space, according to:

$$G(r) = \frac{1}{Nr} \sum_i \sum_{j \neq i} \left[\frac{f_i f_i^*}{\langle f \rangle^2} exp\left(\frac{-(r - r_{ij})^2}{\sigma_{ij}^2} \right) \right] - 4\pi r \rho_0 \tag{2.14}$$

where ρ_0 is the averaged atomic number for the sample and N is the number of atoms in the model.[162] The δ function of eq. 2.11 are here substituted with the broadening term

$exp(-(r-r_{ij})^2/\sigma_{ij}^2)$, where σ_{ij} is defined as

$$\sigma_{ij} = \sigma'_{ij}\sqrt{1 - \frac{\delta_1}{r_{ij}} - \frac{\delta_2}{r_{ij}^2} - q_{broad}^2\ r_{ij}^2} \tag{2.15}$$

σ'_{ij} is the mean squared displacement due to atomic thermal vibrations.[163] δ_1 and δ_2 are correction factors that can be alternatively used to account for correlated atomic motions, while q_{broad} models the PDF peak broadening due to the finite resolution in q of the experimental data. The limited range in q of the scattering data further results in a dampening of the PDF peak intensity, which we model by multiplying the PDF calculated via eq. 2.14 by the dampening function $B(r) = e^{-(r\ q_{damp})^2/2}$. Both q_{broad} and q_{damp} are instrumental parameters which depend on the particular geometry of the experiment and on the size of the detector pixels. In practise, values of q_{broad} and q_{damp} are determined upon a separate refinement of the experimental PDF after measurement of a calibrant, i.e. of a stable micro-crystalline material, at the exact same conditions as the sample.

Finally, the calculated PDF is multiplied by the γ_0 function, accounting for the geometrical shape of the coherent domain. For spherical domains, this takes the form:

$$\gamma_0(r) = \left[1 - \frac{3r}{2d} + \frac{1}{2}\left(\frac{r}{d}\right)^3\right] H(d-r) \tag{2.16}$$

where d is the diameter of the sphere and H is a step function which is equal to 1 for $d < r$ and zero otherwise.[164] Analytical functions also exist for other geometrical shapes.[165].

Quantitative structural information is extracted after minimization of the weighted residual R_w between the calculated and the experimental PDFs. R_w is defined as:

$$R_w(\mathbf{P}) = \sqrt{\frac{\sum_{n=1}^{n} |G_{exp}(r_n) - G_{calc}(r_n, \mathbf{P})|^2}{\sum_{n=1}^{n} G_{exp}(r_n)^2}} \tag{2.17}$$

where r_n are the discrete points of the experimental data and $\mathbf{P}$ is the parameter vector used to build the model structure. Typical parameters involved in the refinement are the lattice constants and angles, the symmetry constrained atomic displacement parameters (ADP), and δ_1 or δ_2. The refinement can further include the dimensions of the coherent crystalline domain, as well as the atomic displacement and occupancy of selected lattice sites.

Modelling the PDF by discrete atomistic models The assumption of periodic boundary conditions doesn't always provide a suitable model to interpret the experimental PDF. During the synthesis of nanoparticles, organometallic intermediate complexes emerge in solution that display short-range order and obviously lack a periodic arrangement. In realistic nanoparticle systems, the presence of twinned boundaries, surface defects, highly anisotropic shapes or locally amorphous structures does not fit the ideal single-crystalline configuration assumed in the AC approximation. In all these cases, the non-periodicity of the sample required more sophisticated discrete atomistic models, which allow to explicitly account for the positions of each individual atom in the sample. Once the model is provided, the scattering intensity is first computed directly from the atomic coordinates via the DSE, and then Fourier transformed to the PDF.

To account for the Debye-Weller effects, the DSE in 2.7 is modified into:

$$F(q) = \frac{1}{N\langle f\rangle^2} \sum_{i\neq j} f_i^0 f_j^{0*} (e^{-\frac{1}{2}\sigma_{ij}^2 q^2}) \frac{sin(q\ r_{ij})}{r_{ij}} \tag{2.18}$$

where σ_{ij} is the correlated broadening factor for the atom pair.[166] The termination effects due to the finite q range of the data are then explicitly accounted in the evaluation of the Fourier transform via eq. 2.13.

A significant drawback of the reciprocal-space calculation lies in its heightened computational cost compared to the real-space counterpart owed to the increased number of atomic pairs which are involved in the calculation. In this work, we perform PDF modelling via DSE by use of the *DebyePDFGenerator* class within *Diffpy-CMI* package.[160] While only few software packages are available for building atomistic models of nanoparticles[167–169], numerous tools exists to create molecular structures. Among those, the freely available software *Avogadro* represents a popular choice.[170]

2.3.3 Small-angle X-ray scattering

In Section 2.3.1 we showed that the intensity measured during a scattering measurement corresponds to the product of the form factors for atomic pairs times a phase term of the form $e^{iq(\mathbf{r}_i - \mathbf{r}_j)}$. We can assume for simplicity a mono-atomic system to rearrange eq. 2.6 into:

$$I(\mathbf{q}) = Nf(\mathbf{q})^2 + f(\mathbf{q})^2 \sum_i \sum_{i \neq j} e^{iq(\mathbf{r}_i - \mathbf{r}_j)} \tag{2.19}$$

where N is the total number of atoms. We can now replace the sum over $i \neq j$ with an integral of the atomic number density over the volume of the atomic arrangement:

$$I(\mathbf{q}) = Nf(\mathbf{q})^2 + f(\mathbf{q})^2 \sum_i \int_V \rho_n(\mathbf{r}_{ij}) e^{iq(\mathbf{r}_i - \mathbf{r}_j)} dV_j \tag{2.20}$$

where dV_j is a volume element located at a position $\mathbf{r}_i - \mathbf{r}_j$. The X-ray scattering signal ultimately arises from local deviations of the electron density from the average density ρ_{at}. I subtract and add a term proportional to ρ_{at} to get:

$$\begin{aligned} I(\mathbf{q}) = & \underbrace{Nf(\mathbf{q})^2 + f(\mathbf{q})^2 \sum_i \int_V \left[\rho_n(\mathbf{r}_{ij}) - \rho_{at}\right] e^{iq(\mathbf{r}_i - \mathbf{r}_j)} dV_j}_{I^{SRO}(\mathbf{q})} \\ & + \underbrace{f(\mathbf{q})^2 \rho_{at} \sum_i \int_V e^{iq(\mathbf{r}_i - \mathbf{r}_j)} dV_j}_{I^{SAXS}(\mathbf{q})} \end{aligned} \tag{2.21}$$

Here, the $I^{SRO}(\mathbf{q})$ is sensitive to the short range order (SRO) and hence contains contribution from typical inter-atomic distances. Conversely, the term $I^{SAXS}(\mathbf{q})$ contributes to the scattering signal for $q \to 0$ and thus contains information over the structure, i.e. size and shape, of larger sized objects, such as polymers, micelles or nanoparticles. This part of the scattering signal is referred to as small-angle X-ray scattering (SAXS).

We can now introduce the single-particle form factor $F(\mathbf{q})$, defined over the particle volume V_p:

$$F(\mathbf{q}) = \frac{1}{V_p} \int_{V_p} e^{i\mathbf{q}r} dV_p \tag{2.22}$$

and model the scattering intensity of an isolated single particle as

$$I_p^{SAXS}(\mathbf{q}) = \Delta\rho^2 V_p^2 |F(\mathbf{q})|^2 \tag{2.23}$$

where $\Delta\rho = \rho_p - \rho_s$ is the scattering length difference between the particle and its surroundings. $F(\mathbf{q})$ can be calculated analytically for few shapes,[171] including spheres:[153]

$$F(q)_{sphere} = 3\left[\frac{sin(qR) - qRcos(qR)}{q^3R^3}\right] \tag{2.24}$$

For polydispersed samples, SAXS intensity is modelled according to the particle size distribution function $D(R)$:

$$I(q)^{SAXS} = \Delta\rho^2 \int_{V_p} D(R) \cdot V_p(R)^2 \cdot |F(q,R)|^2 dR \tag{2.25}$$

We now consider which useful information can be extracted via analysis of the SAXS profiles. In the short wavelength limit, typically with $q > 0.1$ Å^{-1}, qR is much bigger than 1 and eq. 2.24 can be combined to eq. 2.23 to yield the *Porod law*:

$$I(q)^{SAXS} = \frac{4\pi\ \Delta\rho^2}{q^4} S_p \tag{2.26}$$

Therefore, in the Porod regime the intensity of the scattering signal is proportional to the surface area of the sphere S_p and is predicted to decay by a power law with exponent -4. In fact, the exponent of the power law depends on the surface morphology and dimensionality of the scattering object and reduces to smaller (absolute) values for rougher surfaces.[172] The analysis of the scattering intensity in the Porod-regime thus provides information over porosity, shape and interfacial structure of nanoparticles.

Differently, in the long wavelength limit $qR \rightarrow 0$ an appropriate trigonometric expansion of eq. 2.24 leads to:

$$F(q)_{sphere} = 1 - \frac{(qR)^2}{10} \tag{2.27}$$

which can be substituted in eq. 2.23 to outcome, after further rearrangements, in the *Guinier law*:

$$I_p^{SAXS}(\mathbf{q}) = \Delta\rho^2 V_p^2 e^{-q^2 R_g^2/3} \tag{2.28}$$

where R_g^2 is the *radius of gyration*, defined as the root-mean-squared distance from the particle center of gravity. Therefore, fitting the dependency of the X-ray scattering intensity at low-q via eq. 2.28 provides a direct measurement of the size of the nanoparticles.

Finally, when the distances between the particles are comparable to the particle sizes, the SAXS intensity results in:

$$I_p^{SAXS}(\mathbf{q}) = \Delta\rho^2 V_p^2 |F(\mathbf{q})|^2 S(\mathbf{q}) \tag{2.29}$$

where $S(\mathbf{q})$ is the structure factor, which accounts for inter-particles correlations. For completely random arrangements of the particles, $S(\mathbf{q}) = 1$ and eq. 2.29 reduces to eq. 2.23. Conversely, for highly ordered nanoparticle systems such as in colloidal crystals[173,174] or mesocrystals,[55,148] the structure factor exhibits sharps peaks in the small-angle regime.

2.3.4 X-ray diffraction

When an X-ray beam impinges on a crystal, the scattering pattern transforms into a periodic arrangement of high-intensity spots. This phenomenon is called X-ray diffraction (XRD) and can be exploited to determine the atomic structure of crystalline materials.

We define a crystal as a periodic arrangement of atoms forming a lattice with translational simmetry. A set of lattice vectors $\mathbf{R_n}$

$$\mathbf{R_n} = n_1\mathbf{a_1} + n_2\mathbf{a_2} + n_3\mathbf{a_3} \tag{2.30}$$

defines each point of the lattice. Here, $\mathbf{a_1}$, $\mathbf{a_2}$ and $\mathbf{a_3}$ are the lattice vectors, and n_1, n_2 and n_3 are integer numbers. The vectors **a1**, **a2** and **a3** defines the size of the unit cell, i.e. the repeating unit of the lattice. The adoption of a set of lattice vectors to describe a crystal represents a very powerful tool, as by knowing the position $\mathbf{r_j}$ of each of the j-atoms in the unit cell, vectors of the kind $\mathbf{r_j} + \mathbf{R_n}$ can be used to describe all atomic positions in the crystal.

The scattering amplitude from a crystal can be therefore written as:

$$A^{crystal}(\mathbf{q}) = -r_0 \sum_{\mathbf{r_j}+\mathbf{R_n}} f_j(\mathbf{q}) e^{i\mathbf{q}\cdot(\mathbf{r_j}+\mathbf{R_n})} = -r_0 \underbrace{\sum_j f_j e^{i\mathbf{q}\cdot\mathbf{r_j}}}_{A^{unit\ cell}(\mathbf{q})} \underbrace{\sum_n e^{i\mathbf{q}\cdot\mathbf{R_n}}}_{A^{lattice}(\mathbf{q})} \tag{2.31}$$

Since the size of a crystal is much larger than the size of the unit cell, the sum in the second term of eq. 2.31 happens over a very large number of unit cells. Thus, the sum of terms $e^{i\mathbf{q}\cdot\mathbf{R_n}}$ will generally cancel out, unless the scattered waves from different lattice point are all in phase. In that case, they interact constructively, resulting in bright intensities in the diffraction pattern. The condition for constructive interference is expressed by::

$$\mathbf{q} \cdot \mathbf{R_n} = 2\pi \cdot n_{integer} \tag{2.32}$$

To solve eq. , we first introduce the reciprocal lattice $\mathbf{G}$, which is defined similarly to the direct lattice by a set of reciprocal vectors $\mathbf{a}_i^*$:

$$\mathbf{G} = h\mathbf{a}_1^* + k\mathbf{a}_2^* + l\mathbf{a}_3^*, \text{ with } \mathbf{a}_i^* = \frac{2\delta_{ij}}{\mathbf{a}_j} \tag{2.33}$$

where h, k, l are the (integer) Miller indices and δ_{ij} is the Kronecker delta. We notice that $\mathbf{G}$ satisfies eq. 2.3.4, since

$$\mathbf{G} \cdot \mathbf{R_n} = 2\pi(hn_1 + kn_2 + ln_3) \tag{2.34}$$

We therefore conclude that only for the scattering vectors q which coincide with a reciprocal lattice vectors the scattering amplitude from a crystal will be non-vanishing. This is known as the *Laue condition*. An alternative formulation of Laue condition is provided by the well-known *Bragg's law*, where the conditions for constructive interference is formulated for a family of planes (h k l) with an interplane distance of d_{hkl} as:

$$n\lambda = 2d_{hkl}sin(\theta) \tag{2.35}$$

with λ the wavelength of the incoming radiation, θ the angle between the incident X-rays and the lattice planes, and n being an integer number.

The XRD data can be employed to determine the composition and atomic arrangement of the crystal, as well as additional structural features on the atomic level, such as size and anisotropy of the crystallites, strain, and atomic vibrations. In the absence of a single crystal, similar information can be determined after measurement of a large number of randomly oriented crystallites in a powder X-ray diffraction experiment (PXRD). Quantitative analysis of the PXRD data is typically performed in reciprocal space, by the popular textitRietveld refinement method.[161,175]

2.3.5 X-ray absorption spectroscopy

Our discussion has so far restricted to the elastic scattering of X-rays. However, under certain conditions inelastic phenomena prominently dictate the interaction between X-rays and matter. When the X-ray energy approaches the binding energy of a core electron to the nucleus, *X-ray photo-absorption* might take place, determining the annihilation of the incoming photon and the transition of the electron to outer electronic shells or to vacuum. A complete treatment of this process requires quantum mechanical description of both the X-rays and the absorbing electron, which is beyond the scope of this section. However, the phenomenon can be illustrated in a more phenomenological way by describing the absorption by means of the *Lambert-Beer law*, which states that the intensity I_0 of an X-ray beam is attenuated after travelling through a medium of thickness d according to

$$I = I_0 e^{-\mu(\nu)d} \tag{2.36}$$

where I is the transmitted intensity and $\mu(\nu)$ is the absorption coefficient. The value of μ depends on the frequency ν of the X-rays and generally decreases at increasing values of ν. However, when the X-ray energy matches the energy for an electronic transition to vacuum, sudden increases in the absorption properties of the medium are observed. These jumps of the μ values are called *absorption edges.* These edges are commonly labelled with capital letters K, L, M, ... according to the principal quantum number of the initial state of the absorbing electron, while indexes like I, II, III, ... are used to distinguish different electronic sub-shells. Therefore, the excitation of a 1s electron defines a K-edge, while excitation from 2s, $2p_{1/2}$ and $2p_{3/2}$ will generate L_I, L_{II} and L_{III} edges, respectively.

In a simple experimental setup, X-ray absorption spectroscopy (XAS) is performed by tuning the energy of the probing X-rays in the proximity of the absorption edge of a given element and by determining the transmitted intensity as a function of the radiation energy. For assemblies of atoms, such as for crystalline materials or molecules, the resulting spectra display additional features to the absorption edge due to a variety of physical processes, which are collectively referred to as X-ray absorption fine structure (XAFS). **Figure 2.11** shows the X-ray absorption spectrum obtain across the Cu K-edge

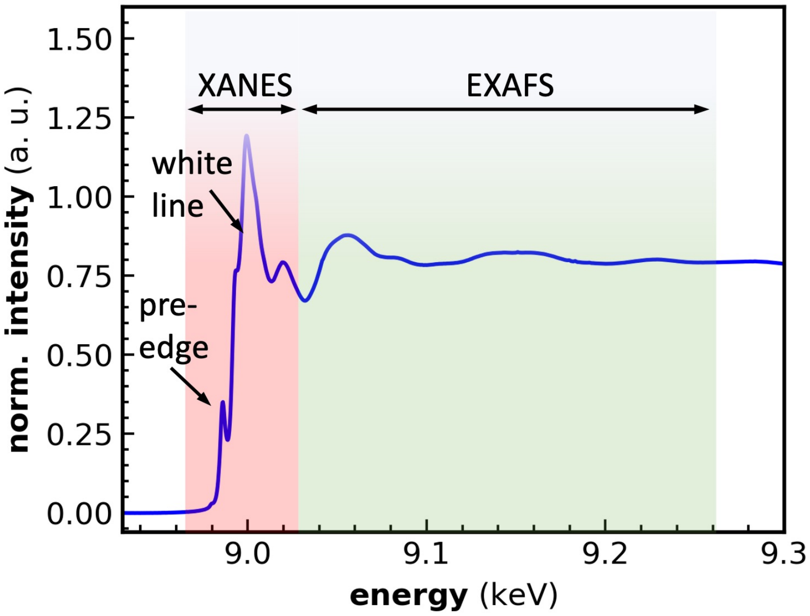

Figure 2.11: X-ray absorption spectrum for a $CuBi_2O_4$ thin film measured at the Cu K-edge. The different regions of the spectrum are highlighted in different colours.

for a film of $CuBi_2O_4$. A XAS spectrum is typically divided into two major regions, the X-ray absorption near-edge structure (XANES) and the extended X-ray absorption fine structure (EXAFS). These regions generally carry different information over the sample and will be therefore treated separately in the following sections.

2.3.5.1 XANES and HERFD-XANES

XANES refers to the part of the spectra in the proximity of the absorption edge. Its shape is usually dominated by a sudden increase in the absorbed intensity, due to the transition of a core electron to unoccupied electronic states just below the continuum. The absorption peak in this part of the spectrum is referred to as *white line*, and its intensity is proportional to the number of unoccupied density of states (DOS), which can be either bound (excitonic) or unbound (continuum) states.

Due to the conservation of the angular momentum, only certain electronic transitions involving symmetry-selected states are allowed, such as $s \rightarrow p$, $p \rightarrow s, d$, $d \rightarrow p, f$, and $f \rightarrow d, g$. However, formally forbidden electronic transitions may also be observed, due the hybridisation of atomic orbitals or quadrupolar coupling. Such transitions may thus determine the appearance of weaker absorption lines in the pre-edge region of the

XANES. In the spectrum showed in **Figure 2.11**, the absorption edge corresponds to a $1s \rightarrow 4p$ transition, while the pre-edge indicates a $1s \rightarrow 3d$, which occurs in violation of the selection rules. Such pre-edge features are often observed in the spectra of transition metals.[176]

XANES probes the oxidation state of the absorbing element, as an increase in the oxidation number determine a shift of the absorption edge to higher energy values. Moreover, it carries information on the molecular geometry of the absorbing site. For instance, a distortion of a centro-symmetric geometry for a transition metal leads to an increase in the pre-edge intensity due to the improved mixing of the 3d and 4f states.[177] Methods for quantitative modelling of the X-ray absorption properties are available, for example via FEFF[178] and FDMNES software,[179,180] although a full quantitative analysis of the XANES data is still limited due to the difficult evaluation of the effect of back-scattered electrons to the absorption profiles.[176] XANES is therefore regarded as carrying fingerprint information of the absorbing atoms, and experimental patterns are typically compared to reported or simulated references.

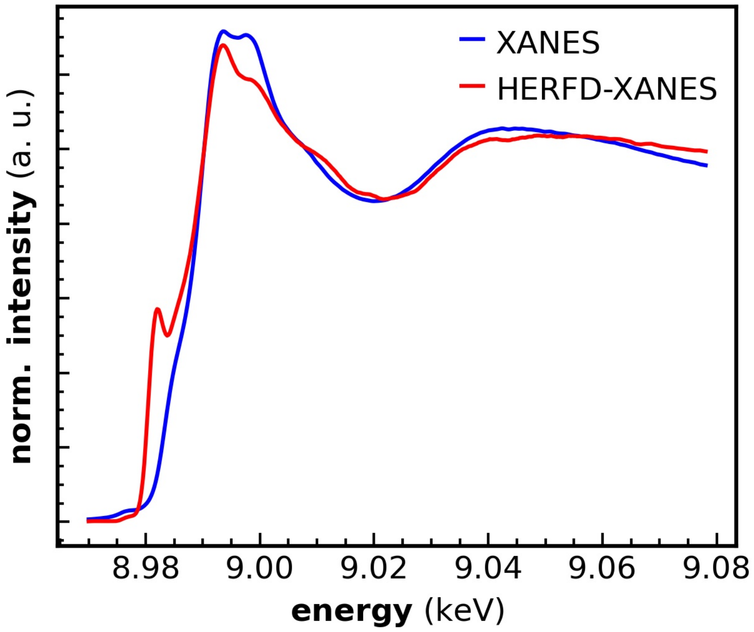

Figure 2.12: Comparison of HERFD-XANES and conventional XANES profiles. The data refers to the same Cu(II) organo-metallic complex measured dispersed in an organic solution. In the HERFD-XANES profile, the pre-edge peak due to the $1s \rightarrow 3d$ transition in the Cu(II) species is significantly more prominent compared to the conventional XANES profile.

As an effect of the Heisenberg uncertainty principle, the short lifetimes of the final state after the absorption event limit the overall energy accuracy of conventional XANES measurement, smearing out the features in the pre-edge region. However, the excited state after absorption typically transits to longer living, lower energy excited states, from which further relaxation to the ground state might occur by fluorescence emission. Due to their longer lifetimes, the energy determination of the lower energy excited states is more accurate. By detecting the X-ray absorption spectrum using the intensity of the emitted X-ray fluorescence, lifetime broadening effect in the XANES can thus be reduced.[181,182] This method is called high-energy resolution fluorescence detected XANES (HERFD-XANES). In **Figure 2.12**, the HERFD-XANES spectrum obtained for a Cu(II)-amino complex in solution is compared to the data obtained via conventional XANES. In the pre-edge region, the $1s \rightarrow 3d$ transition results in a well defined peak in the HERFD-XANES data, in contrast to the smeared shoulder in the conventional XANES pattern.

Since HERFD-XANES requires the measurement of the narrow fluorescence emission while sweeping over the energy of the incident the X-rays, its measurement is technically more demanding compared to standard XAS. Moreover, a major drawback of the high-resolution method reposes in the longer acquisition time due to the low yield of fluorescent emission. Therefore, HERFD-XANES measurements substantially benefits by the use of highly intense radiation, such as the one provided by 3rd or 4th generation synchrotron facilities.

2.3.5.2 EXAFS

For higher X-ray energies than the core-to-valence transitions, ionization takes place and the absorbing electron is ejected from the atom. In the EXAFS region, which extend from 40 to 1000 eV above the absorption edge, oscillations in the intensity results from the scattering of the ejected electron by neighbouring atoms. EXAFS data contains therefore information over the atomic arrangement in the vicinity of the absorbing element.

The oscillations of the EXAFS spectra are commonly referred to the dimensionless quantity $\chi(q)$, defined as:

$$\chi(q) = \frac{\mu_x(\nu) - \mu_0(\nu)}{\mu_0(\nu)} \tag{2.37}$$

where $\mu_0(\nu)$ is the absorption coefficient within an isolated atom, and $\mu_x(\nu)$ is the experimental absorption coefficient. The value of $\chi(q)$ can be modelled by use of the *standard expression for EXAFS data*:

$$\chi(q) = \frac{1}{q}\sum_j N_j \frac{t_j(q) sin(2qR_j + \delta_j(q))}{R_j^2} e^{-2(q\sigma_j)^2} e^{-2R_j/\Lambda} \tag{2.38}$$

where N_j is the number of neighbouring atoms j with distance R_j, t_j is the back scattering amplitude, δ_j is the phase shift, σ_j is the root mean squared displacement value due to atomic vibrations and Λ is a phenomenological parameter accounting for the mean free pathlength of the photoelectron.[153] By Fourier transform of eq. 2.38, the radial distribution function is obtained.

Compared to the PDF from TS data, the radial distribution from EXAFS typically restricts to less than 5 Å from the excited atoms, due to the $e^{-2R_j/\Lambda}$ factor in eq. 2.38. On the other hand, EXAFS selectively probes the local environment surrounding the absorbing elements and thus provides complementary information which turn significantly useful in case of multi-elemental samples compared to the element-unspecific X-ray scattering signal.

By utilizing quick EXAFS (QEXAFS) routines at the synchrotron, the acquisition time of EXAFS profiles can be significantly reduced to only tenths of seconds, therefore permitting to probe the local environment of selected elements during fast chemical transformations in situ.[183–185] Such an increase in the time resolution partly comes at the expense of an increased signal-to-noise ratio in the QEXAFS data compared with slower acquisition protocols.

2.3.6 X-ray refraction and reflection from interfaces

We have so far described the interaction between X-rays and matter by means of an atomistic model. However, X-rays also experience both refraction and reflection phenomena, which are more conveniently accounted by describing the target material as a continuum medium with homogeneous composition and sharp boundaries. With *diffraction* we indicate the phenomena by which an electromagnetic wave bends as it crosses the interface between two different media, as shown in **Figure 2.13**. Generally, a fraction of

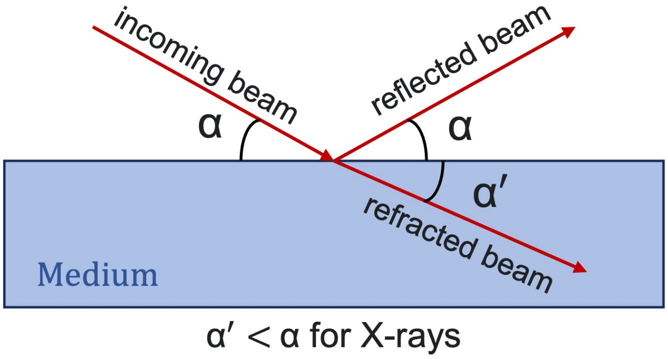

Figure 2.13: Illustration of the reflection and refraction of an X-ray beam from an ideal surface at an angle of incidence α above the critical angle.

the incoming radiation doesn't cross the interface, but returns instead into the medium of origin. This phenomenon is called *reflection* and the angle of reflection with respect to the interface plane is of the same amplitude α as for the incident angle. Differently, the relation between α and the refracted angle amplitude α' is described by *Snell's law*:

$$n_1 cos(\alpha) = n_2 cos(\alpha') \tag{2.39}$$

where n_1 and n_2 are the refractive indexes of the two media, and the refractive index of vacuum equals unity by definition. The magnitude of n depends on the wavelength of the incoming wave. For X-rays, n can be conveniently expressed as:

$$n = 1 - \delta + i\beta \tag{2.40}$$

where δ is a number in the order of 10^{-5} for solids and 10^{-8} for air. The imaginary part β is generally much smaller than δ. The exact value of δ relates to the electron number density ρ in the medium and to the radiation wavelength λ according to:

$$\delta = \frac{\rho r_0 \lambda^2}{2\pi} \tag{2.41}$$

with r_0 being Thomson scattering length.

We note that differently than for visible light, for X-ray radiation the refractive index is smaller than one. By travelling from the vacuum (or air) to a solid medium, the X-ray beam will consequently refract at an angle $\alpha' < \alpha$. It follows that below a certain *critical angle* α_c the X-rays don't penetrate the second medium, but all the incoming radiation undergoes *total external reflection.* At the critical angle and assuming for simplicity the first medium being vacuum, eq. 2.39 becomes

$$cos(\alpha_c) = n \tag{2.42}$$

By expanding the cosine as $cos(\alpha_c) \approx 1 - \frac{\alpha_c^2}{2}$ and by using the relation 2.40, we obtain:

$$\alpha_c = \sqrt{2\delta - 2i\beta} \approx \sqrt{2\delta} \tag{2.43}$$

which relates the critical angle α_c to δ. Since according to eq. 2.41 the value of δ increases with the square of λ, the amplitude of the critical angle is proportional to λ and therefore linearly decreases by increasing the energy of the X-ray radiation.

The ratios between the transmitted a_T and the reflected a_R amplitudes with respect to the amplitude of the incoming radiation a_I is given by *Fresnel equations*:

$$r := \frac{\alpha_R}{\alpha_I} = \frac{\alpha - \alpha'}{\alpha + \alpha'} \; ; \quad t := \frac{\alpha_T}{\alpha_I} = \frac{2\alpha}{\alpha + \alpha'} \tag{2.44}$$

where we introduce the amplitude reflectivity, r, and trasmittivity, t. The corresponding intensity reflectivity (R) and trasmittivity (T) can be calculated from the absolute square of r and t, respectively.

By combining Snell's law to eq. 2.40 and by applying a cosine expansion, we can clearly show that α' is a complex number:

$$cos(\alpha) = ncos(\alpha') \;\rightarrow\; \alpha^2 = \alpha'^2 + 2\delta - 2i\beta \tag{2.45}$$

The imaginary part of α' describes the dampening of the transmitted wave in the medium. We define the penetration depth Λ as the length of material which dampens the transmitted intensity by a factor $1/e$. It can be shown that:

$$\Lambda = \frac{\lambda}{4\pi Im(\alpha')} \tag{2.46}$$

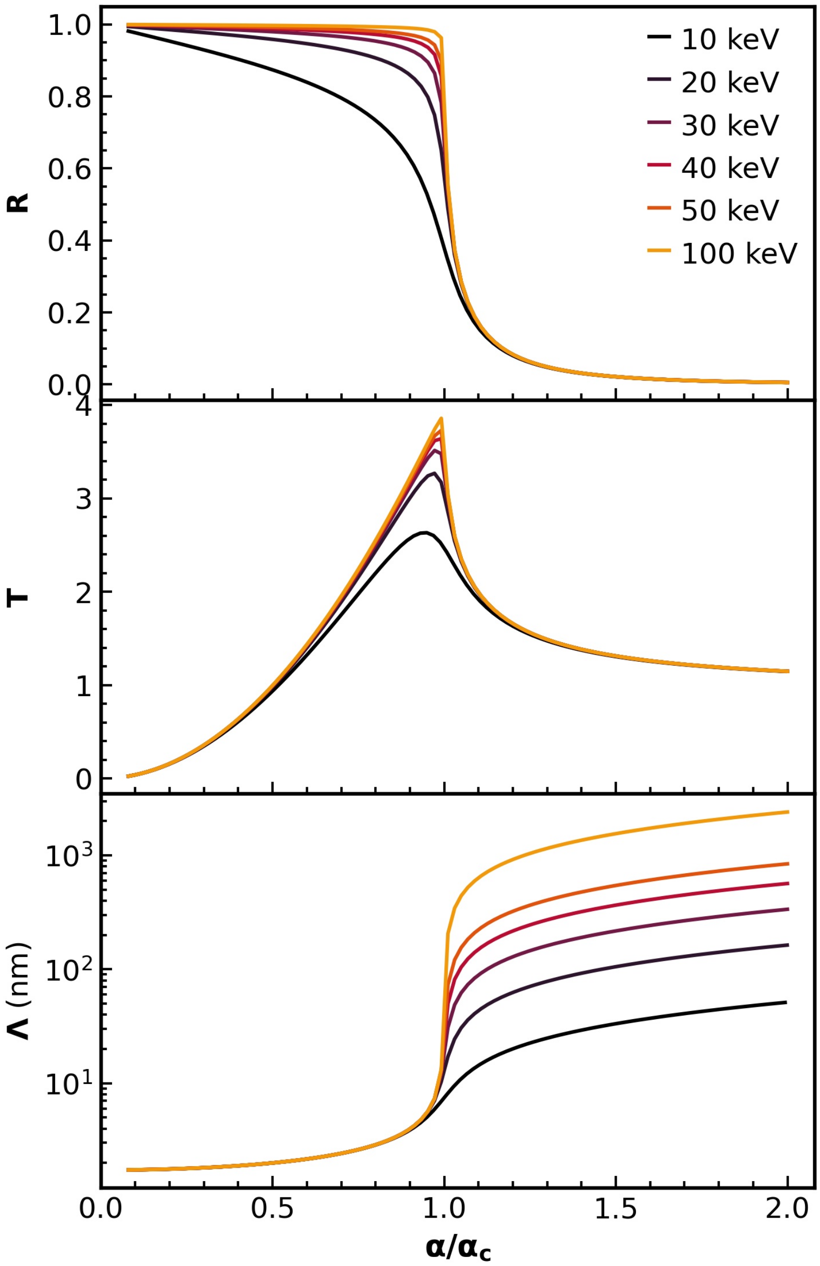

Figure 2.14: The reflectivity, the transmittivity, and the penetration depth calculated for Cu at different X-ray energies and plotted as a function of the incident angle α, normalized over the critical angle α_c.

Figure 2.14 shows the exemplary values of R, T and Λ as a function of α/α_c which we calculated for Cu and for different X-ray energies. The electron density ρ was determined by:

$$\rho = \frac{Z \ N_a \ \rho_{mass}}{\rho_{molar}} \tag{2.47}$$

where N_a is the Avogadro number, while $Z = 29$, $\rho_{mass} = 8.59$ g/cm^3 and $\rho_{molar} = 63.546$ g/mol are the atomic number, the mass density and the molar density of Cu, respectively. For completeness, the imaginary part β was also included in the evaluation of the refractive index by using:

$$\beta = \frac{\mu(\lambda)\lambda}{4\pi} \tag{2.48}$$

where the values of attenuation coefficients $\mu(\lambda)$ were found in the NIST Standard Reference database.[186]

From the plot, three different regimes can be distinguished:

- $\alpha << \alpha_c$: most of X-ray radiation is reflected away from the target. Since the angle of incidence is smaller than the critical angle, the real part of α' is 0 and the transmitted wave propagates along the surface. The penetration depth is minimal, in the order of few Å and independent on the X-ray energy. Due to its small penetration depth, the transmitted wave is called *evanescent wave.* Measurements performed at angles of incidence below the critical angle are referred to as made in *total external reflection* conditions.

- $\alpha \approx \alpha_c$: the reflectivity steeply decreases when the angle of incidence approaches the value of the critical angle. Simultaneously, the intensity of the transmitted radiation increases and reaches a maximum for values of α which are just below α_c. The penetration depth also monotonically increases for α just below α_c. At $\alpha \approx \alpha_c$ a steep jump in the value of Λ occurs, whose magnitude strongly depends on the energy of the incoming radiation. For angles of incidence just above the critical angle, energetic X-rays penetrate deep into the material to penetration length from 100 nm to 1 μm.

- $\alpha >> \alpha_c$: the reflectivity of the target approaches 0 and the X-ray radiation is almost completely transmitted through the target. When measuring at $\alpha >> \alpha_c$ the measurement is referred to as performed *in transmission* or *in glancing angle* conditions.

Measuring at incident angles just below the α_c thus permits to transmit a significant part of the incoming radiation through the sample while preserving low penetration depths below the sample surface. This measurement geometry is called *grazing incidence* and is particularly fitted for probing the surface structure of flat samples and two-dimensional materials.

2.3.7 Toward operando scattering studies on PEC-active films

The structural investigation of PEC-active thin films via high energy X-ray scattering is challenged by the strong scattering signal originating from the thick substrate, which commonly exceeds the thickness of the active films by three orders of magnitude.[187] Attempts have been made to measure the PDF of films in transmission geometry, i.e. by shining the X-ray orthogonal to the sample surface. However, such measurements suffer from unfavorable signal-to-noise ratios which significantly limit the sensitivity of the method.[188–191] Although measurements in grazing incidence are well-established for the study of crystalline films by surface X-ray diffraction,[192–195] the use of high-energy X-rays present significant technical difficulties due to the small amplitude of the critical angle at high photon energies.

Recently, Dippel et al. demonstrated the rapid acquisition of PDF in grazing incidence for thin films down to only a few nanometers in thickness.[187,196] The measurement relied on the careful control of the sample alignment with one millidegree precision. Although the study was limited to the measurement of model films and to ex situ measurements, it also lays the methodological groundwork for investigating complex photocorrosion phenomena via operando acquisition of high-energy X-ray scattering in grazing incidence.

Chapter 3

Materials and methods

3.1 Chemicals

Acetic acid (99%), benzyl alcohol (>99.0%, Sigma Aldrich), copper(II) acetylacetonate ($Cu(acac)_2$, >99.9%), copper(II) nitrate trihydrate ($Cu(NO3)_2 \cdot 3\ H_2O > 99.9\%$), dioctyl ether ($Oct_2O$, 99%), hexane ($> 99\%$), iron(III) acetylacetonate ($Fe(acac)_3$, $> 99.9\%$ trace metals basis), oleylamine (OAm, 99%), palladium(II) acetylacetonate ($Pd(acac)_2$, 99%), sodium hydroxide (NaOH, 99%), and titanium(IV) tetrachloride ($TiCl_4$, 99.9% trace metal basis) are purchased from Sigma Aldricht. [2-(2-methoxyethoxy)ethoxy] acetic acid (MEEAA , 99.7-100.5%), 2-propanol (100%), diethyl ether (>99.9%), ethanol absolute ($> 99.9\%$), glycerol (bidistilled, 99.5%), sodium dihydrogenphosphate (NaH_2PO_4, 100%), and sodium sulphate decahydrate ($Na_2SO_4 \cdot 10\ H_2O$, 100%) are purchased from VWR Chemicals. Bismuth(III) nitrate pentahydrate ($Bi(NO_3)_3 \cdot 5\ H_2O$, 98%) and Triton X-100 are purchased from Alfa Aesar. Toluene (Emsure) is purchased from Merk. Oleic acid (OAc, $> 99.0\%$) is purchased from TCI. Ethylene glycol (EG, 99%) is purchased from Honeywell. Fluorine-doped tin oxide (FTO) coated glass slides 20x15 mm are purchased from Ossilla. All chemicals are used as received without further purification.

3.2 Synthesis of metallic nanoparticles

3.2.1 Synthesis of Pd and Cu nanocrystals

Pd and Cu nanocrystals are prepared via a heat-up method from Pd(acac)$_2$ or Cu(acac)$_2$ precursor salts, respectively. To ensure the reproducibility of the results, all reactions are carried out by use of SHINES reactor, which we also employ during the in situ measurements.

In a typical synthesis, a stock solution of the metal acetylacetonate precursor (0.15 mol/L) is prepared in a solvent mixture consisting of OAm (3 mL), OAc (1 mL), and Oct$_2$O (0.8 mL). Around 80 to 250 µL of the precursor solution is subsequently transferred into a thin-walled borosilicate glass tube or polyether ether ketone (PEEK) tube, which is sealed air-tight by use of a PEEK liner. The latter is accommodated into SHINES reactor, which we heat up to the reaction temperature of 190°C (Pd NCs, 40 min.) or 210°C (Cu NCs, 12h) at a constant ramp of 10 °C min^{-1} and under stirring. When the reaction temperature for the synthesis of Cu nanocrystals is raised to 230°C, phase-pure Cu nanocrystals are obtained after 2.5h. After the synthesis, SHINES cell is allowed to cool down naturally to room temperature. The nanocrystals are isolated from the reaction mixture after addition of ethanol and by centrifugation, and further washed at least three times by centrifugation after dispersion in toluene and subsequent addition of ethanol.

3.2.2 Synthesis and assembly of CuPd icosahedra

In a typical synthesis, a stock solution of the nanocrystal precursors is prepared in an argon-filled glovebox by dissolving Pd(acac)$_2$ (77.6 mg, 0.253 mmol) and Cu(acac)$_2$ (123.1 mg, 0.467 mmol) into a solvent mixture of OAm (3 mL), OAc (1 mL), and Oct$_2$O (0.8 mL). Around 80-250 µL of the precursor solution is subsequently transferred into a thin-walled borosilicate glass tube or PEEK tube, which is sealed air-tight by use of a PEEK liner. The latter is accommodated into SHINES reactor, which is heated up to the reaction temperature of 220 °C at a constant ramp of 10 °C min^{-1} and under stirring. At this temperature, the reaction mixture turns from blue to red, and finally to black, indicating the formation of nanocrystals. After 30 min at 220 °C, the cell is allowed to cool down naturally to 100 °C to promote the formation of the supercrystals. After the synthesis, the nanocrystals are isolated from the reaction mixture after addition of ethanol (three times in volume) and by centrifugation. The nanocrystals are then washed at least three times by centrifugation after dispersion in one aliquot of toluene and subsequent addition of three aliquots of ethanol.

3.3 Fabrication of thin films

3.3.1 Cleaning of the FTO substrates

Before deposition of the thin films, FTO-coated substrates are cleaned three times by ultrasonication in an aqueous solution of Triton X-100 (2% in deionised water), 2-propanol, and deionised water, respectively. In-between each sonication step, the substrates are thoroughly rinsed with deionised water. Finally, we blow dried the cleaned FTO-coated substrates with purified air.

Before each spin coating step, an area of around 4x15 mm^2 of the conductive side of the FTO-coated substrate is masked with Kapton tape, to preserve the electrical contact. The Kapton tape is then always removed before performing any thermal treatment on the deposited films.

3.3.2 Fabrication of Fe_2O_3 films

Maghemite Fe_2O_3 thin films are prepared after spin-coating of a dispersion of magnetite nanoparticles functionalised with MEEAA according to an adapted procedure from[197]. For the synthesis of magnetite nanoparticles, 353.2 mg of Fe(acac)$_3$ (1 mmol) are dissolved in 5 ml of benzyl alcohol and then transferred to a 10 ml glass vial, which is heated at 180°C for 30 minutes by microwave heating. After synthesis, the dispersion is first centrifuged at 4000 rpm for 15 minutes and the supernatant discarded. The nanoparticles are then washed three times by dispersion in 5 ml of absolute ethanol and centrifugation at 4000 rpm for 15 minutes.

Functionalization with MEEAA is carried out after dispersing the nanoparticles in a 0.3 M solution of MEEAA in ethanol. The dispersion is first sonicated for 30 minutes and then left under stirring at room temperature overnight. The functionalised nanoparticles are washed twice by addition of 25 ml of hexane and subsequent centrifugation at 4000 rpm for 5 minutes. Finally, the washed nanoparticles are dispersed in ethanol to a 10 mg/ml concentration. 40 µL of the ethanolic dispersion are spin-coated on cleaned FTO-coated glass slides at a spinning rate of 3000 rpm. After each deposition, the FTO substrate is dried on a hot plate at 100°C for 10 minutes and then further calcined in air at 300°C for 1 hour. The deposition process is repeated for a total of 10 times.

3.3.3 Fabrication of Ti_2O films

To fabricate Ti_2O thin films, Ti_2O nanoparticles are first synthesised, cleaned by centrifugation and dried as a powder according to a procedure reported elsewhere.[198] The dried nanoparticles are then dissolved in ethanol to a concentration of 10 mg/mL. The Ti_2O thin films are then prepared by 15 successive depositions on FTO-substrate. In each deposition, 40 µL of the ethanolic dispersion are spin coated at a spinning rate of 2000 rpm, after which the substrate is calcined at 300 °C for 5 min. At the end of the deposition process, the film undergoes a final calcination at 500 °C for 2h.

3.3.4 Fabrication of $CuBi_2O_4$ films

$CuBi_2O_4$ thin films are prepared by subsequent spin coatings at 3000 rpm of 150 µL of a freshly prepared precursor solution, which we obtain by mixing a 0.2 M solution of copper(II) nitrate trihydrate in ethanol (2.5 mL), a 1.4 M solution of bismuth(III) nitrate pentahydrate in acetic acid (714 µL), and ethylene glycol (78 µL). When indicated in the text, ethylene glycol is substituted with the same amount of glycerol. After each deposition, the film is calcined in a pre-heated furnace at 450 °C for 5 min. This procedure is repeated for 10 times. Finally, the samples undergo a further calcination step at 500 °C for 12h.

3.4 Analytical methods

3.4.1 PXRD

Powder X-ray diffraction (PXRD) patterns are acquired using a Bruker D8 Advance diffractometer equipped with a Cu Kα X-ray radiation source.

3.4.2 In-house SAXS

Laboratory SAXS data is recorded at the SAXS setup at the Soft Condensed Matter chair at LMU Munich. A Mo microfocus source ($\lambda = 0.71$ Å) is collimated to a beam size of ca. 1 × 1 mm (full width at half maximum). Data are recorded using a Pilatus3R 300K detector (Dectris). Ex situ samples (CuPd supercrystals) are accommodated the in situ reaction cell and measured for 1 h at a sample-to-detector distance of 1 m. The in situ data during the synthesis of Cu nanocrystals is collected while running the synthesis in an in situ reaction cell at a sample-to-detector distance of 2.59 m. The signal of an empty borosilicate tube is used as a background in both cases. The detector geometry is calibrated by measurement of silver behenate (AgBh) calibrant in a 1.5 mm polyimide capillary.

3.4.3 FTIR

Fourier-transform infrared (FTIR) spectra in are recorded in attenuated total reflection (ATR) mode with a Bruker Alpha II spectrometer.

3.4.4 UV-vis

UV–vis spectra are recorded using an Agilent Cary 5000.

3.4.5 SEM

Scanning electron microscopy (SEM) is performed using a Regulus 8220 (Hitachi High Technologies Corp., Japan).

3.4.6 TEM

Transmission electron microscopy (TEM) imaging is performed on a JEOL JEM-1011 operating at 100 kV.

3.4.7 HRTEM

High-resolution transmission electron microscopy (HRTEM) imaging are carried out on a JEOL JEM-2200FS operating at 200 kV.

3.4.8 SAED

Selected area electron diffraction (SAED) measurements are performed using a TEM JEM-1011 (JEOL) operating at 100 kV and at a camera length of 30 cm.

3.4.9 EDX

Energy-dispersive X-ray spectroscopy (EDX) measurements are acquired by using a Si(Li) JEOL JED-2300 detector equipped at the a JEOL JEM 2200FS microscope.

3.4.10 ICP-MS

Inductively coupled plasma – mass spectrometry (ICP-MS, Agilent, 7700series) is performed on an aqueous solution containing the elemental analytes. Before each batch measurement, a calibration curve for the elements of interest is determined using 9 concentration points (0 – 2500 ppb) by diluting a multi-element ICP standard solution (Carl Roth). After calibration, the linear regression of the obtained counts per second vs. elemental concentration presents a correlation coefficient R $>$ 0.9999.

For the determination of the metal content in the electrolyte during CA, 2 ml aliquotes of the electrolyte are withdrown from the operando PEC cell and direclty measured without further preparation.

Each analyte solution is injected in the spectrometer for 30 s to generate a stable ion flow, followed by three acquisitions for each sample (0.99 s integration time per mass). In-between each sample, the system is rinsed for 30 s with 2 vol.% HNO_3 to prevent cross contamination. Elemental concentrations are calculated considering the dilution steps and by approximating the density of water to 1 g/mL.

3.4.11 PEC characterization

PEC characterizations of the $CuBi_2O_4$ films are carried out by using Biologic SP150 potentiostat, a Ag/AgCl (3M NaCl) reference electrode, and a platinum wire as a counter electrode in the standard 3-electrode configuration. Unless differently stated, a 0.5 M Na_2SO_4 and 0.1 M NaH_2PO_4 aqueous solution buffered at pH = 5.7 is used as electrolyte. The PEC measurements are performed by either using the in-house designed SCOPE cell or a commercial PEC cell (ZAHNER-elektrik, PECC-2) with a optical area of 0.5 mm^2. During the measurements, the PEC-active films are illuminated either with a Lumixo S (Lumatrix) AM 1.5G solar simulator or with our in-house designed LED light source, with an emission centered at 385 nm. In both cases, we use the same total illumination power density of 100 mW/cm^2. The potentials measured with respect to the Ag/AgCl reference electrode are converted to the RHE scale using the equation:

$$\text{E (V vs. RHE)} = \text{E (V vs. Ag/AgCl (3 M NaCl))} + 0.209 + 0.059 \times \text{pH}$$

OCP measurements are performed in chopped light conditions, with time intervals of light on/off of 30 seconds. LSV is performed at potentials from 0.8 to -0.3 V vs. Ag/AgCl (3 M NaCl) at a scanning rate of 10 mV/second. CA measurements are performed at a constant potential of 0.5 V vs. RHE and under LED light illumination unless differently specified.

3.5 Sample environment for in situ/operando measurements

3.5.1 SHINES reactor

All syntheses of metallic nanoparticles are performed within SHINES cell, unless differently specified. The cell consists of a metallic body accommodating a sealed cylindrical liner in which the synthesis takes place. The metal body is equipped with two low-voltage Cartridge heaters (24V, 100W, Maxiwatt) and a Pt100 temperature sensor (Honeywell) for temperature control. PEEK (Bieglo) plates are used for an improved thermal insulation. The cell is further equipped with a micro-stirrer (Variomag, Thermo Scintific).

The liner is made out of PEEK (Bieglo) and permits to air-tight seal a cylindrical reaction vessel made out of either glass (borosilicate, Hilgenberg, wall thickness = 0.05 mm) or PEEK (Bieglo) and closed on one side. Different sets of liners are used to accommodate reaction vessels of either 4.1, 6.5 or 9.5 mm in diameter, which we utilize to run reactions starting from a volume of 80, 180 and 450 µL of the reaction mixture, respectively. We employ glass vessels for X-ray scattering experiments, while PEEK vessels are preferred for X-ray spectroscopy measurements and in house synthesis. The vessels are filled with the reaction mixture and a stirring bar in an argon-filled glovebox and sealed within the liner by means of a FPM75 o-ring (Hug-Tecknik) which is pressed against the vessel walls by tightening of a screw located in the liner screw cap. All syntheses are then run outside of the glovebox.

3.5.2 SCOPE cell

All the operando PEC high-energy X-ray scattering measurements are carried out in combination to the on-purpose designed SCOPE cell. Additional ex situ in-house PEC characterizations are also performed within SCOPE, unless differently specified.

The body of the cell is made out of PEEK (Bieglo). The sample is positioned over a sample stage of size 26x16 mm^2, which is located at the center of the cell body. The cell displays a total of four polyamide (Kapton) windows, of 125 µm of thickness. Of these, two larger sized windows are located on the front and the back side of the cell and allow the transmission of both the incidence and scattered intensity, up to an angle of 28° measured in the scattering direction from the film surface. Two smaller Kapton windows are placed on the sides of the cell and used during the alignment procedure of the sample surface with respect to the direct beam.

An optical window (quartz glass, Edmund Optics) above the sample position permits to illuminate the film by use of an in-house designed LED illumination unit. All windows are sealed water-tight by use of aluminum frames pressing against FPM gaskets (Reichelt). A Ag/AgCl (3 M NaCl) reference electrode (Biologic) and a platinum wire counter electrode (adapted from Biologic) are positioned close to the sample surface through threaded feedthroughs. Electrical connection of the working electrode (WE), ie.

of the film sample, to an insulated wire is achieved by use of a *WE-connector*, which we equipped with an electrical-conductive foam (Holland Shielding Systems) and a conductive silver paint (Ferro GmbH) which ensures electrical contact between the the wire and the foam. The silver paint is masked from interaction with the electrolyte by use of a 2-component glue (UHU plus schnellfest). Pressing the WE-connector against a bare region of the sample surface connects the sample to the wire via deformation of the conductive foam. The WE connector is further equipped with a FPM75 o-ring (HUG Technik) to prevent the electrolyte to contact with the conductive foam during PEC operation.

The cell accommodates up to 36 mL of electrolyte in static conditions. Lateral feedthroughs are used to load and unload the electrolyte and further permit to optionally operate in flow of electrolyte.

3.5.3 LED illumination setup

Illumination of the film samples via high-power light-emitting diode (LED) is performed via an in-house designed LED unit designed by Kilian Frank at the Center for NanoScience (CeNS, LMU University). In this thesis, we use a Roschwege RSW-P01-385-2 LED with an emission wavelength centered at 385 nm. The illumination setup consists of a light-tight housing (aluminium, Thorlab) accommodating the LED unit, a heatsink, an antireflective-coated aspheric condenser lens (Thorlab ACL12708U-A, focal length = 8 mm) upstream to collimate the light beam, and an antireflective-coated planar-convex lens (Thorlab LA4148-A, focal length = 50 mm) downstream to focus the beam. The positions of both lenses are adjusted to obtained a squared footprint of 10x10 mm^2 at the center of the photoactive area of the film samples. The optical power density on the sample is calibrated to 100 mW/cm^2 (1 sun) by use of a power meter (Thorlabs PM100, with S121B silicon sensor).

3.6 Synchrotron-based characterization methods

3.6.1 Simultaneous TS and SAXS

Simultaneous X-ray Total Scattering (TS) and Small Angle X-ray Scattering (SAXS) data are collected at beamline P07 (second experimental hutch EH2) at the PETRA

III synchrotron facility (DESY, Germany) with an X-ray beam of approx. 103.8 keV and by using two large-area IP X-ray detectors (Varex 4343CT or Varex 4343CT and Dexela 1512) positioned at a distance of around 0.76 and 4.6 m from the sample position, respectively. The sample is positioned on a motorized stage inside a air-tight helium-filled sample chamber. A helium-filled flight tube is further used to reduce the background signal on the SAXS detector. To prevent damaging on the SAXS detector, the direct beam is attenuated by use of a 1 mm tungsteen beamstop, positioned at the exit window of the flight tube. A Kapton foil is used to separate the sample chamber from the flight tube and permits to vent the sample chamber during sample exchange independently from the long flight tube, thus reducing the helium consumption.

The experimental geometry of the X-ray scattering setup is calibrated by measurements of CeO_2 and LaB_6 powder standards packed in 1 mm polyimide capillaries and positioned at the center of the sample holder.

3.6.2 High-energy X-ray scattering in grazing incidence

X-ray scattering measurements in grazing incidence are performed with the experimental setup described in Section 3.6.1 and by using a focused X-ray beam with a vertical size of 3 µm and a horizontal size of 30 µm (full width at half maximum). In place of the tungsten beamstop, we use a semitransparent beamstop consisting of two stacked tantalum blocks (Goodfellow) and placed on the SAXS detector.

Film samples are aligned in height and tilt angles so that their surface is parallel to the incident X-ray beam, and then moved half- way in the vertical beam height to position them in the center of rotation. The alignment procedure of the thin films to the X-ray beam is detailed in **Figure 3.1** and relative caption.

When performing operando X-ray scattering measurements, the samples are placed in SCOPE cell, which is then positioned on the stage inside the sample chamber. For each sample, the critical angle is experimentally determined after alignment of the film to the beam and before conducting the PEC measurements by first scanning over the incidence angle between 0.001° and 0.050° in steps of 0.001° and by then selecting the angle of incidence at which we obtain the most intense scattering signal from the photoactive material while suppressing any signal from the FTO substrate. Operando X-ray

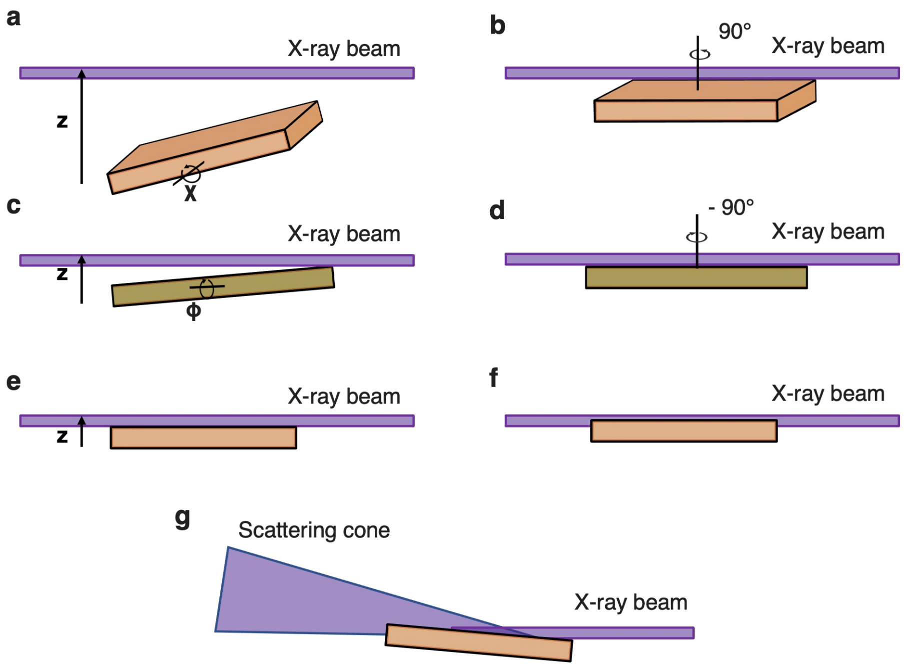

Figure 3.1: Schematic illustration of the alignment procedure of the thin film to the X-ray beam a Alignment of the rotation axis χ. After vertically moving the film below the X-ray beam, its vertical position (z) is iteratively increased and the angle χ in the direction of the beam adjusted to a final configuration where the film barely touches the beam and is parallel to it in the beam direction. **b** The film is rotated 90° around the laboratory vertical axis. **c** The film is aligned on its rotation axis ϕ in the direction of the beam by following the same routine as described in **a**. **d** The film is rotated back of -90° around the laboratory vertical axis. **e** The z position of the film is adjusted so that the film surface is at half position in the beam height. This step results in the X-ray beam footprint laying in the center of the film once the latter is titled to the grazing incidence geometry. **f** Scheme of the film as properly aligned for the grazing incidence measurement. **g** Measurement in grazing incidence is performed by tilting the film in the direction of the X-ray beam.

scattering measurements are performed at an incident angle just below the critical angle. Simultaneous OCP, LSV, and CA experiments are carried out following the same routines as for the in-house characterization.

The experimental geometry of the X-ray scattering setup is calibrated by measurement of a 1 mm polyimide capillary filled with either CeO_2 or LaB_6 powder standards. q_{damp} and q_{broad} instrumental parameters are calibrated after measurement of a CeO_2 or LaB_6 standard powder which had spin-coated on top of a FTO-coated glass substrate.

3.6.3 QEXAFS

Quick extended X-ray absorption fine structure (QEXAFS) measurements are performed in transmission mode at the P64 beamline at PETRA III synchrotron facility, DESY, Germany, on both Pd K-edge and Cu K-edge.[185,199] A fast oscillating torque motor mounting a Si(111) channel-cut monochromator is used for scanning the X-ray energy in the ranges 8860-10140 eV (Cu K-edge) or 24135-25060 eV (Pd K-edge) at the oscillating frequency of 1 Hz. Therefore, the acquisition speed is of 2 spectra/sec. The beam spot size is 0.5 x 0.5 mm^2 and the beam position on the reaction cell is continuously moved to avoid the beam damage effects on the sample.

3.6.4 HERFD-XANES

In situ HERFD-XANES spectra are recorded at the Cu K-edge at ID26 beamline at the European Synchrotron Radiation Facility (ESRF) in Grenoble, France.[200] During the measurement, the incident X-ray energy is varied from 8970 to 9060 eV in continuous scans of 20 seconds with a step size of 0.2 eV by means of a Si (111) double crystal monochromator (DCM). The HERFD-XANES spectra are then acquired in fluorescence mode with an energy resolution of 1.7 eV after detection of the emitted photons with a maximum intensity at the Cu $K_{\alpha 1}$ fluorescence line (8046 eV) by use of an emission spectrometer in Rowland geometry mounting five spherically bent Si (444) analyzing crystals aligned at the Bragg angle of 79.4°.[201] The beam spot size is approx. 200 x 200 μm^2 and the beam position on the cell is moved every two consecutive full scans to avoid sample damage due to the protracted exposure to the X-rays. All powder reference samples are measured as pellets.

3.6.5 XANES

The X-ray Absorption Near Edge Spectroscopy (XANES) data on $CuBi_2O_4$ films is collected at the beamline P64 at the PETRA III synchrotron facility (DESY, Germany). XANES spectra are acquired in fluorescence mode with a Passivated Implanted Planar Silicon (PIPS) Detector (Canberra) while scanning the incident photon energy from 8730 eV to 9030 eV with a stepsize of 0.3 eV and from 9030 eV to 10000 eV with a linear increasing stepsize from 0.5 to 1.5 eV.

3.7 Data processing and analysis

3.7.1 Processing of the TS-PDF data

pyFAI[202] is used to calibrate and azimuthally integrate the 2D diffraction patterns into the 1D curves. Background subtraction is performed by self-developed routines employing NumPy[203] Python library. For in situ syntheses, background patterns are determined after independent measurements of the time-resolved TS signal of the heated solvent mixture in the absence of the nanoparticle precursors. For operando films, the scattering signal generated by the SCOPE cell filled with electrolyte and in the absence of the thin film is used as background. xPDFSuite[204] is preliminary used to identify the optimal values of q_{min} and q_{max} for the Fourier transformation of selected TS patterns. The Fourier transformation of the in situ TS data is then performed by using PDFgetX3[205] within the q-ranges reported in **Table 3.1**. When measuring thin films in grazing incidence, the 1D TS signal is aberration-corrected by using the routine described in **Section 3.7.1.4** before performing the Fourier transformation to the PDF.

data	q_{min} / Å^{-1}	q_{max} / Å^{-1}
in situ Pd synthesis	2.30	14.80
in situ Cu synthesis	2.33	14.80
in situ CuPd synthesis	2.35	14.60
operando $CuBi_2O_4$	1.80	20.10

Table 3.1: q_{min} and q_{max} values for the Fourier tranformation of the TS into the PDF.

3.7.1.1 Refinement by AC approximation

PDF refinement by attenuated crystal (AC) approximation is performed within the *PDF-Generator* class implemented in Diffpy-CMI library.[160] During the fit, the following structural parameters are refined per each modelled phase: a scaling factor, the lattice constants, the atomic displacement parameters (ADP) adjusted by symmetry, a parameter accounting for correlated atomic motions (δ_2), and the diameter of spherical crystalline domains, unless differently specified.

3.7.1.2 Refinement by discrete atomistic models

The PDF of individual discrete atomistic models is calculated by a Fourier transform of the Debye scattering equation (DSE) according to the method reported in[206].

For the organometallic compounds, isolated molecular structures are generated by modification of the crystalline structures referenced in the Result and Discussion section and obtained from either the CCDC[207] or COD[208] crystallographic databases. In all cases, the respective atomic positions between the Cu or Pd center and the neighboring O, N, and C atoms are kept unaltered as reported in the original crystallographic structure, while the backbones of the complexes away from the Cu center are adjusted to linear aliphatic group, thus mimicking the aliphatic tails of OAm and OAc ligands. For Cu-complex 1, we additionally tested fully relaxed organometallic structures. Manipulation and relaxation of the organometallic model structures are performed within *Avogadro*.[170] During the fit of the PDF, a scaling factor value is refined by least-squared refinement, while other structural parameters are kept constant to the values reported in **Table 3.2**.

parameter	value / Å^2
ADP (Pd)	0.012
ADP (Cu)	0.015
ADP (O)	0.030
ADP (N)	0.030
ADP (C)	0.030
ADP (H)	0.050
δ_2	6.0

Table 3.2: Values for fixed parameters during the PDF fit from organometallic complexes.

Discrete atomistic models for nanocrystals with different arrangement are generated by using the Atomic Simulated Environment (ASE) Python library.[167] The PDF fit is performed following a similar procedure as reported in[209]. During the fit, minimization of the Rw by least-squares refinement is performed after variation of the following structural parameters: a scaling factor, an isotropic expansion coefficient, two distinct ADP parameters for Cu and Pd atoms, and δ_2. In the case of atomistic models with P4/mmm symmetry, an expansion coefficient parameter in the direction of the lattice vector c is also included to account for the tetragonal symmetry of the unit cell.

The calculation of the model PDF of discrete cluster models is performed within the *DebyePDFGenerator* class implemented in the Diffpy-CMI package.[160]

3.7.1.3 Refinement by discrete atomistic models and Monte Carlo optimization algorithm

When indicated in the Result and Discussion section, a self-developed Monte Carlo optimization algorithm is used in combination to the discrete cluster fit. In this way, we account for deviations of the particle structure from the ideal models by simulating random atomic displacements.

In the fit routine, we first define the starting atomic positions by a discrete atomistic model fit, as outlined above. We then performed subsequent optimization cycles, each one consisting of:

- a Monte Carlo optimization. Here, we consider $\mathrm{N_{step}} = 5000$ of random atomic displacements of module between 0 and $\mathrm{d_{max}} = 0.003$ Å. Atomic displacements leading to a decrease of the agreement factor Rw are accepted, while all those leading to an increase of Rw are rejected (zero temperature Monte Carlo). The acceptance rate for the tentative displacement is approx. 50%.

- a discrete atomistic model fit, which is performed after the Monte Carlo optimization

We repeat the optimization cycles $\mathrm{N_{cycles}}$ times, and interrupt the refinement before the position of any atom in the cluster model varied more than a threshold distance, corresponding to 5% of the mean shortest interatomic distance in the starting atomic model. The threshold distance for an icosahedron with $\mathrm{N_{shells}} = 7$ amounts to 0.125 Å.

3.7.1.4 Correction of aberration for total scattering data from thin films

In the measurement of thin films, the aberration in the X-ray scattering data due to an imperfect alignment of the film samples at the center of the incident X-ray beam is corrected according to the formula:

$$q_{ab.corr.} = \frac{4\pi}{\lambda} sin\left(\frac{1}{2} arctan\left(K tan\left(2 arcsin\left(q_{calib.} \frac{\lambda}{4\pi}\right)\right)\right)\right) \tag{3.1}$$

where $q_{abb.coor}$ is the array of aberration-corrected values of the scattering vector, q_{calib} are the corresponding values of the scattering vector as obtained from the calibration routine of the center position of the film surface and λ is the wavelength of the X-ray probe. The correction coefficient K is determined by fitting the position of a Bragg's reflection peak which is displayed in the overlap region of the SAXS and TS patterns. For example, in the measurement of $CuBi_2O_4$ films, K is determined as:

$$K = \frac{tan\left(2 arcsin\left(q_{(211),SAXS} \cdot \frac{\lambda}{4\pi}\right)\right)}{tan\left(2 arcsin\left(q_{(211),TS} \cdot \frac{\lambda}{4\pi}\right)\right)} \tag{3.2}$$

with $q_{(211),SAXS}$ and $q_{(211),TS}$ being the position of the (211) reflection of the $CuBi_2O_4$ phase as observed in the SAXS and TS detector, respectively. Fitting of the Bragg's reflection peak is performed by use of a Pseudo-Voigt function within SciPy library.[210]

3.7.2 Processing of the SAXS data

The analysis of the in situ SAXS is performed by Kilian Frank at the Center for NanoScience (CeNS, LMU University). Tjark Gröne assists Kilian Frank in the analysis of the in situ Pd nanocrystal synthesis.

pyFAI[202] is used to calibrate and azimuthally integrate the 2D diffraction patterns into the 1D curves. For in situ measurements of nanocrystal and supercrystal syntheses, the signal of an empty capillary is subtracted as background. Then, the analysis of the SAXS profile is performed by different routines, depending on the different datasets, as illustrated in the following sections.

3.7.2.1 Analysis of in situ Pd data

The inter-particle distance within agglomerates of Pd nanocrystals is determined after fitting the position of the corresponding structure factor peak emerging at around 0.09 Å^{-1} in the in situ SAXS data. A background signal, corresponding to the entire SAXS pattern except the intensity peak of interest, is fitted as the summed contribution of a constant background, a power law, a sphere, as expressed by eq. 2.24 with a fixed R value of 29.21 Å, and a symmetric pseudo-Voigt function, with fixed position at 0.2513 Å^{-1} and full-width at half-maximum of 0.09615 Å^{-1}. The peak at 0.09 Å^{-1} is then fitted by an asymmetric pseudo-Voigt function, as defined in[211]. The refinement in performed in SasView 5.0.5[212] by use of DREAM[213] minimization algorithm.

3.7.2.2 Analysis of in situ Cu data

In situ SAXS data measured during the synthesis of Cu nanocrystals is modelled in SasView 5.0.5[212] using as the sum of two populations of solid spheres and a power law background with a fixed exponent of 4. For each population a scale factor, the mean diameter and the (Gaussian) polydispersity of the diameters is refined. In addition, we refine also a scale factor for the background. The minimization routine is performed by using DREAM[213] algorithm implemented in SASView with default settings.

3.7.2.3 Analysis of CuPd crystals and supercrystals

SAXS intensities I(q) is analyzed using SasView version 5.0.5[212] or by custom fit routines using the *lmfit* Python package.[214]

Before nucleation of the supercrystals, the time resolved SAXS intensity is fitted by using a polydisperse spherical form factor according to eq. 2.25, where $\Delta\rho$ is set to 1. Differently we use a exponentially decaying scattering contrast (“onion” model in SasView) to model the organic shell surrounding the nanocrystal metallic cores. Here, the scattering density profile of the shell is chosen as:

$$\rho_{shell}(r) = B \exp\left(\frac{A(r - r_{core})}{\Delta t_{shell}}\right) + C \tag{3.3}$$

where the value of the decay constant A is fixed to -5, the core scattering length density B is set to 1, the solvent scattering length density C is set to 0 and the shell thickness

Δt_{shell} is set to 1 nm.

For comparison, we also fit one selected SAXS intensity before the supercrystal formation by use of a discrete icosahedral model. Here, the SAXS intensity due to the nanocrystal is calculated via Debye scattering equation as:

$$I(q) = \frac{1}{\sum_i V_i} \left(\sum_i f_i^2 + \sum_{ij} 2 f_i f_j \frac{sin(q\ d_{ij})}{q\ d_{ij}} \right) \tag{3.4}$$

where f_i are the atomic form factors and $V_i = \frac{4\pi}{3} r_i^3$ are the corresponding volumes of the scattering atoms. The value of r_i is determined as the distance between neighboring atoms.

In all cases and before nucleation of the supercrystals, we further fit the background intensity as the sum of a constant term and a power law term.

We fit the time resolved SAXS intensity during the evolution of the supercystals by a multi-component model. Free particles are modelled as polydisperse spheres with a Gaussian distribution of particle radii. A SRO phase is modelled according to the Percus–Yevick structure factor of hard spheres,[215,216] which is implemented in SASview. The intensity of the fcc supercrystals is modelled as the product of the form factor of the free nanocrystals with the structure factor $S_{fcc}(q)$ for the fcc arrangement, which we calculate as the sum of gaussian peaks following Forster et al.[217] and Yager et al.[218] The intensity of the solvent lamellae is modelled by two Gaussian peaks with coupled peak positions $q_2 = 2q_1$ and independent heights and widths. Finally, the background contribution to the intensity is modelled by a constant term, a power law, and a Guinier law,[219] describing short-range density fluctuations.

Porod invariants are calculated as:

$$\int_0^\infty I(q) q^2 dq = 2\pi^2 \overline{\Delta\rho^2} \tag{3.5}$$

where $\overline{\Delta\rho^2}$ is calculated by trapezoidal integration of the model curves in the fit range $0.018 < q < 0.42$ Å^{-1}.

In the SRO phase, the typical inter-particle distance of nearest neighbors is calculated as:

$$d_{nn,SRO} = \sqrt[3]{\frac{\frac{4}{3}\pi r_{eff}^3}{\eta}} \tag{3.6}$$

where r_{eff} is is the effective radius of the hard sphere interaction within the short-range ordered phase, and η is the volume fraction of the effectively interacting particles in this phase. The nearest-neighbour distance in the fcc phase is calculated as $d_{nn,fcc} = \frac{a}{\sqrt{2}}$ where a is the lattice constant of the fcc unit cell obtained from the fit. The surface-to-surface separation distance is evaluated as $d = d_{nn} - 2R$, where $2R$ is the diameter of a sphere fully enclosing the icosahedron model used in the analysis of the simultaneous TS-PDF data.

3.7.2.4 Analysis of the GISAXS data

GISAXS data is transformed into a two-dimensional scattering vector grid (q_{xy}, q_z) using pyFAI, where q_{xy} is the in-plane scattering signal and q_z is the scattering signal perpendicular to the substrate. Line cuts at constant q_z are modelled by the sum of a power law exponent, a Guinier term, and a constant background term, according to:

$$I(q_{xy}) = \frac{A}{q_{xy}^n} + Ce^{-\frac{1}{3}(q_{xy}R_g)^2} + bkg \tag{3.7}$$

The values of the numerical parameters A, C, and bkg, the exponent n, and the radius of gyration R_g are refined in SasView 5.0.5.[212]

3.7.3 Processing of the QEXAFS data

The analysis of the in situ QEXAFS is performed by Jagadesh Kopula Kesavan at the Hybrid Nanostructures Group in CHyN.

In situ QEXAFS data is normalized and energy corrected within ProQEXAFS 2.43 software.[220] To reduce the noise, the spectra are averaged over 30 scans before analysis.

3.7.3.1 MCR-ALS analysis

Multivariate Curve Resolution by Alternating Least Squares (MCR-ALS) method[221] in the energy ranges 8900-9080 eV (Cu K-edge) or 24280-24450 eV (Pd K-edge) is performed by use of the analytical expressions developed by Jaumot et al. and included in MATLAB R2011b.[222,223] We initially guess the values for both the uncorrelated spectra ($\mathbf{S^T}$) and the respective concentration profiles ($\mathbf{C}$) by use of the SIMPLISMA algorithm.[224] The final values of $\mathbf{S^T}$ and $\mathbf{C}$ are then calculated iteratively within a total of 50 iterations.

3.7.3.2 Fit of the EXAFS profiles

EXAFS profiles are calculated and analysed by using Athena and Artemis software of the IFEFFIT package.[225] Fourier transformation of the EXAFS profiles is performed in the ranges 3-11.7 Å^{-1} and 3-11.5 Å^{-1} for data collected at the Cu K-edge and Pd K-edge, respectively. Analysis of selected in situ EXAFS profiles is performed by using the scattering paths simulated with FEFF 6.0[226] and after fixing the many-body amplitude reduction factor (S_0^2) to a value we obtain by separate fit of the reference measurements of either a Cu or a Pd foil. In the fit, a common value for the energy origin shift (ΔE_0), the interatomic distances (R), and the Debye-Weller factors (σ) are refined. The goodness of the fit parameter (R) resulted below 0.02 for all performed fits.

3.7.4 Processing of the HERFD-XANES data

The analysis of the in situ HERFD-XANES is performed by Jagadesh Kopula Kesavan at the Hybrid Nanostructures Group in CHyN.

In situ HERFD-XANES data is preliminarily visualised with PyMCA[227] and then pre-processed using using slix,[228] Whittaker filter,[229], NumPy,[203] and SciPy[210] Python packages. Ex situ HERFD-XANES data is pre-treated using the Athena software of the IFEFFIT package.[225]
Theoretical HERFD-XANES spectra are calculated by use of FDMNES[180] with the input card:

Edge K

Energpho

Range -30.0 0.2 5.0 0.5 20.0 1.0 130.0

Density state_ all

Delta_ E_ conv 0.1

Z_ absorber

Radius 5.0

Convolution

End

3.7.5 Processing of the XANES data

The analysis of the ex situ XANES on $CuBi_2O_4$ electrodes is performed by Lars Klemeyer at the Hybrid Nanostructures Group in CHyN.

XANES spectra are normalized and then analysed by Linear Combination Analysis (LCA) using Larch: Data Analysis Tools for X-ray Spectroscopy.[230]

3.8 Calculation of the pairwise interaction potential of CuPd nanocrystals

We estimate the pairwise interaction potential between CuPd nanocrystals as the sum of the van der Waals attraction between spherical CuPd nanocrystal cores and steric repulsion due to the hydrocarbon capping ligands according to[123,231]. The van der Waals term is calculated as:

$$U_{vdW} = -\frac{A}{3}\left[\frac{r^2}{4rd_i + d_i^2} + \frac{r^2}{(2r+d_i)^2} + \frac{1}{2}ln\frac{4rd_i + d_i^2}{(2r+d_i)^2}\right] \tag{3.8}$$

where $r = 1.5$ nm is the particle radius and d_i is the interpaticle separation. The Hamaker constant is calculated as 2.1 eV according to:[123,231]

$$A = \frac{3}{4}k_BT + \frac{3h\nu_e}{16\sqrt{2}}\frac{(\sqrt{2}+c)^3 - (\sqrt{2}+2c)(n^2-1) + (n^2-1)/c}{\left((\sqrt{2}+c)^2 + n^2 - 1\right)^{1.5}} \tag{3.9}$$

where k_B is Boltzmann's constant, h is Plank's constant, T= 373.15 K, $n = 1.44$ is the refractive index of the medium, and $c = \nu_e/\nu_{ed}$, where $\nu_e = 5.2 \cdot 10^{15}$ Hz is the averaged plasma frequency for Cu and Pd[232,233] and $\nu_{ed} = 3 \cdot 10^{15}$ Hz for oleylamine/oleic acid.[233]

The steric repulsion term is calculated as:

$$U_{steric} = k_B T \frac{\pi^3 \sigma r L_0^3}{120 R_e^2}(-45 - ln(u) + 54u - 10u^3 + u^6) \tag{3.10}$$

where $\sigma = 10$ nm^{-2} is the grafting density, $L_0 = 2$ nm is the ligand length, $R_e^2 = 2$ nm^2 is the entropic repulsion parameter, and $u = \frac{d_i}{2L_0}$.

The calculation is performed by Kilian Frank at the Center for NanoScience (CeNS, LMU University).

Chapter 4

Results and discussions

4.1 Technical and methodological advancements towards multi-modal X-ray scattering measurements

Part of the content of this section was published in Small, 2311714 (2024) or in Angew. Chem. Int. Ed. 62, e202307948 (2023).
My contribution to the study encompasses the testing of the simultaneous SAXS and PDF setup at the beamline, the acquisition of the X-ray scattering measurements, the analysis of the TS-PDF data, the development and testing of the aberration correction algorithm, and the design and commissioning of SHINES and SCOPE cells.

In this section, we pose the methodological basis to realize multi-modal X-ray scattering measurements either in situ or operando. We illustrate an experimental setup to the simultaneous acquisition of SAXS and TS in transmission, and then demonstrate a method to complement the experimental TS dataset by including X-ray scattering information covered by the SAXS detector. We then detail an in situ reactor, aimed to investigate the synthesis of nanocrystals and nanocrystal assemblies by simultaneous SAXS and TS.

We further showcase the application of high-energy X-rays scattering measurements in grazing incidence to determine the structure of film-based materials with enhanced surface sensitivity. We develop a PEC cell aimed to investigate the structure of photoactive thin films while simultaneously probing their PEC-performances. Finally, we show that the X-ray beam does not affect the PEC properties on model $CuBi_2O_4$ thin films.

4.1.1 The simultaneous SAXS and PDF acquisition

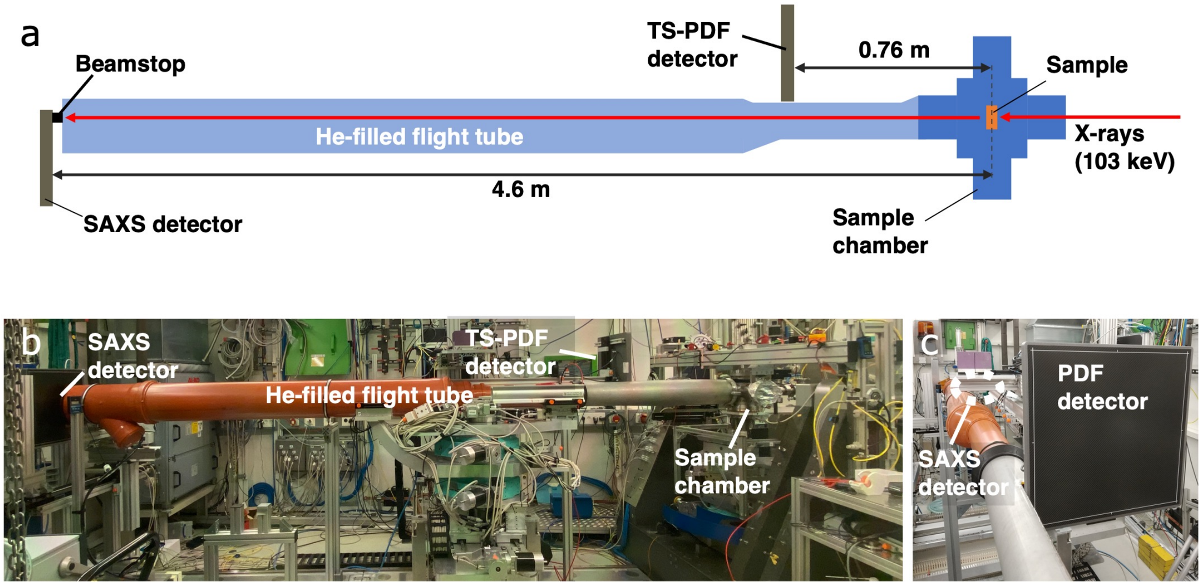

Figure 4.1: The experimental setup for simultaneous SAXS and TS-PDF acquisition. **a**) Schematic illustration of the setup. **b**) Picture of the setup mounted at P07 beamline, DESY (Germany). **c**) Same as **b**, taken from the exit window of the sample chamber

Figure 4.1 shows the experimental setup developed by the beamline scientists of the P07 beamline at DESY (Germany) for the simultaneous acquisition of SAXS and TS. A detailed description of the setup can be found in Section 3.6.1. In short, the measurement relies on the presence of two IP detectors positioned at different distances from the sample to collect distinct regions of the scattering pattern. The TS detector is close to the sample position and records the TS signal in a range of q between 1.6 and 27 Å^{-1}. The SAXS detector is located at a sample-to-detector (SDD) distance of 4.6 m and acquires X-ray scattering at small angles within 0.01 and 2.6 Å^{-1}. The use of an air-tight sample chamber and a helium-filled flight tube reduces the background signal on both detectors.

4.1.1.1 Joining SAXS and TS data

Figure 4.2a-b displays representative detector images for a Fe_3O_4 nanocrystalline magnetite powder measured in transmission by the simultaneous SAXS and TS acquisition setup. Due to the presence of the flight tube and SAXS detector, the TS pattern displays a significant higher experimental q_{min} value compared with conventional TS experiments.

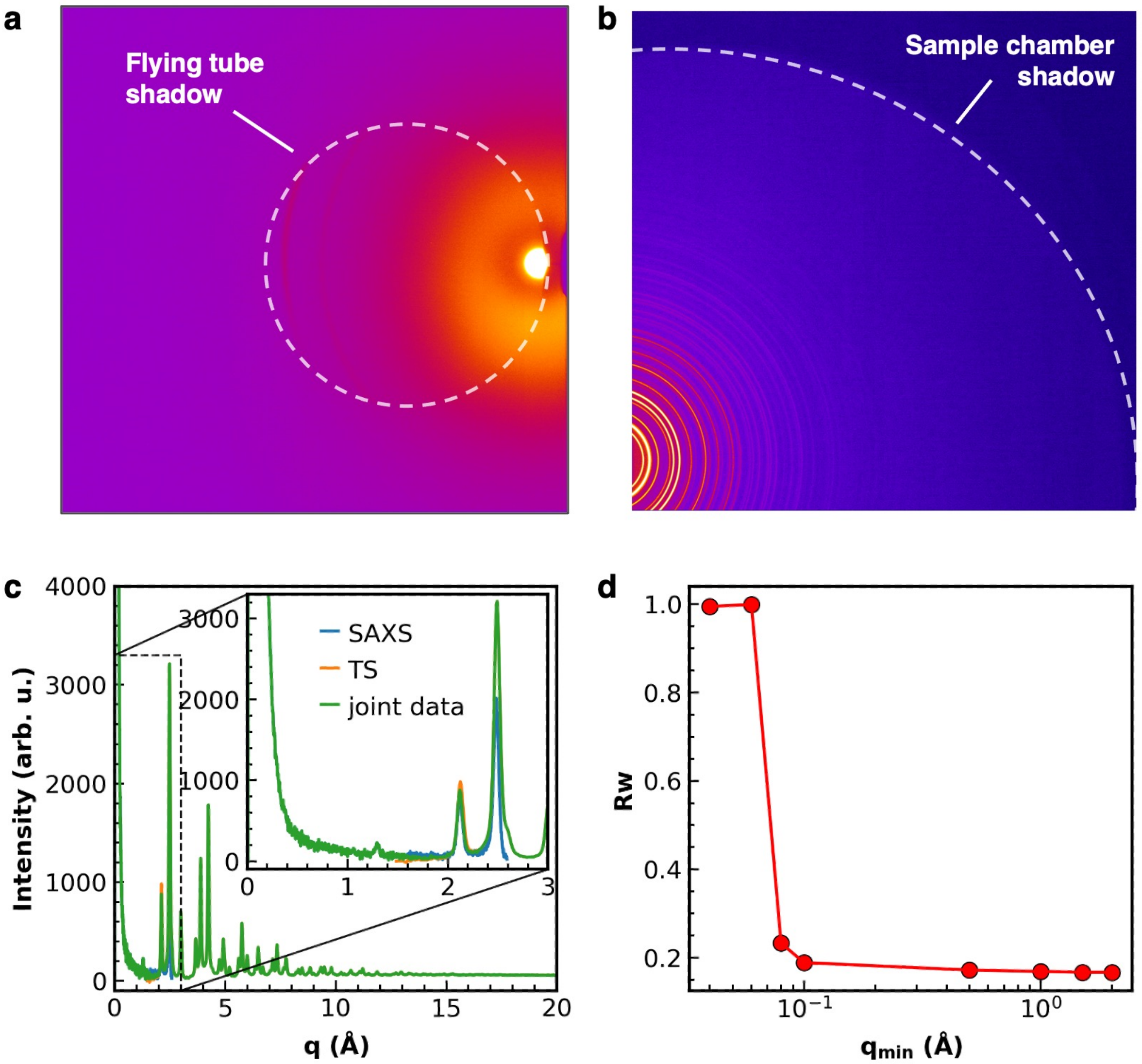

Figure 4.2: Data generated by simultaneous acquisition of SAXS and TS for a magnetite Fe_3O_4 powder sample. **a**) SAXS detector image. A dotted circle indicates the shadow of the flying tube on the detector, which determines the upper limit of measurable scattering angles for the SAXS signal. **b**) TS detector image. The shadow from the sample chamber is indicated by a dotted circle. **c**) 1D plot of the azimuthally integrated SAXS (blue) and TS (orange) patterns shows in **a** and **b**. The joint SAXS-TS pattern is additionally shown (green). **d**) Rw values from the refinement of the PDF obtained via Fourier transform of the joint SAXS-TS pattern shows in **d** with different q_{min} truncation.

We find that for most samples such experimental constrain does not compromise the quality of the PDF. However, in some cases we observe that relevant information displayed in the low-angle region of the TS signal bypasses the TS detector and is instead captured by the SAXS detector. In **Figure 4.2c**, the weak (111) magnetite (Fe_3O_4) reflection at 1.3 $Å^{-1}$ is below the q_{min} for the TS detector and therefore only appears in the SAXS pattern.

We developed a routine to join the TS and the SAXS data for isotropic samples, such as powders or dispersions, in a single extended X-ray scattering pattern, which we then Fourier transform to the PDF. We show that joining the two datasets is possible after removal of the respective background signal, and by selecting an appropriate scaling factor for the SAXS pattern. The latter step in necessary since the solid angles probed by pixels of same size but distinct distance from the sample are generally different. Moreover, the angular amplitudes of the scattering cone collected by the two detectors is also different. The joint SAXS-TS pattern is shown in **Figure 4.2c**.

We calculate the PDF from the extended X-ray scattering pattern for different values of q_{min} and then fit the data by use of a magnetite crystalline model. **Figure 4.2d** shows the Rw values resulting from distinct fits. For $q_{min} > 0.1$, Rw is below 0.15 and we consistently determine identical values for the refined structural parameters through all fits. Conversely, the quality of the fit dramatically declines when extracting the PDF with a q_{min} below 0.08 Å^{-1}. In fact, we find that including the intense SAXS signal within the Porod's region in the TS pattern results in intense oscillations in the outcoming PDF that do not correspond to any inter-atomic distance. To preserve the quality of the PDF, we therefore restrict the experimental q_{min} to values above 0.1 Å^{-1}.

4.1.2 SHINES reactor for nanoparticle synthesis

We establish a reaction environment which allows to investigate the synthesis of nanoparticles in solution by simultaneous in situ SAXS and TS, as well as by X-ray absorption spectroscopy. To ensure compatibility with in situ X-ray measurements and the faithful reproduction of nanoparticle synthesis at the beamline, the desired setup must meet several requirements:

1. be thermally and mechanically stable and allow control over the temperature of the reaction mixture during the synthesis;
2. permit to homogenize the reaction mixture to minimize temperature and composition profiles and prevent sedimentation of the nanoparticles;

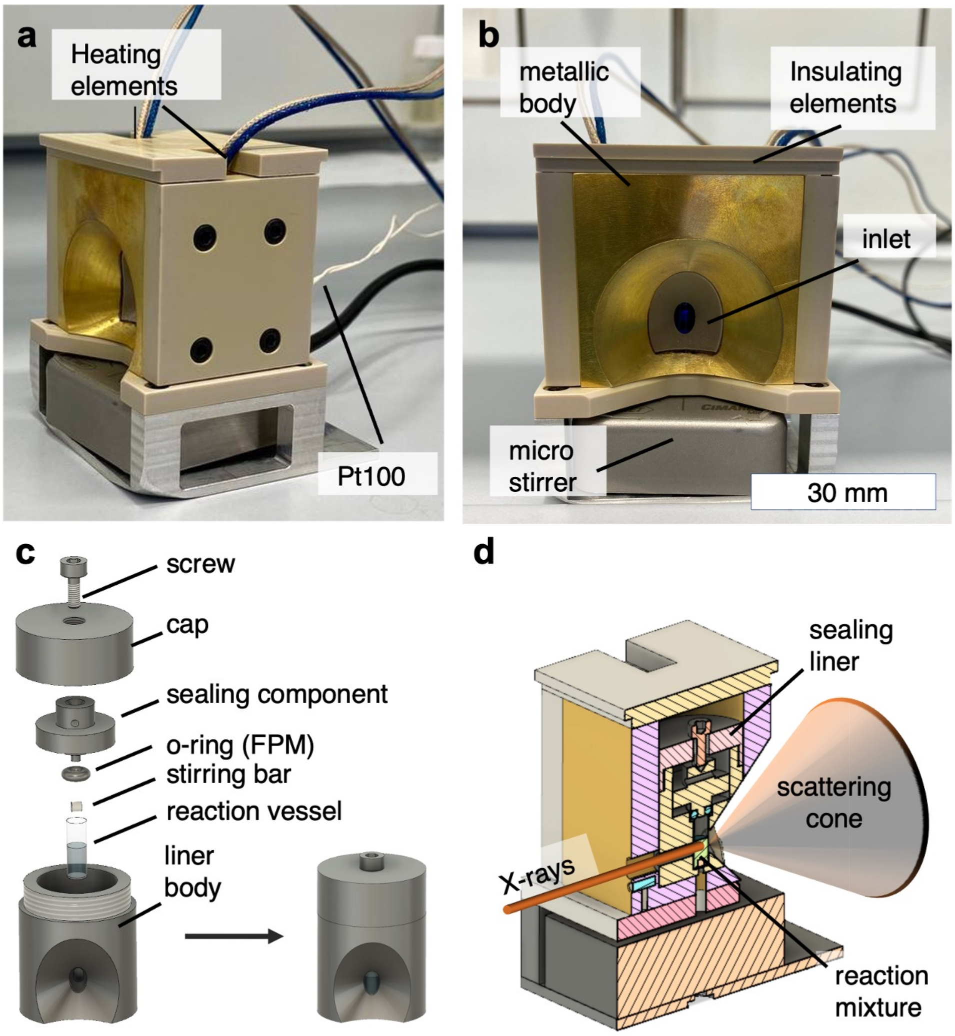

Figure 4.3: SHINES reactor for in situ nanoparticle synthesis. a-b) Pictures of SHINES reactor. **c**) Exploded view of the liner used to seal the reaction vessel against ambient air infiltration. **d**) Cross-sectional illustration of the assembled SHINES reactor during the X-ray scattering measurements.

3. permit to avoid ambient air contamination by sealing the reaction environment in a glovebox;

4. permit to adjust the sample length according to the in situ measurement. For the X-ray absorption measurements, the optimal sample length varies with the sample concentration. For combined SAXS and TS measurements, the sample length should compromise between long lengths to allow high scattering intensity in SAXS and short lengths to prevent large broadening of the TS signal at high-q;

5. the setup should produce feature-less and low intensity scattering background;

6. all components in contact with the solvent mixture should be chemically inert;

7. the cell should be small-sized to fit the spatially tight sample chamber of the acquisition setup at the P07 beamline.

We designed an in situ cell that meets the requirements outlined above, and name it with the acronym SHINES (**S**tirring and **H**eating **I**n situ cell for **N**anoparticl**E** **S**ynthesis). **Figure 4.3** illustrates SHINES main components, while a detailed description of the cell is provided in **Section 3.5.1**. In short, the cell consists in an air-tight polyether ether ketone (PEEK) inlet, which is inserted in a metal block to allow control of the reaction temperature. The reaction environment consists of a cylindrical vessel accommodated in the inlet. We use thin-walled borosilicate vessels due obtain weak, featureless background in the scattering measurements. Conversely, we prefer PEEK vessels for XAS measurement due to their improved mechanical stability. Different sets of inlets allow to accommodate cylindrical vessels of various diameters. We find that the sample length of 4.1 mm permits the acquisition of both in situ SAXS and PDF data with good signal-to-noise ratios and low broadening effects. Finally, we integrate a micro-stirrer in the in situ cell to homogenize the reaction mixture during the nanoparticle synthesis.

4.1.3 High-energy X-ray scattering in grazing incidence

4.1.3.1 Technical requirements

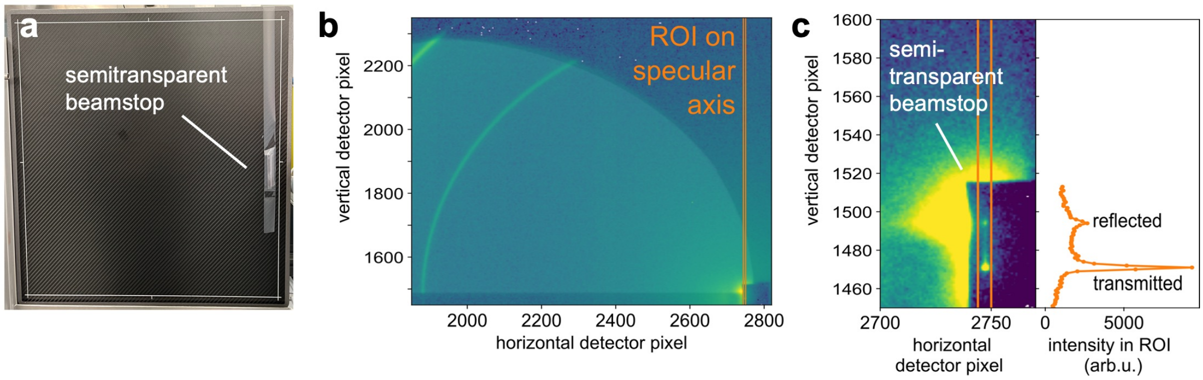

Figure 4.4: The semitransparent beamstop during grazing incidence measurements of thin films a) Picture of the tantalum semitransparent beamstop positioned on the SAXS detector. **b**) A SAXS detector image for a $CuBi_2O_4$ thin film measured in grazing incidence. A region of interest (ROI) compromissing the specular axis is displayed. **c**) A magnified view of **b**. A plot of the scattering intensities measured for horizontal slices of the detector image within the ROI is also shown.

We conducted high-energy X-ray scattering measurements in grazing incidence by using the setup shown in **Figure 4.1** and by operating at the same X-ray energy of approx. 103 keV. Since at high X-ray energy the amplitude of critical angle α_c is in the order of only few millidegrees, we employ a tightly focused beam with a vertical size of 3 µm to reduce the size of the beam footprint on the sample. **Figure S4.1** displays the dependence of the footprint size with respect to α_i in our experimental conditions.

We use a semitransparent beamstop positioned in front of the SAXS detector to capture both the transmitted and reflected beams during the measurement of thin films, as illustrated in **Figure 4.4**. Since the incident and reflected beam occur at the same angle, by detecting the signal from the reflected beam on the SAXS detector we experimentally determine the precise value of α_i. We therefore continuously assess the sample alignment with respect to the beam during the extended operando measurements. For the operando PEC measurements shown in this thesis, we determine a better stability in the sample alignment than 0.3 millidegrees.

4.1.3.2 Surface sensitivity studies

We measure high energy X-ray scattering at various angles of incidence α_i to illustrate the capability of the X-ray scattering measurements in selectively probing the surface structure of thin films. **Figure 4.5a-c** graphically illustrates three stages of the measurement, which we perform on a sample consisting of a maghemite Fe_2O_3 thin film deposited on top of a fluorine-doped tin oxide (FTO)-coated glass substrate and immersed in an electrolyte solution. **Figure 4.5d** exhibits the experimental TS intensity as a function of α_i. The scattering intensity from the Fe_2O_3 thin film increases with α_i at low incident angles and maximizes at around $\alpha_i = 0.012$ °. At this angle, the positions of the Bragg's reflections match with the simulated ones for the maghemite phase, as shown in **Figure 4.5e**. Thus, at $\alpha_i = 0.012$ ° no scattering signal from the FTO substrate is observed and the X-ray scattering measurements exhibits enhanced surface sensitivity. At higher angles of incidence, intense peaks, corresponding to the X-ray diffraction pattern of crystalline FTO, gradually emerge and eventually dominate the TS pattern at $\alpha_i = 0.030$ °, as shown in **Figure 4.5f**. Operating at angle of incidence of approximately 0.012 ° is therefore crucial to detect the structure of the Fe_2O_3 alone.

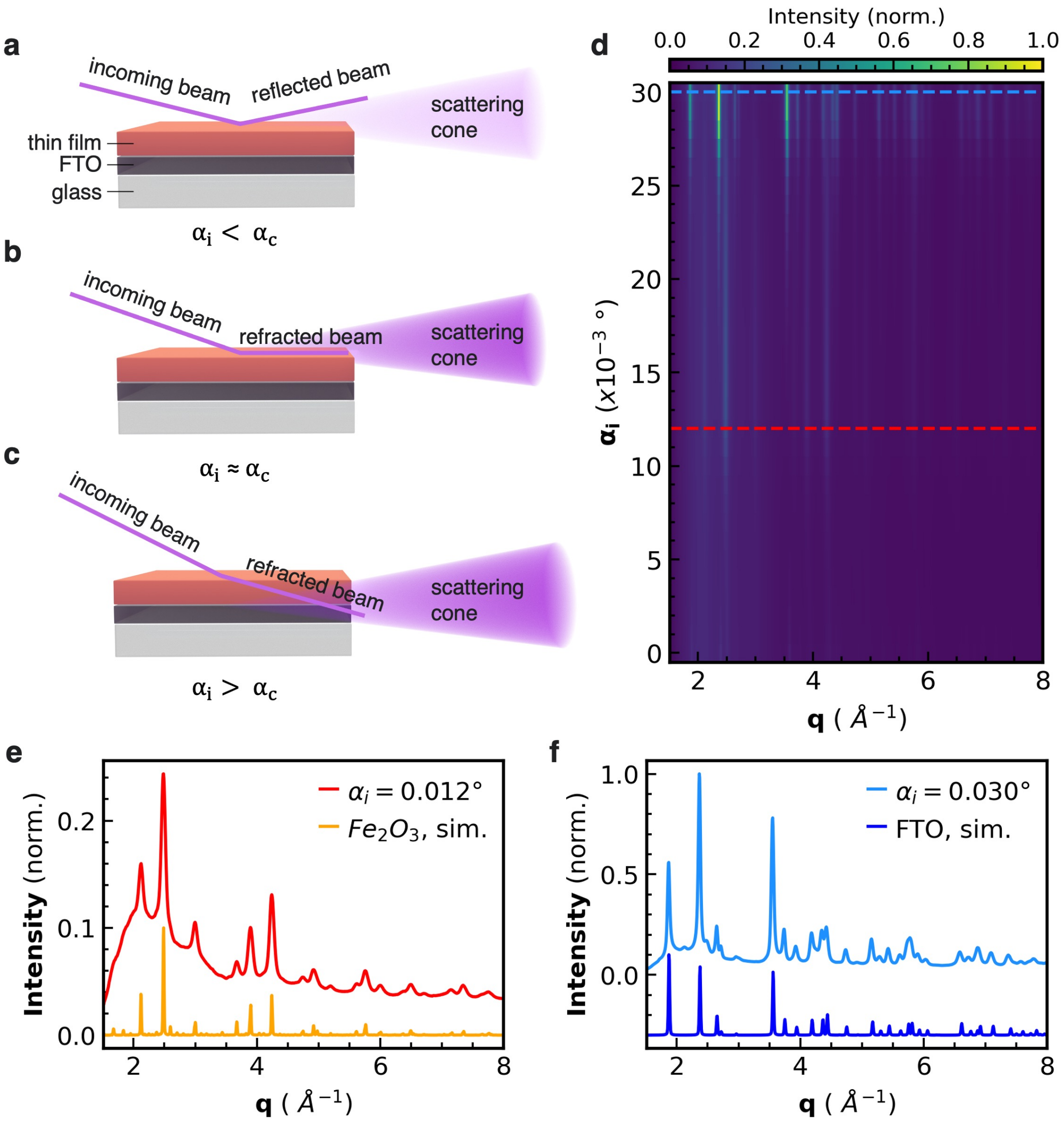

Figure 4.5: Grazing incidence high-energy X-ray scattering measurements on Fe_2O_3 thin films. a-c) Schematic illustration of the X-ray scattering measurements in total external reflection (**a**), grazing incidence (**b**) and glancing incidence (**c**) geometry for a sample consisting of a thin film deposited on FTO-coated glass substrate. **d**) 2D plot of the X-ray scattering intensity as a function of the incident angle α_i for a Fe_2O_3 thin film sample deposited on a FTO-coated glass substrate and immersed in an electrolyte solution. Horizontal dashed lines indicates the region of the plot with $\alpha_i = 0.012\,°$ and $0.030\,°$. **e-f**) The TS intensities measured at $\alpha_i = 0.012\,°$ (**e**) or $\alpha_i = 0.030\,°$ (**f**) are compared to the simulated patterns for Fe_2O_3 (maghemite) and FTO (SnO_2), respectively. In both plots, a broad background intensity originates from the scattering signal due to the electrolyte environment.

We compare the experimental value of α_c determined by **Figure 4.5d** with the calculated value for a compact Fe_2O_3 films at 100 keV. Here, α_c is experimentally defined as the angle of incidence at which the signal of the thin film maximizes, while no intensity from the FTO substrate is detected. We find that the experimental value of 0.012 ° is much smaller compared to the calculated $\alpha_c = 0.024$ °. We attribute this discrepancy to the film porosity, which decreases the effective electron density of the film compared to bulk Fe_2O_3. Given the inherent difficulty in precisely quantifying the porosity in nanostructured materials, for each electrode in this work we first determine α_c experimentally by scanning over the angle of incidence, and then operate the operando measurements at α_i just below α_c.

We further investigate the effect of the film morphology on the surface sensitivity of the X-ray scattering measurement. The fabrication of $CuBi_2O_4$ electrodes results in films of different morphology depending on the nature of the stabilizer utilized during the spin-coating procedure, as illustrated by scattering electron microscopy (SEM) in **Figure 4.6 a-d**. The use of glycerol produces films exhibiting surface defects and moderate roughness, while much smoother films are obtained by use of ethylen glycol (EG). In **Figure 4.6e**, the X-ray scattering pattern collected in grazing incidence from the $CuBi_2O_4$ films produced with glycerol displays additional diffraction peaks from FTO even at the experimental critical angle of 0.022 °. Conversely, the signal from the FTO substrate is completely suppressed in the case of the smoother electrode of comparable thickness and produced with EG, as shown in **Figure 4.6f**. These results indicate that the the film morphology largely influences the penetration depth of the X-ray beam. To retain high surface sensitivity during the high energy X-ray scattering measurements, a good control over the surface roughness during the fabrication of the electrode is therefore essential.

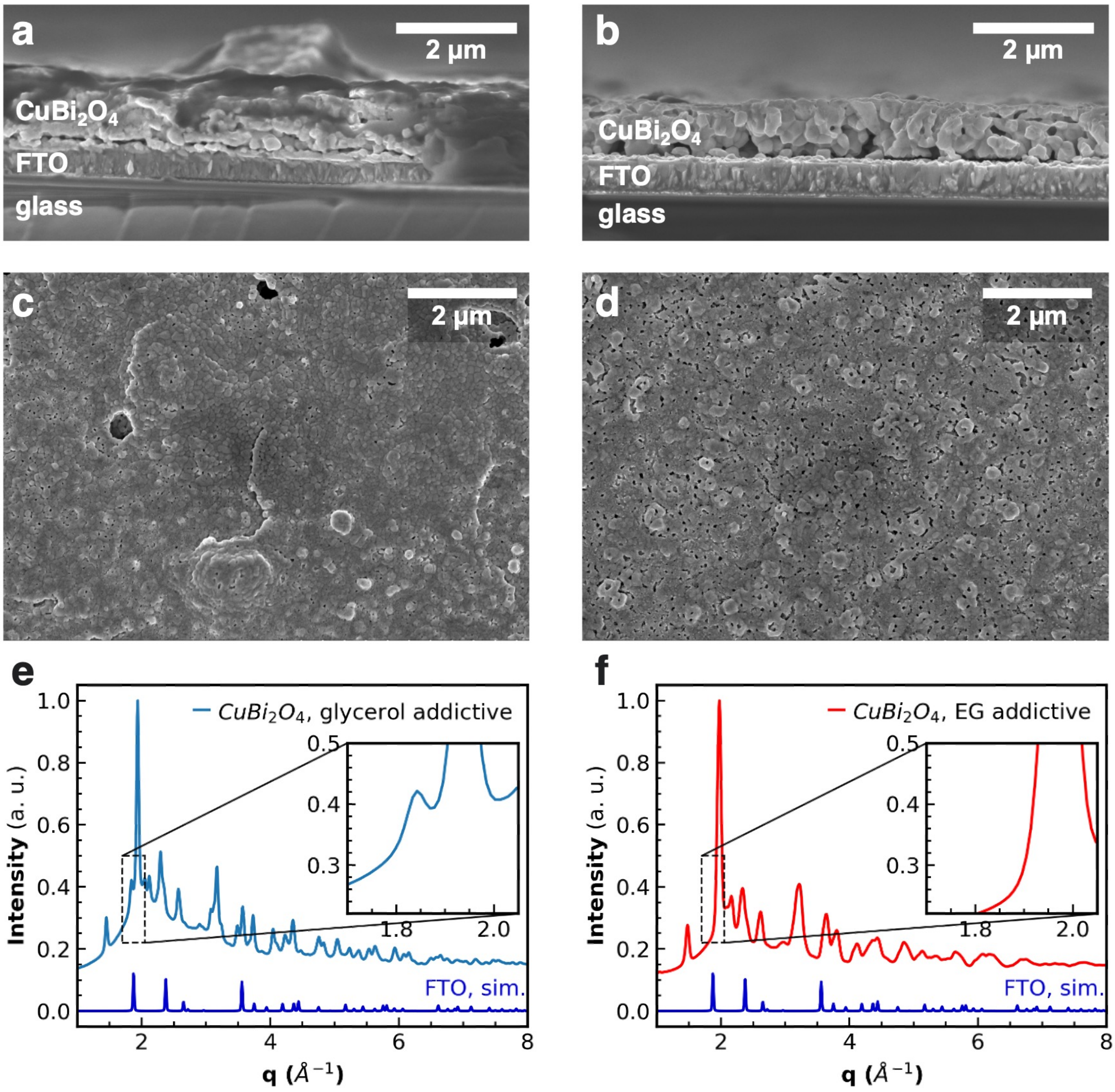

Figure 4.6: The effect of the thin film morphology over the surface sensitivity of hard X-ray scattering. Cross-section (**a-b**) and top view (**c-d**) SEM images for $CuBi_2O_4$ thin films deposited on FTO-coated glass substrates. The sample shown in **a, c** was prepared by using glycerol as addictive, while ethylen glycol (EG) was employed for the sample in **b, d**. **e-f**) Plots of the X-ray scattering patterns for the same samples collected at the angle of incidence $\alpha_i = 0.022$ °

4.1.3.3 Effect of the data-aberration correction algorithm

We investigate the effect on the X-ray scattering data of slight misalignment of the thin films with respect to the X-ray beam. **Figure 4.7a** exhibits the SAXS and the TS patterns measured simultaneously in grazing incidence for a $CuBi_2O_4$ electrode. The two patterns clearly display a slight offset, which we attribute to an imprecise positioning of the sample surface in the height center of the X-ray beam during the film alignment. An

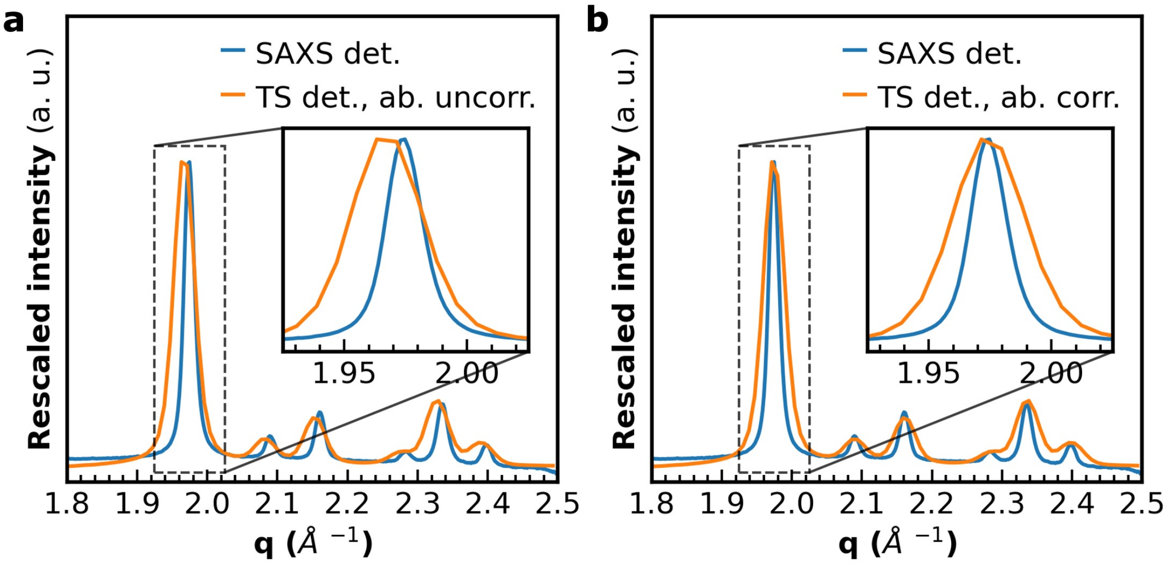

Figure 4.7: Effect of the aberration correction algorithm for the TS patterns. a) Plot of the TS (orange line) and SAXS (blue line) patterns measured for a $CuBi_2O_4$ thin film in grazing incidence geometry with $\alpha_i = 0.025°$ before application of the aberration correction algorithm. **b**) Same as **a** after application of the aberration correction algorithm to the TS data.

uncertainty over the film vertical position Δ_z with respect to the beam propagates into an uncertainty in the sample-to-detector distance Δ_{SDD} according to:

$$\Delta_{SDD} = \frac{\Delta_z}{tan(\alpha_i)} \tag{4.1}$$

For our experimental conditions, Δ_z is in the order of few tenths of micrometers, which results in Δ_{SDD} typically below 1 mm at angles around 0.025 °. The magnitude of Δ_{SDD} is negligible when compared to the absolute sample-to-detector distance (SDD) of the SAXS detector (approx. 4600 mm), but becomes significant when compared to the SDD for the TS detector (approx. 760 mm). We show that the aberration of the scattering data collected by the TS detector can be corrected by using the routine reported in Section 3.7.1.4. In short, the method consists in fitting the position in q of a Bragg's reflection in the overlap region of both SAXS and TS patterns, and in recalculating the experimental SDD distance for the TS detector so that the position of the two Bragg's reflection matches. The validity of the applied algorithm is demonstrated in Section S4.1. **Figure S4.2b** reports the SAXS and TS patterns after use of the proposed algorithm in which the position of the diffraction peaks nicely match. In **Table 4.1** we further report the structural parameters obtained via PDF fit of the TS data both before and after aberration correction. We find that the corrected data outcome in values of lattice constants closer to the ones reported in literature for the $CuBi_2O_4$ phase.[234] We therefore conclude that the proposed algorithm effectively mitigates the effects of sample misalignment in the TS patterns. We therefore implement the aberration correction algorithm in our data processing routine and always apply it in the rest of the thesis prior to the Fourier transformation of the grazing incidence TS signal in the PDF.

	Scale factor (a. u.)	a (Å)	c (Å)	δ_2 (Å^2)	Rw
without aberr. correction	0.139 ± 0.001	8.538 ± 0.006	5.837 ± 0.008	6 ± 3	0.108
with aberr. correction	0.139 ± 0.001	8.516 ± 0.006	5.823 ± 0.008	6 ± 3	0.109

Table 4.1: Effect of the aberration correction algorithm on the PDF fit of a $CuBi_2O_4$ electrode. The PDFs were fit by modeling of a $CuBi_2O_4$ phase with the AC model. Psize values were fixed to 800 Å, ADP values were constrained to the crystal space group symmetry and refined in the 0-0.06 Å^2 range.

4.1.4 SCOPE cell for operando measurements on PEC films

We developed a sample environment that meets the technical requirements for the measurement of operando X-ray scattering on PEC-active thin films:

1. it allows to accommodate and electrically connect a PEC-active electrode, operating as working electrode (WE).
2. it allows to accommodate a reference electrode (RE) and a counter electrode (CE);
3. it permits to illuminate the sample;
4. it is small-sized, water-tight, and chemically inert;
5. it foresees a longer sample length than the footprint size on the sample, which is in the order of 5-15 mm, (see **Figure S4.1**);

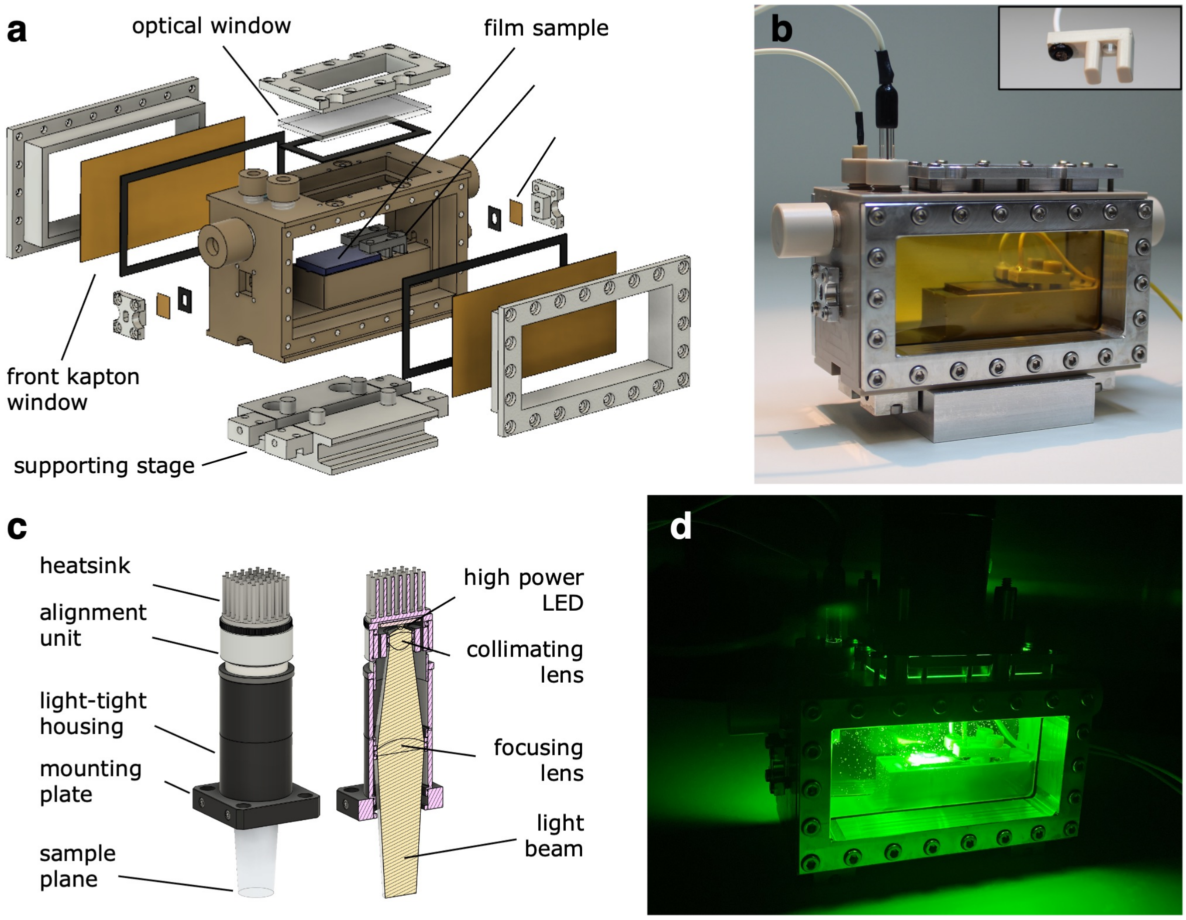

Figure 4.8: The SCOPE cell for operando PEC measurements. a) Exploded view of SCOPE. **b**) Picture of SCOPE accomodating a PEC-active thin film sample, the Ag/AgCl RE, and the CE. In the inset, a picture of the WE connector is shown. **c**) External and cross-sectional view of the high-power LED unit. **d**) Picture of SCOPE during PEC measurements with a 535 nm LED.

6. it allows to align the sample to the X-ray beam in two orthogonal directions;

7. it generates low intensity, featureless X-ray scattering background.

Figure 4.8 provides an overview of the operando cell and illumination unit, which we refer to by the acronym SCOPE (**S**cattering **C**ell for **O**perando **P**hoto-**E**lectrochemistry). The technical details of SCOPE are further illustrated in in **Sections 3.5.2 - 3.5.3**. The cell is equipped with a Ag/AgCl RE, a Pt-wire as CE, and it allows to accommodate PEC films up to 25x15 mm^2 in size. The illumination at the sample position is provided by focusing the emitted light generated by a high-power LED positioned above the sample. The selection of various LEDs permits to adjust the wavelength of the illumination emission. Here, we prefer the use of the LED over a simulated solar source due to the spatially constrained sample chamber at the beamline.

4.1.4.1 Background contribution to the Total Scattering signal

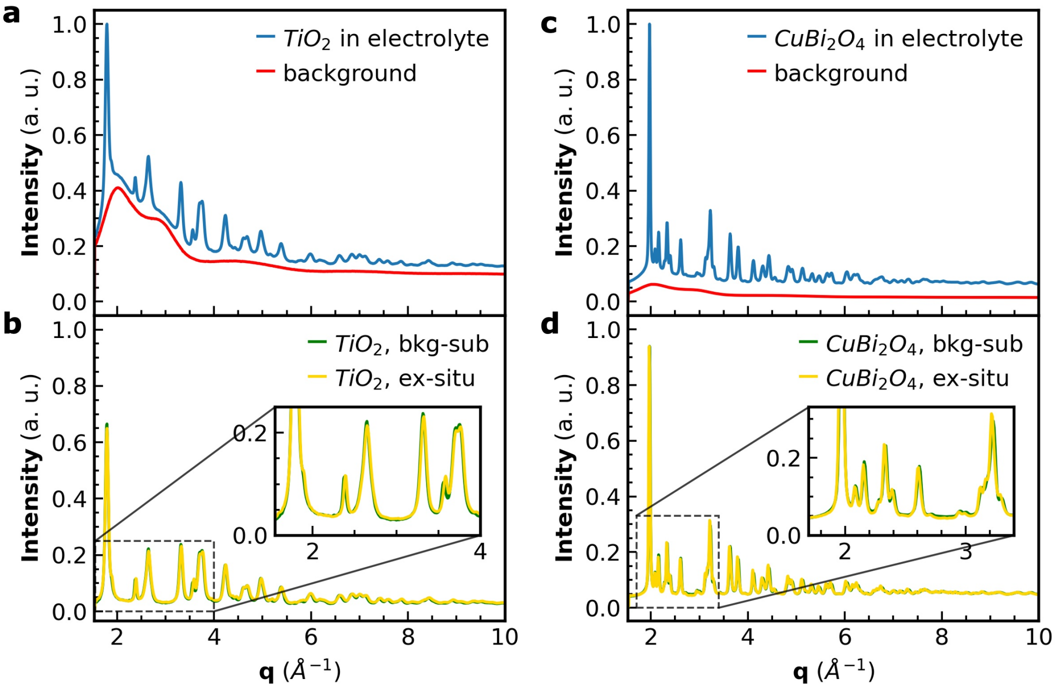

Figure 4.9: Contribution of the electrolyte to the TS intensity. a) Plot of the TS intensity for a TiO_2 thin film deposited on a FTO-coated glass substrate. The contribution of the electrolyte to the overall TS signal is also shown. **b**) The background subtracted TS pattern shown in **a** is compared to the X-ray scattering signal from the same sample measured ex situ, ie. without immersion in the electrolyte **c**) Same as **a** for a sample consisting of a $CuBi_2O_4$ deposited on FTO-coated glass substrate. **d**) Plot of the background subtracted pattern in **c** and of the relative ex situ measurements.

We verify that the presence of a 17 mm-thick layer of electrolyte in SCOPE is compatible with the measurement of thin film samples in grazing incidence. We measure either a TiO_2 or a $CuBi_2O_4$ thin film deposited on a FTO-coated glass substrate and immersed in an electrolyte solution as model systems for a low-scattering and a high-scattering PEC-active metal oxide electrodes. We then compare the isolated TS intensity after subtraction of the electrolyte background to the respective patterns obtained ex situ, ie. without electrolyte immersion. The results are summarized in **Figure 4.9**. We show that the background subtracted intensities nicely matches with the ex situ measurements. The results thus demonstrate that penetrative high-energy X-rays constitute an effective tool to probe thin film samples that are buried in a thick PEC cell.

4.1.4.2 PEC properties probed within SCOPE

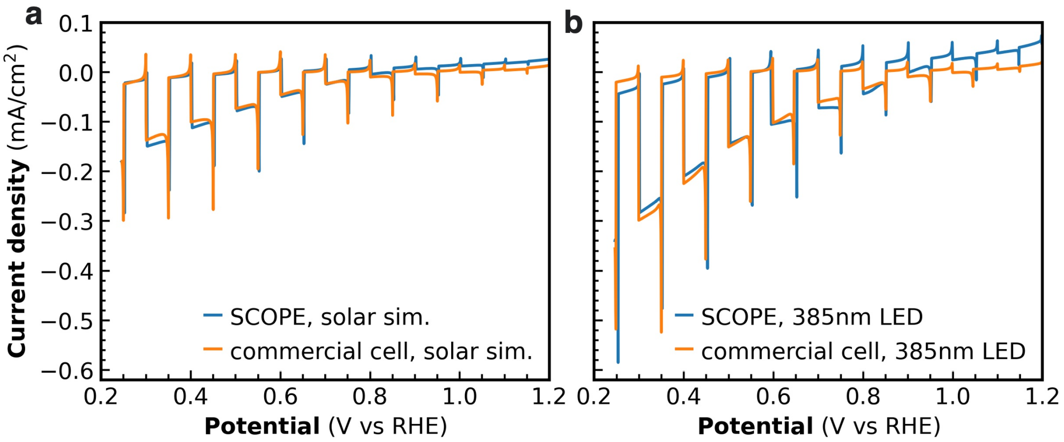

Figure 4.10: PEC properties probed with SCOPE compared to a commercial cell a) LSV on a $CuBi_2O_4$ electrode under simulated solar emission probed either within SCOPE or within a commercial PEC cell. **b**) Same as **a** by use of a high power LED illumination with emission wavelength centered at 385 nm.

We validate that SCOPE allows reliable PEC measurements when compared to a commercial cell for PEC characterization (ZAHNER-elektrik, PECC-2). The LSV measured for the same $CuBi_2O_4$ electrode and by use of a simulated solar light source (Lumixo S, Lumatrix) results in similar values of photocurrents by using either of the two cells, as shown in **Figure 4.10a**. We further prove the reproducibility of the PEC proprieties by LSV measurements on the same $CuBi_2O_4$ electrode and by use of a high-power LED illumination centered at 385 nm (**Figure 4.10b**). We select an emission wavelength above the bandgap of 1.6-1.8 eV[144] of $CuBi_2O_4$ to enhance the photoresponse of the photocathode, as demonstrated by the highest absolute values of photocurrents reported in **Figure 4.10b** compared to **a**.

We further assess the effect of the high-energy X-ray probe on the measured photocurrents for a $CuBi_2O_4$ electrode in the absence of light illumination and at different applied potentials. Since the energy of the 103 keV is well above the absorption edges of the element constituting the photoabsorbing material, we expect to record similar values of current densities regardless of the interaction between the X-ray probe and the sample. Indeed, **Figure 4.11** proves that the X-ray induced photocurrents are negligible.

Our results demonstrate that the use of high energy X-rays does not affect the PEC properties of $CuBi_2O_4$ electrodes, while at the same time permits to probe the structure of thin film within a PEC cell with enhanced surface sensitivity. These findings thus lay the groundwork for performing multi-modal high-energy X-ray scattering measurements on PEC-active thin films under operation conditions.

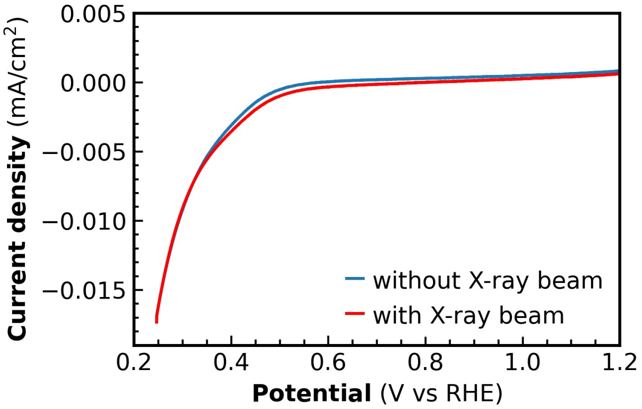

Figure 4.11: The effect of X-ray beam induced photocurrents during LSV measurements in dark LSV on a $CuBi_2O_4$ electrode without light illumination in the presence or absence of the high energy X-ray probe (103 keV).

4.1.5 Supporting information

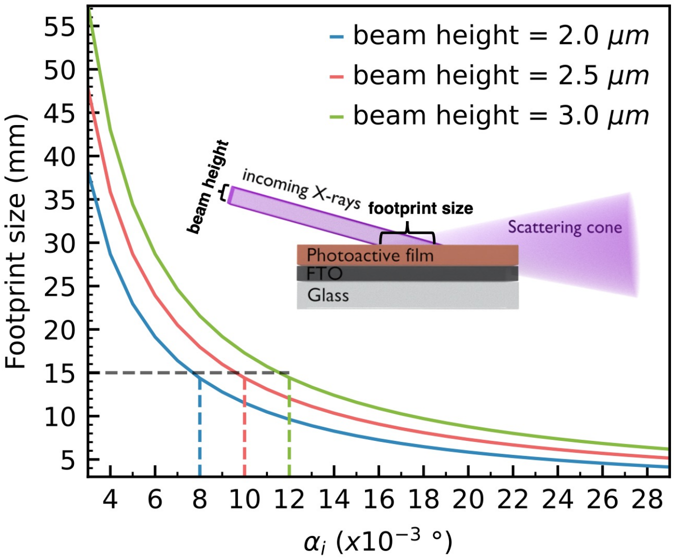

Figure S4.1: Plot of the X-ray footprint size of film samples measured in grazing incidence as a function of α_i. The size dependence for the footprint size for focused beams with beam heights of 2.0, 2.5, and 3.0 μm is shown. The dotted lines indicate the maximum sample length for a thin film accommodated in the SCOPE cell. The maximum sample length determines the smallest value of α_i which can be used for the grazing incidence measurements. In the inset, a schematic illustration of the X-ray scattering measurement in grazing incidence of a photo-active electrode.

Demonstration of the aberration-correction algorithm

The demonstration illustrated in this section has been already reported by us in *Angew. Chem. Int. Ed.* 62, e202307948 (2023).

Let us consider a sample that is positioned in S at a sample-to-TS-detector distance SDD_{exp} which is different from the sample-to-TS-detector distance SDD_{calib} that was calibrated at the calibration point C. The acquired intensity by a certain detector pixel P will relate to different scattering angles $2\theta_{calib}$ and $2\theta_{exp}$ depending on the center of the scattering event being at C or at S, respectively.

The relations between the SDD_{calib} or SDD_{exp} and the relative scattering angle subtending the distance D_{pixel}, which separate P from the X-ray point of normal incidence (PONI) are:

$$2\theta_{calib} = arctan\left(\frac{D_{pixel}}{SDD_{calib}}\right) \tag{4.2}$$

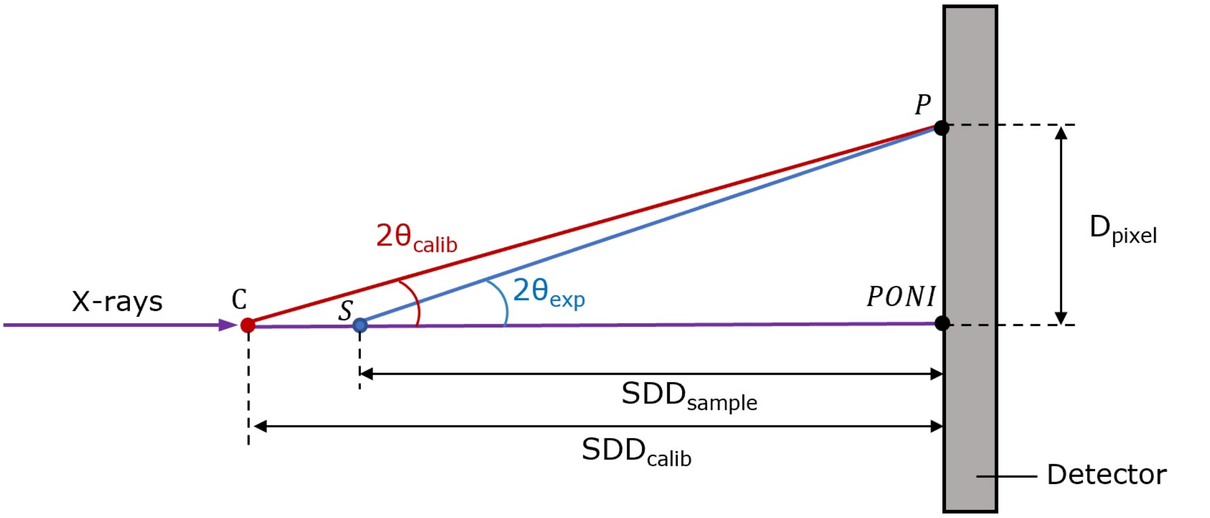

Figure S4.2: Geometrical considerations for the measurement in grazing incidence by use of an area detector. When the vertical position of a film surface is not exactly centered to the X-ray beam height, the sample position (S) differs from the calibrated position (C) once the sample is tilted in the direction of the beam. SDD_{exp} indicates the experimental effective sample-to-detector distance, as opposed to the calibrated distance SDD_{calib}. D_{pixel} indicates the radial distance of a given detector pixel P from the center of the direct beam on the detector. $2\theta_{calib}$ and $2\theta_{exp}$ represent the scattering angle subtended by the segment of length D_{pixel} and centered in C and S, respectively.

$$2\theta_{exp} = arctan\left(\frac{D_{pixel}}{SDD_{exp}}\right) \tag{4.3}$$

Additionally, one can combine Bragg's law and the relation between direct and reciprocal space to derive the expression relating the scattering angle 2θ to the scattering vector q:

$$2dsin(\theta) = lambda;\ q = \frac{2\pi}{d} \rightarrow q = \frac{4\pi}{\lambda}sin(\theta) \tag{4.4}$$

where d is an interatomic distance in direct space and λ is the X-ray wavelength.

By substituting either 4.2 or 4.3 in 4.4 and thus considering the scattering angle either centered in C or S, one obtains the relations:

$$q_{calib} = \frac{4\pi}{\lambda}sin\left(\frac{1}{2}\ arctan\left(\frac{D_{pixel}}{SDD_{calib}}\right)\right) \tag{4.5}$$

$$q_{exp} = \frac{4\pi}{\lambda}sin\left(\frac{1}{2}\ arctan\left(\frac{D_{pixel}}{SDD_{exp}}\right)\right) \tag{4.6}$$

SDD_{calib} is known from the calibration measurement, while SDD_{exp} is unknown. One can then substitute the value of D_{pixel} from 4.5 in 4.6 and rearrange to find an expression for evaluating SDD_{exp}:

$$SDD_{exp} = SDD_{calib} \left(\frac{tan\left(2\ arcsin(q_{calib}\ \frac{\lambda}{4\pi})\right.}{tan\left(2\ arcsin(q_{exp}\ \frac{\lambda}{4\pi})\right.} \right) \tag{4.7}$$

4.7 is generally valid for any pixel on the detector.

For the $CuBi_2O_4$ films, we considered the position of the $CuBi_2O_4$ (211) reflection on both the SAXS and TS patterns to experimentally determine SDD_{exp} under the assumption that the length of the segment CS is negligible compared to the calibrated sample-to-SAXS-detector distance. It follows that $q_{exp} \approx q_{(211),SAXS}$ and SDD_{exp} can be estimated as:

$$SDD_{exp} = SDD_{calib} \left(\frac{tan\left(2\ arcsin(q_{(211),TS}\ \frac{\lambda}{4\pi})\right.}{tan\left(2\ arcsin(q_{(211),SAXS}\ \frac{\lambda}{4\pi})\right.} \right) \tag{4.8}$$

where $q_{(211),TS}$ and $q_{(211),SAXS}$ are the position of the $CuBi_2O_4$ (211) reflection as observed in the in the SAXS and TS detector patterns, respectively.

Once SDD_{exp} is known, its value can be substituted in 4.7 to convert any value of the scattering vector evaluated at the calibration position C as being instead at the actual sample position S. The general expression for the aberration correction becomes:

$$q_{exp} = \frac{4\pi}{\lambda} sin\left(\frac{1}{2} arctan\left(K tan\left(2 arcsin\left(q_{calib.} \frac{\lambda}{4\pi}\right)\right)\right)\right) \tag{4.9}$$

where the correction coefficient K is defined as:

$$K = \frac{tan\left(2 arcsin\left(q_{(211),SAXS} \cdot \frac{\lambda}{4\pi}\right)\right)}{tan\left(2 arcsin\left(q_{(211),TS} \cdot \frac{\lambda}{4\pi}\right)\right)} \tag{4.10}$$

By looking at 4.9 and re-labelling q_{exp} one obtains the same expression shown in section 3.7.1.4.

4.2 Elucidating the formation mechanisms of Pd and Cu metallic nanocrystals

A manuscript disseminating the content of this section is currently in preparation. The finalization of the in situ XAS analysis is still ongoing.
My contribution to this study compromises the synthesis of the nanocrystals, the measurements of the in situ scattering and absorption spectroscopy, the analysis of the in situ PDF and TS data, the electron microscopy and infrared spectroscopy characterization, and the overall interpretation of the results.

In the previous section we demonstrated the simultaneous acquisition of TS and SAXS to determine structural information over multiple length scales at once. We additionally illustrated the design of an in situ reactor which enables measurement of both X-ray scattering and XAS. In this section, we benefit from the complementary information provided by in situ PDF, SAXS, and XAS to unveil complex nucleation pathways during the synthesis of Pd and Cu nanocrystals in the presence of oleylamine and oleic acid, as schematically illustrated in **Figure 4.12**. We further support our results by additional ex situ techniques, such as infrared spectroscopy and electron microscopy.

4.2.1 Synthesis and ex situ characterization of Pd and Cu nanocrystals

We synthesize Pd and Cu nanocrystals after dissolving the respective metal acetylacetonate (acac) precursor salts in a mixture containing oleylamine and oleic acid, and by heating up the resulting solution to 190 or 210 °C at a constant rate of 10 °C min^{-1}. In **Figure 4.13 a-b**, high-resolution transition electron microscopy (HRTEM) imaging reveals the formation of single-crystalline Pd nanocrystals of approximately 4 nm in size. In **Figure 4.13c** the respective powder X-ray diffraction (PXRD) pattern displays broad diffraction peaks, which are compatible with the formation of phase pure Pd crystals.

The analogous synthesis of Cu nanocrystals results in nanoparticles of much larger size and higher polydispersity, as revealed by the scanning electron microscopy (SEM) images in **Figure 4.13 d-e**, while the PXRD measurements in **Figure 4.13f** displays sharp

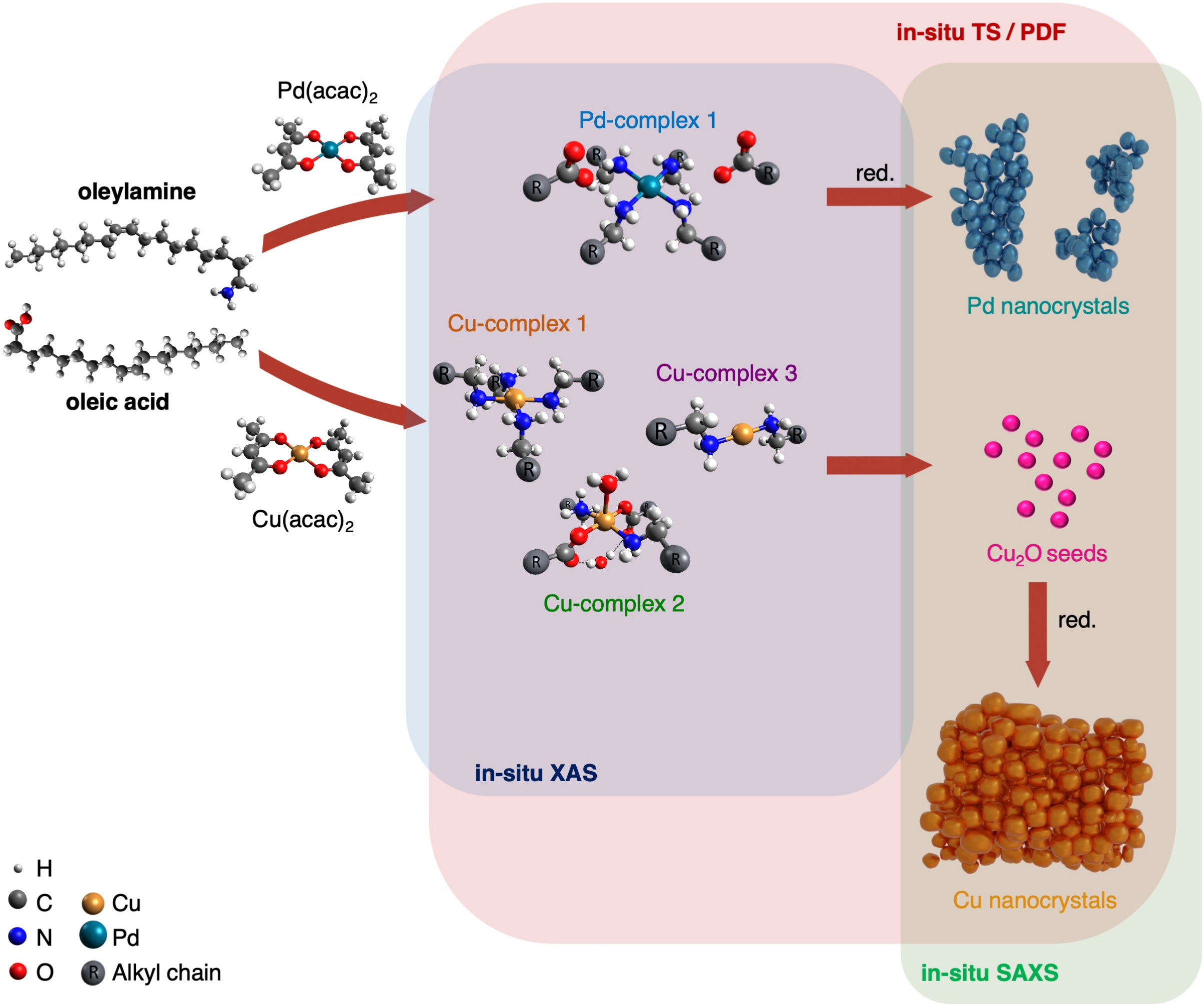

Figure 4.12: Overview of the structural transformations leading to the synthesis of Pd and Cu nanocrystals. Once dissolved in oleylamine (OAm)/ oleic acid (OAc) mixture, Pd(acac)$_2$ precursor transforms into the oleate-coordinated ($^-$OAc) amino-complex Pd-complex 1, [Pd(II)(OAm)$_4$($^-$OAc)$_2$], which ultimately converts into Pd nanocrystals' aggregates upon reduction at 190 °C. Dissolution of Cu(acac)$_2$ salt and heating of the reaction mixture lead to the sequential formation of three different organocopper complexes at increasing temperature, which we identify as [Cu(II)(OAm)$_4$]$^{2+}$, [Cu(II)(OAm)$_2$($^-$OAc)$_2$)2H$_2$O], and [Cu(I)(OAm)$_2$]$^+$, respectively. Upon prolonged heating, the partially reduced Cu(I)-complex converts into small Cu$_2$O seeds, which further fuse and reduce to produce Cu nanocrystals. Our understanding of the synthetic mechanisms to Pd and Cu nanocrystals largely benefits from the complementary information provided by in situ TS-PDF, SAXS, and XAS, as schematically indicated by the coloured overlays.

reflections due to the presence of the crystalline Cu phase. We further perform Fourier-transformed infrared spectroscopy (FTIR) on the Cu nanocrystal dispersions and reveal intense vibrational bands due to the presence of OAm and OAc capping agents on the Cu nanocrystal surfaces (**Figure S4.3**). Differently, no vibrational bands are detectable by FTIR measurement on a dried dispersion of Pd nanocrystals. This result suggests that the interactions between the capping ligands and the Pd metal cores are very weak, as washing the nanocrystals by a single re-dispersion and centrifugation cycle proves to remove most of the organic molecules from the nanocrystal surface.

In summary, the proposed synthetic method outcomes in nanometer-sized, phase-pure crystalline metal nanoparticles. However, our ex situ characterization does not provide insights into the reaction mechanisms driving the acetylacetonate precursors to convert into the nanocrystal products. We thus turn to in situ analytical methods to uncover this information.

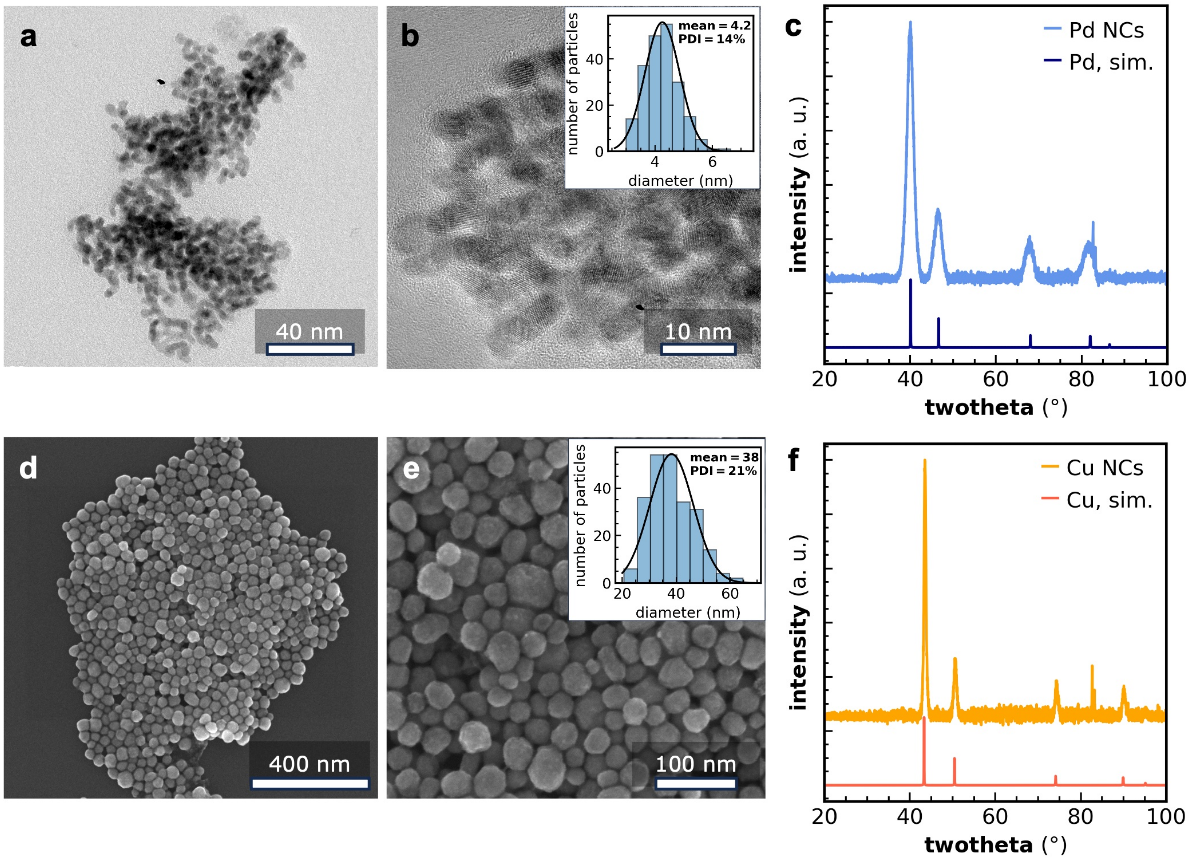

Figure 4.13: Overview of the reaction products for Pd and Cu nanocrystal syntheses. a, b) HRTEM images of 4-nm Pd nanocrystals. In the inset in **b**, the histogram of the nanocrystal diameters as reveal by HRTEM is shown. **c**) Plot of the PXRD pattern of Pd nanocrystals as compared to a simulated pattern for a pure Pd phase. **d-e**) SEM images of Cu nanocrystals of approximately 40 nm in size. The inset in **e** displays the histogram of the particle diameters, as determined from SEM imaging. **f**) Plot of the PXRD pattern of Cu nanocrystals as compared to a simulated pattern for a pure Cu phase.

4.2.2 The formation of Pd nanocrystals studied in situ

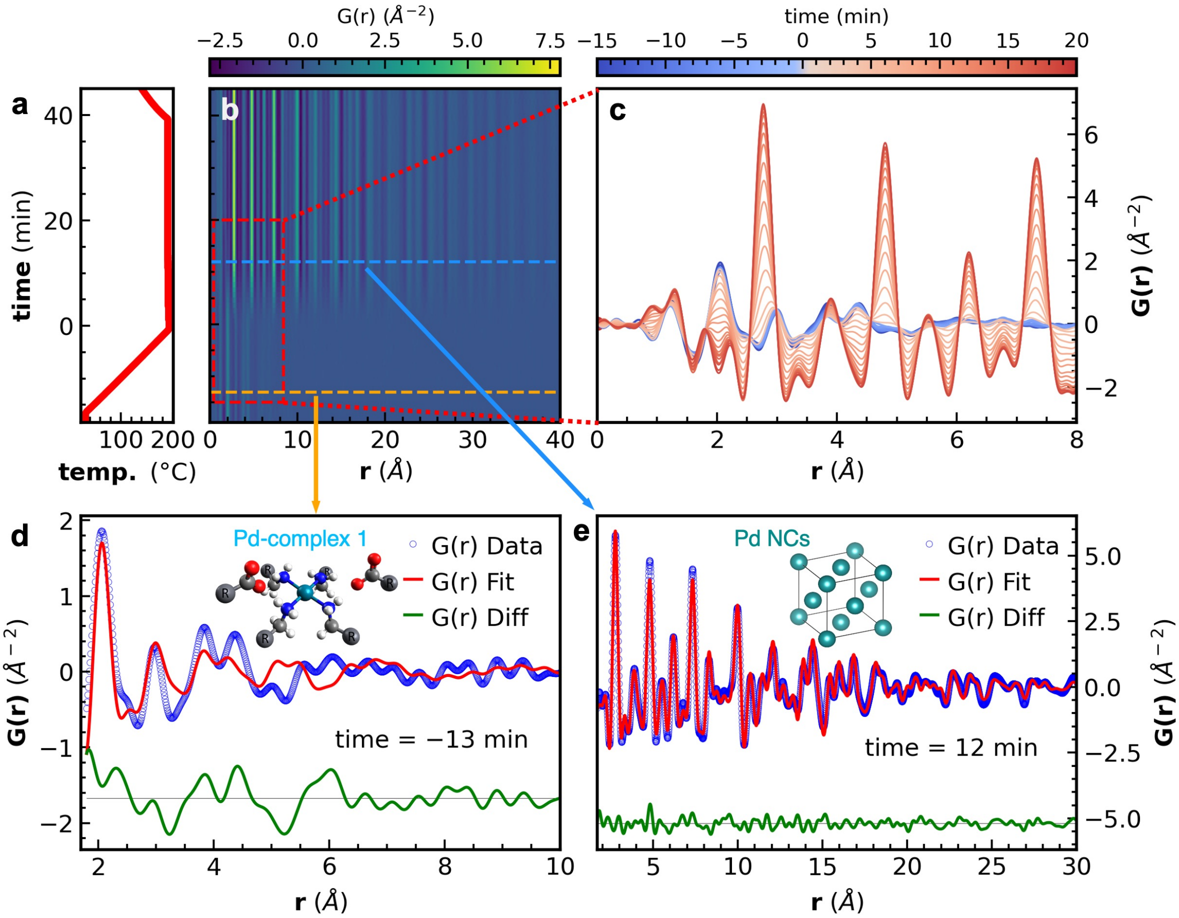

Figure 4.14: Overview of the in situ PDF data during the synthesis of Pd nanocrystals. **a**) Plot of the temperature profile during the in situ measurement. At time = 0 the reaction temperature of 190 °C is reached. **b**) 2D plot of the in situ PDF data as a function of the reaction time. **c**) 1D PDF profiles from the selected region of the 2D plot in **b**. **d-e**) Fits of selected PDF profiles by means of a discrete organometallic structural model (Pd-complex 1) and of a single-crystalline Pd phase, respectively. In the insets, a graphical representation of either of the two models is shown.

We employ the experimental setup illustrated in Section 4.1.1 to record high-energy X-ray scattering during the synthesis of Pd nanocrystals. **Figure S4.4** offers an overview of the simultaneous in situ SAXS and TS data. The fast formation of the nanocrystals in solution determines an abrupt increase in the SAXS intensity immediately after the reaction mixture reaches 190 °C. At the same time, the broad scattering signal in the TS pattern rapidly evolves into well-defined diffraction peaks, due to the formation of crystalline domains.

We Fourier transform the TS signal into the PDF of **Figure 4.14** to get insights into the structural transformations leading to the emergence of the nanocrystals. At room temperature, the presence of a molecular species exhibiting short-range order results in low intensity peaks in the PDF up to short interatomic distances (blue line in **Figure 4.14c**). The shape of the PDF is unaltered up to 190 °C, suggesting that the initial species is stable in solution up to this temperature. Subsequently, upon reaching 190 °C, the PDF rapidly evolves and intense peaks appear in the data up to long interatomic distances, evidencing the formation of the nanocrystals.

We scrutise the PDF at low temperatures to determine the structure of the organometallic precursor prior to the nanocrystal nucleation. In **Figure 4.14d** the PDF exhibits an intense peaks at 2.07 Å. This distance is significantly longer compared to the reported palladium-oxygen bond length of 1.98-1.99 Å for the $Pd(acac)_2$ precursor[235] and hints to the formation of an amine coordinated complex of Pd^{2+} cations upon dissolution, in agreement with previous reports.[71] We calculate the PDF of isolated molecular models by Fourier transformation of the X-ray scattering intensity determined via the Debye scattering equation. We obtain a good fit to the experimental PDF by considering a organometallic complex in which the Pd^{2+} center is coordinated by four oleylamine substituents in a squared-planar configuration. The additional presence of two deprotonated oleic acid ligands in a second coordination sphere neutralizes the overall charge of the complex. The proposed structure, which we label as Pd-complex 1, agrees with previous findings from Yin at al., who successfully isolated this intermediate by crystallization and then determined its structure via single-crystal X-ray diffraction.[71] Here, we confirm the presence of the same complex in solution up to high temperatures. After nucleation of the nanocrystals, the experimental PDF is adequately described by means of a single crystalline Pd phase, which we simulate within the AC approximation (**Figure 4.14d**).

We analyse the time-resolved PDF to determine the formation of eventual intermediate species during the conversion of Pd-complex 1 into the Pd nanocrystals. To this goal, we fit the experimental PDF by means of a two-phase refinement in which the summed contributions of both the organometallic complex and the crystalline phase are accounted by use of scaling factors. In **Figure S4.5**, the scale factor relative to Pd-complex 1 reduces upon reaching of the reaction temperature of 190 °C, while the contribution of the Pd phase increases. The smooth decrease in the weighted residual error Rw obtained from the fit suggests that no further intermediate species form during the process. Thus, the analysis indicates that Pd-complex 1 directly converts into the Pd nanocrystals.

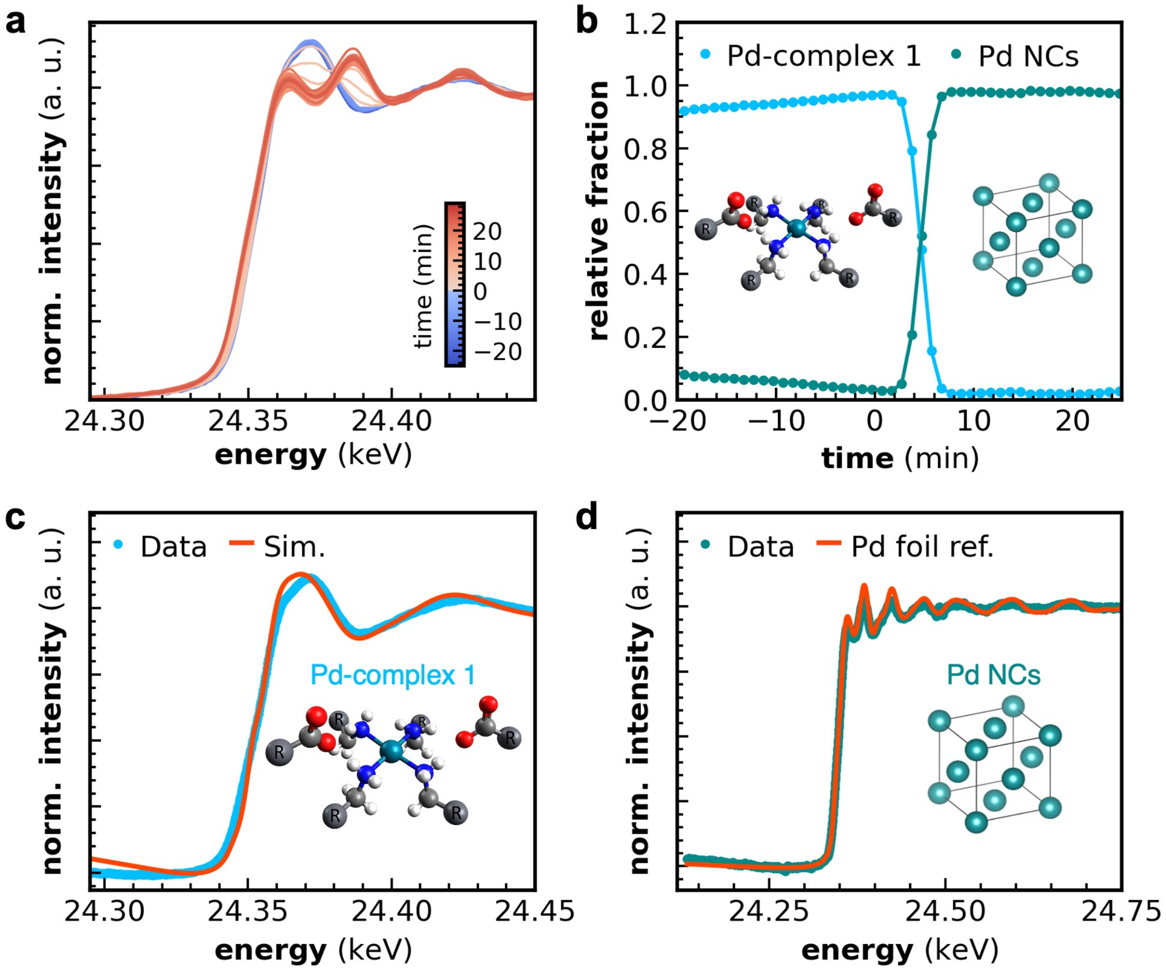

Figure 4.15: Overview of the XANES region of the in situ QEXAFS data during the synthesis of Pd nanocrystals. a) Plot of the in situ X-ray absoption profiles measured at the Pd K-edge during the synthesis of Pd nanocrystals. At time = 0, the reaction temperature of 190 °C is reached. **b**) Plot of the relative fractions for different components obtained by MCR-ALS analysis of the XANES data. **c**) Plot of the experimental XANES profile at the beginning of the synthesis. The calculated plot for Pd-complex 1 is also shown. **d**) Plot of the experimental XANES profile at the end of the synthesis as compared to the measured absorption spectrum for a Pd foil reference. Graphical representations of the two structural models are shown in the insets of pannels **b, c**, and **d**.

We support the result obtained from the in situ PDF analysis by measurement of in situ quick extended X-ray absorption fine structure (QEXAFS) at the Pd K-edge. X-ray scattering already indicates that the initial organometallic complex reduces into the metallic phase in only few minutes. Therefore, a rapid acquisition of X-ray absorption profiles, as enabled by QEXAFS routines, is essential to detect the emergence of eventual short living intermediates before the nucleation stage. **Figure 4.15a** provides an overview of the in situ QEXAFS data. The conversion of the Pd^{2+} species into the reduced form corresponds to a change in the shape of the white line and in a shift of the edge position to lower energy. We perform Multivariate Curve Resolution - Alternating Least Squares (MCR-ALS) analysis to decompose the spectral data in the XANES region into its primary constituents, as shown in **Figure 4.15b**. The analysis reveals the existence of two main components and agrees with the subsequent formation of Pd-complex 1 and crystalline Pd phase in solution, as illustrated by **Figure 4.15c** and **d**, respectively. We also compare the experimental spectrum at room temperature with the simulated ones for alternative Pd^{2+} complexes, as shown in **Figure S4.6**. Although the analysis tends to support the formation of the tetra-amino Pd(II) complex we identified via PDF, the quality of the data does not allow to fully discriminate between squared-planar palladium(II)-complexes displaying different nucleophilic ligands. Nevertheless, both the identified Pd-complex 1 structure and the crystalline Pd phase provide a good fit to the EXAFS profiles measured at early and late stages of the synthesis, as illustrated in **Figure S4.7**. The overall analysis of the QEXAFS confirms that the organometallic complex directly converts into the reduced Pd crystal form, as we detect no formation of intermediate species within the temporal resolution of the measurements.

We measure FTIR of the palladium precursor at room temperature to determine the role of oleylamine and oleic acid ligands in the formation of Pd-complex 1. In **Figure 4.16**, mixing the $Pd(acac)_2$ salt with oleic acid alone results in a vibrational spectrum which is the direct sum of the spectra of pure oleic acid and $Pd(acac)_2$, therefore indicating that the precursor salt doesn't dissolve in oleic acid. In fact, over time we observe the sedimentation of $Pd(acac)_2$ salt at the bottom of the container, as shown by the picture in **Figure S4.8**. Conversely, mixing $Pd(acac)_2$ with oleylamine drives the formation of freely dispersed acetylacetonate groups due to the substitution of the acac ligands with amines. As a result, we detect a vibrational peak at 1603 cm^{-1} and additional peaks at 3170 and 3103 cm^{-1}, which we assign to the vibration of the C=O bond and to the asymmetrical vibration of CH_3 groups in loosely coordinating acetylacetonate, respectively.[236] This finding is in line with previous reports.[67,71] Finally, we measure FTIR after addition of

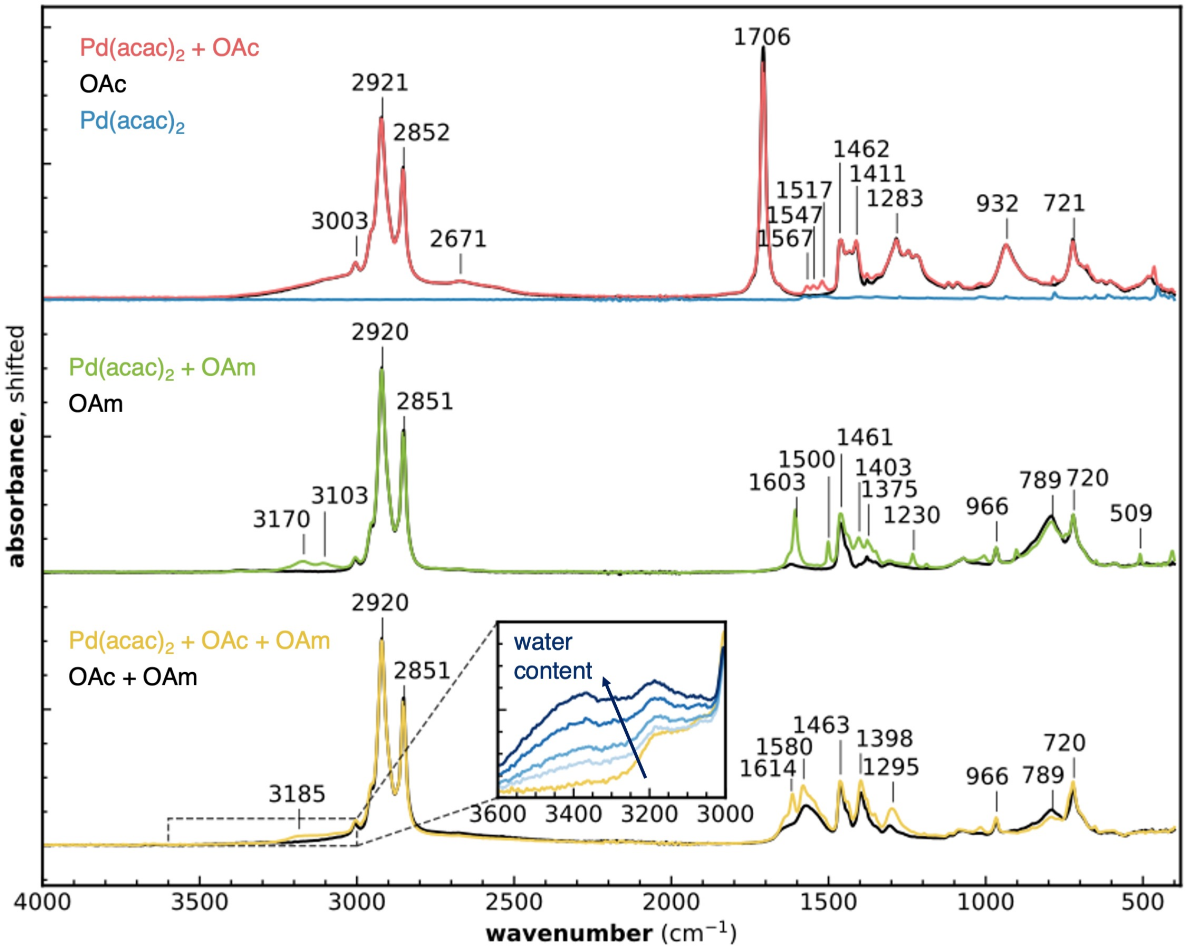

Figure 4.16: FTIR measurements for mixtures of Pd(acac)$_2$ with different solvents. *Top*: The FTIR spectra of pure Pd(acac)$_2$ and OAc is compared with the mixture of the two. *Center*: Comparison of the FTIR spectra of OAm and the mixture Pd(acac)$_2$ + OAm. *Bottom*: Comparison of the FTIR spectra of the OAm/OAc mixture before and after addition of Pd(acac)$_2$ salt.

oleic acid to the Pd(acac)$_2$/oleylamine solution. We observe a split of the 1603 cm^{-1} peak into two main peaks at 1614 and 1580 cm^{-1}, which we attribute to the formation of an amino-ketone species after condensation of the acetylacetonate group with oleylamine in acidic environment.[71] The intensity of the peak at 3185 cm^{-1} in the original FTIR spectrum gradually increases after addition of small amounts of water, as shown in the inset of **Figure 4.16**. We therefore conclude that the 3185 cm^{-1} band stems from the formation of bound water molecules as a result of the condensation reaction between the protonated acetylacetonate group and oleylamine, according to eq. 4.1.

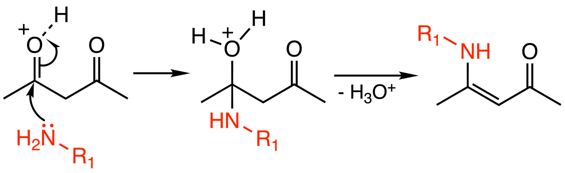

(eq. 4.1)

The overall transformation of Pd(acac)$_2$ salt in Pd-complex 1 complex can be expressed by eq. 4.2.

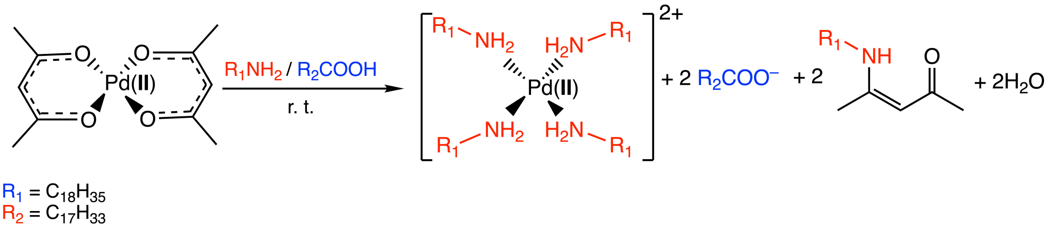

(eq. 4.2)

So far, our analysis of the Pd formation restricted to the chemical conversion of the Pd precursor into the Pd metal phase. We now direct our attention to determine the structure and morphology of the Pd nanocrystals as they emerge in solution. In **Figure 4.17a** the background subtracted in situ SAXS data displays a broad peak centered at 0.09 Å^{-1}, which stems from the fast formation of nanocrystal agglomerates after reaching 190 °C. At low-q, the scattering signal due to the presence of the agglomerates overlaps with the form factor of the individual nanocrystals. As a result, an estimation of the nanocrystal sizes by fit of the scattering profiles in the Guinier region is unviable.

We determine the mean inter-particle distance within the agglomerates as $2\pi/q$ after fit the position q of the structure factor at around 0.09 Å^{-1}. In **Figure 4.17b**, the inter-particle distances found by SAXS fit overestimate the nanocrystal diameter sizes provided by PDF and electron microscopy, likely due to the presence of a soft shell of organic ligands surrounding the nanocrystal cores. However, when we subtract twice the length of fully extended oleylamine/oleic acid ligands (4 nm)[237] from the mean inter-particle distances, the size profiles determined by SAXS and PDF closely match. The result thus suggests that at this stage of the synthesis the Pd nanocrystals are covered by a soft shell of organic capping agents. More importantly, the match between the nanocrystal sizes determined by SAXS and PDF indicates that the nanocrystals nucleate as single crystals and further grow by simple incorporation of monomeric species into the existing crystalline lattice. The absence of twin-boundaries in the HRTEM images

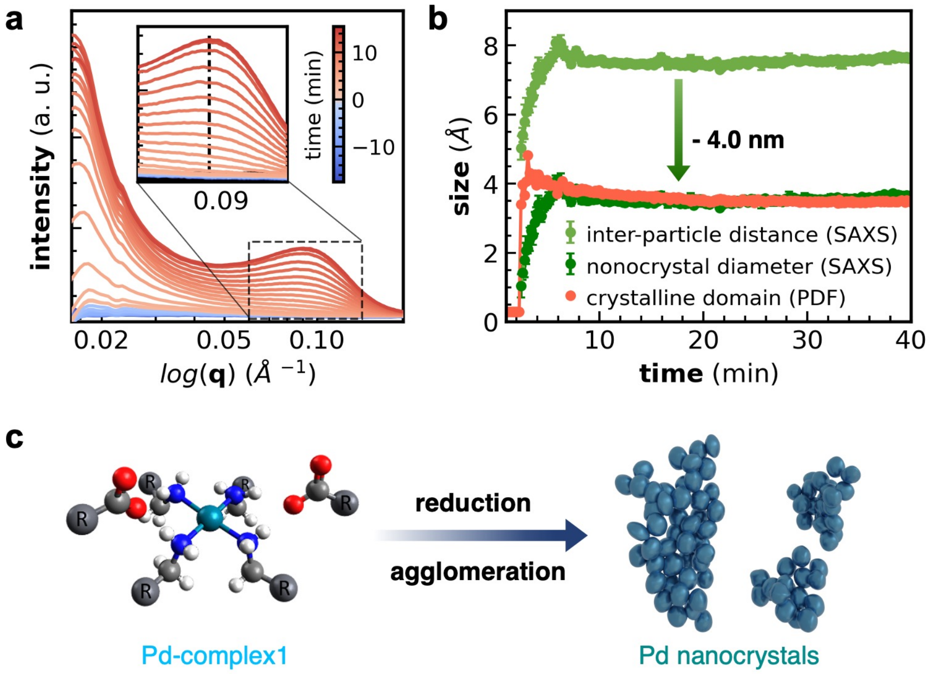

Figure 4.17: The agglomeration of Pd nanocrystals as revealed by in situ SAXS. **a**) Plot of the background subtracted in situ SAXS profiles collected during the synthesis of Pd nanocrystals. At time = 0 min, the reaction time of 190 °C is reached. The quick increase of the scattering intensity at approximately 0.09 Å^{-1} stems from the fast agglomeration of the colloidal Pd nanocrystals immediately after their formation. **b**) Plot of the particle diameters and inter-particle distances as obtained by fit of the in situ PDF (red) and SAXS (light green) data, respectively. The size profile obtained by SAXS is additionally shown downshifted of 4.0 nm to subtract the contribution of twice the thickness of a soft organic shell from the inter-particle distance. The resulting profile (dark green) corresponds to the diameter of individual nanocrystals. **c**) Schematic representation of the conversion of Pd-complex 1 into Pd nanocrystal agglomerates.

of **Figure 4.13 a-b** further supports this hypothesis. The small time shift between the SAXS and PDF profiles in **Figure 4.17b** likely stems from the short delay between the emergence of the nanocrystals and their aggregation.

In **Figure 4.17b**, both size profiles determined by SAXS and PDF exhibit a maximum immediately after formation of the nanocrystals. Differently, at later times during the synthesis the nanocrystal sizes appear to gradually decrease. We ascribe the observation to the effect of a prolonged nucleation stage on the mean nanocrystal size. After overcoming the energy barrier to nucleation, the first nuclei grow quickly by consumption of the monomeric species in solution. As a result, the concentration of the free monomer reduces, and the nuclei forming at later stages during the synthesis grow to progressively shorter final sizes. We thus determine a decrease in the average nanocrystal diameter over time. Our results provide experimental evidence to previous reports, where the formation of polydispersed Pd nanocrystals from $Pd(acac)_2$ precursor is ascribed to the multinucleation events caused by the low reducing power of oleylamine.[238] The final nanocrystal size of 3.6 nm determined by both PDF and SAXS analysis is smaller compared to the mean diameter of 4.2 nm measured by HRTEM. However, we suggest that this discrepancy originates from the poor statistics of electron microscopy measurements compared to the large amount of nanocrystals probed by the X-ray scattering techniques.

Figure 4.17c provides a schematic illustration of the synthesis of Pd nanocrystals as revealed by our in situ investigation. Dissolution of $Pd(acac)_2$ determines the formation of the amino-substituted Pd-complex 1. Upon reduction, Pd-complex 1 converts into capped Pd nanocrystals, which quickly aggregate into disordered agglomerates in solution. Multinucleation events unfold, resulting in polydispersed single-crystalline nanoparticles. The overall nucleation and growth of the nanocrystals occur in agreement with the predictions from the classical nucleation theory.

4.2.3 Overview on the formation of Cu nanocrystals by in situ PDF

We investigate the synthesis of Cu nanocrystals by acquisition of high energy X-ray scattering. **Figure S4.9** exhibits the in situ TS and SAXS data collected simultaneously during the colloidal synthesis. We Fourier transform the TS data to obtain the PDF shown in **Figure 4.18**. Due to its sensitivity to both short- and long-range order, in situ PDF provides a comprehensive overview of the structural transformation ultimately leading to the emergence of the nanocrystals. At room temperature, the PDF exhibits an intense peak at 2.03 Å. This distance is larger than typical Cu(II)-O bond lengths and rather hints to the formation of an amine coordinated complex of Cu^{2+}, similarly to what we already observed for Pd^{2+}.

Upon heating of the reaction mixture, the inter-atomic distances in the PDF modify and the position of the 2.03 Å peak reduces to 1.96 Å at 115 °C, and then further to 1.84 Å at 210 °C, while no long-range order structures are formed, as illustrated in **Figure**

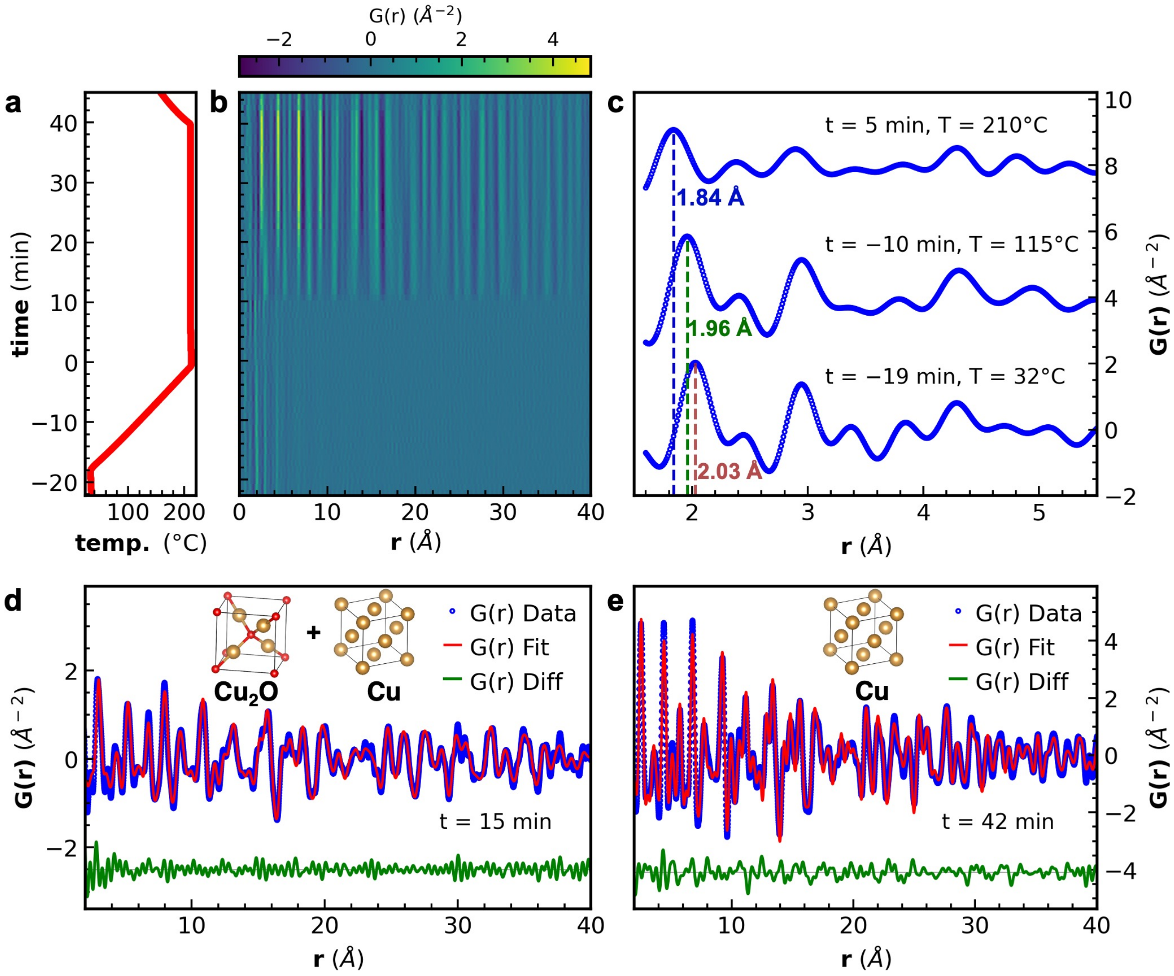

Figure 4.18: Overview of the in situ PDF during the synthesis of Cu nanocrystals. a) Plot of the temperature profile during the in situ measurement. At time = 0 the reaction temperature of 210 °C is reached. **b**) 2D plot of the in situ PDF data as a function of the reaction time. **c**) 1D plot of selected PDF profiles from the data shown in **b**. **d**) Fit of a selected PDF profile by means of a two-phase model compromising a Cu_2O and a Cu crystalline phase. **e**) Fit of a selected PDF profile at late times during the synthesis by means of a single Cu crystalline phase.

4.18c. After prolonged heating at 210 °C we further determine the emergence of a long-range ordered crystalline Cu_2O phase, which progressively converts into reduced Cu, as illustrated by the exemplary fits in **Figure 4.18d, e**. This result is in agreement with previous reports.[79]

Overall, in situ PDF hints to the formation of few metal-coordinate species which proceed the emergence of Cu_2O and Cu nanocrystals. However, PDF alone does not permit to fully discriminate between copper complexes with similar structures due to its limited sensitivity to the local chemical environment. In the next section, we will thus extend our study to the chemical transformations prior to the nanocrystal nucleation via element-sensitive X-ray absorption methods.

4.2.4 Chemical transformations prior to Cu nanocrystal nucleation

We measure in situ QEXAFS at the Cu K-edge during the synthesis of Cu nanocrystals. Due to its rapid acquisition rate, by QEXAFS we reveal the formation of various chemical intermediates during the fast heating rate of 10 °C min^{-1} utilized for the nanocrystal synthesis. In **Figure 4.19a**, the time-resolved plot of the X-ray absorption data in the near-edge region displays a shift of the absorption edge to lower energies during the initial heating ramp. Later, at 220 °C, we observe the emergence of an intense peak at around 8.88 keV, which subsequently reduces in intensity upon prolonged heating.

We perform MCR-ALS analysis of the in situ spectra and identify the evolution of five separate components during the synthesis, as shown in **Figure 4.19b**. The first three components form during the temperature ramp from room temperature to 220 °C and correspond to the short-range ordered species detected by PDF. We thus label them as Cu-complex 1, Cu-complex 2, and Cu-complex 3, respectively. We assign the later two components to the formation of crystalline Cu_2O and Cu phases, as determined by comparison of the respective spectra with reference measurements in **Figure S4.10**. Our assignment perfectly agrees with the PDF observations.

Although QEXAFS permits the fast detection of different chemical species emerging during the synthesis, the reduced energy resolution of the measurement limits our ability to accurately determine the characteristic structural motives of the various Cu-complexes. We therefore complement our results by measuring in situ high-energy-resolution fluorescence detection X-ray absorption near-edge structure (HERFD-XANES) prior to the nanocrystal nucleation. The MCR-ALS analysis of the data reveals the formation of three Cu-complexes, as shown in **Figure S4.11**. In **Figure 4.19c-d**, we compare the HERFD-XANES spectrum of each of the Cu-complexes with simulated profiles calculated for the structural motifs shown in the respective insets. Simulated profiles for alternative structural motifs are reported in **Figure S4.12**, **S4.13**, and **S4.14**, respectively. For

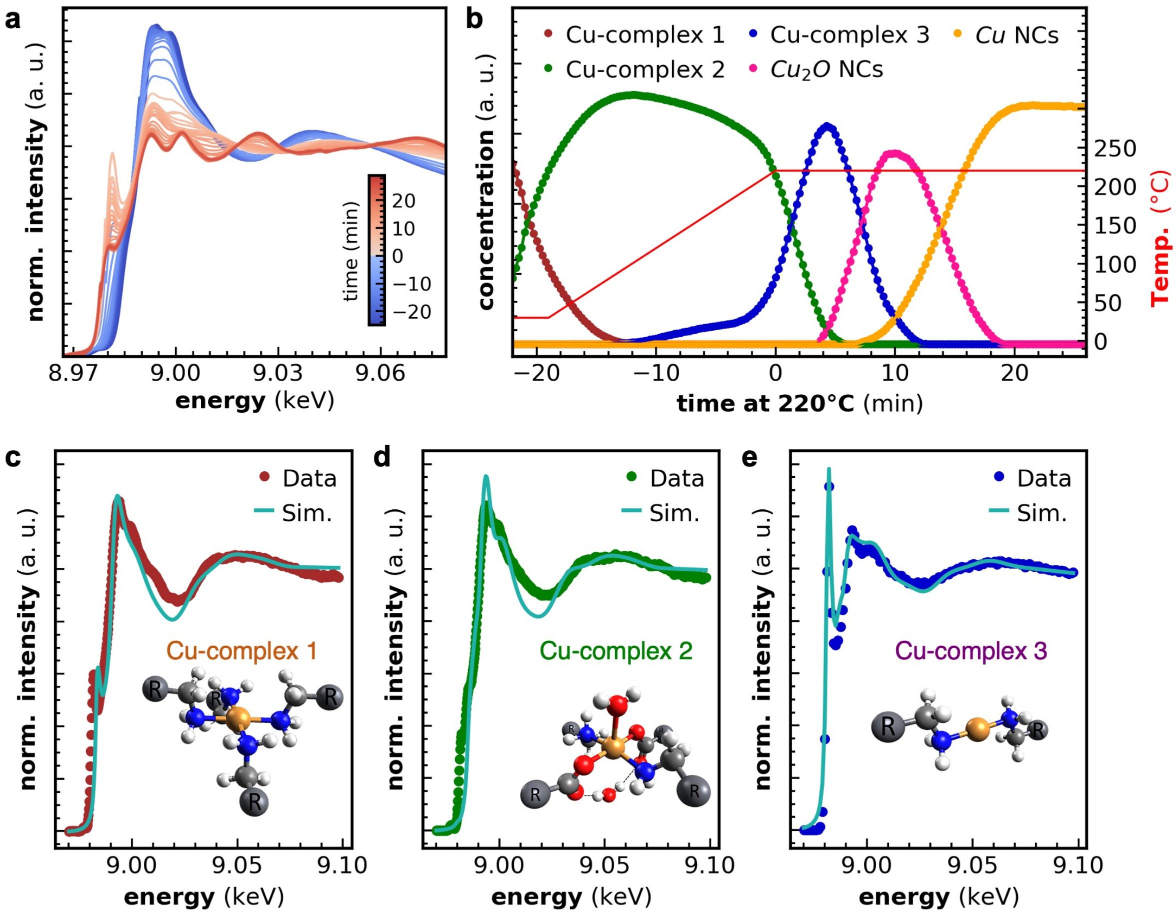

Figure 4.19: Overview of the in situ QEXAFS and HERFD-XANES data during the synthesis of Cu nanocrystals. **a**) Plot of the XANES profiles measured by in situ QEXAFS at the Cu K-edge during the synthesis of Cu nanocrystals. At time = 0, the reaction temperature of 210 °C is reached. **b**) Plot of the relative fractions for different components obtained by MCR-ALS analysis of the QEXAFS data shown in **a**. **c-e**) Plots of the experimental and simulated HERFD-XANES profiles for Cu-complex 1, Cu-complex 2, and Cu-complex 3, respectively. The simulated spectra are calculated from the discrete structural models graphically shown in the respective insets.

Cu-complex 1, we obtain the best agreement between experimental and simulated data after considering a squared planar complex of Cu^{2+} coordinated by four oleylamine ligands ($[Cu(II)(OAm)_4]^{2+}$). In the case of Cu-complex 2, the best agreement is reached with a squared pyramidal complex of Cu^{2+} displaying two oleylamine and two oleate substituents in equatorial position, and one water molecule in axial position. We further suggest the presence of a second water molecule in an outer coordination sphere and loosely bound to the carbonylic oxygens of the oleate groups via hydrogen bonds, to yield the organometallic complex $[Cu(II)(OAm)_2(^-OAc)_2)2H_2O]$. Finally, we assign the spectrum of Cu-complex 3 to a partially reduced Cu^+ metal center linearly coordinated with two oleylamine ligands ($[Cu(I)(OAm)_2]^+$). We suggest that the overall charge of Cu-complex 1 and Cu-complex 3 is balanced by the presence in an outer coordination sphere of anionic oleate groups, which are not shown in the insets of **Figure 4.19c, e**. In addition to the good agreement between the experimental and simulated HERFD-XANES profiles of **Figure 4.19c-e**, the proposed structures allow a good fit of both the in situ QEXAFS spectra and in situ PDF data, as demonstrated in **Figure S4.15** and **S4.16**.

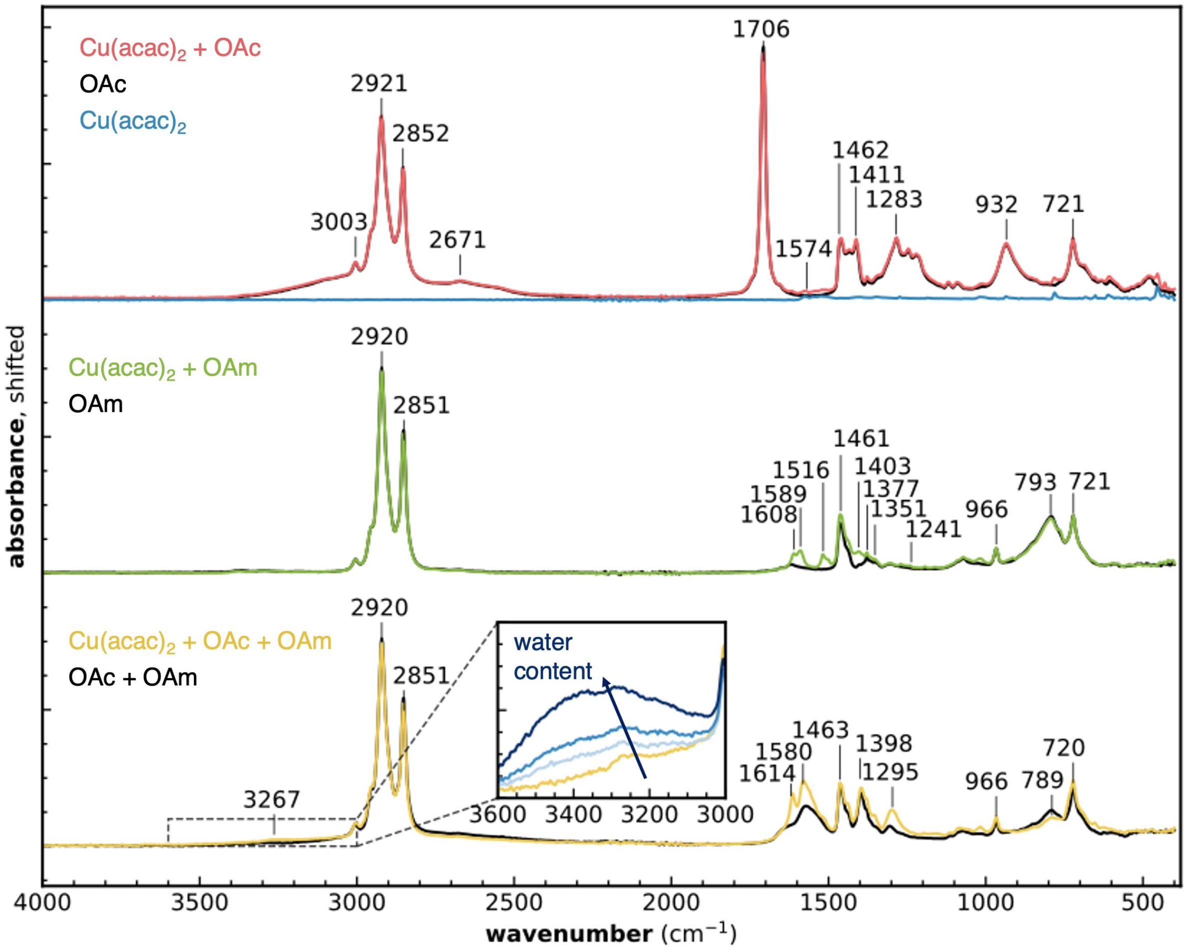

Figure 4.20: FTIR measurements for mixtures of Cu(acac)$_2$ with different solvents. *Top*: The FTIR spectra of pure Cu(acac)$_2$ and OAc is compared with the mixture of the two solvents. *Center*: Comparison of the FTIR spectra of pure OAm with the mixture Cu(acac)$_2$ + OAm. *Bottom*: Comparison of the FTIR spectra of the OAm/OAc mixture before and after dissolution of the Cu(acac)$_2$ salt.

We further use FTIR spectroscopy to determine the role of oleylamine and oleic acid ligands in dissolving the Cu(acac)$_2$ precursor. In **Figure 4.20**, the FTIR measurements demonstrate that OAc alone doesn't dissolve Cu(acac)$_2$, since the summed spectra of pure OAc and Cu(acac)$_2$ salt is recovered. The addition of Cu(acac)$_2$ salt to pure oleylamine doesn't lead to the tetra-amino Cu(II) complex, but rather to a Cu(acac)$_2$-amine complex displaying weakened Cu-O bonds, as indicated by the emergence of weak vibrational bands in the 1500-1620 cm^{-1} region.[239] The presence of additional electron-donor ligands in the coordination sphere of Cu(acac)$_2$ species increases the splitting of the d-orbitals of Cu(II) and determines a shift of color from blue to green, as shown in **Figure S4.17**.[240] The Cu(acac)$_2$/OAm mixture is difficult to handle at room temperature due to its high viscosity and is thus not an ideal starting solution for the synthesis. Conversely, the addition of OAc to the Cu(acac)$_2$/OAm mixture results in a clear solution with low viscosity and which exhibits the characteristic deep blue color of Cu(II)-amino complexes, as shown in **Figure S4.17**. We attribute the formation of the latter complex to the acid-catalysed condensation of acetylacetonate ligands with OAm, as further indicated by the emergence in the FTIR apectrum of the vibrational bands of the amino-ketone species at 1614 and 1580 cm^{-1}, as well as of a broad band at 3267 cm^{-1} due to the formation of bound water molecules. We therefore conclude that the joint use of OAm and OAc is crucial to cleave the Cu-acac bond and convert the Cu(acac)$_2$ complex into Cu-complex 1 at room temperature.

In summary, the combination of complementary in situ PDF, QEXAFS, and HERFD-XANES, along with ex situ FTIR spectroscopy, enables us to propose a multi-step transformation pathway, wherein Cu(acac)$_2$ salt converts into a partially reduced Cu(I)-amino species according to eq. 4.3.

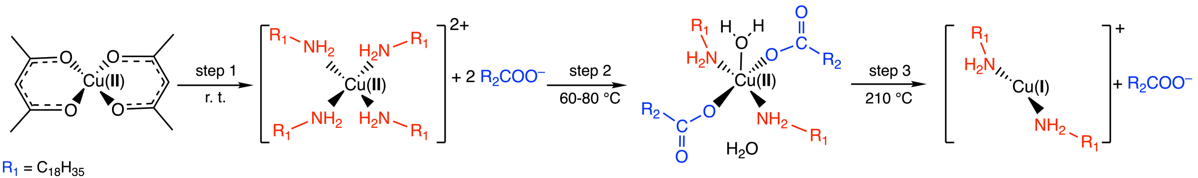

(eq. 4.3)

In the next section, we focus on later stages of the synthesis to uncover the structural transformations driving Cu-complex 3 into Cu nanocrystals. To this scope, we will consider the in situ TS-PDF and SAXS data, and further perform ex situ HRTEM.

4.2.5 Structural rearrangement to Cu nanocrystals

Figure 4.21a displays selected in situ TS patterns collected at the reaction temperature of 210 °C. The data indicates the first emergence of a Cu_2O crystalline phase, which later converts into reduced Cu. We analyse the TS profiles by Rietveld refinement to extract the crystal sizes and scales for the two phases, as shown in **Figure 4.21b**. At t = 11 min, we reveal the rapid emergence of Cu_2O crystallites with an initial size of of 18 nm. At t = 13 min we further observe the progressive formation of anisotropic Cu crystals displaying a preferential growth in the (111) lattice direction. After prolonged heating, the amount of Cu_2O phase declines and the Cu crystals become the majority phase in solution.

We perform a multi-phase analysis of the in situ PDF data to identify the early formation of small nuclei that cannot be detected by Rietveld refinement. We model the data by including the calculated PDF from the Cu-complexes' structures, as well as from separate Cu_2O and Cu phases. The result of the analysis are shown in **Figure S4.18**. We detect the emergence of Cu_2O nanocrystals already at t = 9 min exhibiting crystallites of 3 nm in size. These small Cu_2O nanocrystals are stable in solution for at least 2 minutes, after which we detect the sudden emergence of large Cu_2O nanocrystals, in agreement with the Rietveld analysis.

We perform additional in situ SAXS measurements to confirm the formation of small nanoparticles prior to the emergence of larger Cu_2O and Cu nanocrystals. **Figure S4.19** offers an overview of the in situ SAXS data, which we collected by use of an in-house acquisition setup. In **Figure 4.21b** the analysis of the SAXS profiles reveal the presence of two distinctive populations of nanoparticles with a constant diameter of approximately 5 and 45 nm, respectively. The 5-nm particles are detected first, while the emergence of the larger particles is delayed. The trend in the nanoparticle diameter lengths suggests that the larger particles suddenly form due to the agglomeration of smaller ones. After agglomeration, fusion of the crystalline domains leads to larger Cu_2O crystalline domains, which eventually convert into Cu, as supported by TS-PDF.

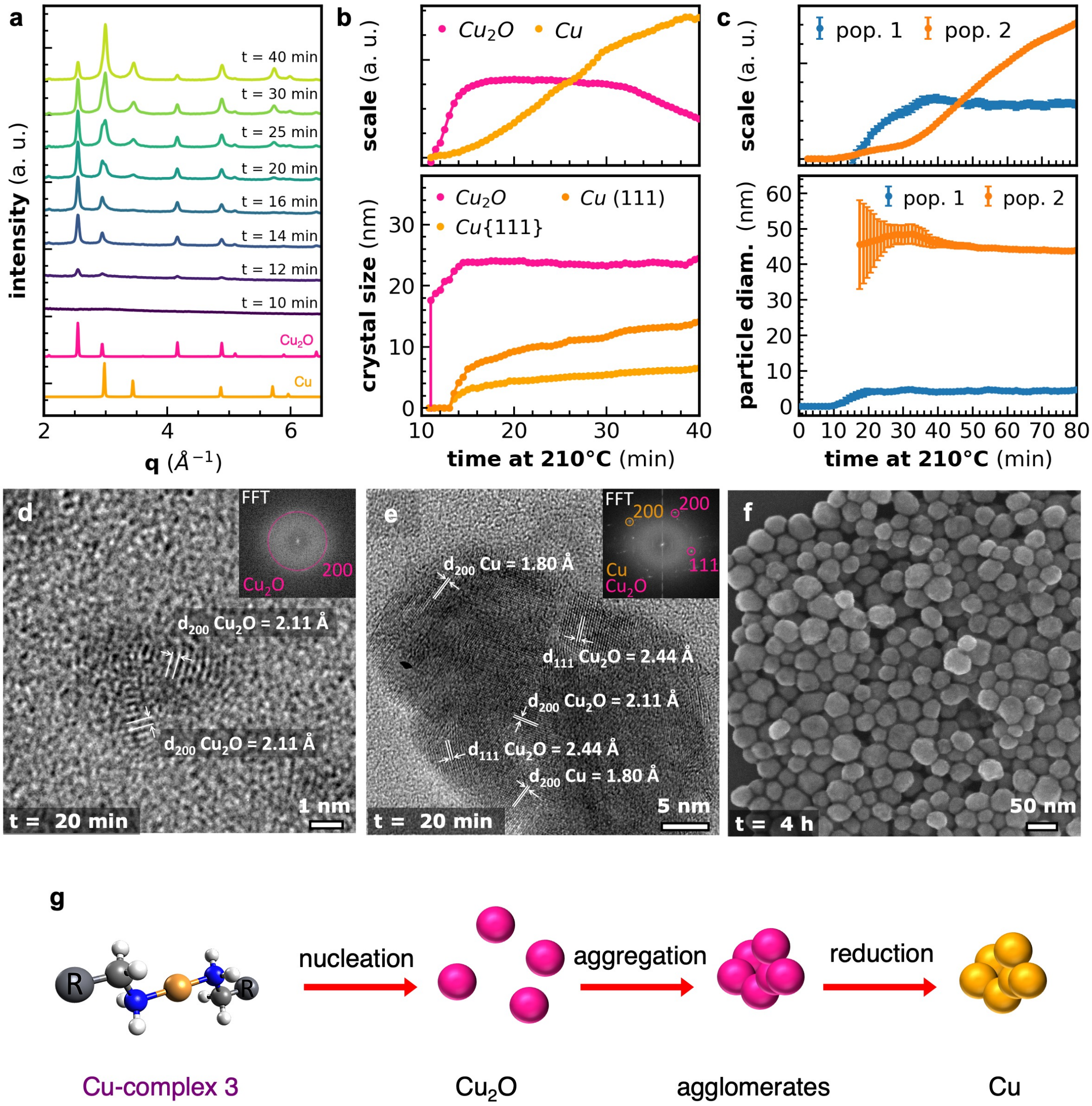

Figure 4.21: The crystallization pathway of Cu nanocrystals as revealed by in situ TS, in situ SAXS, and ex situ EM. **a**) Plot of selected in situ TS profiles during the synthesis of Cu nanocrystals. At time = 0, the reaction temperature of 210 °C is reached. **b**) Plot of the scale factors and the crystal sizes obtained by Rietveld refinement of the in situ TS data. **c**) Plot of the scale factors and the particle diameters obtained by fit of the in situ SAXS data. **d-e**) Selected ex situ HRTEM images measured after 20 minutes of reaction time at 210 °C. Both twinned Cu_2O nanocrystals, 5 nm in size (**d**) and large polycrystalline nanoparticles of mixed Cu and Cu_2O composition (**e**) are detected in the sample. In the HRTEM images, the spacing distances for different lattice directions for both Cu_2O and Cu phases are also shown. In the insets, selected bright spots or arcs in the FFT of the HRTEM images are assigned to different spacing distances for either of the two phases. **f**) SEM image of the Cu nanocrystals at the end of the syntesis. **g** Schematic representation of the formation mechanism of Cu nanocrystals starting from Cu-complex 3.

We repeat the synthesis and measure ex situ HRTEM after 20 min of reaction time at 210 °C to validate our hypothesis. At this stage of the synthesis, we expect the presence of both small and large nanoparticles, as revealed by SAXS, as well as the mixed formation of Cu_2O and Cu phase, according to TS-PDF. Electron microscopy confirms the presence of both small and large sized nanoparticles in the specimen, as shown in **Figure S4.20a**. The 5-nm nanoparticle in **Figure 4.21d** exhibits twinned Cu_2O domains, as indicated by the (200) interplanar distances of 2.11 Å. The result agrees with both PDF and SAXS observations. In **Figure S4.20b** we determine the presence of a large nanoparticle which display multiple Cu_2O crystalline domains of approximately 5 nm in size. Thus, **Figure S4.20b** supports the hypothesis that smaller particles coalesce to form larger ones by un-oriented attachment. A similar mechanism has been already suggested by previous observations via TEM.[73] The polycrystalline nanoparticle of **Figure 4.21e** exhibits both Cu_2O and Cu domains due to the progressive reduction of the oxide into the metallic phase, in agreement with TS-PDF data. Further re-arrangement of the crystalline lattice outcomes into large crystalline domains displaying either Cu_2O or Cu composition, as shown in **Figure S4.20c-d**. Finally, **Figure 4.21f** reports the SEM image of the phase-pure Cu nanocrystals at the end of the synthesis.

Figure 4.21f provides a schematic illustration of the formation of Cu nanocrystals, as revealed by the analysis of the in situ and ex situ data. The Cu(I)-complex 3 exhibits moderate stability in solution at 210 °C and slowly converts into small polycrystalline Cu_2O nanoparticles. After their emergence, the Cu_2O nuclei quickly fuse together by un-oriented attachment to build larger polycrystalline nanoparticle structures which further rearrange into coherent crystal domains, as revealed by in situ TS-PDF. The Cu_2O phase then progressively converts into Cu via a solid-state reduction to deliver Cu nanocrystals exhibiting a preferential growth in the (111) direction. Therefore, we conclude that the synthesis of Cu nanoparticles unfolds via a complex multi-step formation mechanism, which lies outside the prediction of the classical nucleation theory.

4.2.6 Supporting information

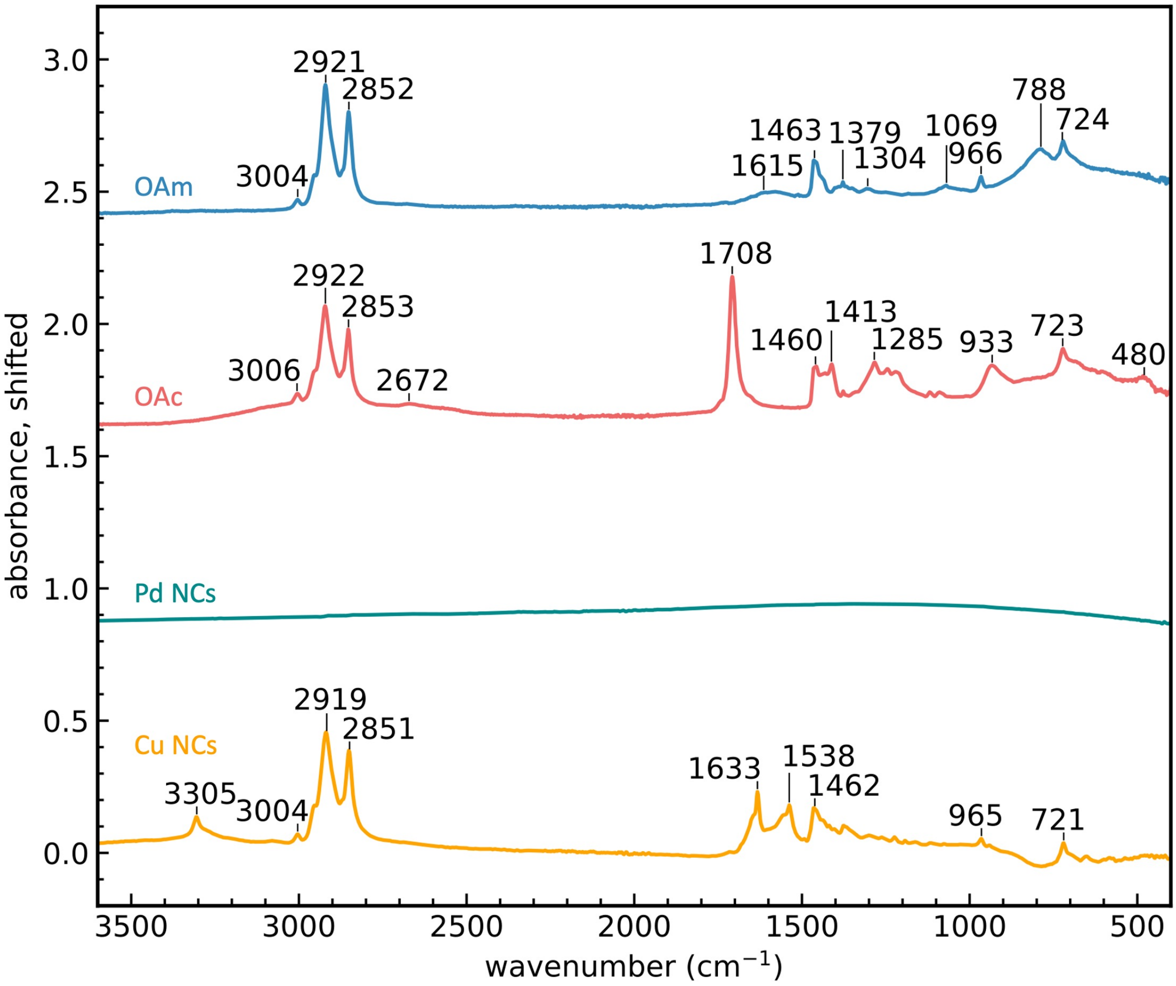

Figure S4.3: FTIR measurements of Pd and Cu nanocrystals compared to the spectra of pure oleylamine and oleic acid. In the Cu NCs spectrum, the position of the absorption bands is consistent with the presence of oleylamine and oleic acid ligands adsorbed at the surface of the NCs according to[241,242].

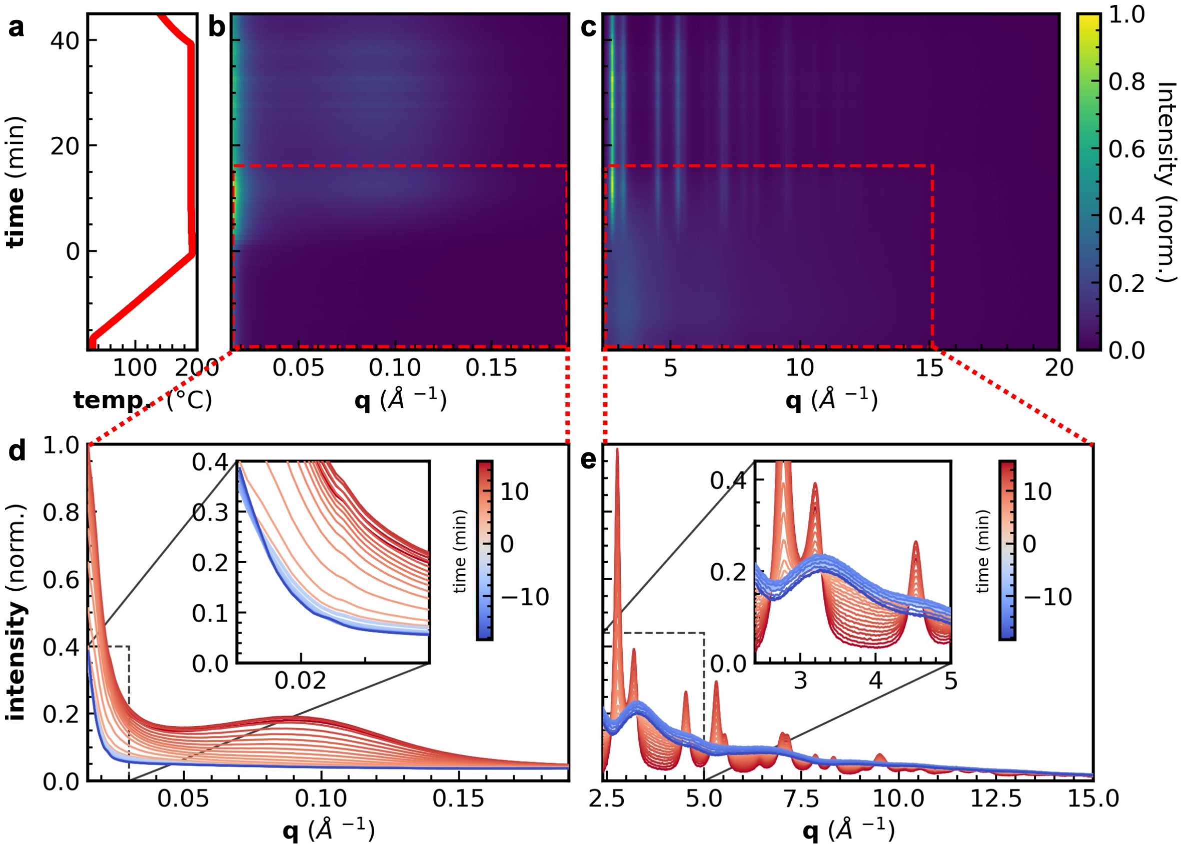

Figure S4.4: Simultaneous in situ SAXS and TS during the synthesis of Pd nanocrystals. a) Temperature profile during the synthesis of Pd nanocrystals. At time = 0 min the reaction temperature of 190 °C is reached. **b**) 2D plot of the background unsubtracted in situ SAXS intensity as a function of time. The corresponding 1D plots are shown in **d**. **c**) 2D plot of the in situ PDF as a function of time. The corresponding 1D plots are shown in **e**.

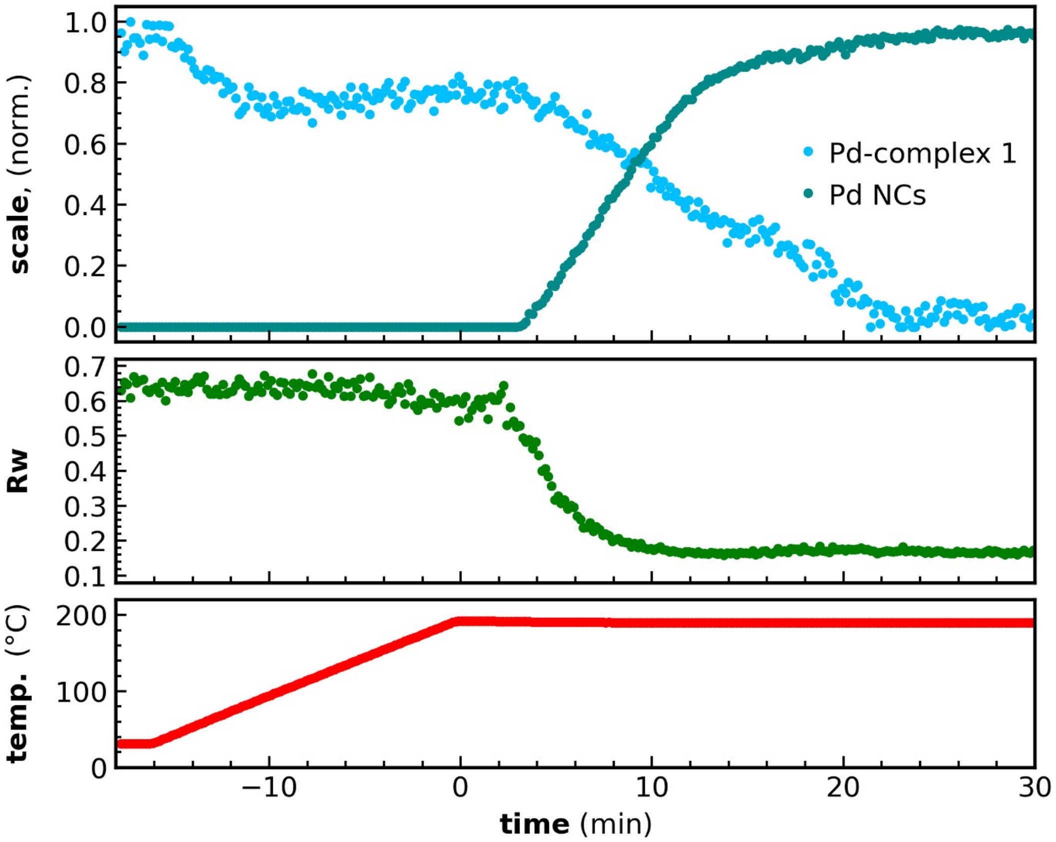

Figure S4.5: Fit of the in situ PDF during the formation of Pd nanocrystals. *Top*: Plot of the scale factors obtained from the 2-phase refinement of the data, which we perform by considering both Pd-complex 1 structure and a crystalline Pd phase. We calculate the PDF of the organimetallic model via Fourier transformation of the X-ray scattering signal determined from the Debye Scattering equation. The PDF of the crystalline phase is calculated within the AC approximation. *Center*: Plot of the Rw value obtained from the fit routine as a function of time. *Bottom*: Plot of the temperature profile during the synthesis of the nanocrystals.

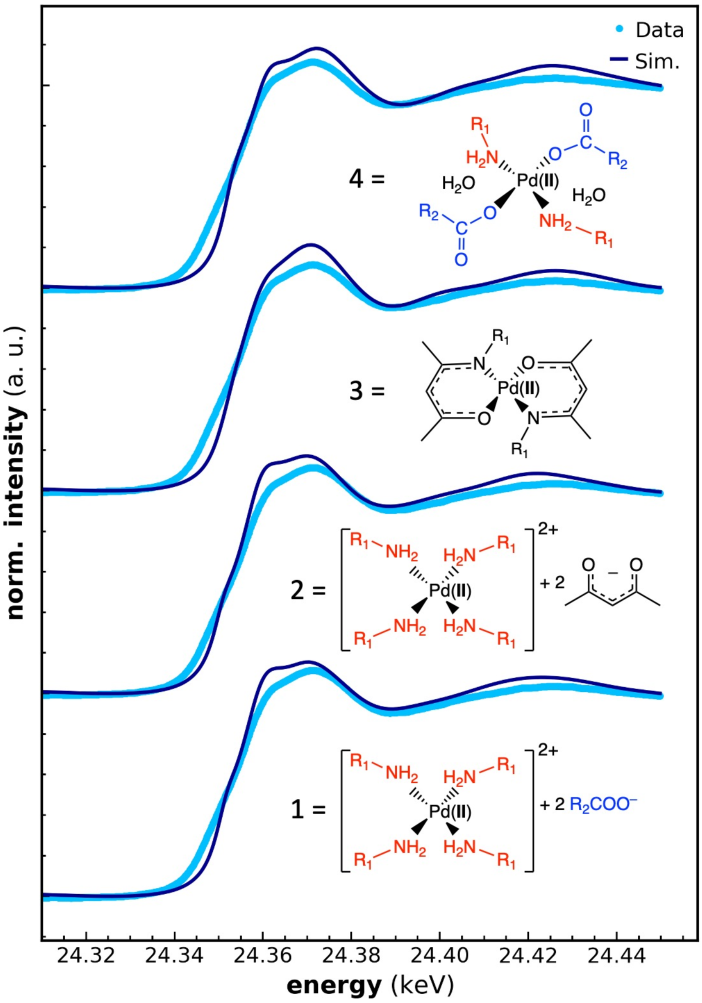

Figure S4.6: Comparison of the Pd-complex 1 XANES profile with simulated spectra for different candidate structures. The simulated spectrum at the bottom corresponds to the suggested structure for Pd-complex 1, i.e. to a tetra-amino complex of Pd(II) with squared planar geometry and two carboxilic acids as counter anions. In structure 2, the tetra-amino complex displays a tetragonal symmetry. In structure 3, the Pd(II) center is coordinated by two amino-ketone ligands. In structure 4, two amine and two carboxilic acids coordinate the Pd(II) metal center, while two water molecules belong to outer coordination shells. The groups R_1 and R_2 correspond to alkyl chains. The simulated model structures are isolated from CCDC 1557612,[243] 1557610,[71] 1557613,[71] and 1557614,[71] respectively.

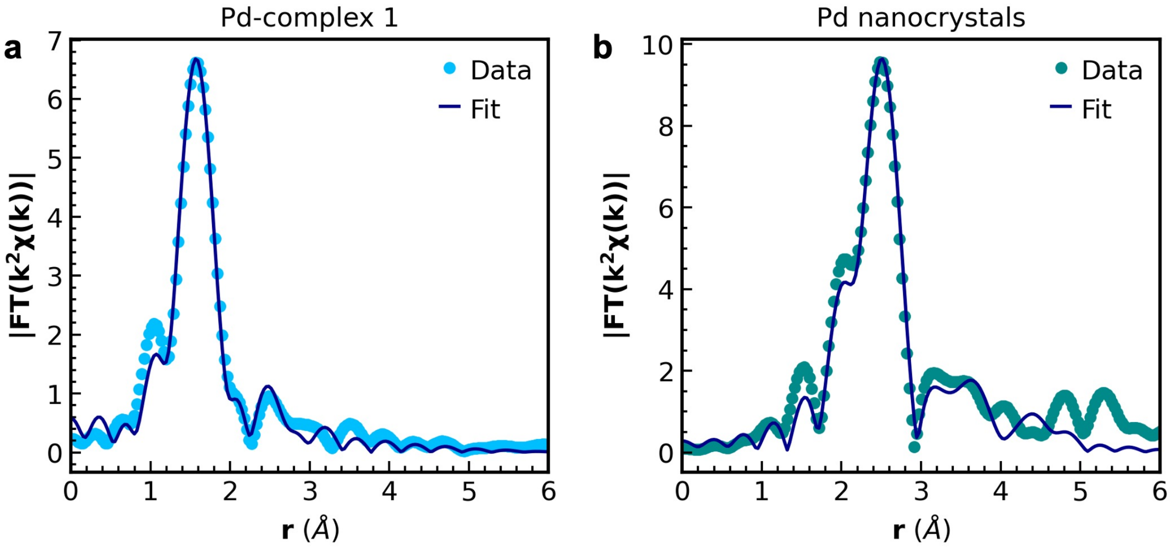

Figure S4.7: Plot of the EXAFS fits for Pd-complex 1 and Pd nanocrystals.

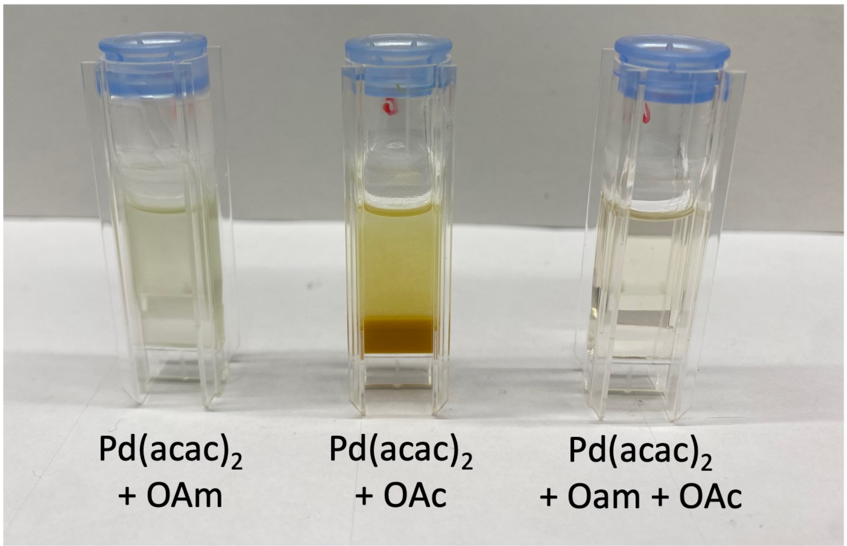

Figure S4.8: Pictures of mixtures of $Pd(acac)_2$ with different solvents. Over time, $Pd(acac)_2$ salt sediments at the bottom of the vessel containing OAc solvent.

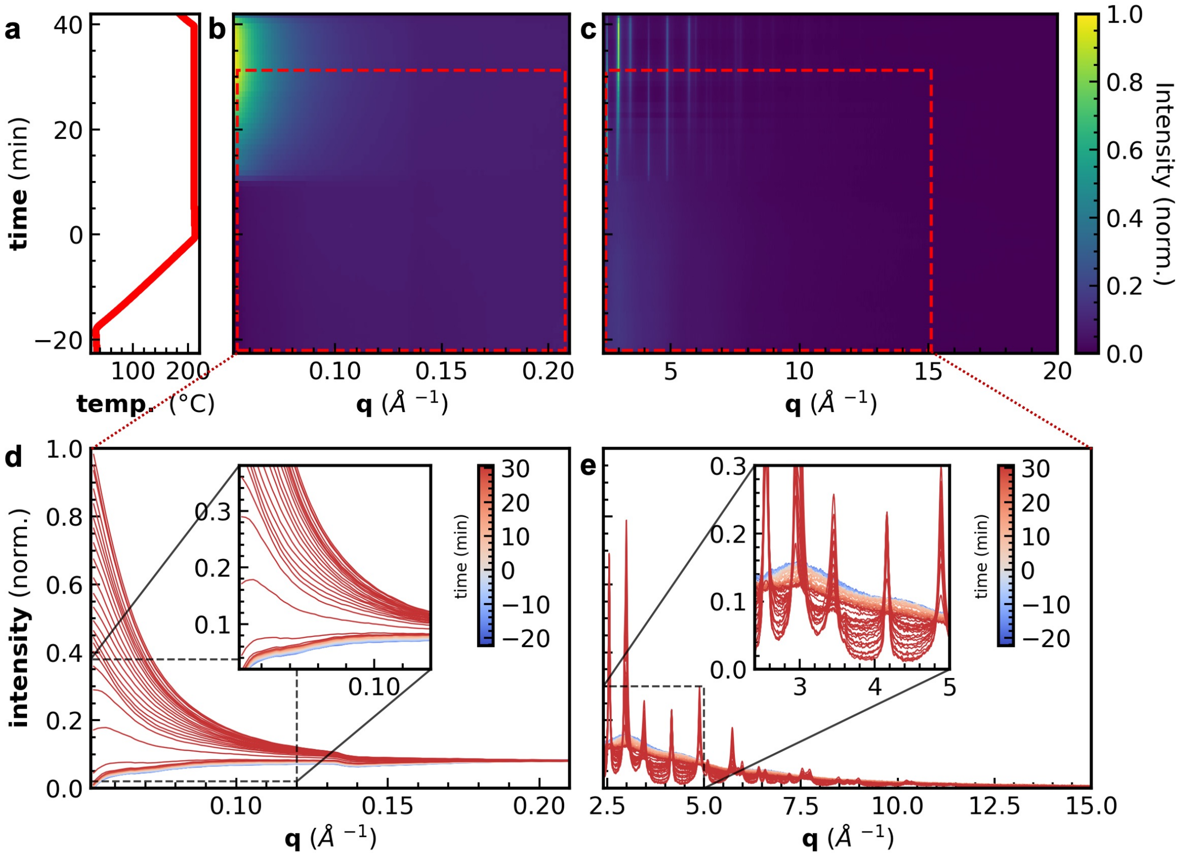

Figure S4.9: Simultaneous in situ SAXS and TS during the synthesis of Cu nanocrystals. a) Temperature profile during the synthesis of Cu nanocrystals. At time = 0 min the reaction temperature of 210 °C is reached. **b**) 2D plot of the in situ SAXS intensity as a function of time. The corresponding 1D plots are shown in **d**. **c**) 2D plot of the in situ PDF as a function of time. The corresponding 1D plots are shown in **e**.

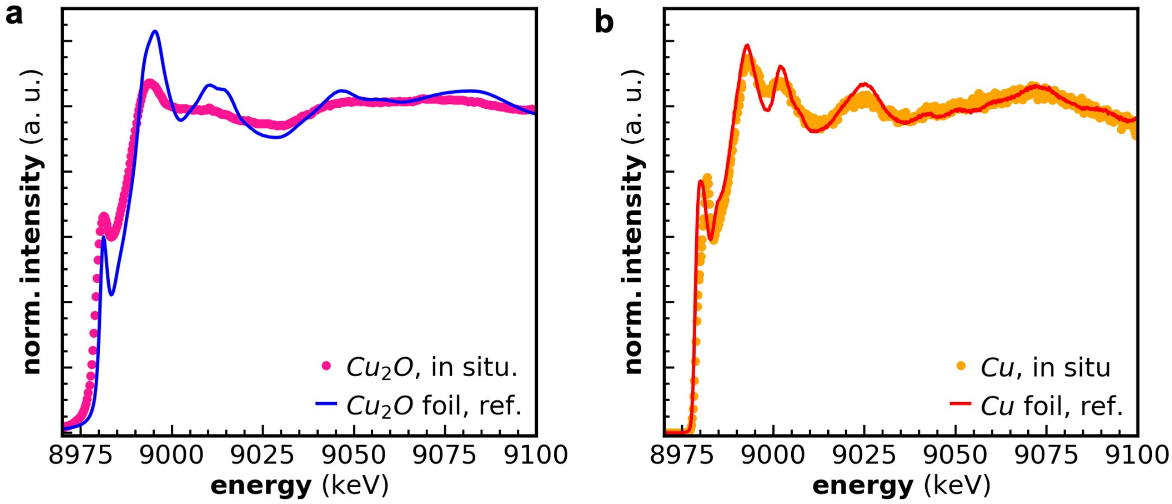

Figure S4.10: Comparison of selected in situ XANES spectra with Cu_2O and Cu references. **a**) The in situ XANES spectra attributed to the intermediate formation of Cu_2O nanocrystals during the synthesis of Cu nanocrystals is compared to a reference measurement of a Cu_2O foil. **b**) The in situ XANES spectra which attributed to the emergence of Cu nanocrystals is compared to a reference measurement of a Cu foil. Both XANES data are collected during in situ QEXAFS measurements.

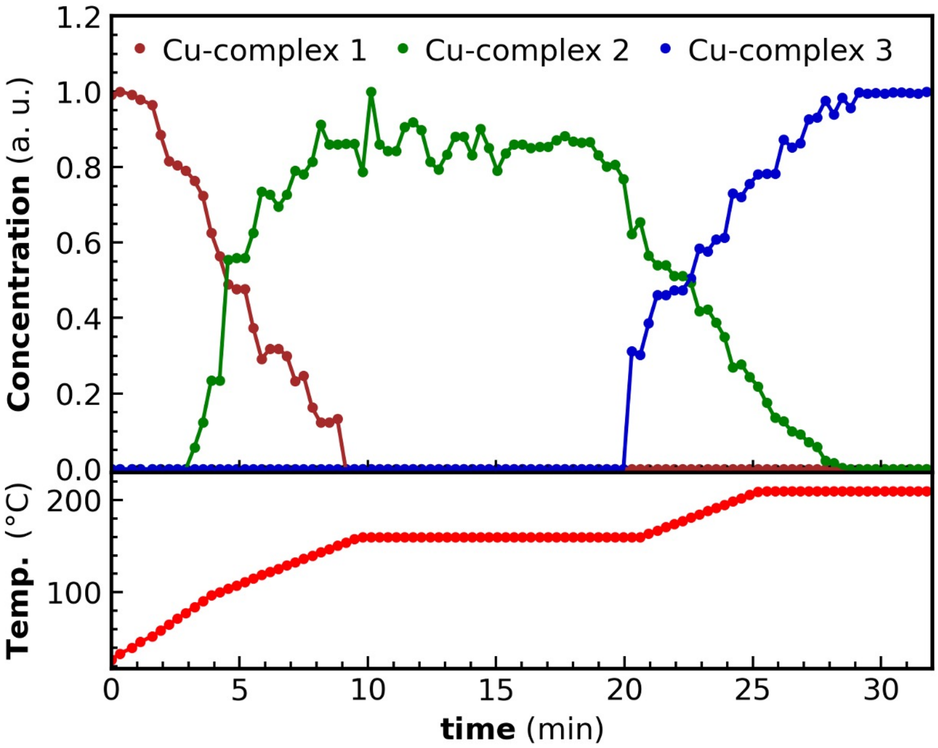

Figure S4.11: MCR-ALS analysis of the in situ HERFD-XANES measurement during the synthesis of Cu nanocrystals. *Top*: plot of the concentration profiles extracted from the MCR-ALS analysis of the in situ HERFD-XANES data. Three different components are here determined. *Bottom*: Plot of the temperature profile during the in situ HERFD-XANES measurement.

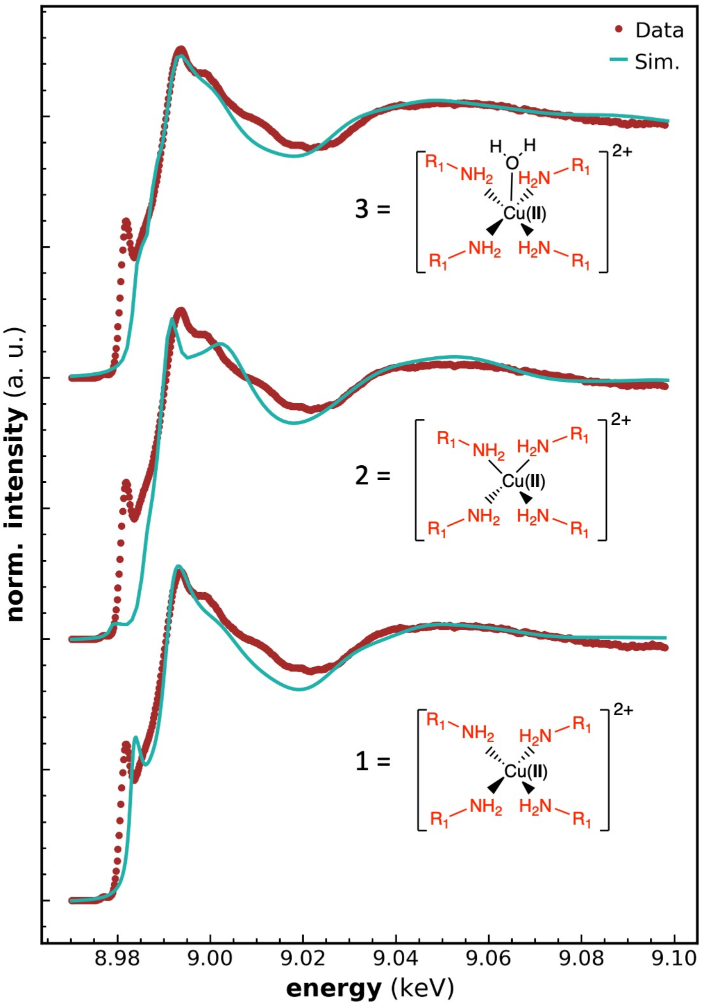

Figure S4.12: Comparison of the Cu-complex 1 XANES profile with simulated spectra for different candidate structures. The simulated spectrum at the bottom corresponds to the suggested structure for Cu-complex 1, i.e. to a tetra-amino complex of Cu(II) with squared planar geometry. In structure 2, the tetra-amino complex displays a tetragonal symmetry. In structure 3, the squared-planar Cu-complex 1 displays an additional water molecule in axial position, to outcome in a square-based pyramid arrangement. The R_1 group corresponds to an alkyl chain. The model structure for Cu-complex 1 is adapted from CCDC 1942113.[244]. The model structures 2 and 3 are manipulated and fully relaxed in *Avogadro*.[170] All complexes are simulated with an overall neutral charge to account for the screening effect of the counter ions in solution.

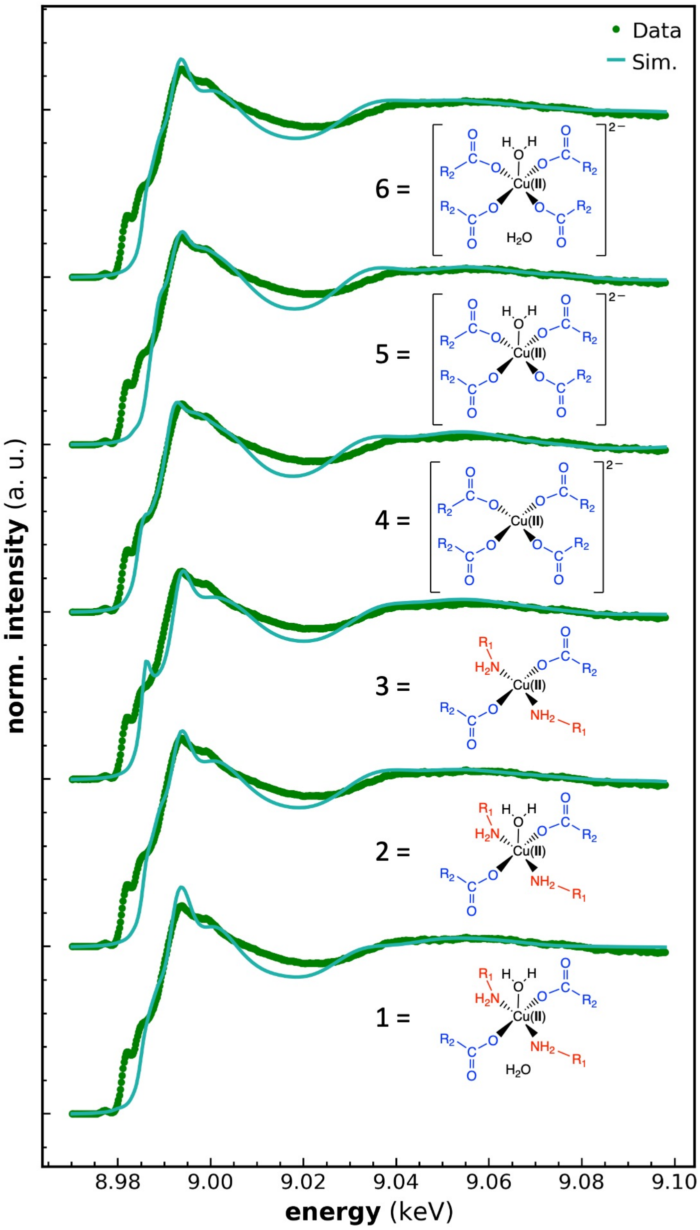

Figure S4.13: Comparison of the Cu-complex 2 XANES profile with simulated spectra for different candidate structures. The simulated spectrum at the bottom corresponds to the suggested structure for Cu-complex 2, i.e. a squared planar complex of Cu(II) with two amines and two carboxylic acids in equatorial position, one water molecule in axial position, and one water molecule in an outer coordination shell. The latter water molecule is removed in structure 2, while both molecules are removed in structure 3. Structure 4 corresponds to a squared planar complex with four carboxylic acids in equatorial position. Adding a water moleculs in axial position leads to structure 5, while the further addition of a water molecule in an outer coordination shell leads to structure 6. The groups R_1 and R_2 correspond to alkyl chains. The first three structures are adapted from CCDC 1851976,[245,246] the last three from 1851979.[246,247] All complexes are simulated with an overall neutral charge to account for the screening effect of the counter ions in solution.

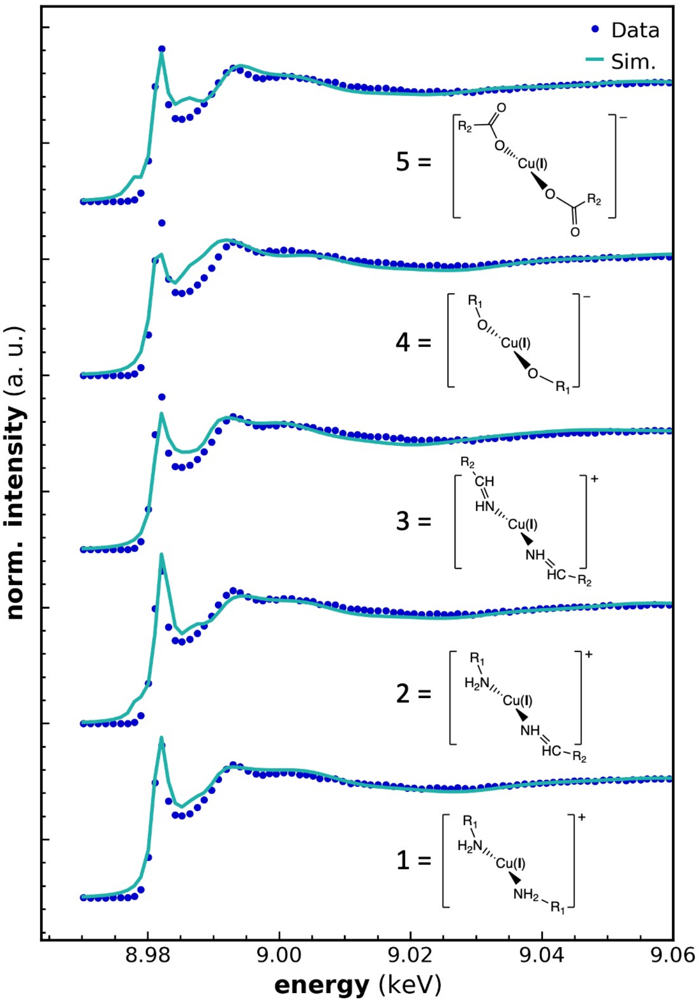

Figure S4.14: Comparison of the Cu-complex 3 XANES profile with simulated spectra for different candidate structures. The simulated spectrum at the bottom corresponds to the suggested structure for Cu-complex 3, i.e. a linear complex of Cu(I) with two amino ligands. Substituting one or both amino with imino ligands leads to structures 2 and 3, respectively. Structures 4 and 5 corresponds to the linear complex of Cu(I) with either alkoxy or carboxylate acids, respectively. The groups R_1 and R_2 correspond to alkyl chains. The Cu(I)-N distance in the amino complexes are obtained from CCDC 2105533,[248] Cu(I)-N distance in the imino complexes from CCDC 1250839,[249] and the Cu(I)-O distance from COD 9007497.[250] All complexes are simulated with an overall neutral charge to account for the screening effect of the counter ions in solution.

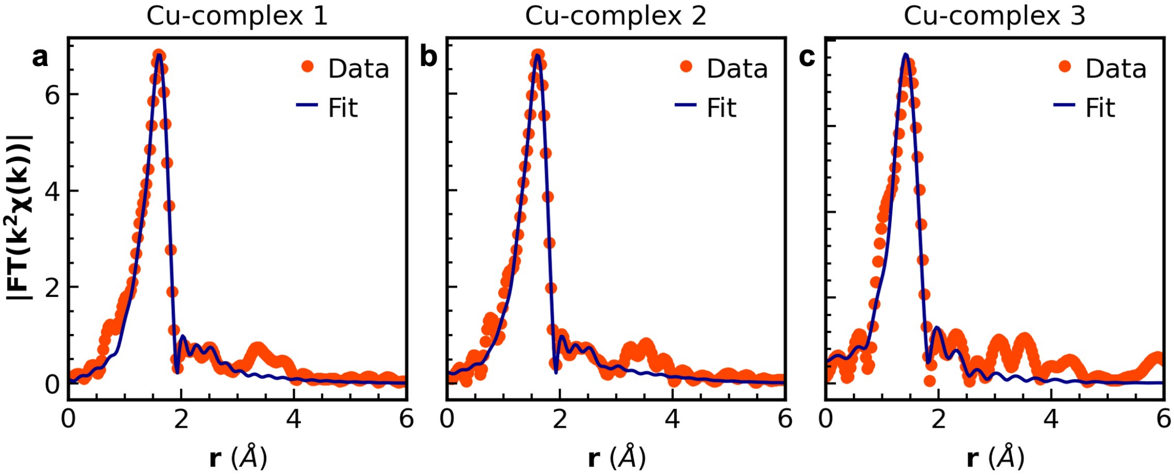

Figure S4.15: EXAFS fits for Cu-complex 1, Cu-complex 2, and Cu-complex 3. The EXAFS data are collected during in situ QEXAFS measurements.

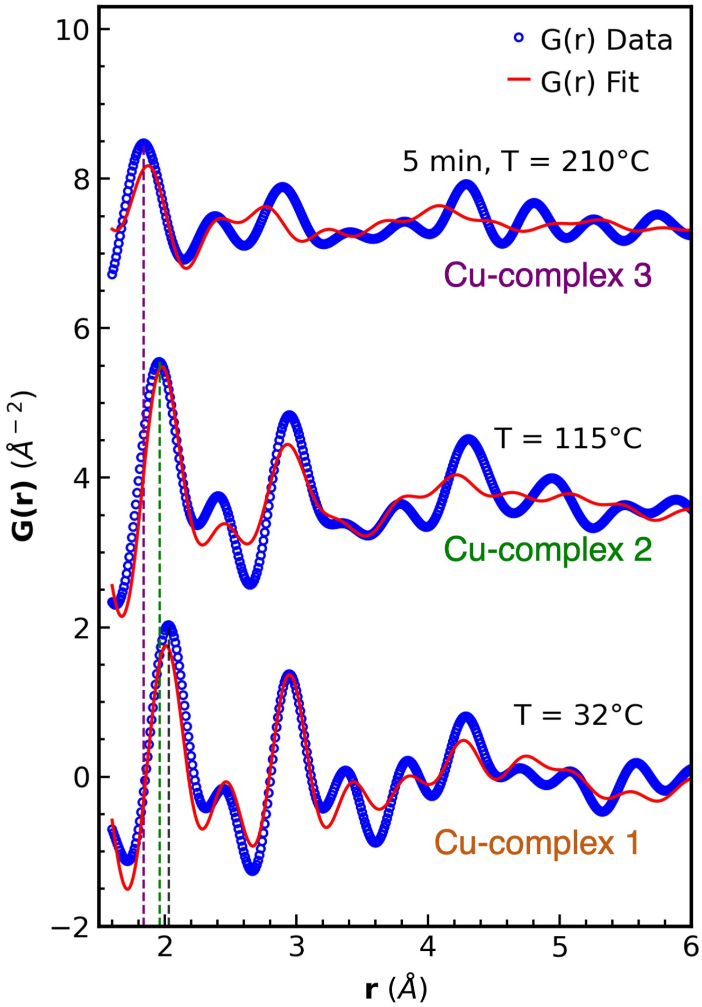

Figure S4.16: Fit of the in situ PDF with the Cu-complex structures. The experimental PDF profiles are the same as reported in **Figure 4.18b**. The fit PDF is calculated for either Cu-complex 1, Cu-complex 2, or Cu-complex 3 structures by Fourier transform of the X-ray scattering signal determined via DSE.

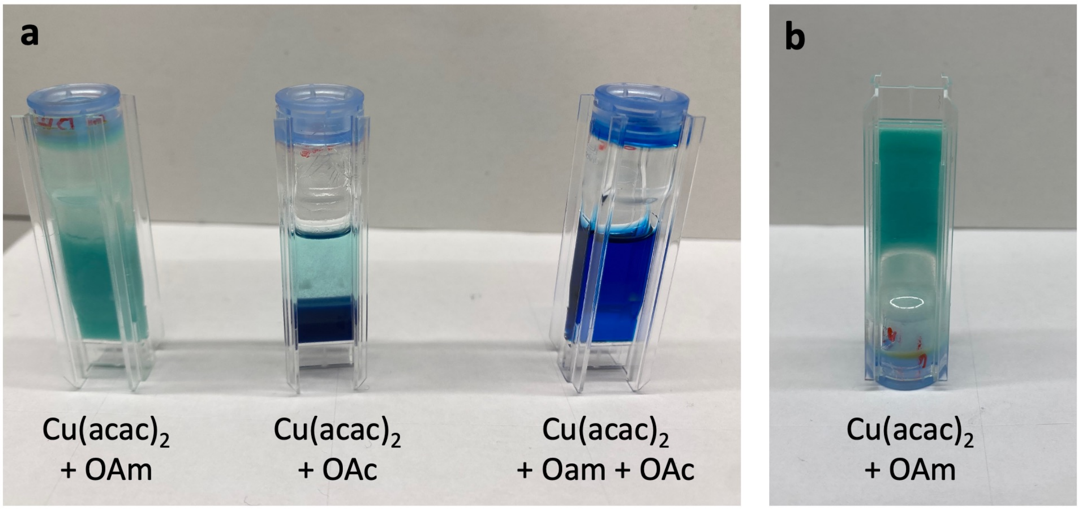

Figure S4.17: Pictures of mixtures of Cu(acac)$_2$ with different solvents. a) Picture of three vessels containing Cu(acac)$_2$ mixed with OAm, OAc, and a mixture of OAm and OAc, respectively. Over time, we observe the sedimentation of Cu(acac)$_2$ salt at the bottom of the vessel containing only OAc solvent. **b**) Picture of the highly viscous Cu(acac)$_2$/OAm mixture at room temperature.

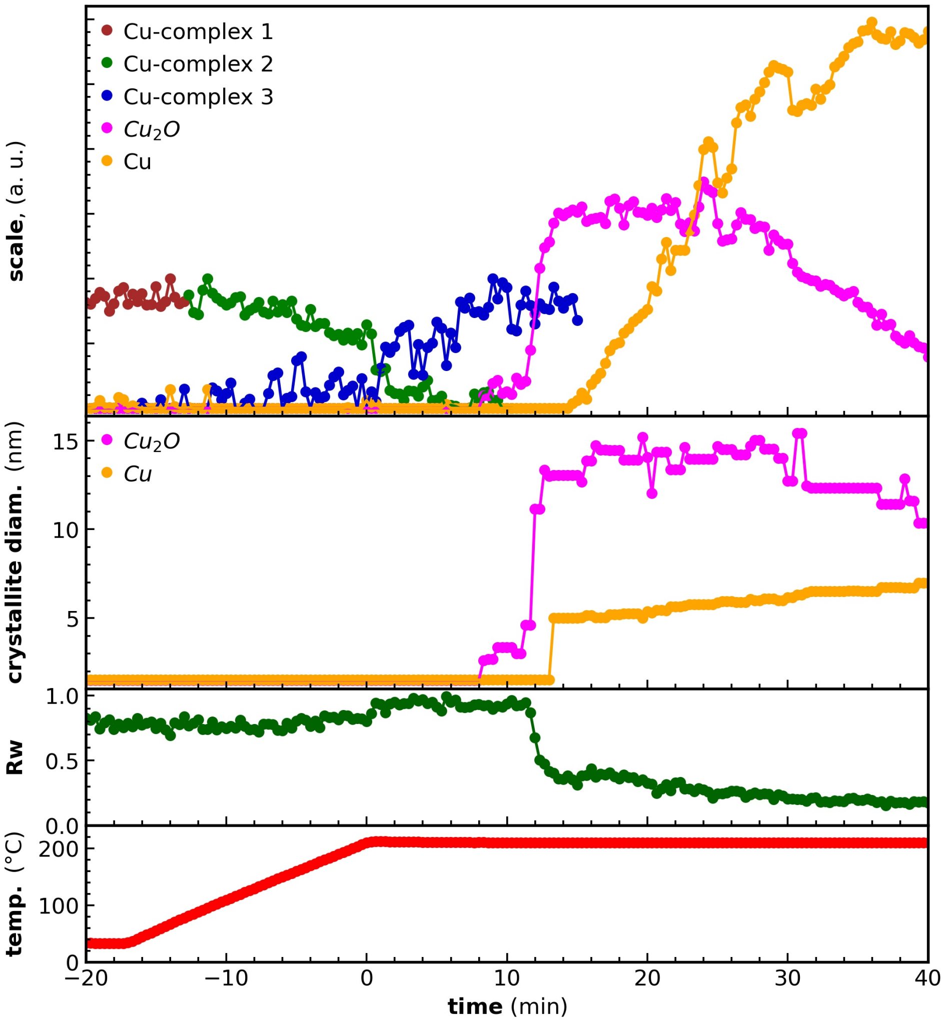

Figure S4.18: Fit of the in situ PDF during the synthesis of Cu nanocrystals. The fit PDF is calculated by a multi-component analysis compromising the 3 Cu-complex structures and Cu_2O and Cu crystalline phases. The fits of some components are dropped at later times of the synthesis to improve the robustness of the fit. Cu-complex 1 and Cu-complex 2 are never simultaneously included in the fit as the calculated PDFs from the two models are too similar to be effectively distinguished during the sequential refinement of the in situ data. The model PDFs for Cu_2O and Cu phases are calculated by means of the AC approximation and for spherical crystalline domains. The dampening of the PDF intensity at very long interatomic distances leads to underestimate the diameters of large crystallites above 10-15 nm. Above this size range, the values extracted from Rietveld refinement are more accurate. Plots of the Rw and temperature as a function of the synthesis time are also shown.

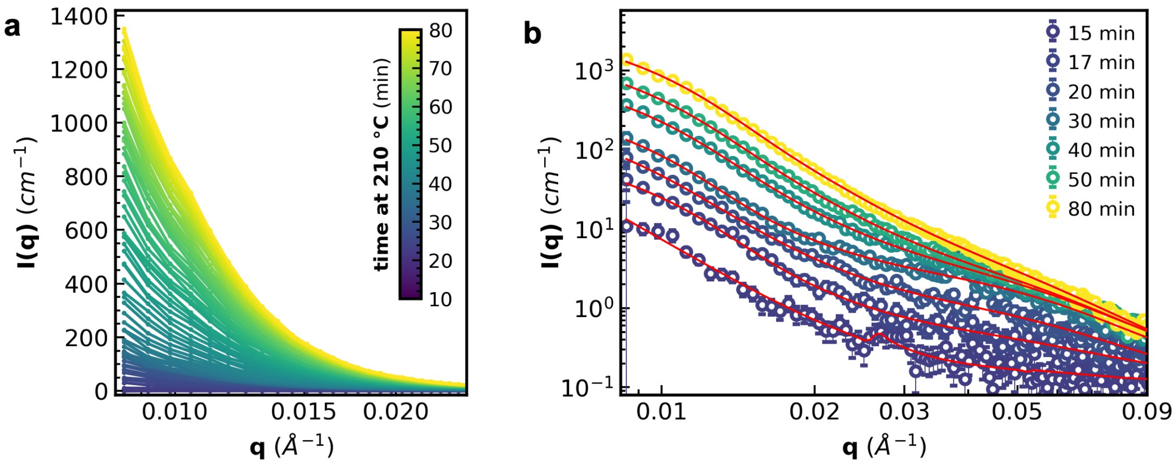

Figure S4.19: In situ SAXS during the synthesis of Cu nanocrystals and relative fit. a) Plot of the background subtracted in situ SAXS data at different time. **b**) Plot of selected SAXS profiles and relative fits. The SAXS data is collected via an in-house setup to achieve a reduced value of the experimental q_{min} compared with the P07 data. SAXS intensities are averaged over 1 minute.

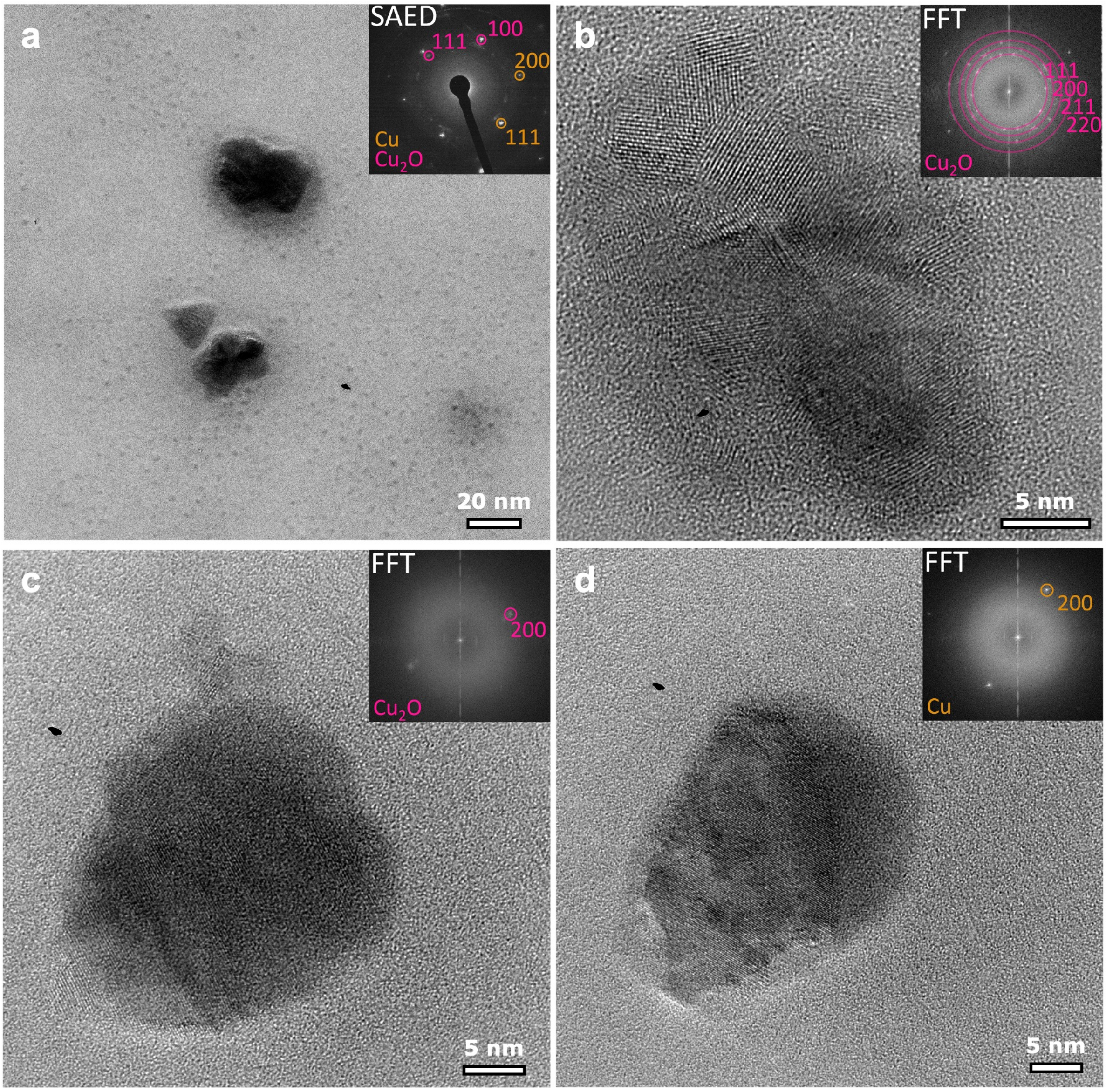

Figure S4.20: Ex situ HRTEM investigation of the Cu nanocrystal synthesis product after 20 minutes of reaction time at 210 °C. a) A low magnification HRTEM image display both small (approx. 5 nm) and large nanoparticles. In the inset, the SAED diffractogram displays diffraction peaks from both Cu_2O and Cu phases. **b**) A HRTEM image and its respective FFT for a large nanoparticle displaying twinned Cu_2O crystalline domains. **c-d**) HRTEM images and their FFT for single-crystalline Cu_2O or Cu nanocrystals, respectively.

4.3 Revealing the nucleation and self-assembly of alloyed CuPd icosahedra

The content of Sections 4.3.1 and Section 4.3.3 - 4.3.7 were accepted for publication in Small, 2311714 (2024). Sections 4.3.2 will be included in a separate publication, which is currently in preparation. Analysis of the in situ XAS data is ongoing.
My contribution to this study compromises the synthesis of the nanocrystals and supercrystals, the nanocrystal ex situ characterization, the measurement of the simultaneous in situ X-ray scattering, the collection of the in situ absorption spectroscopy, and the analysis of the PDF data.

In the previous section, we combined the use of in situ PDF, SAXS, and XAS to determine the formation pathways of monometallic Pd and Cu nanocrystals. Here, we turn our attention to the direct synthesis of supercrystals made up of mixed CuPd nanocrystals. We simultaneously acquire PDF and SAXS to bridge over multiple length scales and to observe the one-pot nucleation, growth, and self-assembly of CuPd icosahedra into close-packed superlattices, as summarized in **Figure 4.22**. We follow the chemical transformation leading both Cu and Pd precursors to convert into the metallic icosahedra by in situ XAS and PDF. Our analysis shows that the Pd precursor accelerates the reduction kinetics of Cu cations, which directly convert into the metal without formation of the Cu_2O intermediate phase. After synthesis, we direct the assembly of CuPd icosahedra upon cooling of the reaction mixture. By in situ SAXS, we first observe the emergence of a short-range ordered (SRO) phase of nanocrystals preceding the supercrystal formation. We show that the organization of oleic acid/oleylamine solvent molecules into lamellar structures drives the nanocrystal assembly by creating an excluded volume to particle diffusion. Our study thus demonstrates that entropic forces can be crucial in the direct synthesis of supercrystals.

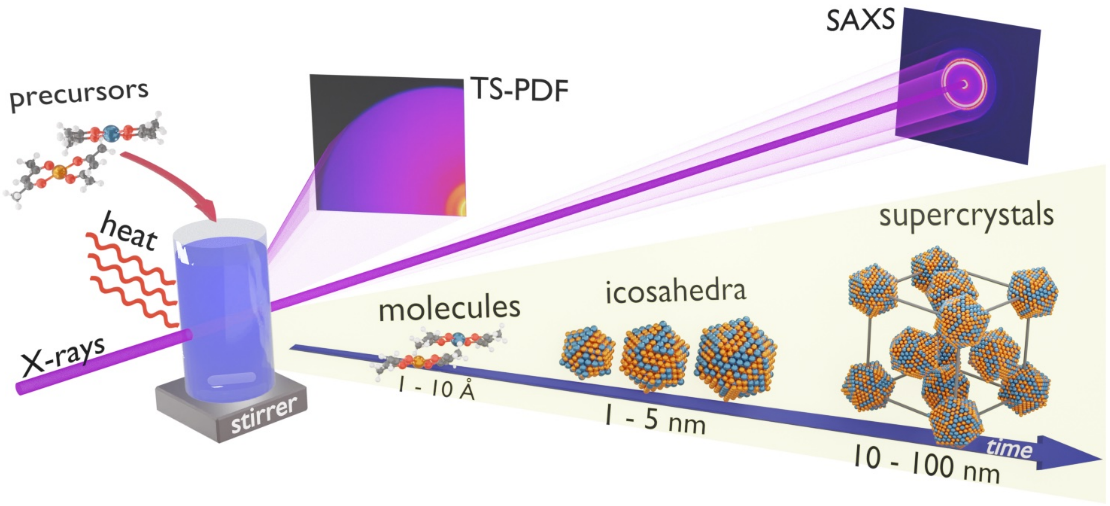

Figure 4.22: Schematic illustration of the simultaneous in situ TS-PDF and SAXS experiment during the direct synthesis and assembly of CuPd icosahedra supercrystals. A reaction mixture containing the Cu and Pd precursors is stirred during temperature ramps. The X-ray TS and SAXS signal of the reaction mixture is recorded simultaneously by two large-area detectors. Metallic CuPd icosahedra nucleate from the molecular precursors and subsequently assemble into colloidal supercrystals with a fcc arrangement.

4.3.1 Overview of the simultaneous PDF/SAXS data during the synthesis of CuPd nanocrystals

We synthesize CuPd nanocrystals by heating copper and palladium acetylacetonate (metal ratio Cu : Pd = 70 : 30) precursors in a solvent mixture consisting of oleylamine, oleic acid and dioctyl ether to 220 °C at 10 °C min^{-1}. We conduct the synthesis within SHINES reactor, and acquire multi-modal in situ X-ray scattering by use of the experimental setup described in Section 4.1.1. **Figure 4.23** provides an overview of the in situ PDF and SAXS data collected simultaneously during the colloidal synthesis, while the background subtracted in situ TS data is reported in **Figure S4.21**.

At room temperature, the PDF of **Figure 4.23b, d** exhibits an intense peak at 2.01 Å, which is consistent with the formation of amine coordinated complexes of Cu^{2+} and Pd^{2+} cations upon dissolution of the acetylacetonate precursors, similarly to what observed in the synthesis of Cu and Pd nanocrystals. Upon heating of the reaction mixture, the evolution of the PDF indicates the rapid nucleation and growth of CuPd nanocrystals of approximately 3 nm in size. The finding hints to a substantially different reduction pathway for the mixed CuPd system compared to the slow nucleation process determined in the synthesis of Cu nanocrystals. After 5 min at 220 °C no further changes are observed in the PDF, suggesting that the nanocrystal synthesis is completed.

At low temperatures, the complementary SAXS data in **Figure 4.23c, e** displays a broad peak at 0.24 Å^{-1} which stems from the metallic complexes in solution. About 95 s after reaching the reaction temperature of 220 °C, we observe a dramatic increase in the intensity at low scattering vector q, which identifies the emergence of nanometer-sized particles followed by particle growth, in line with the PDF analysis.

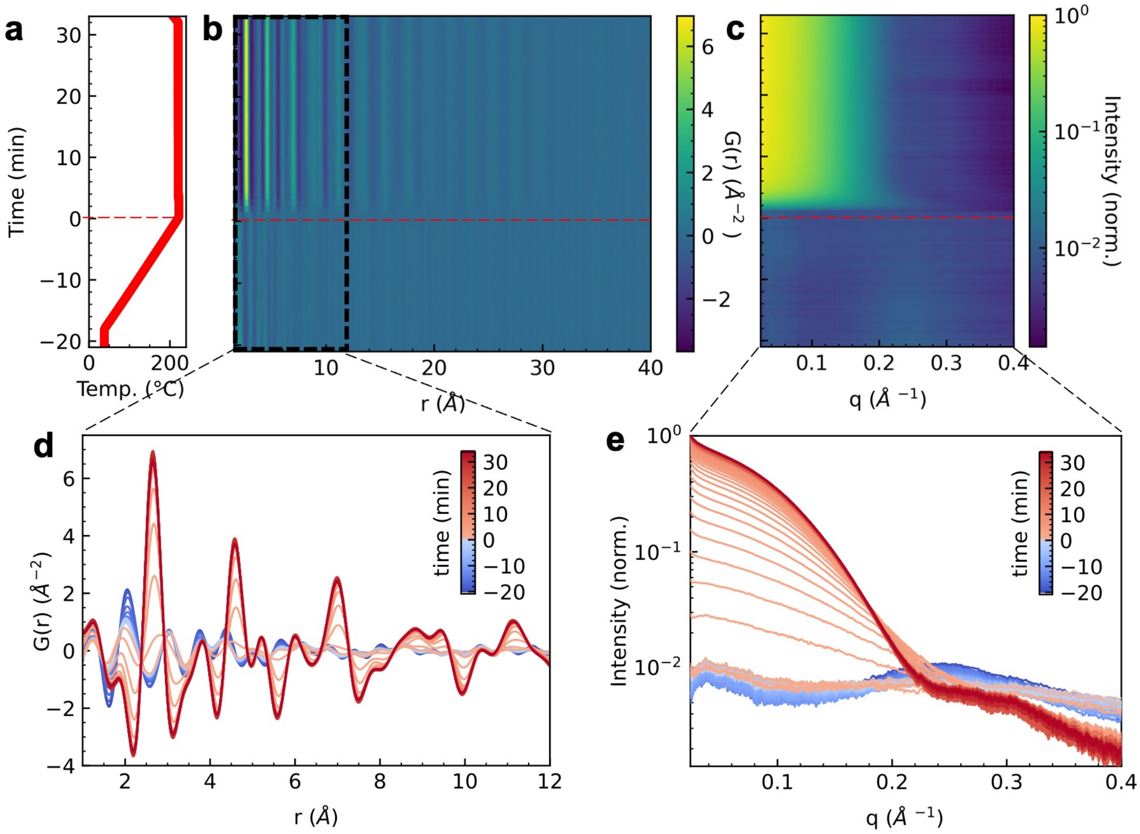

Figure 4.23: Simultaneous in situ PDF and SAXS during CuPd nanocrystal formation. **a**) Temperature profile during the synthesis of CuPd nanocrystals. At time = 0 min the reaction temperature of 220 °C is reached. **b**) 2D plot of the in situ PDF as a function of time. The corresponding 1D plots are shown in **d**. **c**) 2D plot of the in situ SAXS intensity as a function of time. The corresponding 1D plots are shown in **e**.

4.3.2 Chemical transformations affecting Cu and Pd precursors

Subtle variations in the PDF in **Figure 4.23b, d** hint at the formation of intermediate species between the starting precursors and the nanocrystal nuclei. Since the scattering signals from both Cu and Pd intermediates are convoluted to generate the TS intensity, isolating the structural features of each individual component from the PDF alone poses significant challenges. We overcome these limitations by performing complementary X-ray absorption measurements, which permits to selectively probe the local chemical environment of either Cu or Pd metal centers during the synthesis.

In **Figure 4.24a**, we report the X-ray absorption profiles in the near-edge region collected by in situ QEXAFS at the Pd K-edge. Here, we run the synthesis starting from 180 µL of precursor solution, which we then heat up to 220 °C within SHINES cell in a 6.5 mm PEEK vessel. We further analyse the data in **Figure 4.24a** by MCR-ALS. We find that the X-ray absorption signal at room temperature is identical to the one detected for Pd-complex 1 species in the synthesis of Pd nanocrystals, as shown in **Figure S4.22a**. In **Figure 4.24b**, the concentration profiles extracted from the MCR-ALS analysis reveal the fast conversion of Pd-complex 1 into the reduced metal form at high temperature, similarly to what we already observed in the synthesis of pure Pd nanocrystals (**Figure 4.15b**). We therefore conclude that the reduction kinetics of Pd-complex 1 is fast and likely independent of the presence of the Cu intermediate species in solution.

We further measure in situ QEXAFS at the Cu K-edge to follow the transformation of Cu precursor into CuPd nanocrystals. We perform MCR-ALS analysis of the X-ray absorption spectroscopy data in **Figure 4.24c** to obtain the concentration profiles shown in **Figure 4.24d**. We determine the formation of the same organocopper species as revealed for the synthesis of Cu nanocrystals, as further demonstrated by the HERFD-XANES measurements in **Figure S4.22b-d**. However, here we observe the direct conversion of the Cu-complex 3 into the metallic form without the intermediate formation of a Cu_2O phase. Moreover, the reduction of Cu-complex 3 is fast and completes in only few minutes after reaching 210 °C. These observations clearly indicate that the presence of Pd species in solution promotes the reduction of Cu intermediates.

We propose that the reduction of Pd-complex 1 shortly precedes the reduction of Cu-complex 3 to generate Pd-rich nuclei. Once formed, these nuclei act as seeds for the

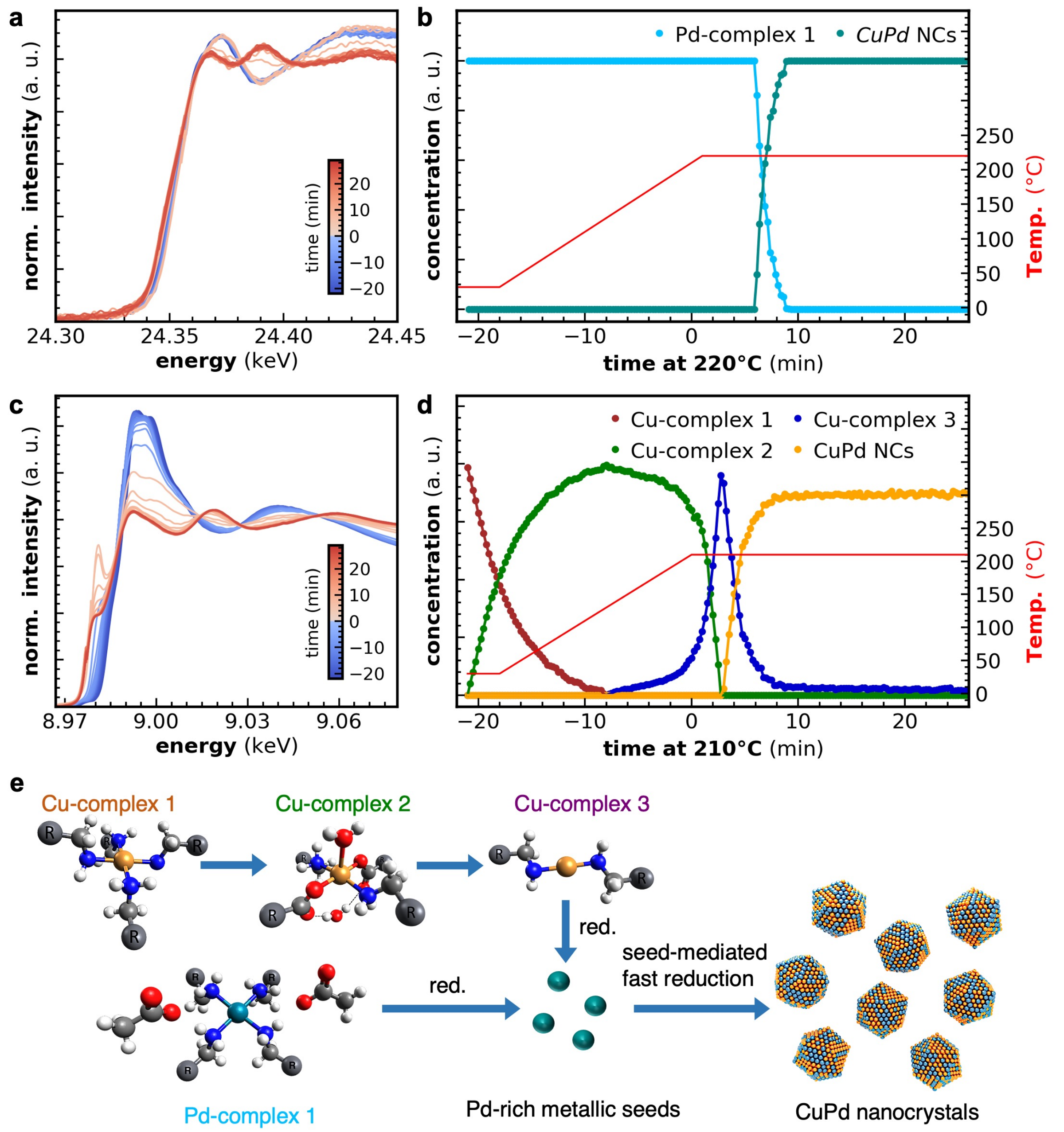

Figure 4.24: Overview of the chemical tranformations to CuPd nanocrystals as revealed by in situ XAS. a, **c**) Plots of the XANES region of the QEXAFS data measured at the Pd K-edge (**a**) or the Cu K-edge (**c**). **b**, **d**) Concentration profiles for different species as revealed by MCR-ALS analysis of the data shown in **a** and **d**, respectively. Plots of the temperature profiles during the measurements are additionally shown. The data in **a-b** are collected while heating 180 µL of precursor solution in a PEEK reaction vessel with a diameter of 6.5 mm, while data in **c-d** are measured while heating 450 µL of the same solution in a PEEK vessel with a diameter of 9.5 mm. **e**) Schematic illustration of the chemical transformations driving the nucleation of CuPd nanocrystals.

co-reduction of both Cu and Pd species, which thereafter convert at a similar fast rate to outcome into alloyed CuPd nanocrystals. **Figure 4.24e** schematically illustrates the proposed mechanism for the seed-mediated formation of the CuPd nanocrystals. Since we cannot assume a complete reproducibility of the synthesis over very fast time scales, the reduction rates measured via separate in situ QEXAFS runs at the Cu or Pd K-edges cannot be directly compared. To prove the intermediate formation of the short living Pd-rich seeds, an analysis of the individual in situ EXAFS datasets is currently ongoing.

4.3.3 Atomic structure of the inorganic CuPd nanocrystal cores

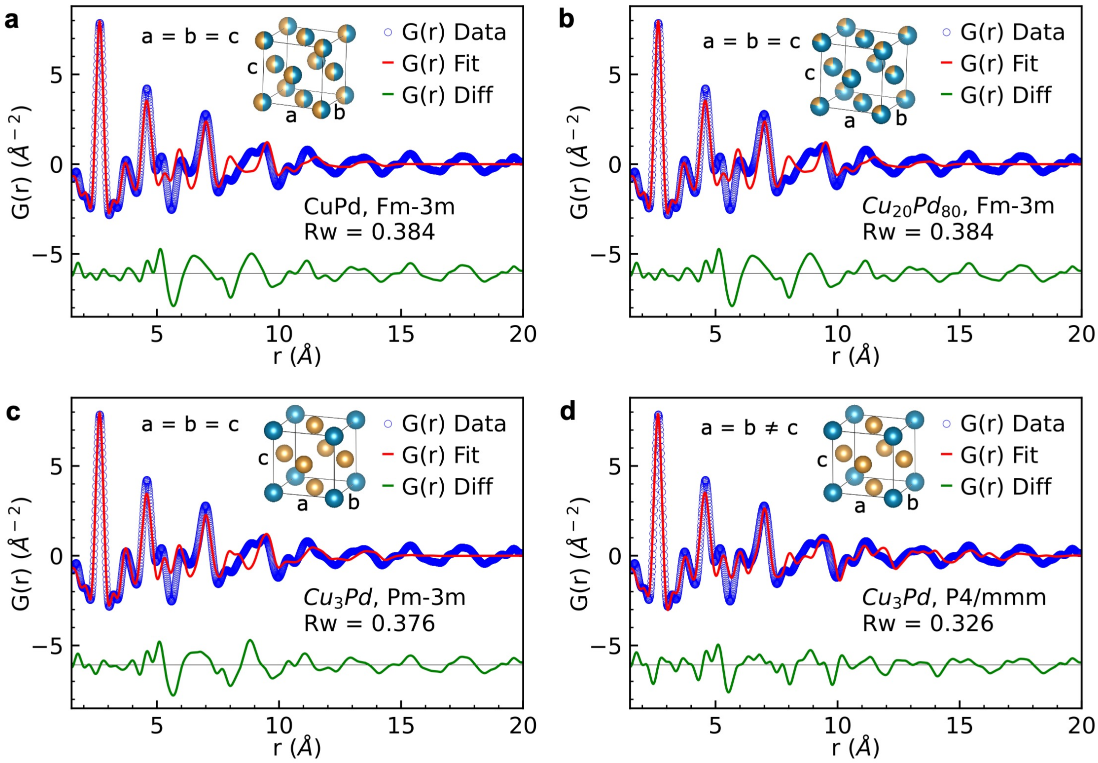

Figure 4.25: Fit of the PDF of the nanocrystals by the AC approximation a-b) Fits by CuPd cubic Fm-3m alloy, for Cu:Pd ratios of 50:50 and 20:80, respectively. **c-d**) Fits by intermetallic Cu_3Pd of cubic (space group Pm-3m) and tetragonal (space group P4/mmm) symmetry, respectively. In the insets, the respective unit cells, where orange indicates Cu atoms and blue Pd atoms, are schematically illustrated. The nanocrystal diameters determined by the 4 fits are 16 Å, 16 Å, 17 Å and 21 Å, respectively.

We now focus on determining the final atomic structure of the CuPd nanocrystals after analysis of the PDF signal at a late stage of the synthesis (t = 10 min). We first model the PDF data by means of the well-established attenuated crystal (AC) approximation, which assumes that the nanocrystals are single-crystalline spheres. However, this model provides a poor fit to the experimental data, both in the case of bulk CuPd alloys of different composition (space group Fm-3m, **Figure 4.25a, b**) and cubic or tetragonal intermetallic phases (space group Pm-3m and P4/mmm, respectively, **Figure 4.25c-d**).

To capture the structural features encoded in the PDF, we therefore extend the candidate structures beyond single-crystalline, spherical models. To this goal, we generate many discrete atomic nanoparticle models of various sizes and displaying different atomic arrangements, and then test each model individually against the experimental PDF. This approach is referred to as *cluster mining* and was recently established for the PDF analysis of monometallic nanocrystal powders.[209] In this work, we apply the method for the first time to the analysis of in situ data. We consider various structural motifs displaying either single-crystalline domains (spheres, octahedrons, and truncated octahedrons), or 5-fold twin boundaries (decahedrons and icosahedrons) and build alloyed CuPd models by fixing the Cu:Pd atomic ratio to 60:40, as determined by TEM-energy dispersive X-ray spectroscopy (EDX) measurements on the final nanocrystals (**Figure S4.23**).

We further employ the weighted residual error (Rw) value to quantify the goodness-of-fit provided by each cluster model, as summarized in **Figure 4.26a** and **Figure S4.24**. In **Figure 4.26b-c** and **Figure S4.25**, we report the best fit for each structural motif. The decahedral model provides an excellent fit to the PDF at short atomic pair distances. However, the differential curve in **Figure 4.26c** displays weak, non-random oscillations at longer inter-distances which indicate that the model does not fully capture the nanocrystal structure. Moreover, the decahedral model predicts particles with a maximal axial size of 1.6 nm and a diameter of 2.1 nm, which are much smaller compared to the sizes revealed by TEM (**Figure S4.26**). Conversely, the icosahedral model predicts nanocrystal sizes of 3.2 nm, in line with the TEM analysis. Additional HRTEM measurements further evidence the presence of the twinned, icosahedral nanocrystals as synthetic products (**Figure 4.26e-f** and **Figure S4.27**).[251–253]

An icosahedral nanocrystal is made up of 20 face-sharing tetrahedrons displaying fcc structure. Compared to the ideal model, we expect the CuPd nanocrystal sample to exhibit a certain degree of heterogeneity due to the presence of e.g. point defects, inter-

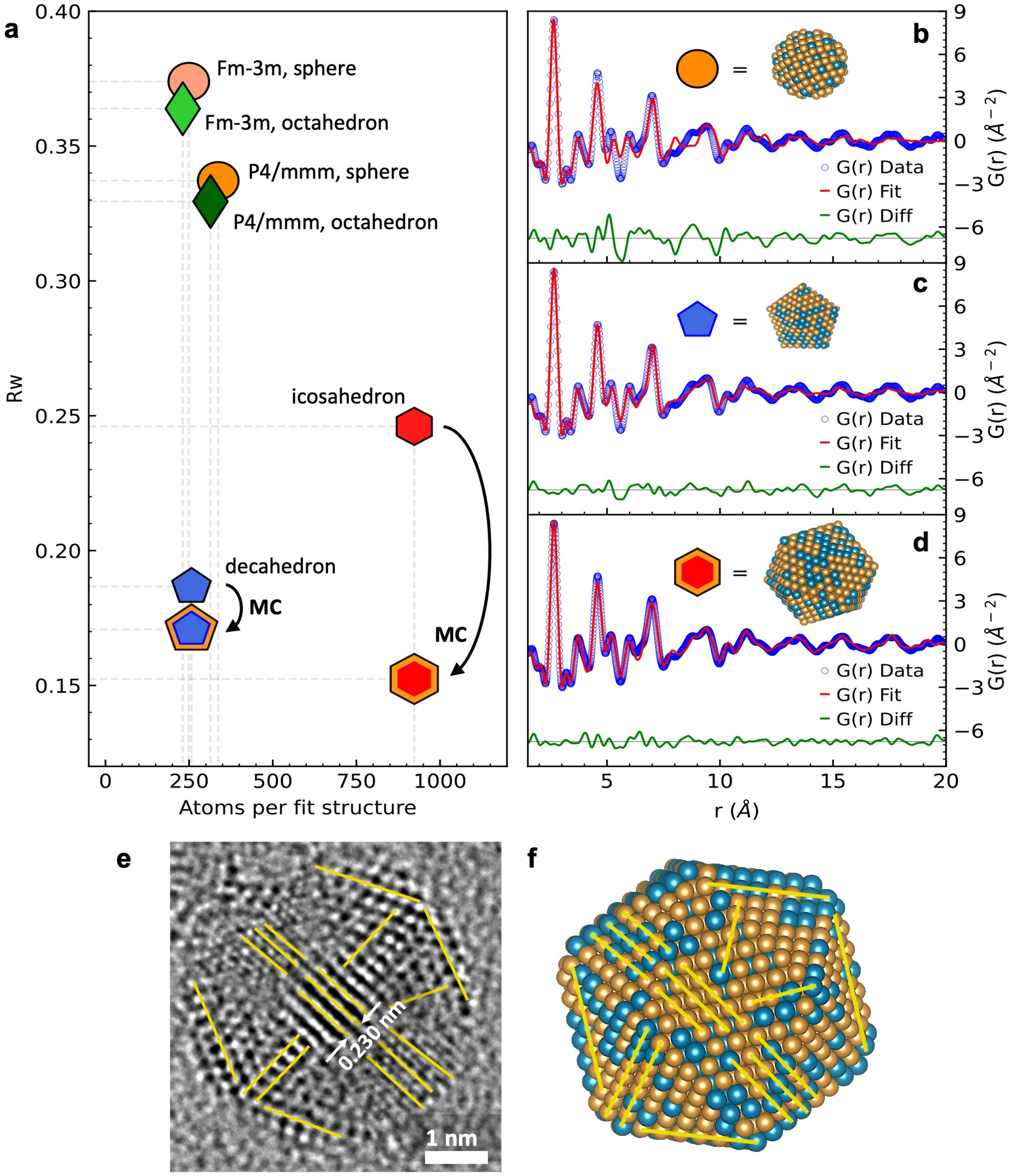

Figure 4.26: Determination of the nanocrystal core structure by PDF and HRTEM a) Scatter plot of the number of atoms per structure and of the agreement factor (Rw) obtained by fit of the PDF of the final product. Discrete atomistic models of different structural motifs are used. For each motif, the information relative to the best-fit structure is shown. A yellow frame outlines the fit structures obtained by using a Monte Carlo (MC) routine. **b-d**) Best fits of the PDF for selected structural motifs in **a**. In the insets, the structural models relative to each fit are shown. **e-f**) A HRTEM image of a CuPd nanocrystal (**e**) is compared to an icosahedral cluster model (**f**). Yellow lines are guides to the eye underlining the major structural motifs for both.

stitial atoms between the tetrahedral domains, size polydispersity, and inhomogeneous composition or distribution of the Cu and Pd atoms in the lattice. We suggest that the summed contribution of all these structural defects results in very small, randomized deviations in the averaged atomic arrangement of the CuPd nanocrystals from the ideal icosahedral configuration and causes the discrepancy between the experimental and simulated PDF in **Figure S4.25d**. We test our hypothesis after developing a Monte Carlo sampling procedure which allows minor atomic displacements in the model structure. In **Figure 4.26d** we show that the relaxed model perfectly fits the experimental PDF while retaining the overall icosahedral arrangement, as demonstrated by **Figure S4.28**. **Figure S4.28** also shows that the atomic displacements introduced by the Monte Carlo algorithm are seemingly randomised and similarly affect atoms belonging to either the nanocrystal core or surface structure. The application of the same sampling routine to the decahedral model does not significantly improve the fit, as shown in **Figure S4.29**. Our results thus indicate that the icosahedral arrangement provides the best description of the CuPd nanocrystals, as consistently supported by both EM analysis and PDF.

4.3.4 Revealing the nucleation of CuPd nanocrystals during synthesis

We analyse both the in situ PDF and SAXS data to extract quantitative information from the nucleation and growth of the CuPd icosahedra. Qualitative inspection of the time-resolved PDF in **Figure 4.27a** indicates that as the nanocrystals grow, the amplitude of the PDF oscillations increases and the structural features extend to longer interatomic distances. We thus fit the time-dependent in situ PDF by a series of CuPd icosahedra models of different sizes, which consist of a varying number of discrete atomic shells N_{shells}. We further fit the simultaneous in situ SAXS data by a form factor model of moderately polydisperse spheres, as shown in **Figure 4.27b**.

The particle diameters determined by fit of PDF and SAXS data follow a similar trend throughout the reaction time, as illustrated in **Figure 4.27c**. The particle diameter revealed by SAXS increases smoothly whereas PDF analysis results in a stepwise increase of the nanocrystal sizes due to the discrete number of shells utilised in the icosahedral models. While the PDF signal mainly originates from interatomic distances limited to the

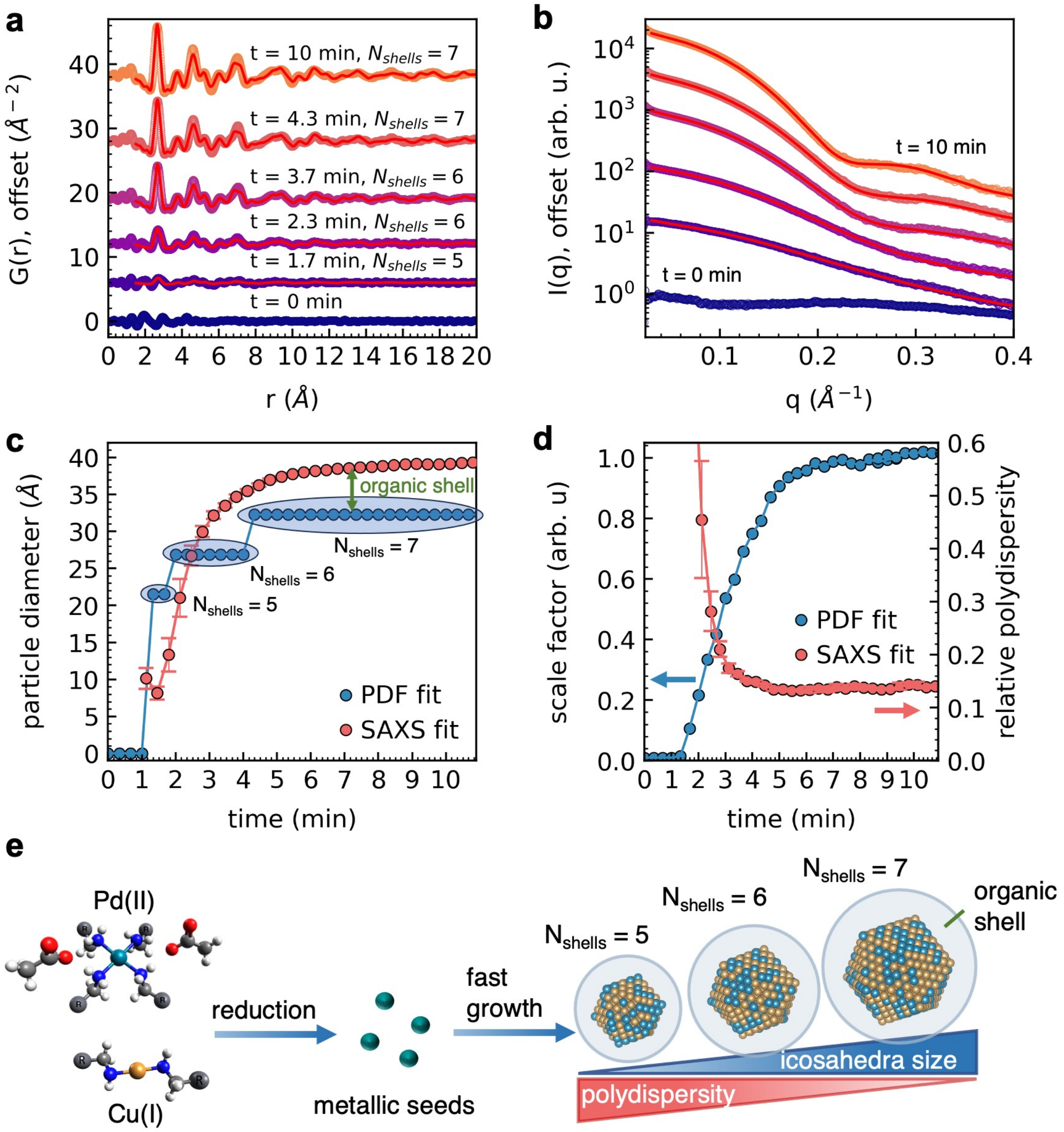

Figure 4.27: CuPd nanocrystal nucleation and growth. a) PDF data measured at selected times during the nanocrystal formation. Red lines indicate the fit of the experimental data with an icosahedral model characterized by a discrete number of atomic shells (N_{shells}). **b**) SAXS intensities at the same selected times as in **a**. **c**) Particle diameter as a function of time as obtained by fit of PDF and SAXS data. The larger diameters predicted by SAXS stem from the presence of a soft organic shell surrounding the nanocrystals. **d**) Scale factor and relative polydispersity as determined by the fit of PDF and SAXS data, respectively. **e**) Schematic illustration of the growth process of colloidal CuPd icosahedra.

nanocrystal inorganic cores, we suggest that the SAXS intensities are also partly sensitive to the presence of a soft shell of organic ligands which surrounds the nanocrystal surface. This shell consists of highly packed organic molecules and thus exhibits a higher electron-density compared with the bulk isotropic solvent. Thus, modelling the SAXS signal via a simple sphere model systematically overestimates the diameters of the nanocrystal metallic cores compared with the PDF values. We therefore consider an improved model of the colloidal nanocrystals form factor, in which we include a decaying scattering contrast shell which surrounds the high scattering contrast cores. **Figure S4.31** shows that the improved model for the nanocrystal form factor results in similar sizes of the nanocrystal cores by fit of both SAXS and PDF data. In **Figure S4.32**, FTIR measurements on the nanocrystal product further confirms the presence of an organic shell of oleylamine and oleic acid ligands at the nanocrystal surface.[241,242]

In **Figure 4.27d** the scale factor determined by PDF fit reaches a plateau at t = 5 min. At this time, the formation of the CuPd icosahedra therefore completes. Fit of the SAXS profiles during the nanocrystal growth further reveals a decreasing trend in the particle polidispersity, which reaches the constant value of 13.5% at t = 5 min. **Figure 4.27e** provides a schematic illustration of the nucleation and growth of CuPd icosahedra, where we combine the findings from the simultaneous in situ PDF and SAXS data with the results from our QEXAFS and HERFD-XANES investigation.

4.3.5 The directed self-assembly of CuPd icosahedra

We use in situ SAXS to monitor the self-assembly of CuPd icosahedra into the supercrystals. We induce the nanocrystal assembly after lowering the temperature of the reaction mixture to 100 °C immediately after synthesis. In **Figure 4.28a**, representative one-dimensional SAXS patterns reveal the gradual emergence of intense diffraction peaks from the free particles form factor due to the formation of a crystalline superlattice. We assign the symmetry of the superlattice to the close-packed fcc arrangement, with a lattice constant of 10.24 nm, as shown in **Figure 4.28a**.

Further inspection of the SAXS profiles reveals the formation of intensity peaks at at 0.16 and 0.32 Å^{-1} which indicate the emergence of a lamellar phase with a repeating unit size of 3.9 nm in addition to the supercrystal formation, as shown in **Figure**

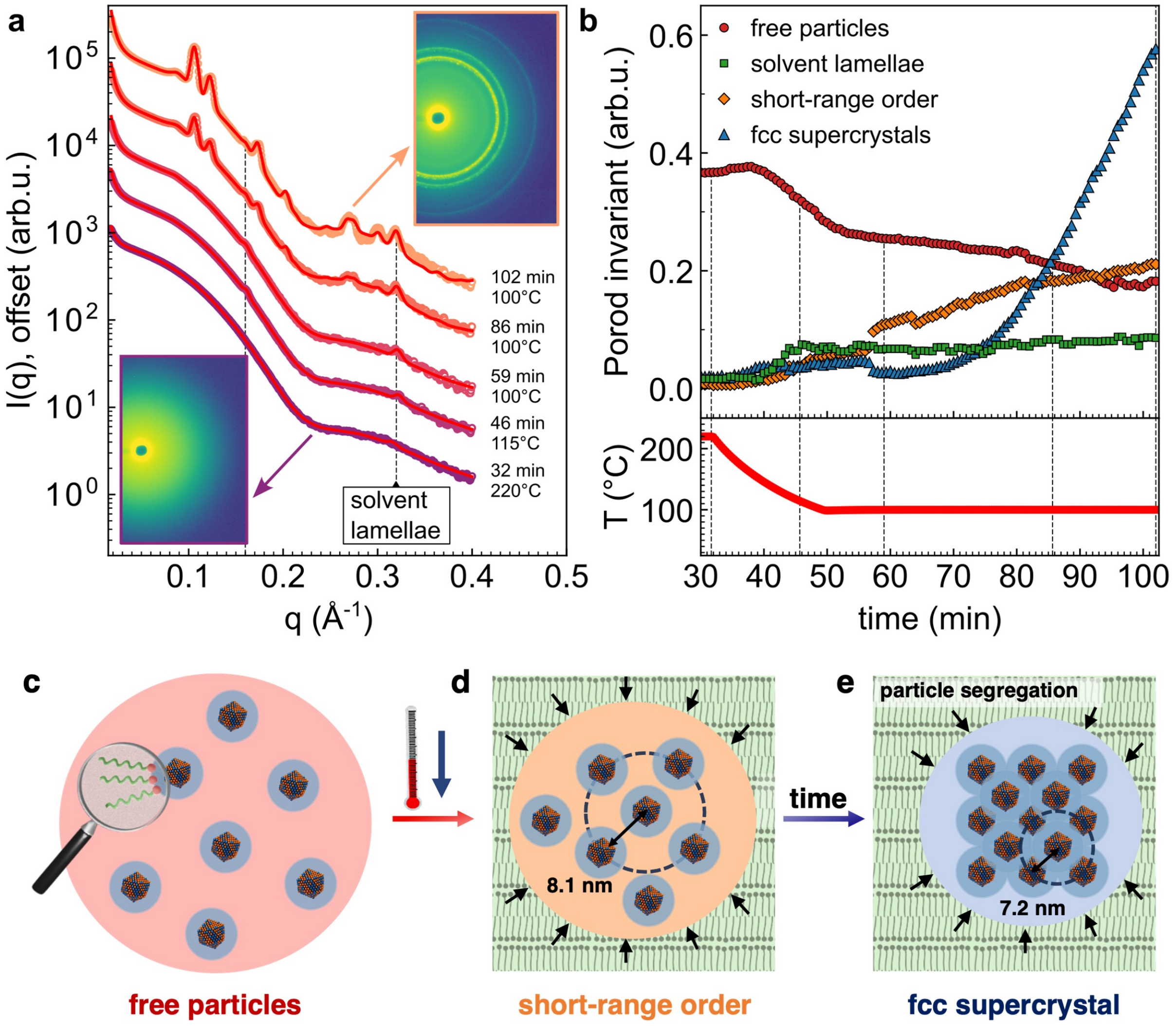

Figure 4.28: Formation of the supercrystals. a) SAXS profiles at selected times before, during, and after formation of the supercrystals. Red lines indicate the fit of the experimental data. Dashed black lines indicate the position of the peaks originating from solvent lamellae. In the insets, the detector images corresponding to the first and last profiles are shown. **b**) Time-resolved plot of the Porod invariants, which quantify the contribution of the free particles, solvent lamellae, SRO particles, and fcc supercrystals to the SAXS intensity over time. The temperature profile during the cooling of the reaction mixture and the subsequent thermal treatment at 100 °C after the nanocrystal synthesis is additionally shown. At time = 0 min the reaction temperature of 220 °C was first reached (data shown in **Figure 4.23**). **c-e**) Schematic illustration of the formation mechanism of the supercrystals. Cooling of the reaction mixture induces the freely dispersed particles (**c**) to arrange into the SRO phase (**d**) due to the emergence of solvent lamellae and the subsequent formation of particle-dense subphases. Over time, the SRO phase further evolves into supercrystals of fcc arrangement and of shorter interparticle distance (**e**).

S4.33. The 3.9 nm size is characteristic of bilayer structures of oleic acid/oleylamine solvent molecules.[237,254,255] We additionally observe the presence of a SRO phase of CuPd nanocrystals with a typical interparticle distance of ca. 8-9 nm, i.e. wider than the nanocrystal core diameter (3.2 nm) plus a shell of fully extended oleic acid/oleylamine molecules (4 nm).

We calculate the Porod invariant Q from the SAXS intensity (see **Figure S4.34**) for each of the four detected phases (free particles, solvent lamellae, SRO phase, and supercrystals) to quantify their respective volume fractions during cooling of the reaction mixture. The time-resolved evolution of the Porod invariants is reported in **Figure 4.28b**. The formation of the solvent lamellae during the cooling ramp starts at approximately 130 °C and is immediately followed by the slow emergence of the SRO phase. Extended heating at the constant temperature of 100 °C for 30 min promotes a continuous growth of the SRO phase and eventually the formation of the supercrystals. The supercrystal nucleation occurs homogeneously within the solvent, as revealed by the isotropic diffraction rings in the SAXS pattern shown in the inset of **Figure 4.28a**. After nucleation, the supercrystals rapidly grow above 100 nm in only 15 min, see **Figure S4.35**. We therefore detect an assembly process which is much faster than common self-assembly procedures of colloidal nanocrystals.

4.3.6 Mechanism of the supercrystal formation

Increasing the particle density by e.g. solvent evaporation is a common strategy to induce the assembly of colloidal crystals.[109,131,256,257] In freezing-induced self-assembly methods, the crystallization of the solvent and the subsequent expulsion and aggregation of solutes constitute the driving force of the assembly process.[258,259] Here, we show that cooling of the surfactant-rich reaction mixture induces the formation of solvent lamellae, which in turn promotes the emergence of the SRO phase and finally of the supercrystals.

Figure S4.36 shows the SAXS data after heating up and then cooling down the solvent mixture in the absence of the Cu and Pd precursors. During the process, we observe the formation of lamellae with a repeating unit size of 3.84 nm, i.e. very close to the one determined in the presence of the nanocrystals. This result suggests that the organization of the solvent molecules into the lamellar phase coincides with a simultaneous segregation of the nanocrystals, which accumulate into particle-dense subphases. We thus observe the emergence of a particle-dense SRO phase. As the solvent lamellae rearrange over time, a growing number of nanocrystals segregate from the lamellar phase into a restricted environment. We accordingly determine a decrease in the fraction of freely dispersed nanocrystals. During the process, the typical interparticle distance of the SRO phase progressively reduces from 9.2 nm to 8.1 nm, as shown in **Figure S4.37**. The SRO finally evolves into the fcc arrangement, which allows to maximize the nanocrystals packing density in the reduced volume. We therefore conclude that the supercrystals nucleation occurs via a two-step process in which the formation of an amorphous dense phase precedes the nanocrystal crystallization.[108,260] The overall self-assembly mechanism is illustrated in **Figure 4.28c-e**.

Previous studies suggest that a competition of long-ranged van der Waals attractive forces and short-ranged steric repulsion is crucial for the direct synthesis of colloidal supercrystals. In the presence of core-core attraction, the soft shells stabilizing adjacent nanocrystals in the superlattice partially interpenetrate, resulting in a shorter surface-to-surface separation than the thickness of the two shells. For example, a 1.95 nm separation was observed for superlattices of 6 nm Pd nanocrystals capped with oleic acid, and a 3 nm separation is predicted for identical particles of 3 nm in size at 503K.[123] However, here we find a larger surface-to-surface separation within the supercrystals of 4 nm, corresponding to twice the length of a fully extended oleylamine/oleic acid molecules. The result indicates that no interpenetration of the organic shells between adjacent nanocrystals is present. Moreover, it suggests that attractive forces between the metal cores are rather weak.

We confirm our observation by calculating the effect of the van der Waals attraction and steric repulsion between 3-nm CuPd nanocrystals in presence of surface ligands. In **Figure S4.38**, the resulting pair-wise potential displays a very shallow minimum located at a 3.9 nm surface-to-surface separation of –0.02 K_BT, i.e. much smaller than the kinetic energy of the nanocrystals. We therefore conclude that long-ranged van der Waals attraction alone is too weak to drive freely dispersed nanocrystals to assemble. Instead, we propose that the lamellar formation and the subsequent nanocrystal segregation likely act as an initiator of the self-assembly process by limiting the available volume to nanocrystal

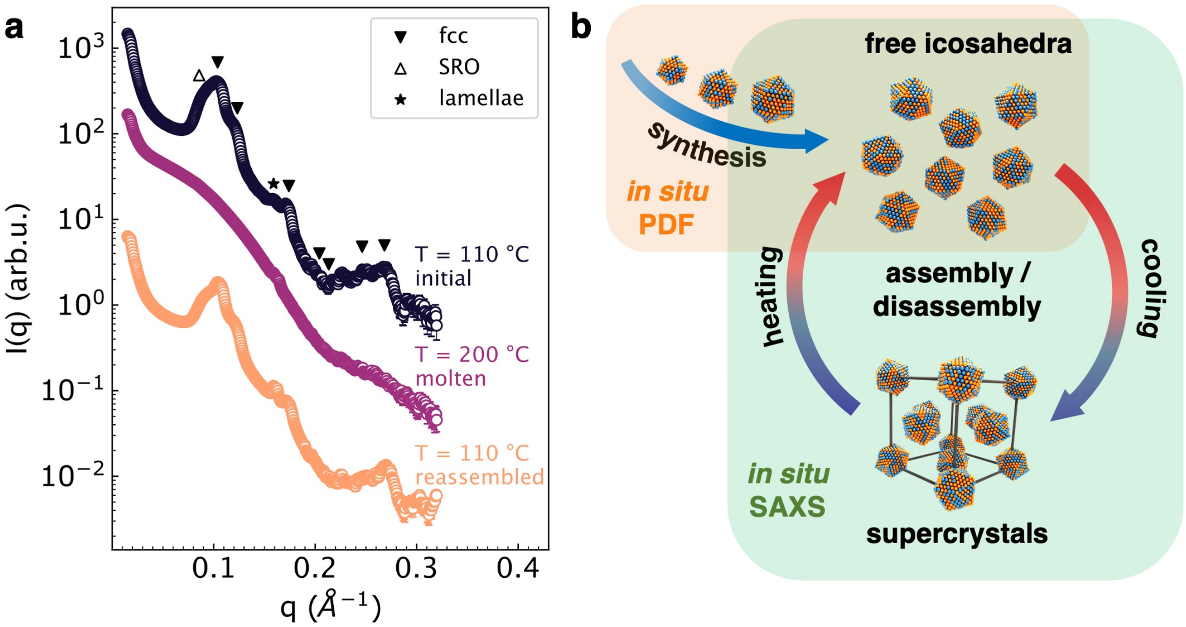

Figure 4.29: Temperature-mediated melting and recrystallization of the supercrystals. a) Plot of the SAXS intensities before and after melting. After synthesis, the reaction mixture is cooled to 110 °C to induce the nanocrystals self-assembly into the fcc supercrystals (*top*). Heating the mixture to 200 °C dissolves the assemblies, and the smooth form factor of free particles dominates the in situ SAXS intensity (*middle*). Re-cooling of the mixture to 110 °C further induces the emergence of the supercrystals (*bottom*). Above the uppermost profile, solid downward triangles point to Bragg reflections due to the supercrystals, an open upward triangle to the characteristic intensity of the SRO phase, and an asterisk to the lamellae peak, respectively. **b**) Schematic illustration of the synthesis of CuPd icosahedra and of the temperature-mediated crystallization of the supercrystals revealed by in situ PDF and SAXS.

diffusion. At increased particle density, the crystallization of CuPd icosahedra leads to an overall increase in the total entropy of the system, in analogy to hard spheres.[261,262] In fact, diluting a dispersion of the supercrystals at room temperature with either polar or apolar solvents leads to the immediate disruption of the crystalline order due to a decrease of the local particle volume fraction, as shown by SAXS in **Figure S4.39**. Although the result does not exclude the existence of short-range attractive forces, such as core-core or ligand-ligand interactions, within the supercrystals, it nevertheless indicates that these interactions are rather weak, even at short interparticle distances. We therefore conclude that interparticle attractions play only a minor role in the observed assembly process.

We demonstrate that the supercrystals disassemble and subsequently re-assemble upon increasing and then decreasing the temperature of the dispersion between 200 and

110 °C, as shown in **Figure 4.29a**. During the heating, the supercrystals melt first while decomposition of the SRO phase unfolds at higher temperatures. Upon cooling, the emergence of the SRO phase precedes the supercrystal formation, as observed before. In situ PDF shows that the structure of the icosahedral inorganic cores is unaffected by both the melting and re-assembly, as evidenced in **Figure S4.40**. In **Figure 4.29b** we offer a schematic illustration of the direct synthesis and assembly of CuPd icosahedra, as determined by simultaneous in situ PDF and SAXS.

4.3.7 Supporting information

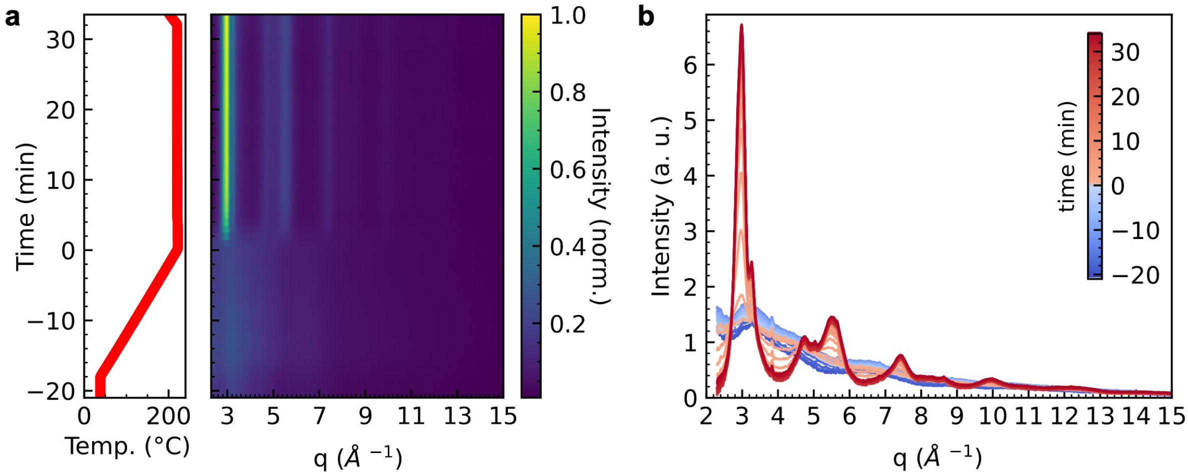

Figure S4.21: Background subtracted in situ TS data during CuPd nanocrystal synthesis. **a**) 2D plot of the background subtracted TS data as a function of the reaction time and temperature. **b**) The corresponding 1D plot of the TS data shown in **a**.

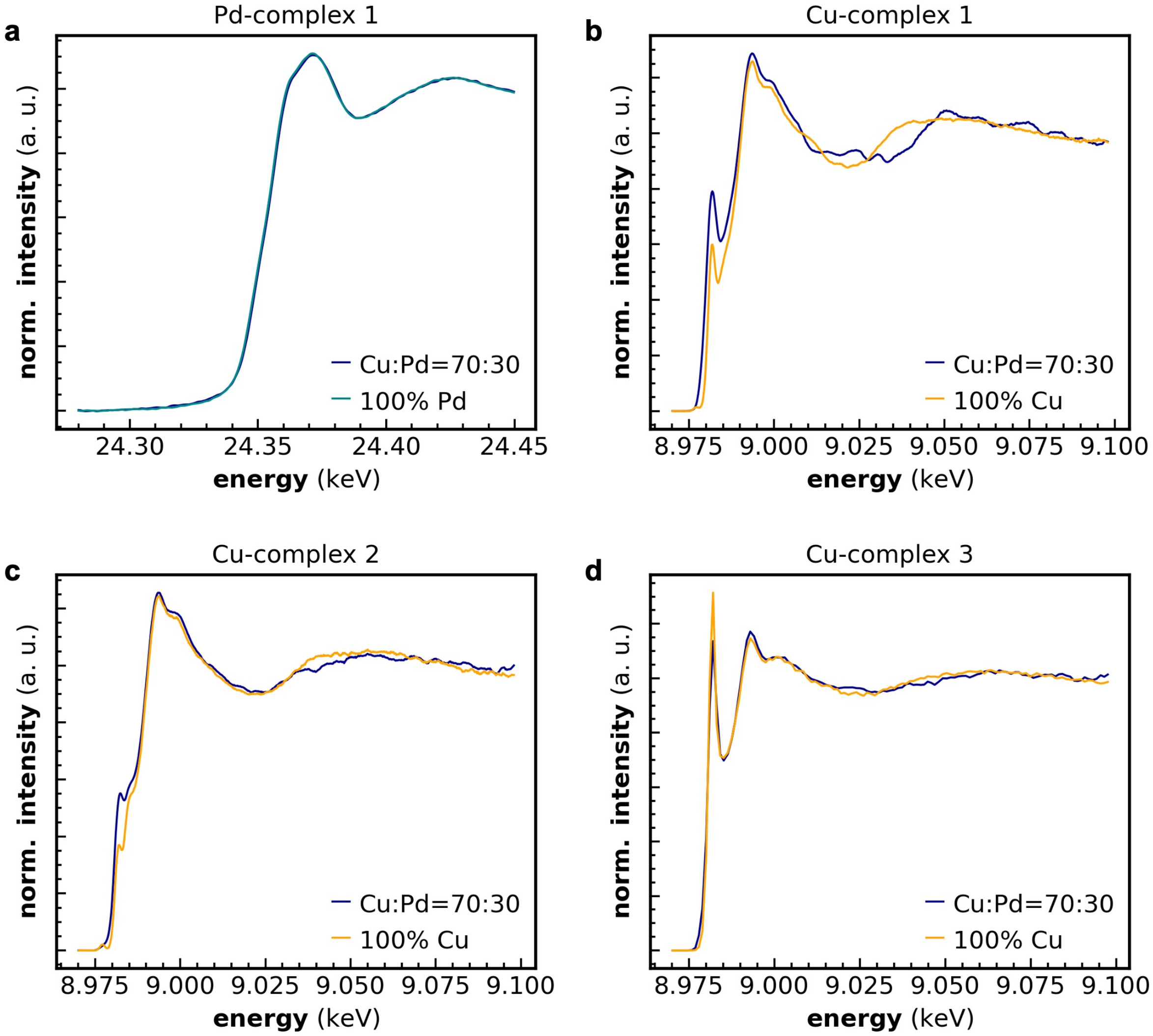

Figure S4.22: Comparison of selected in situ XANES profiles detected during the synthesis of CuPd icosahedra and Pd or Cu nanocrystals. **a**) Plot of the XANES data for Pd-complex 1 measured by in situ QEXAFS during the synthesis of either CuPd icosahedra or Pd nanocrystals. **b-d**) Plot of the in situ HERFD-XANES data for Cu-complex 1 (**b**), Cu-complex 2 (**c**), Cu-complex 3 (**d**) measured during the synthesis of either CuPd icosahedra or Cu nanocrystals.

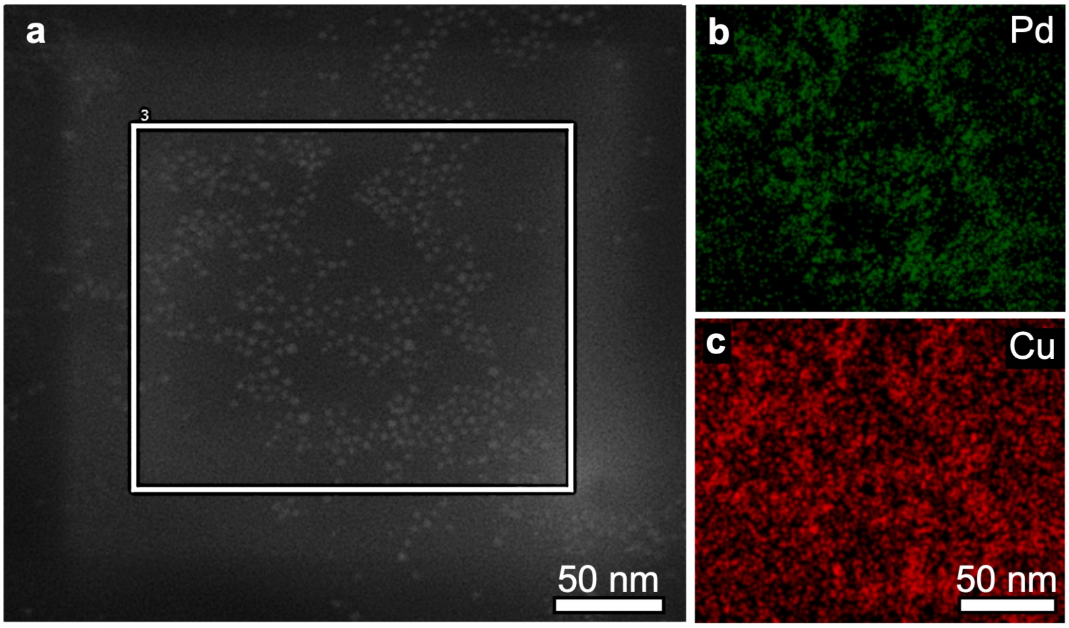

Figure S4.23: TEM-EDX measurement for icosahedra nanocrystals. **a**) TEM micrograph of the icosahedra nanocrystals deposited on a gold TEM grid. **b-c**) Pd and Cu elemental maps relative to the area enclosed by the white square in **a**. The relative atomic composition for Pd and Cu is determined as 38 % and 62 %, respectively.

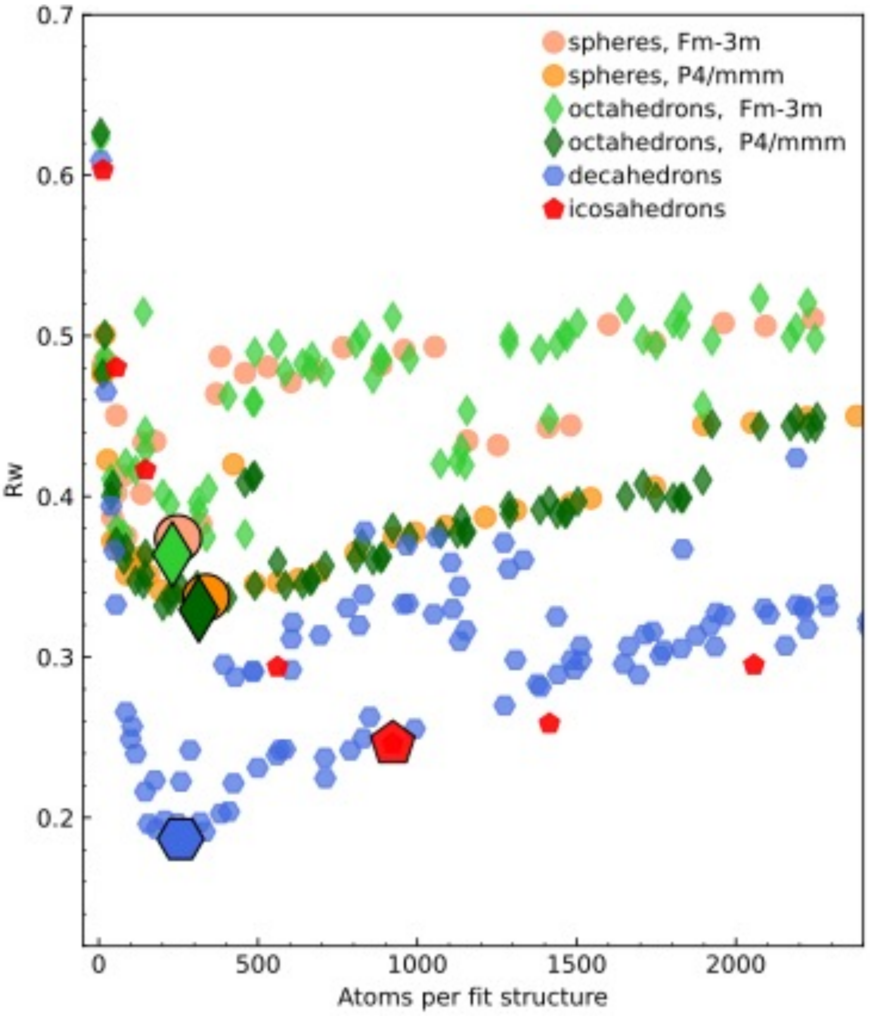

Figure S4.24: Outcome for the cluster mine fit of the CuPd nanocrystals. Each scatter point refers to an independent fit with a different discrete atomic model. Models belonging to the same structural motif are indicated by the same scatter point shape, while scatter points of same shape but different colors refer to different crystalline phases, as illustrate by the legend. The best-scoring fit within a particular structural motif and crystalline phase is displayed with a scatter point of increased size.

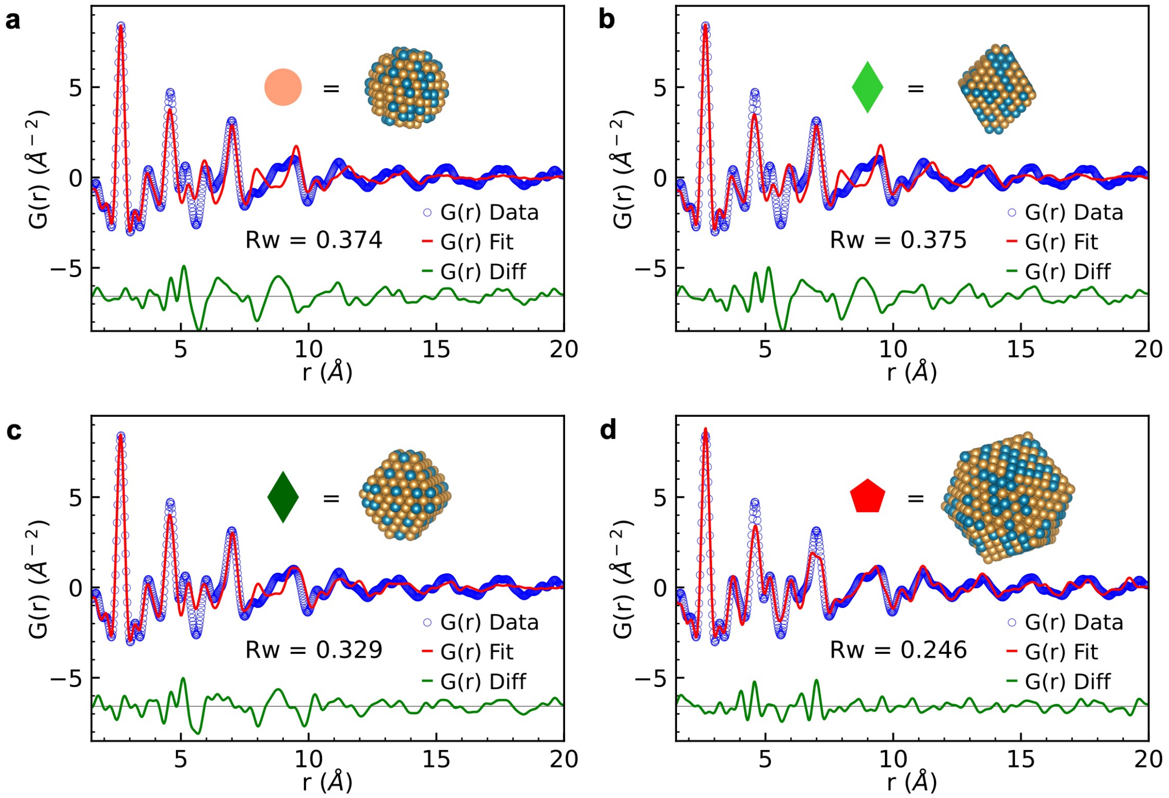

Figure S4.25: PDF fits of the best-scoring cluster models for different structural motifs. **a**) sphere (space group Fm-3m), **b**) octahedron, (space group Fm-3m), **c**) octahedron, (space group P4/mmm), **d**) icosahedron. In the insets, the respective discrete atomic structures are shown. Orange indicates Cu atoms, blue Pd atoms. All fits are performed with the standard routine for PDF fit of discrete atomic models, ie. without Monte Carlo sampling.

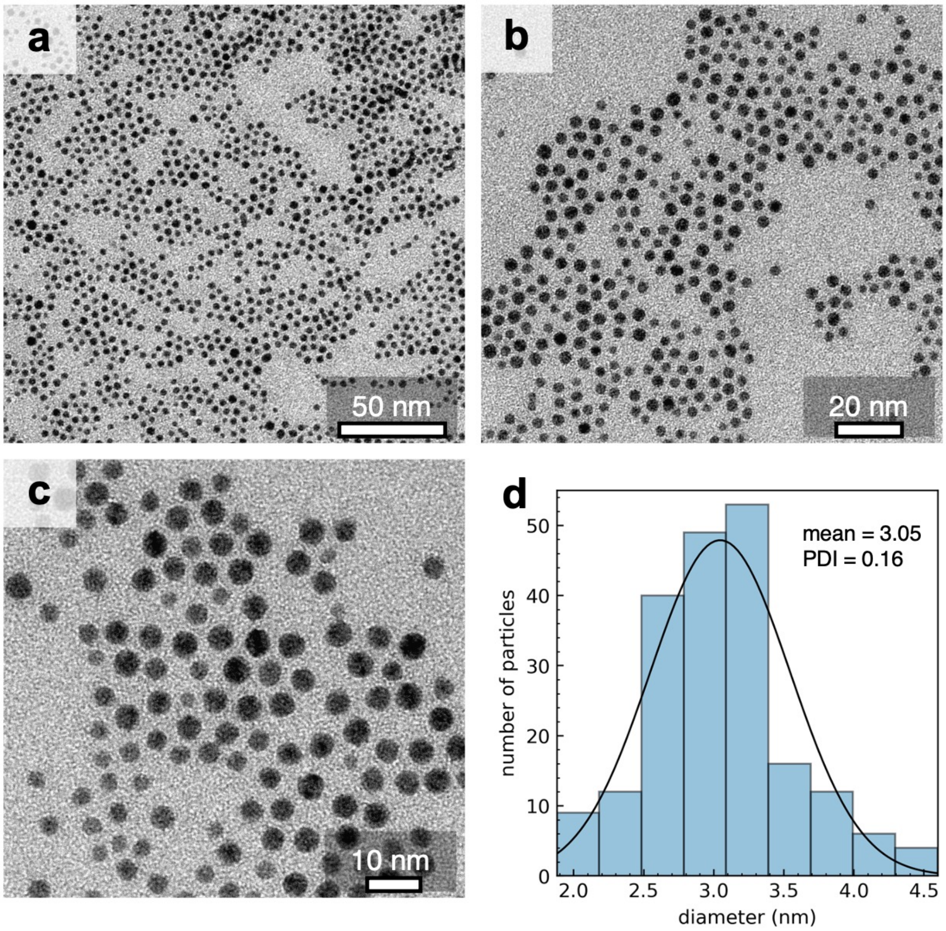

Figure S4.26: TEM analysis of the CuPd nanocrystals. a-c) TEM micrographs of the nanocrystals. **d**) Histogram of the nanocrystals diameters, determined after measurements of 200 particles. The envelope for an ideal gaussian distribution is also shown. The mean diameter determined by analysis of the TEM is 3.05 nm, with a relative polydispersity index (PDI) of 0.16.

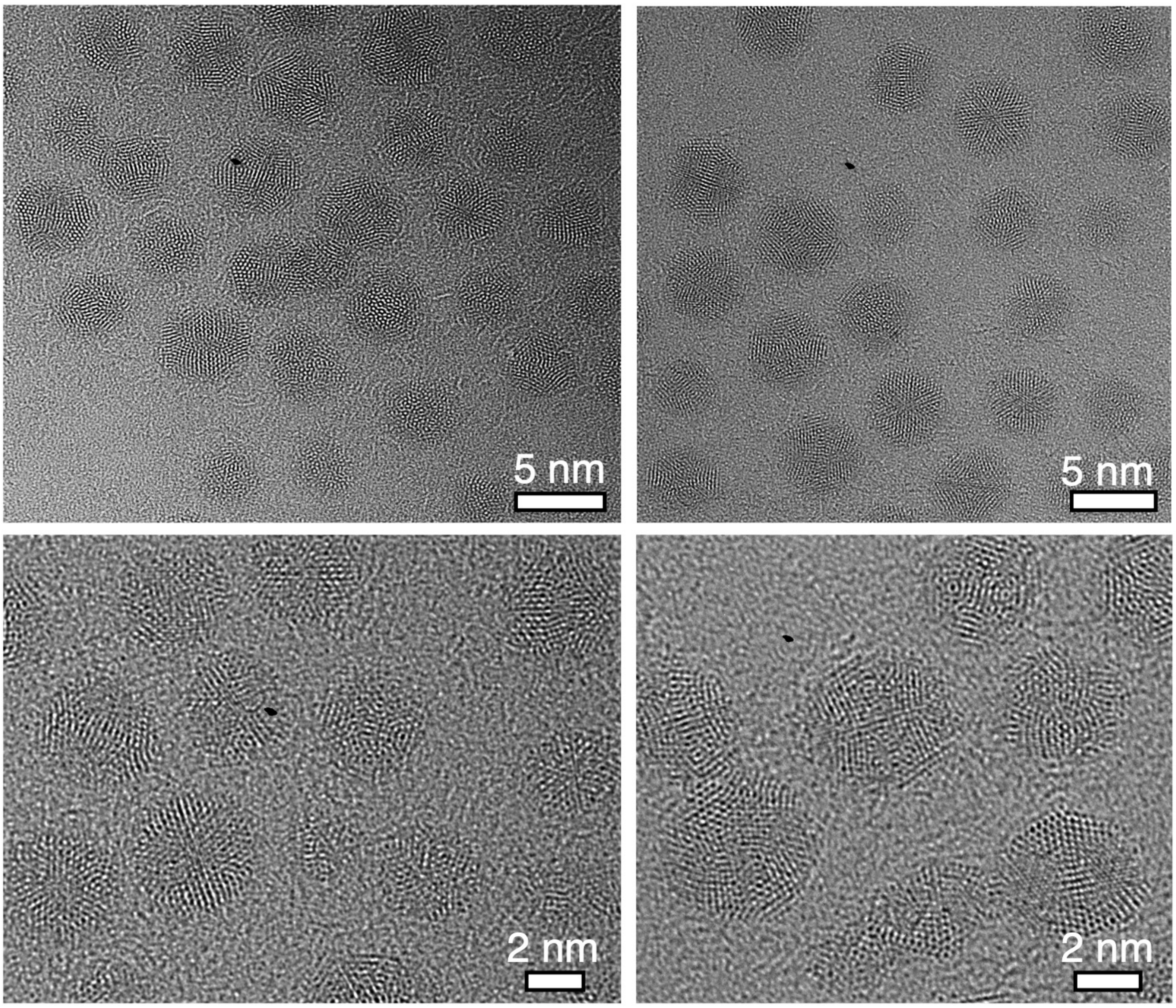

Figure S4.27: HRTEM micrographs of the CuPd nanocrystals.

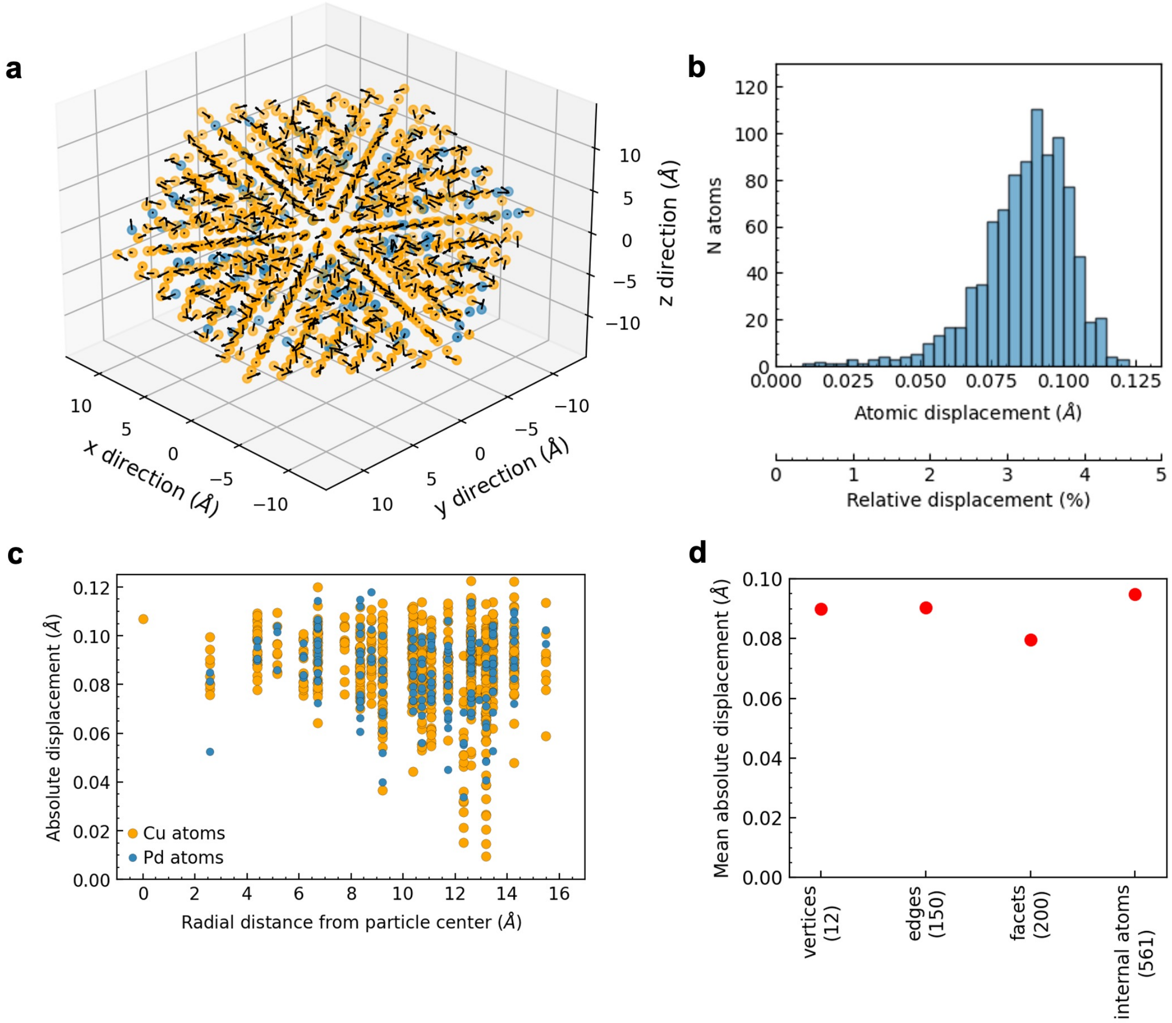

Figure S4.28: Analysis of the structural modification introduced by the Monte Carlo (MC) sampling procedure to an ideal icosahedral model. **a**) The atomic displacement for individual atoms in the structure. Cu atoms are shown in orange, while Pd atoms in blue. The vectors indicate the direction of the atomic displacement introduced by the MC sampling procedure, while their length corresponds to 10 times the absolute atomic displacement, to increased readability of the figure. **b**) Histogram of the absolute atomic displacements for individual atoms constituting the cluster model. Relative displacement values are normalized over the shortest inter-atomic distance in the original model (0.125 Å). **c**) Scatter plot of the absolute atomic displacement for individual atoms as a function of the radial distance from the center of the particle. **d**) Mean absolute atomic displacement values for atoms belonging to either vertices, edges, and facets, or for internal atoms of the icosahedron.

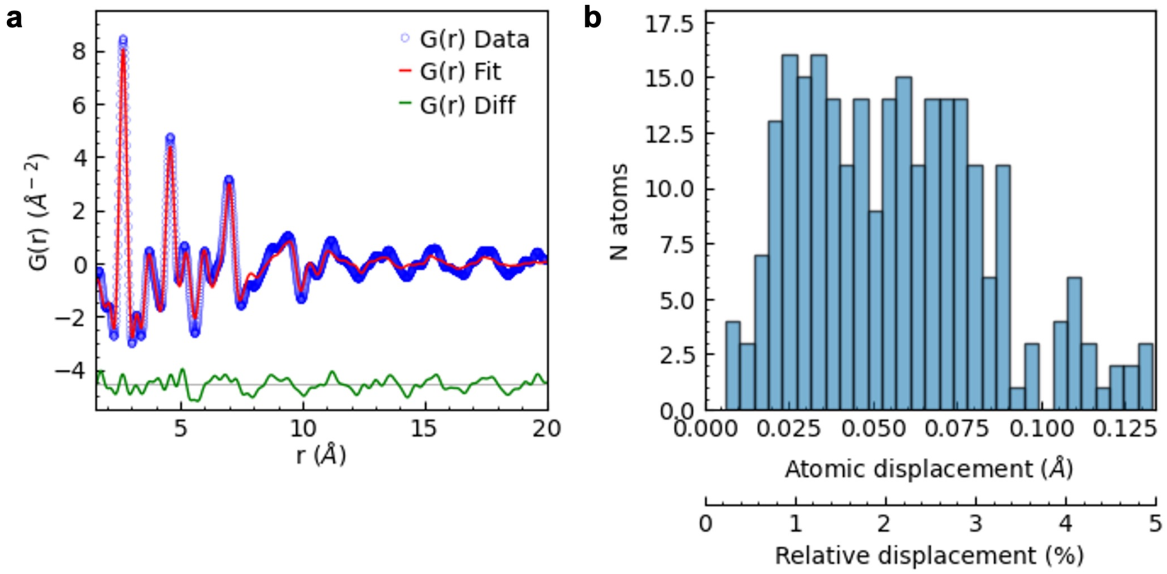

Figure S4.29: Outcome of the Monte Carlo sampling procedure for the decahedral structure. **a**) Plot of the PDF fit (Rw = 0.170). **b**) Histogram of the absolute atomic displacement for individual atoms constituting the cluster model. Relative displacement values are normalized over the shortest inter-atomic distance in the original model (0.133 Å).

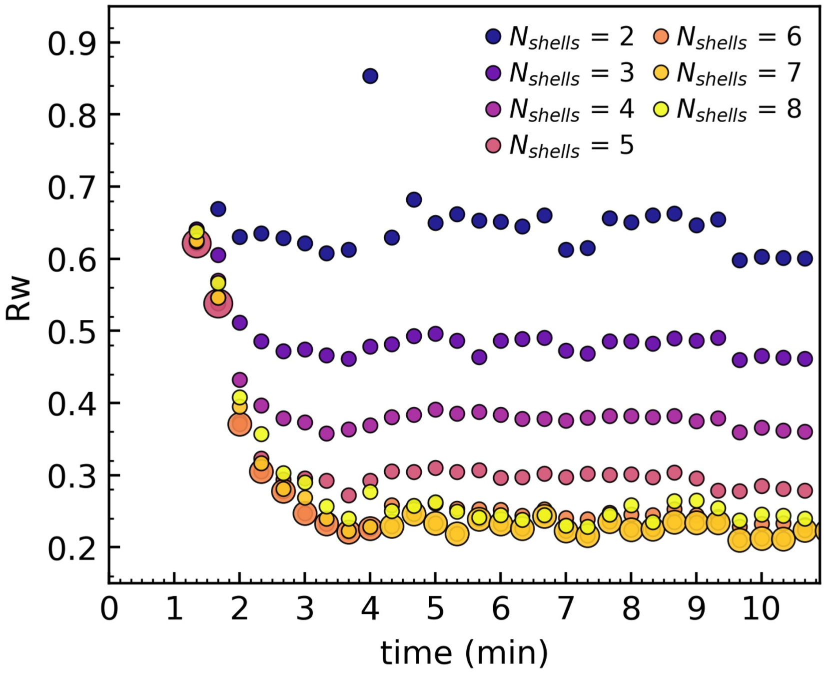

Figure S4.30: Scatter plot of the Rw values as a function of the reaction time for independent PDF fits with icosahedral models. Scatter points of different colors indicate icosahedra consisting of different number of shells (N_{shells}). At each point in time, the best fit is indicated by a scatter point of increased size. While the synthesis of the nanocrystals proceeds, icosahedra of increased number of shells provide the best fit to the in situ PDF. All fits are performed with the standard routine for PDF fit of discrete atomic models, ie. without Monte Carlo sampling.

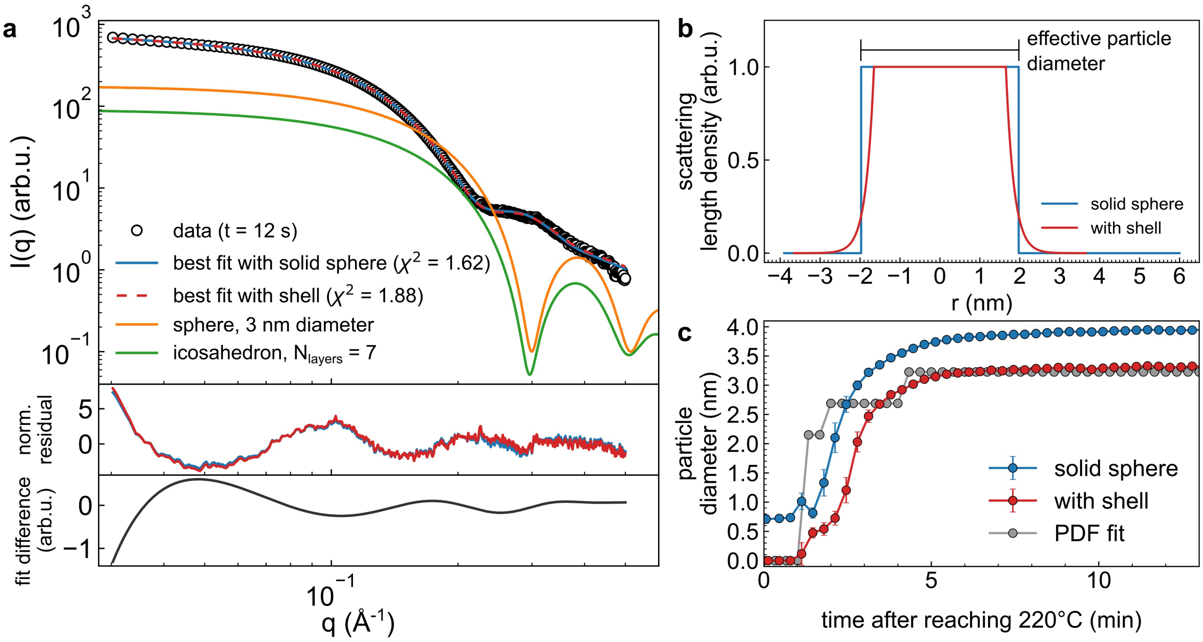

Figure S4.31: Exemplary fit of SAXS data at the end of the nanoparticle growth phase
a) Blue dashed line: Best fit using a model of solid, polydisperse spheres (mean diameter 3.95 nm, polydispersity = 0.138).

Red dashed line: best fit with an additional shell (mean core diameter 3.30 nm, polydispersity = 0.152, shell thickness $\Delta t_{\mathrm{shell}} = 1$ nm). In the middle panel the normalized fit residual is shown for both models. In the lower panel the difference of the shell model and solid sphere model is shown to emphasize the contribution of the shell.

Orange line: exemplary model curve of spheres of 3 nm diameter, i.e. of the size obtained from PDF analysis. The mismatch in intensity between the experimental data and the 3-nm model hints to the presence of an additional shell.

Green line: exemplary model curve of an icosahedral particle with N=7 layers, as found by PDF analysis.

b) The scattering length density profiles of the solid sphere and "sphere with shell" models used in **a**.

c) Plot of the mean particle diameter as a function of time as obtained by both the solid sphere model and the model with a shell (in the latter case, the diameter of the core is shown). The result of the PDF fit is given for comparison. The core diameter in the model with a shell is smaller than the effective diameter of the sphere model due to the contribution of the shell. At late times, the core size of the model with a shell closely agrees with the PDF fit results. The discrepancy at earlier times may result from an incomplete formation of the ligand shell at early nucleation stages.

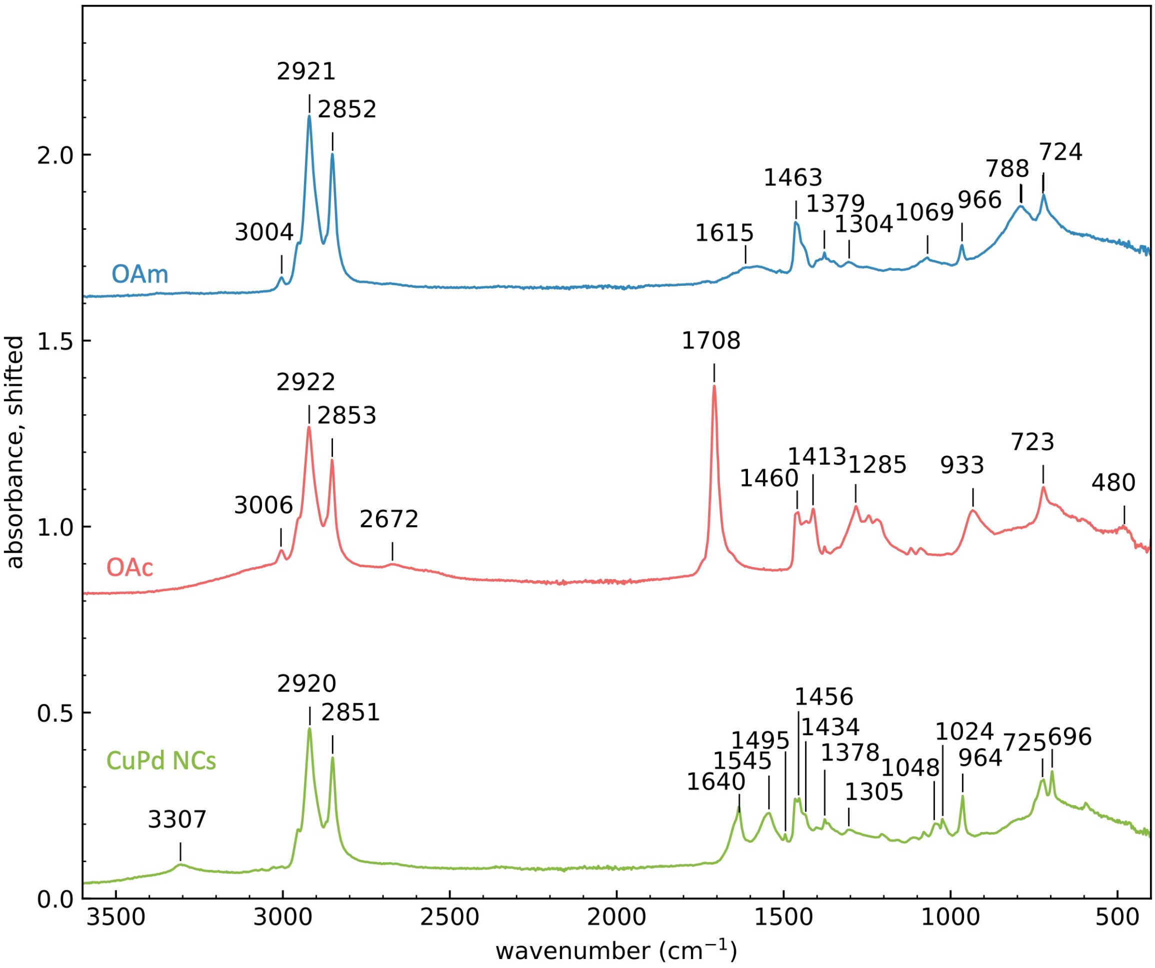

Figure S4.32: FTIR spectra on the CuPd nanocrystals (NCs) and pure oleylamine (OAm) and oleic acid (OAc) ligands The NCs underwent two centrifugation/redispersion washing cycles before FTIR measurement. In the bottom spectrum, the position of the intense absorption bands is consistent with the presence of oleylamine and oleic acid ligands adsorbed at the surface of the NCs according to[241,242].

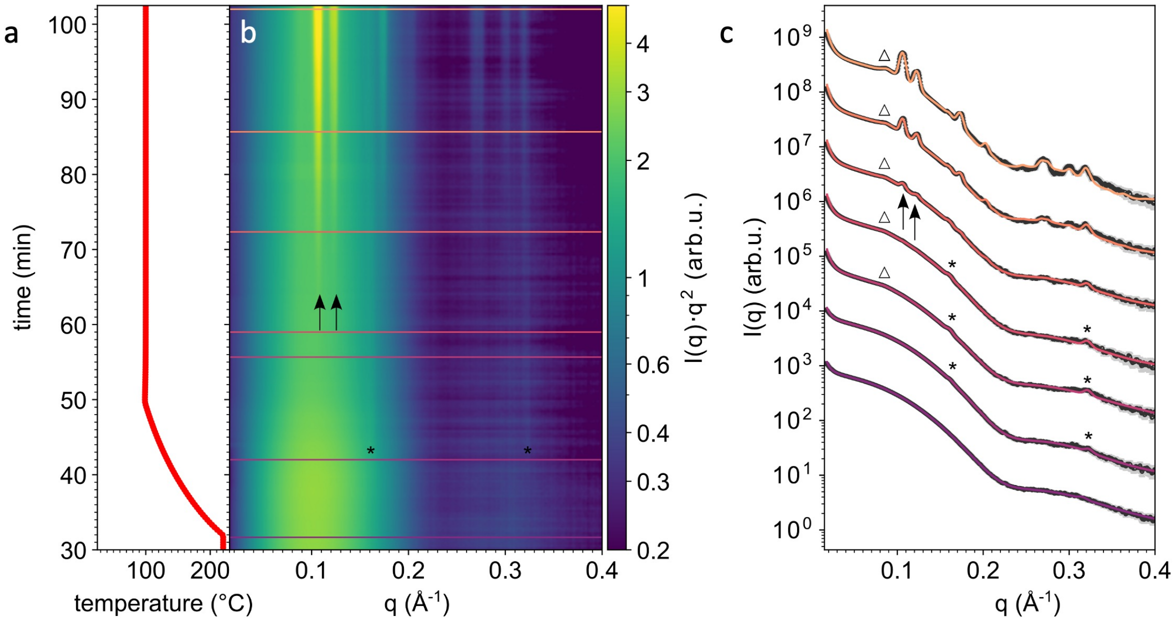

Figure S4.33: Identification of characteristic SAXS signals before nucleation of the fcc supercrystals. **a**) Plot of the temperature profile promoting the supercrystal formation within the reaction mixture. **b**) 2D representation of SAXS intensity vs. time. **c**) Selected 1D plots at the times indicated by dashed horizontal lines in **b**. Red lines in **c** are fits to the data. Asterisks (*) highlight the emergence of the lamellar phase of ca. 3.9 nm during the cooling phase. Arrows indicate the emergence of fcc supercrystals after prolonged annealing at 100 °C. The signature of SRO phase is indicated by triangles.

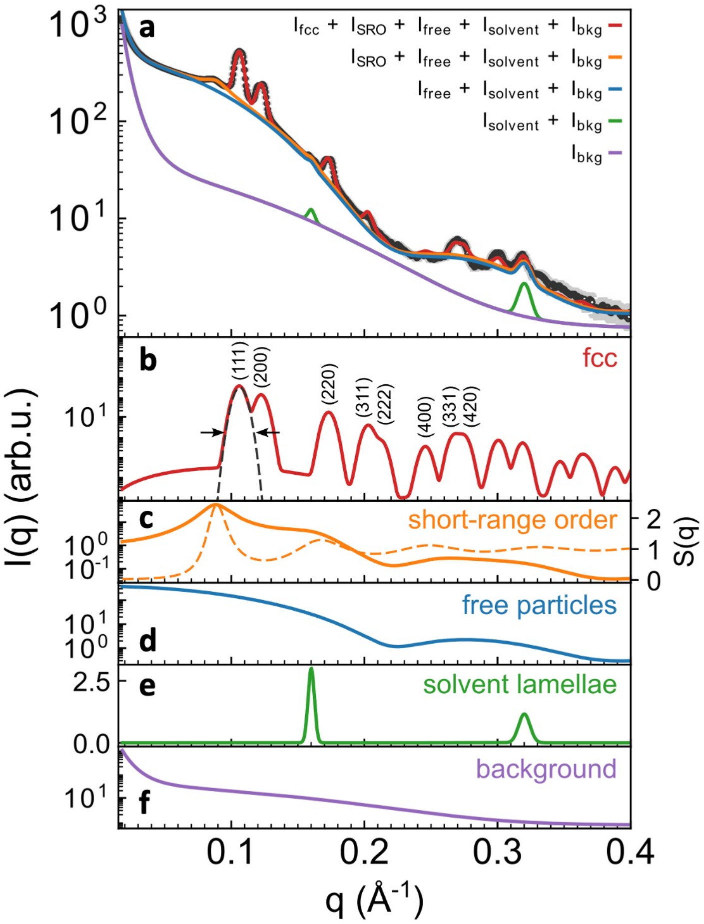

Figure S4.34: Decomposition of SAXS intensity into five distinctive components. a) Plot of the SAXS intensity at t = 102 min (dots) and of the contributions of individual components to the total intensity. **b-e**) Separate plots of the contribution of individual components to the SAXS intensity. **b**) Intensity of the fcc supercrystals. Here, selected peaks from the fcc phase are indexed. A dashed line indicates the Gaussian peak shape and the full width at half maximum of the (111) reflection. **c**) Intensity I(q) (solid line) and structure factor S(q) (dashed line) of the SRO phase. **d**) Intensity of the freely dispersed particles. **e**) Intensity of the solvent lamellae. **f**) Background intensity, modelled by a q^{-4} power law and a Guinier law corresponding to short-range density fluctuations (R_g = 1.2 nm).

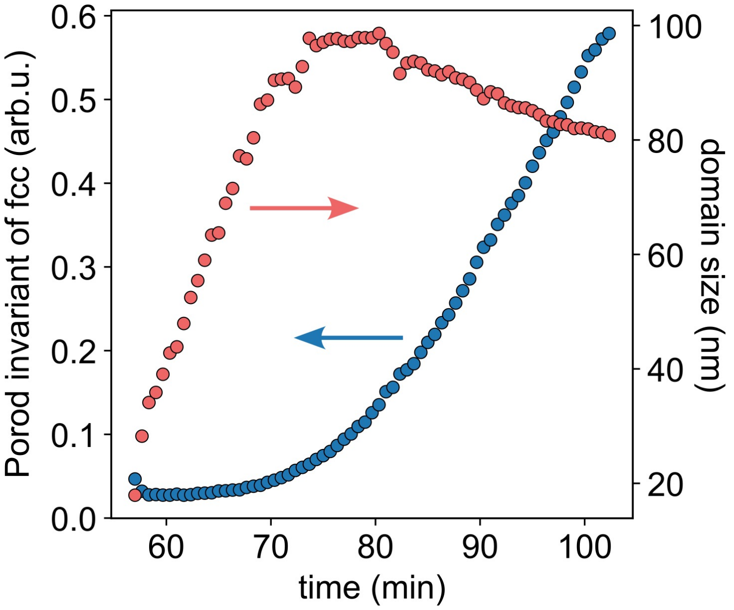

Figure S4.35: Supercrystal domain size as a function of time. Red dots: domain size ($2\pi/\text{fwhm}$) of the fcc assemblies, where fwhm is the full width at half maximum of fcc diffraction peaks as obtained from the fit. Blue dots: corresponding Porod invariant of the fcc assemblies, indicating an increase of the number of assemblies over time. The domain size reaches a maximum of at least 100 nm at ca. 75 min. This value corresponds to the maximum observable domain size due to the limit in the detector resolution. At later times we observe a slight decrease in the domain size to ca. 80 nm, which we ascribe to sedimentation of larger assemblies below the X-ray beam at the bottom of the reaction vessel. Simultaneously, the Porod invariant of fcc assemblies increases, indicating that an increasing number of nanocrystals is incorporated in the supercrystals.

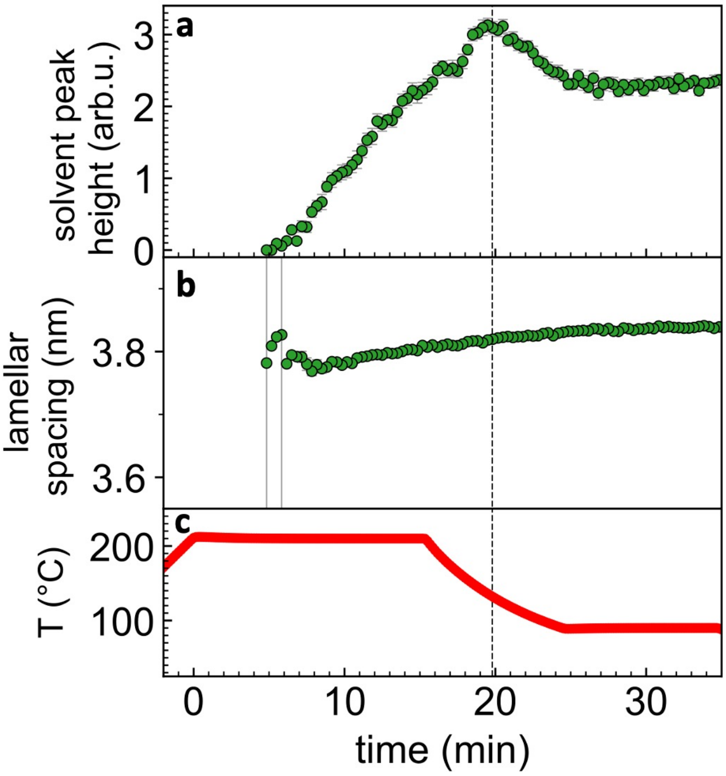

Figure S4.36: Solvent ordering in the absence of metal precursors. a-b) Peak heights and lamellar spacing ($2\pi/q$) extracted from fitting one intensity peak occurring in SAXS data of a heated solvent mixture. Oleic acid, oleylamine, and dioctyl ether are mixed in the same ratio as for the particle synthesis and subjected to the same heating/cooling ramp. **c**) Plot of the corresponding temperature profile.

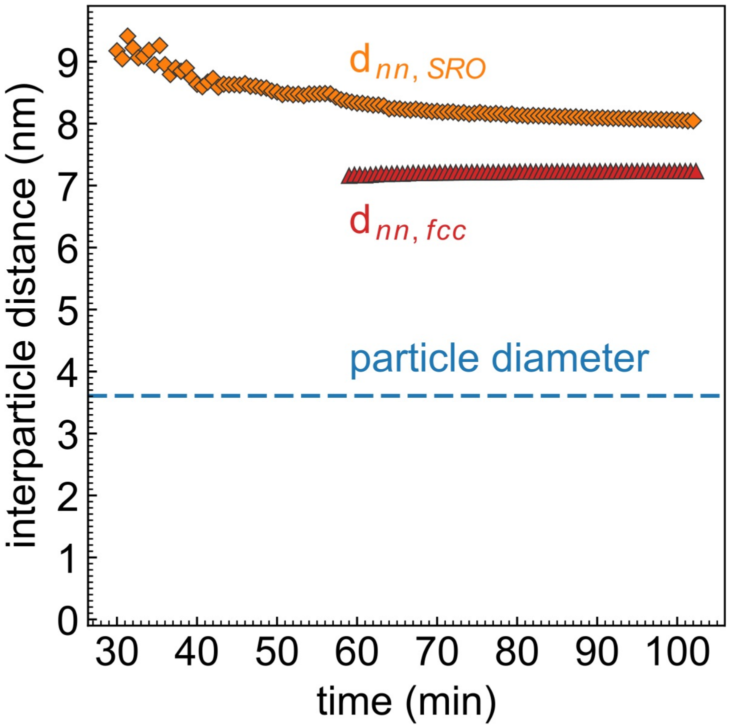

Figure S4.37: Interparticle distance in the SRO phase and in the fcc assemblies. The dashed horizontal line indicates the diameter of the nanocrystal inorganic core, as obtained from a PDF fit.

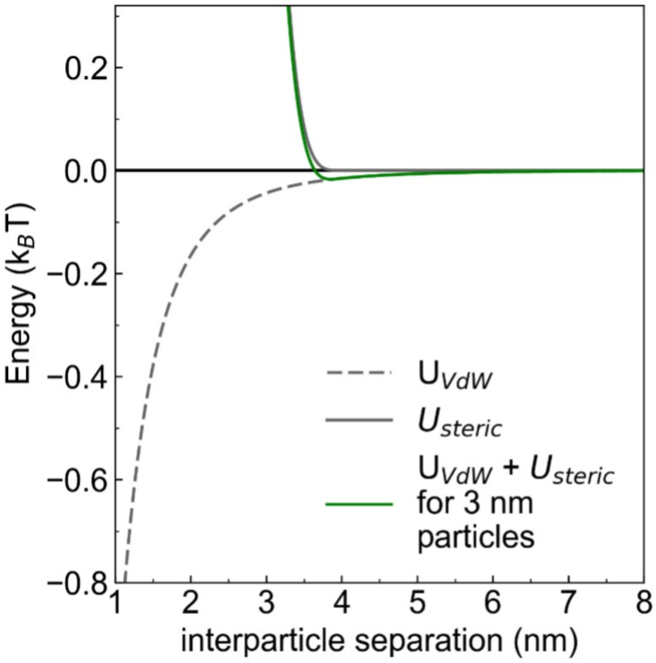

Figure S4.38: Estimated pairwise interaction potential of CuPd nanocrystals. The interaction potential between two nanocrystals is estimated as a sum of the core-core attraction due to van der Waals force and the steric repulsion due to the ligand shells. The overall potential displays a very shallow minimum of -0.02 k_BT at a surface-to-surface separation distance of 3.9 nm.

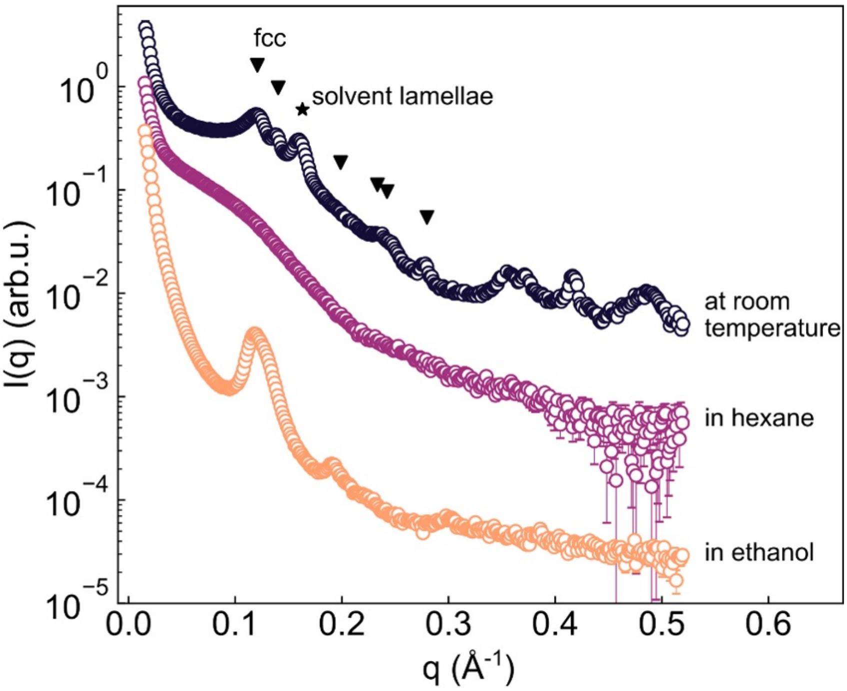

Figure S4.39: Plot of the SAXS profiles after dilution of the supercrystals in different solvents. Dots: In-house ex situ SAXS intensities of CuPd samples before and after redispersion in different solvents at room temperature. In hexane, the fcc supercrystals and solvent lamellae are fully dissolved and the SAXS intensity corresponds to the signal of free particles. Nanocrystal agglomerates are still present in ethanol, but the characteristic long-range order of fcc supercrystals is not preserved.

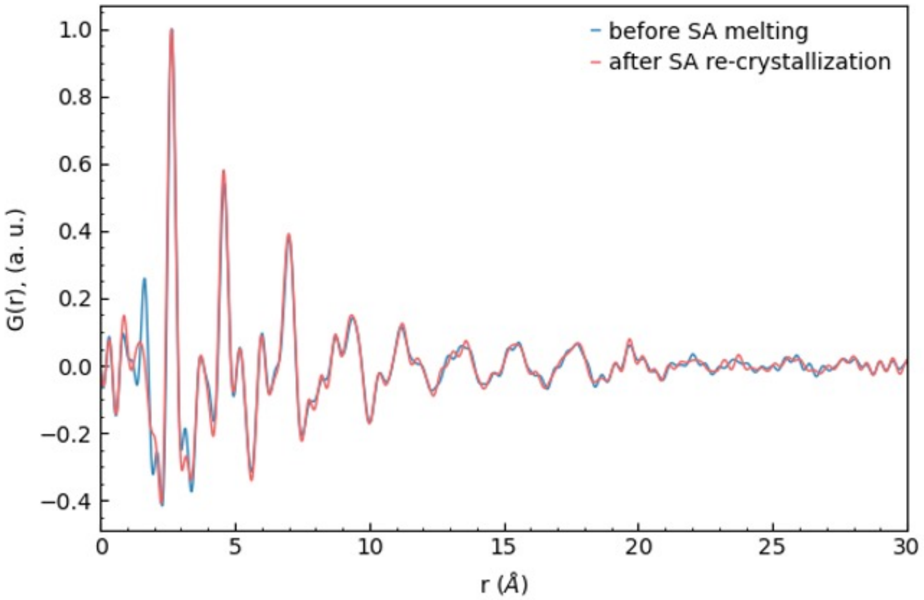

Figure S4.40: Comparison of PDF before melting and after re-crystallization of the supercrystals. The two curves are in very close agreement, showing that the structure of the icosahedral metallic cores is not affected by melting and recrystallization of the supercrystals. The small deviations in the peak widths below 2.5 Å appear at shorter distances than any spacing between the metal atoms in the nanocrystals and originate from the slightly different background subtraction.

4.4 Elucidating the photodegradation of $CuBi_2O_4$ films by operando surface-sensitive X-ray scattering

The content of this section was published in Angew. Chem. Int. Ed. 62, e202307948 (2023).
My contribution to this work compromises the realization of the operando X-ray scattering measurement, the analysis of the TS-PDF data, the SAED characterization, and the analysis of the ICP-MS measurements.

In this section of the Results and Discussion we extend our scope to investigate the photocorrosion of PEC-active $CuBi_2O_4$ films via a multi-modal X-ray scattering approach. By use of SCOPE cell, we acquire both TS and SAXS, and at the same time measure the PEC response of the electrode under applied bias and illumination, as illustrated in **Figure 4.30a**. The simultaneous acquisition of TS and SAXS permits to reveal transformations in both the atomic structure and morphology of the electrode, and to correlate such transformations with a decrease in the material photoactivity. We further complement the operando X-ray scattering with ex situ measurements, including XANES, electron microscopy, and inductively coupled plasma mass spectroscopy (ICP-MS). Overall, our results reveal that multiple degradation pathways affect the stability of $CuBi_2O_4$ electrodes under operation, as summarized in **Figure 4.30b-d**.

4.4.1 Morphological and photo-electrochemical characterization of $CuBi_2O_4$ electrodes

Figure 4.31a-b shows the cross-section SEM image for the $CuBi_2O_4$ electrodes used in this study. The films display a polycrystalline porous morphology consisting of partially sintered particles forming a reticulated nanostructure, similarly to other $CuBi_2O_4$ films previously reported.[145,263,264] During the fabrication of films, considerable efforts were dedicated in the production of films with a high morphological homogeneity and surface smoothness. In fact, the realization of smooth film is a pre-requisite to the performance high-energy X-ray scattering measurements with enhanced surfaced sensitivity, as demonstrated in Section 4.1.3.2. We find that many factors during the preparation

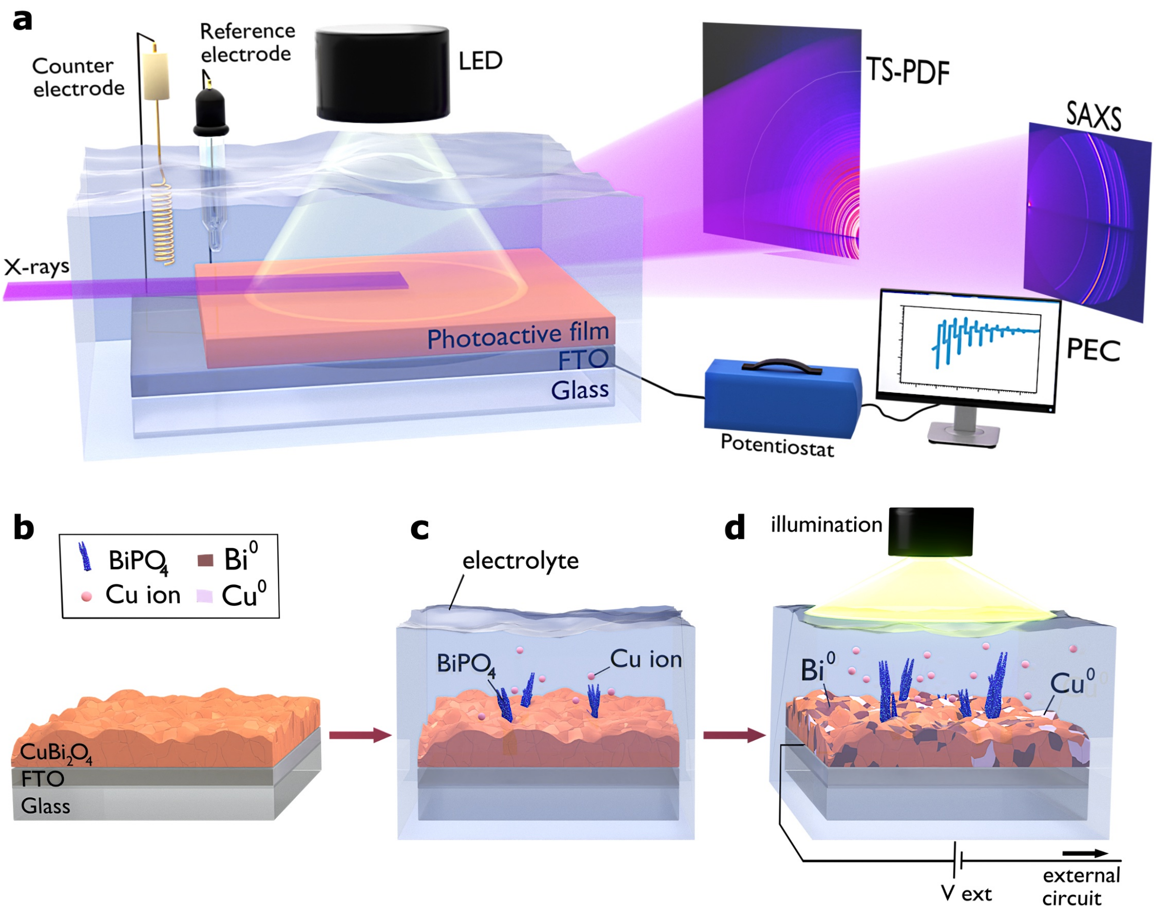

Figure 4.30: Overview of the operando photo-electrochemical setup and of the main findings related to the photocorrosion of $CuBi_2O_4$ electrodes. a) Schematic illustration of the multi-modal experimental setup. The PEC properties of a photoactive thin film under illumination and immersed in an electrolyte solution are probed by use of a potentiostat in a standard 3-electrode configuration. Two large-area X-ray detectors permit the simultaneous measurement of both TS and SAXS signals from the film surface in a grazing incidence geometry. **b-d**) A schematic illustration of the structure of a pristine $CuBi_2O_4$ electrode (**b**) deteriorating due to simple immersion in the electrolyte (**c**), and under illumination and external bias (**d**).

routine, such as the grade of the FTO-coated substrate, the spinning speed used during the spin-coatings, the temperature profile of the thermal treatments, and the nature of the additive, largely influence the final morphology of the films. These affects have been already reported elsewehere.[137,265] The optimized fabrication procedure is described in Section 3.3.4.

We characterize the PEC activity of the $CuBi_2O_4$ by LSV measurements and by using either a solar simulator or a 385 nm LED source. We employ a sulfate-phosphate electrolyte at pH 5.7. This electrolyte solution constitutes a standard in the case of Cu-

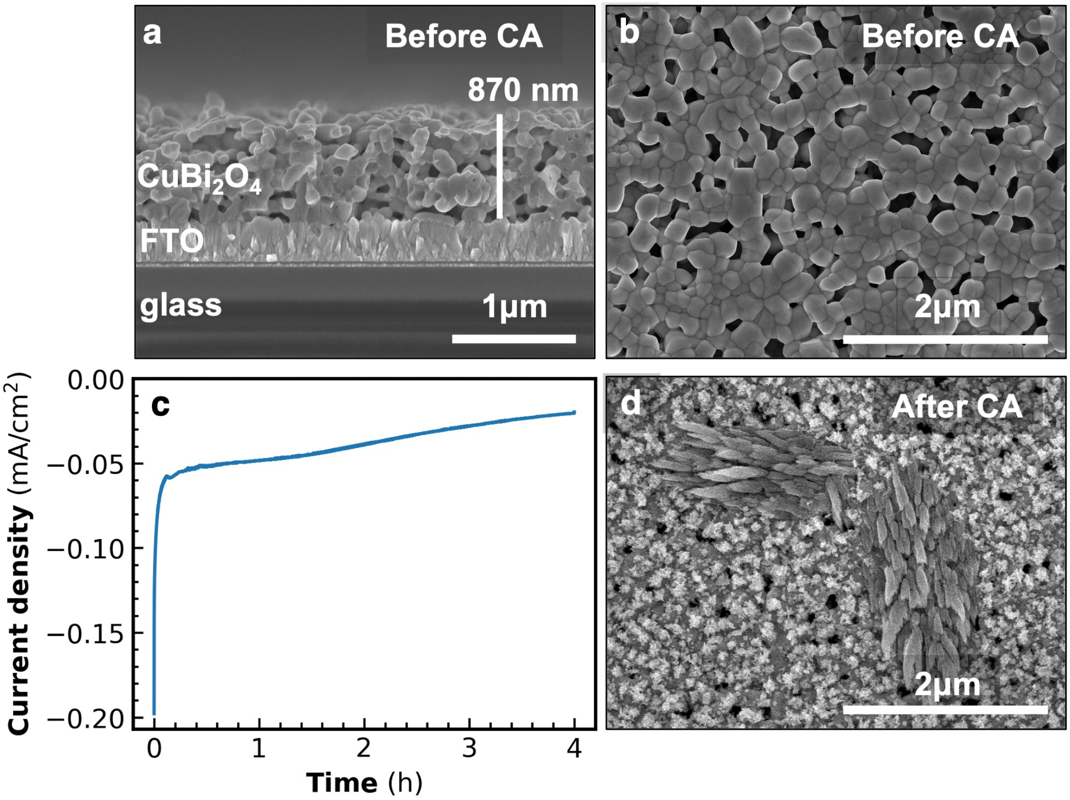

Figure 4.31: Morphological characterization of $CuBi_2O_4$ electrodes before and after operation. a-b) Cross-section (**a**) and top-view (**b**) SEM images of the $CuBi_2O_4$ films deposited on a FTO substrate. **c**) Long-term CA measured at 0.45 V vs. RHE under 375 nm LED illumination. **d**) SEM image of the $CuBi_2O_4$ surface after the CA measurement shown in **c**.

based photocathodes, which are generally unstable in acidic solutions.[139,266,267] The plot of the LSV scans is shown in **Figure 4.10**. Under solar illumination, the LSV profiles display an onset potential of 0.95 V vs. RHE and cathodic photo-currents of ca. 200 μA cm^{-2} at 0.3 V vs. RHE, in line with previously reports.[145,263,268] In **Figure 4.10b** the larger photo-absorption cross section at 385 nm allows to record higher photocurrents compared to the ones obtained using a solar simulator.

To test the stability of the $CuBi_2O_4$ electrode under continuous operation, we measure a long CA under LED illumination (**Figure 4.31c**). For the measurement, we select an external bias of 0.45 V vs. RHE, since at this potential we observe the highest electrode photoactivity while the dark current densities are negligible, as revealed by LSV. The CA shows that the photoactivity of the electrode largely reduces over time. In **Figure 4.31d**, SEM imaging of the electrode surface after 4h of CA reveals the appearance of nanoparticles of high electron-contrast, as well as the formation of micro-sized branched structures. The measurement thus proves that the $CuBi_2O_4$ undergoes severe photocorrosion process during prolongues continuous operation.

4.4.2 Ex situ characterization of the photocorrosion of $CuBi_2O_4$ electrodes

We measure ex situ surface-sensitive X-ray scattering to reveal the structural changes affecting $CuBi_2O_4$ films after their photodegradation. We investigate two electrodes which were treated with either a 24 h immersion in the electrolyte solution and in the absence of applied bias, or with a 4 h CA at 0.5 V vs RHE and under illumination. In **Figure 4.32a** the respective TS patterns are compared against a pristine $CuBi_2O_4$ film pattern. For the treated electrodes, we observe the emergence of a hydrated crystalline $BiPO_4$ phase (space group $P3_121$), which clearly forms even without applied bias and in the dark by a prolonged immersion of the electrode in the electrolyte. The electrode treated with the CA additionally displays intense Bragg's reflections characteristic of metallic Bi (space group R-3m) as well as traces of metallic Cu phase (space group Fm-3m), both as a result of cathodic photocorrosion.

In **Figure 4.32b** we show the detected concentration of Cu and Bi anions in the electrolyte as revealed by ICP-MS. We determined a steady increase in the concentration of Cu species in solution both before and during the CA. However, no Bi ions could be detected in the electrolyte at any stage of the PEC measurement. While ICP-MS does not provide information over the oxidation state of the detected Cu species, the Pourbaix diagram of Cu indicates that the most stable copper species at the electrolyte pH of 5.7 and the OCP potential of the $CuBi_2O_4$ electrode is Cu^{2+}.[147]

We perform cross-section SEM imaging and EDX mapping to reveal the composition of the branched micro-sized structures growing on the film surface during CA (**Figure 4.32c**). Although the EDX measurement shows that these micro-structures are P-rich, the high contribution of the background to the EDX signal does not allow to determine the element distribution with sufficient accuracy. We therefore transfer one of the branched structures shown in **Figure 4.32c** to a carbon-coated gold grid and record the TEM and

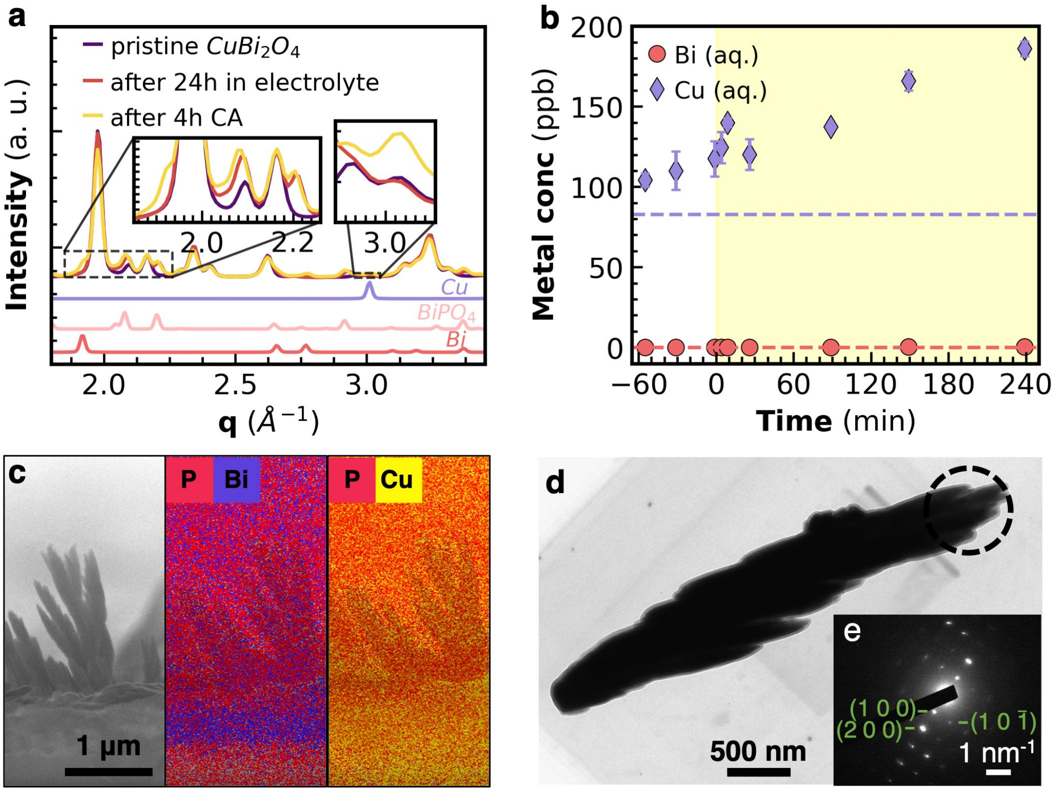

Figure 4.32: Ex situ determination of the degradation of $CuBi_2O_4$ electrodes. **a**) Plot of the scattering signal from a pristine $CuBi_2O_4$ electrode (purple) and after either 24h immersion in the electrolyte (red) or 4h CA (yellow). In the inset, zoomed regions of the same plots. **b**) Time-resolved plot of the Bi (red circles) and Cu (pink rhombi) ion content of an electrolyte solution in contact with a $CuBi_2O_4$ electrode as revealed by ICP-MS measurements before and during the CA. Dashed lines indicate the respective ion content determined for the pure electrolyte solution before immersion of the film. The yellow patch highlights the times at which we conducted the CA measurement, which we started at time = 0 min. **c**) Cross-sectional SEM image of the electrode surface after 4h CA. The EDX maps for either the P and Bi or P and Cu elements are also shown. **d**) TEM image of a single branched micro-structure isolated from the $CuBi_2O_4$ surface after 4h CA. The dotted patch highlights the area of the specimen used to perform SAED. **e**) The corresponding SAED pattern displaying the diffraction peaks of BiPO4 phase (space group $P3_121$).[269]

selected-area electron diffraction (SAED) data in **Figure 4.32d-e**. Indexing of the SAED pattern clearly demonstrates that the branched structure consist of a highly crystalline $BiPO_4$ phase.

We measure ex situ XANES at the Cu K-edge to confirm the formation of metallic Cu in the electrode after CA. In **Figure 4.33a**, the XANES spectrum obtained from the $CuBi_2O_4$ film after CA displays subtle differences compared to the spectrum of the pristine electrode. In **Figure 4.33b-c** we use a linear-combination analysis (LCA) to reveal the presence of 1.5 % and 12 % of metallic Cu in the $CuBi_2O_4$ film after 1h and 4h of CA, respectively.

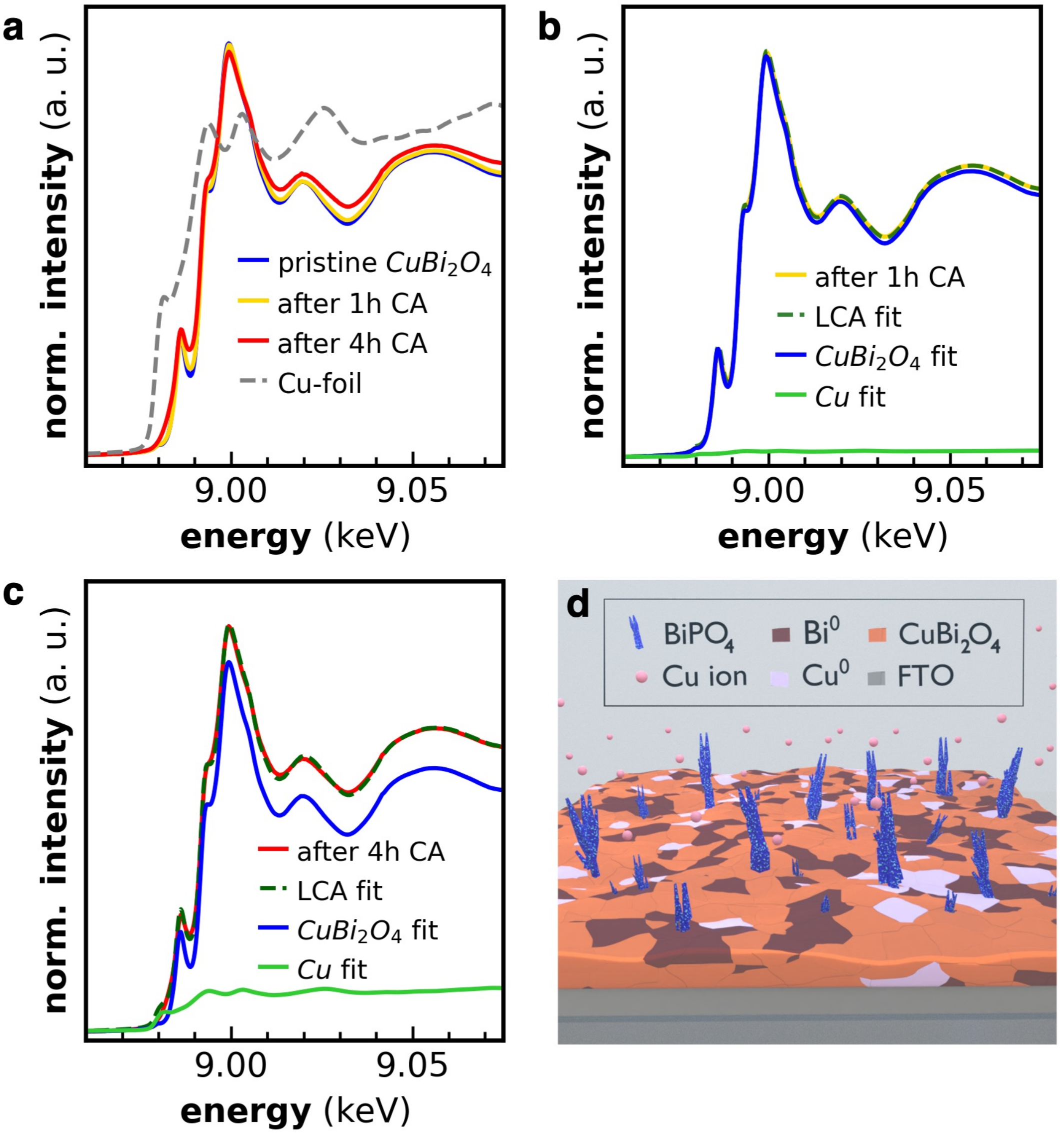

Figure 4.33: Determination of the metallic Cu content before and after CA by Cu K-edge XANES measurements and summary of the ex situ findings. a) Ex situ XANES spectra measured at the Cu K-edge for a series of $CuBi_2O_4$ electrodes before and after CA. The spectrum for a pure Cu foil is shown for reference. **b**) LCA fit of the XANES spectrum after 1h CA by use of a Cu foil and a pristine $CuBi_2O_4$ electrode as references. The analysis determines a 1.5 % content of metallic Cu in the electrode after CA. **c**) Same as **b**, for a $CuBi_2O_4$ electrode after 4h CA. The content of metallic Cu is 12 % of the total Cu-species in the electrode film. **d**) Schematic illustration of the various morphologies and phases present on a $CuBi_2O_4$ after CA as revealed by the ex situ characterization.

To further understand the photodegradation phenomena affecting the material, we perform additional stability measurements under a range of different experimental conditions and measure in-house XRD patterns of the electrodes before and after the PEC measures, as reported in **Figure S4.41**. **Figure S4.41 a-b** demonstrates that when the CA is carried out either in the dark (0.5 V vs RHE) or under illumination at the OCP (1.125 V vs RHE), low current densities are measured and the emergence of metallic Bi is not observed. In **Figure S4.41c** we show that the absence of the phosphate buffer in the electrolyte prevents the formation of $BiPO_4$ during the CA. Additionally, we verify that the use of H_2O_2 as an electron-hole scavenger in the electrolyte inhibits the formation of both the metallic Bi and $BiPO_4$ phases (**Figure S4.41d**).

Figure 4.33d schematically illustrates the chemical and structural modifications affecting the $CuBi_2O_4$ electrode in the sulfate/phosphate electrolyte. Overall, the ex situ characterization demonstrates that under applied external bias and illumination the $CuBi_2O_4$ film reduces to metallic Cu and Bi. Moreover, $BiPO_4$ structures grow on the semiconductor surface and the material releases Cu ions in solutions. However, the ex situ investigation provides limited information over the time scales and dynamics of the photocorrosion process. In the next section, we will therefore extend our study to monitor the structural transformations affecting the surface of the $CuBi_2O_4$ electrode via operando X-ray scattering.

4.4.3 Operando high energy X-ray scattering studies during chronoamperometry

We record simultaneous TS and SAXS during CA at an angle of incidence $\alpha_i = 0.025°$ and concurrently measure the $CuBi_2O_4$ electrode activity, as shown in **Figure 4.34**. Under applied illumination and bias, we immediately observe a rapidly decreasing intensity of the characteristic reflections for $CuBi_2O_4$ phase in the TS signal. Simultaneously, we observe a new feature at q = 1.92 $Å^{-1}$, which corresponds to the (012) reflection of metallic Bi. During the first 40 minutes, we observe neither formation of $BiPO_4$ nor Cu. Although ex situ XANES already revealed the formation of Cu after operation, we ascribe the lack of evidence of reduced Cu from the X-ray scattering to its limited overall

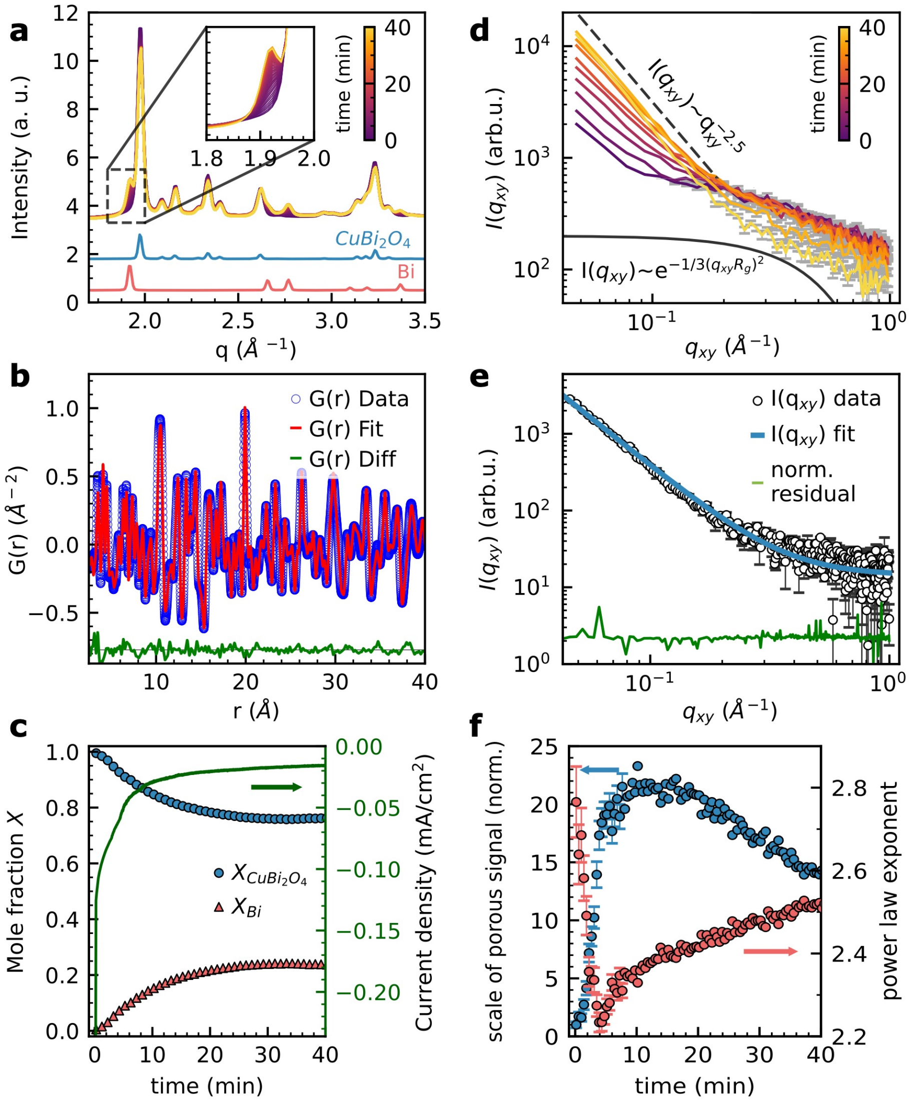

Figure 4.34: Operando studies on the photodegradation of $CuBi_2O_4$ a) Time-resolved plot of the operando X-ray scattering signal collected from the surface of a $CuBi_2O_4$ during CA. In the inset, a zoom into the 1.8-2.0 Å^{-1} region highlights the formation of metallic Bi over time. **b**) Fit of the operando PDF obtained after 40 min of CA by two-phase refinement. A red line indicates the fit, blue circles the experimental data, and a green line the residual between the two. **c**) Evolution of the relative amounts of the $CuBi_2O_4$ (blue circles) and Bi (red triangles) phases during the CA measurement as obtained from the PDF fit. The change in the measured current density over time (green curve) is additionally shown. **d**) Time-resolved plot of the operando GISAXS in-plane signal during the CA. The dashed line indicates the power law $q_{xy}^{-2.5}$, while the solid black line shows the Guinier law representing the background signal of small structures (< 0.5 nm) at early times. **e**) Fit of the GISAXS in-plane signal obtained after 40 min of CA. The normalized residual is shown in green. **f**) Evolution of the scale and exponent of the power law obtained by fit of the operando GISAXS in-plane signal during CA.

content and the relatively small scattering cross-section of Cu atoms compared to Bi.

To quantify the respective contribution of the $CuBi_2O_4$ and Bi phases, we Fourier transformed the TS signal into the PDF and fit the data by use of a two-phase model compromising a $CuBi_2O_4$ and a Bi phase within the AC approximation. The time-resolved structural parameters determined by PDF are reported in **Figure S4.42**. **Figure 4.34b** shows an exemplar fit of the PDF data after 40 minutes of CA. Our model provides a very good fit to the experimental data with a R_w value of 0.110, while the difference curve does not indicate the presence of any additional amorphous or locally-ordered phase. We compared the signal from the spot exposed to the X-rays during the operando measurement to a previously unexposed spot and observe similar structural changes (**Figure S4.43**). Therefore, we can exclude that the Bi formation was induced by the X-ray beam. Interestingly, the appearance of a Bi phase correlates with the decay in measured photocurrent density during the CA, as shown in **4.34c**. In the first 8 minutes, the photocurrent density rapidly decreases by almost one order of magnitude from around -0.20 mA/cm^2 to just -0.03 mA/cm^2. Simultaneously, a reduced Bi phase forms and rapidly grows to constitute 12% of the total detected material. After 30 minutes, the photocurrent density reaches a plateau at -0.015 mA/cm^2 and the fraction of Bi concurrently saturates to 24%.

In addition to quantifying the crystalline composition of the film via PDF analysis, we probe the change of nanoscale morphology during CA by simultaneous GISAXS. **Figure 4.34d** shows the time-resolved in-plane GISAXS intensity, $I(q_{xy})$, from which structural features along the electrode-electrolyte interface are determined.[270] We fit the time-resolved intensities with a power law decay and further model an additional background arising from small structures (<0.5 nm) by a Guinier law. **Figure 4.34e** shows a representative fit to the data and **Figure 4.34f** the evolution of structural parameters. The exponent n of the power law q^{-n}, obtained from the fit, measures the ruggedness or dimensionality of the surface.[172] During the CA, n varies between 2 and 3, which are typical values for porous interfaces probed at low q.

In the first 8 minutes of operation the scale of the porous signal quickly increases and reaches a maximum after 20 min, thus indicating that the bulk porosity increases during the initial stage of CA. This result likely comes from the consumption of $CuBi_2O_4$

electrode material and the growth of small metallic Bi deposits. After a steep decline at the beginning of the CA, the exponent n slowly increases, indicating that the contribution of compact deposits to the total GISAXS signal becomes increasingly dominant at intermediate and later stages of the measurement. This behavior likely results from the onset of $BiPO_4$ deposition at the surface of the electrode, which leads to a local increase of the surface compactness. The value of n does not saturate at 40 min, suggesting that the restructuring of the surface may further extend to later times.

4.4.4 Overview of the photocorrosion mechanisms affecting $CuBi_2O_4$ electrodes

Our operando X-ray scattering experiments, together with ex situ XANES, ICP-MS, and electron microscopy, allow us to outline the reaction pathways and respective time scales for the photocorrosion of $CuBi_2O_4$ films during PEC operation, as schematically illustrated in **Figure 4.35**. In the scheme, we do not include the HER since previous studies have already demonstrated that bare $CuBi_2O_4$ electrodes do not promote the reduction of water in the absence of co-catalysts.[146]

We found that the abrupt drop of the photocurrents occurring during the first few minutes of the CA tests (**Figure 4.31c** and **Figure 4.35c**) is dominated by the consumption of $CuBi_2O_4$ and the concurrent formation of metallic Bi at the surface of the electrode. This results from a cathodic photocorrosion process, in which the photogenerated electrons are consumed for the reduction of lattice Bi^{3+} ions into Bi^0 species which segregates and crystallizes as a metallic Bi phase (eq. 4.4):

$$\text{cathodic photocorrosion } (\textit{fast})\text{: } Bi^{3+} + 3e^- \leftrightharpoons Bi^0 \qquad \text{(eq. 4.4)}$$

$$(e^- = \text{photogenerated electron})$$

The quick formation of metallic Bi is not limited by use of a LED illumination but was also determined for a $CuBi_2O_4$ electrodes undergoing CA under simulated solar radiation (**Figure S4.44** and **Table 4.2**). The cathodic photocorrosion of Cu^{2+} ions to metallic Cu^0 is also observed, but proceeds at a much slower rate, as evidenced by the ex situ X-ray scattering and XANES measurements (eq. 4.5):

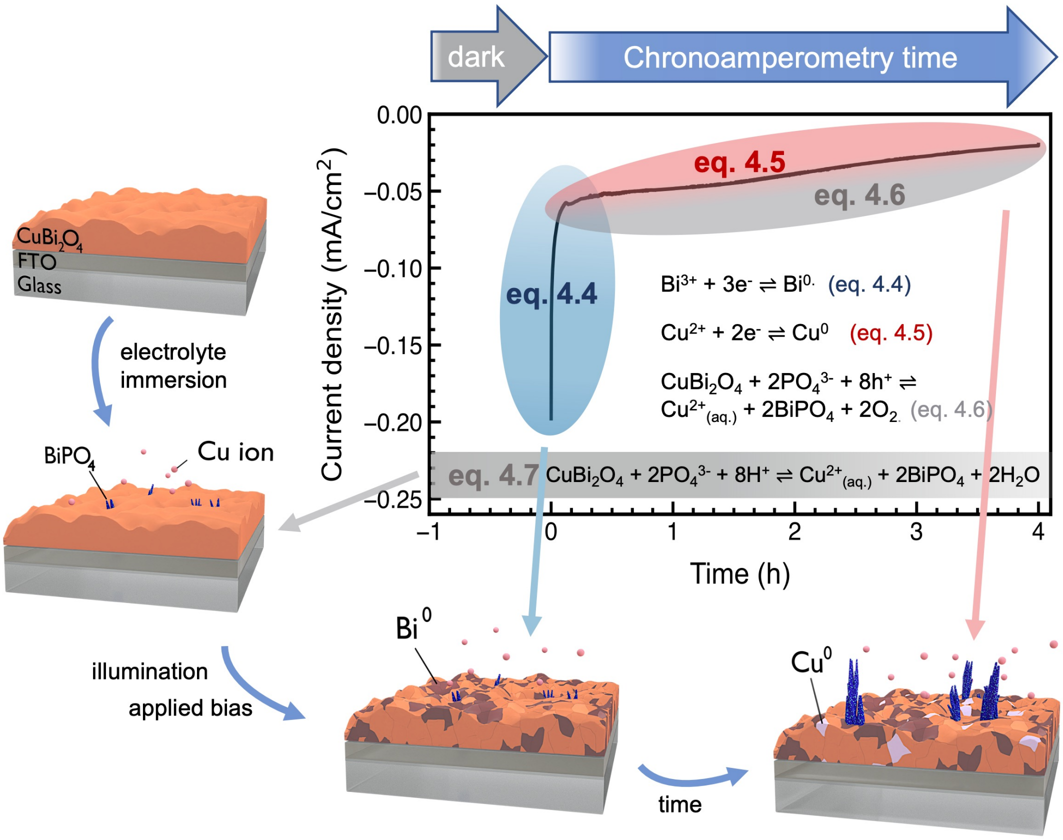

Figure 4.35: Schematic illustration of the multiple reaction pathways and relative timescales determining the degradation of $CuBi_2O_4$ electrodes both before and during a CA measurement.

$$\text{cathodic photocorrosion } (\textit{slow}):\ Cu^{2+} + 2e^- \leftrightharpoons Cu^0 \qquad \text{(eq. 4.5)}$$

Therefore, we ascribe the fast drop in photocurrents at early stages during the CA to the presence of metallic Bi which massively reduces the $CuBi_2O_4$ surface area in direct contact with the electrolyte. The ICP-MS investigation, electron microscopy characterization, and ex situ X-ray scattering reveal the release of Cu^{2+} ions into the electrolyte and the formation of $BiPO_4$ at the surface of the $CuBi_2O_4$ films both in the presence or absence of applied bias and illumination. Under light, these results can be rationalized as outcoming from an anodic photocorrosion process, as photogenerated holes which are not collected at the back contact of the electrode can convert O^{2-} ions from the lattice into O_2 molecules and concurrently release metal ions in the solution (eq. 4.6). While the Cu^{2+} are effectively released into the electrolyte, the Bi^{3+} cations quickly react at the electrode-electrolyte interface with the solvated PO_4^{3-} anions, determining the formation of $BiPO_4$ crystalline structures.

anodic photocorrosion: $CuBi_2O_4 + 8h^+ + 2\ PO_4^{3-} \leftrightharpoons Cu^{2+} + 2BiPO_4 + 2O_2$ (eq. 4.6)

(h^+ = photogenerated hole)

Although anodic photocorrosion is a common degradation process for n-type semiconductors, it has also been observed for p-type semiconductors of poor hole transport properties,[271] including $CuBi_2O_4$.[272] In this work, we show that this process is inhibited when a hole scavenger such as H_2O_2 is present in the electrolyte (**Figure S4.41d**).
Finally, the presence of a mildly acidic environment might also determine the release of Cu^{2+} ions and the formation of $BiPO_4$ in dark due to an acidic dissolution process (eq. 4.7):

acidic dissolution: $CuBi_2O_4 + 8H^+ + 2\ PO_4^{3-} \leftrightharpoons Cu^{2+} + 2BiPO_4 + 2O_2$ (eq. 4.7)

We suggest that the slow formation of $BiPO_4$ structures at the surface of the electrode is mainly responsible for both the decrease in the electrode porosity at later stages of the CA and the concurrent decline in the measured photocurrents determined by the growth of an insulating material which effectively screens the $CuBi_2O_4$ surface from the electrolyte, thus reducing the overall electrode activity.

4.4.5 Supporting information

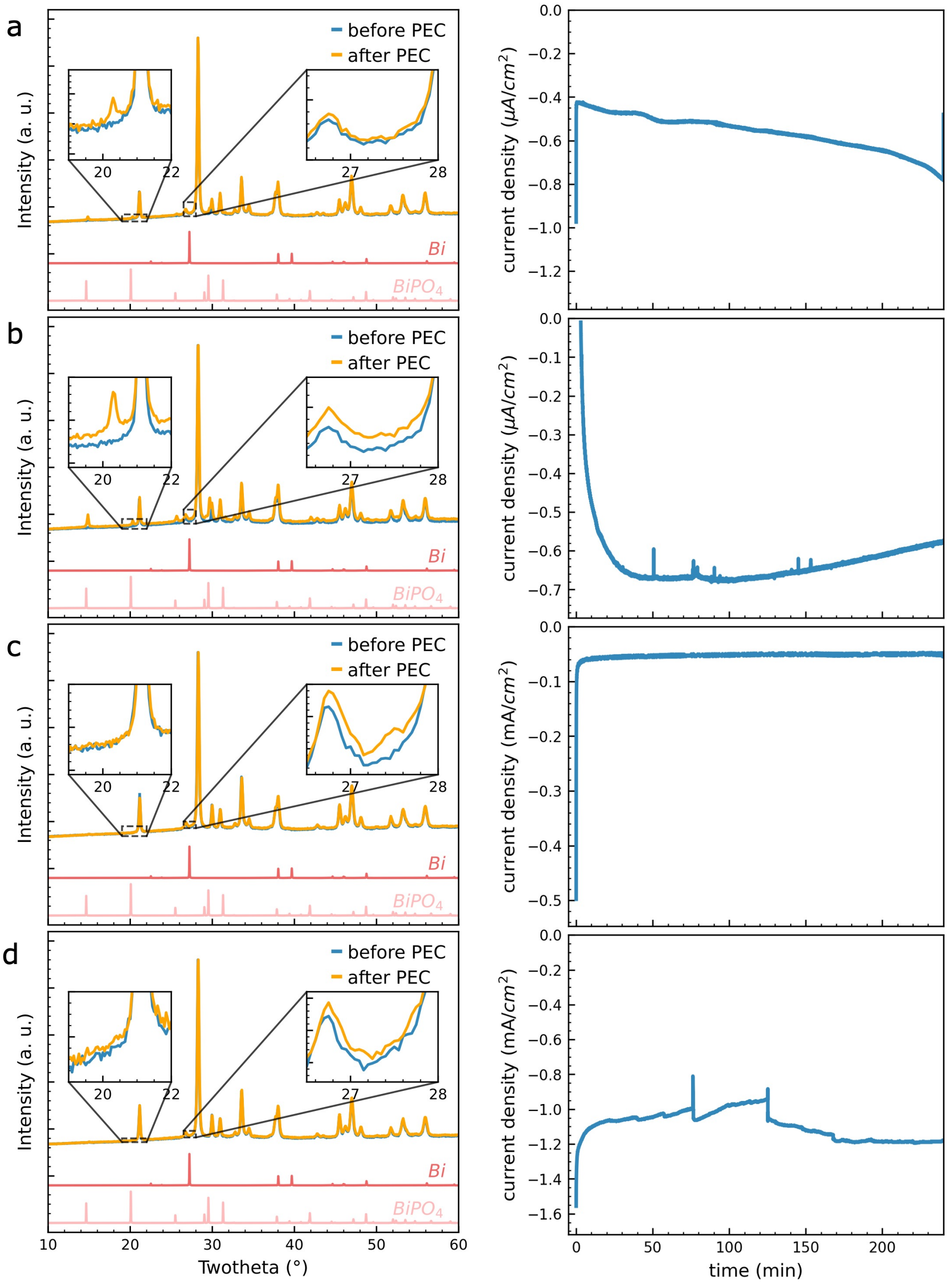

Figure S4.41: The effect of CA measurements at different experimental conditions on the structure of $CuBi_2O_4$ electrodes. **a)** *Left*, XRD patterns before and after a CA measurement performed at 0.5 V vs RHE in dark. *Right*, the related CA measurement. **b)** Same as **a** for a CA performed at the OCP (1.125 V vs RHE) and under LED illumination. For both **a** and **b** the current densities are expressed in $\mu A/cm^2$. **c)** XRD and CA measurements on a $CuBi_2O_4$ electrode undergoing a CA at 0.5 V vs. RHE and under LED illumination by using a 0.5 M Na_2SO_4 electrolyte solution at pH = 5.8, i.e. without the presence of phosphate ions in the electrolyte. **d)** XRD and CA measurements on a $CuBi_2O_4$ electrode undergoing a CA at 0.5 V vs. RHE and under LED illumination by using a 0.5 M Na_2SO_4 / 0.1 M NaH_2PO_4 electrolyte at pH = 5.8 in the presence of 0.2 v% of H_2O_2.

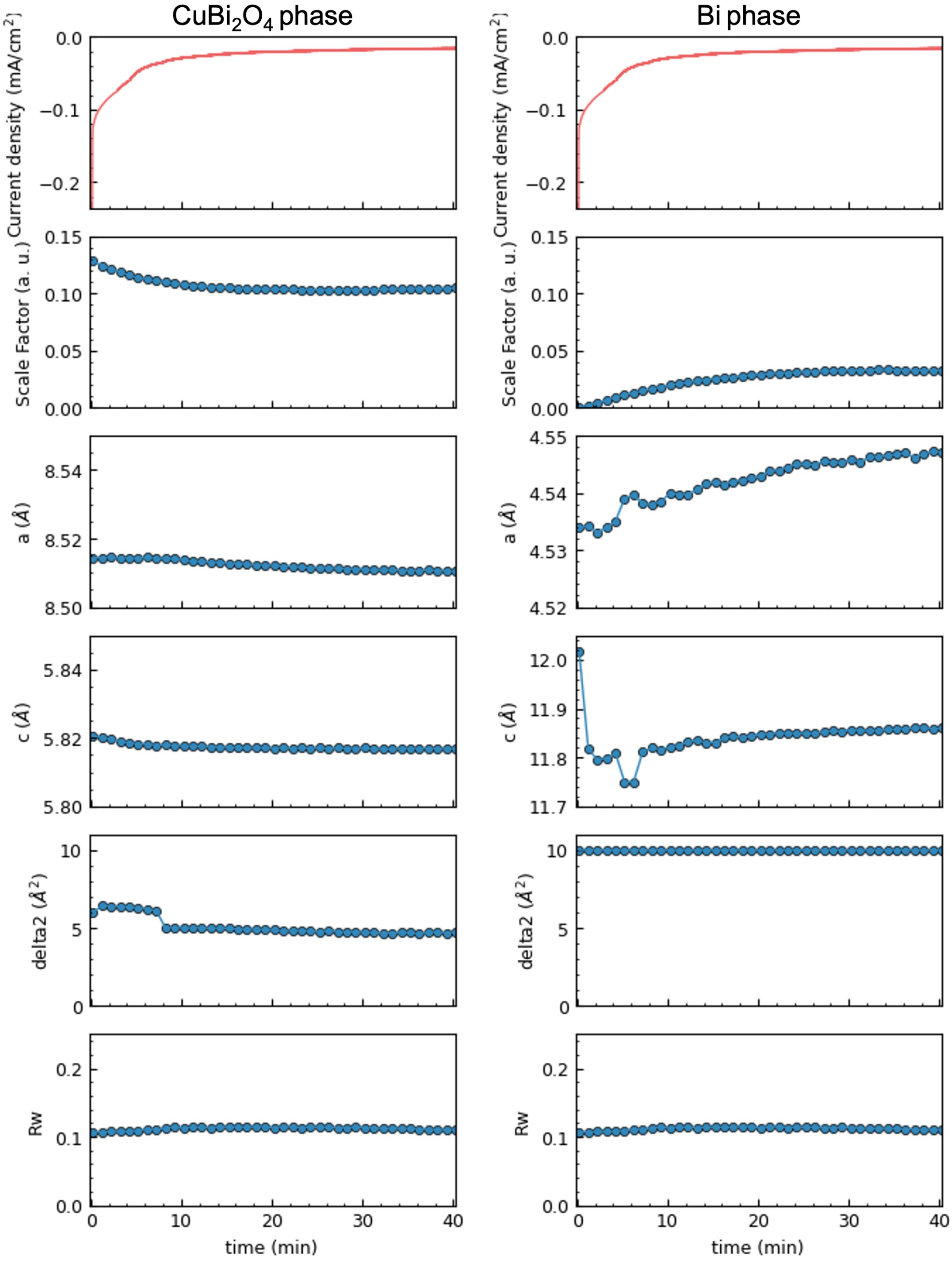

Figure S4.42: Refined values for selected parameters of $CuBi_2O_4$ and Bi phases during operando CA The unphysical behavior of delta2 for the Bi phase is attributed to an artifact due to the broad size distribution of metallic Bi crystallites.

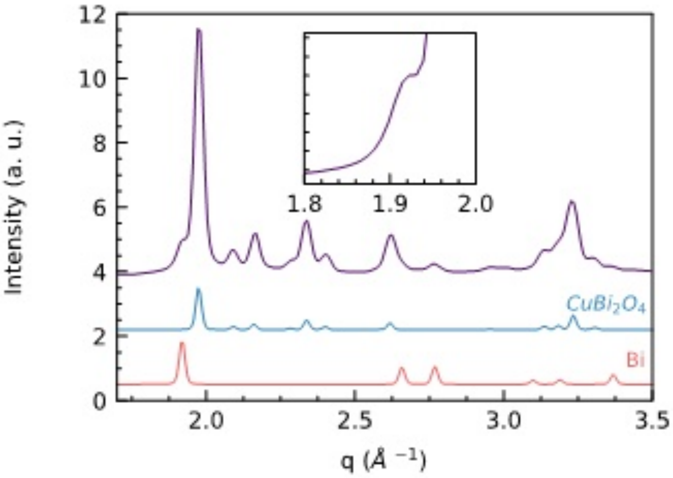

Figure S4.43: X-ray TS pattern of a CuBi$_2$O$_4$ electrode collected at the end of the operando CA and at a different location of the electrode surface. After continuous measurement of X-ray scattering signal during the CA, the sample was moved to probe a region of the surface that has not been previously probed by the X-ray beam. The detection of a reduced Bi phase also in the latter region let us conclude that the observed photo-degradation phenomena are not influenced by the utilization of the X-ray probe.

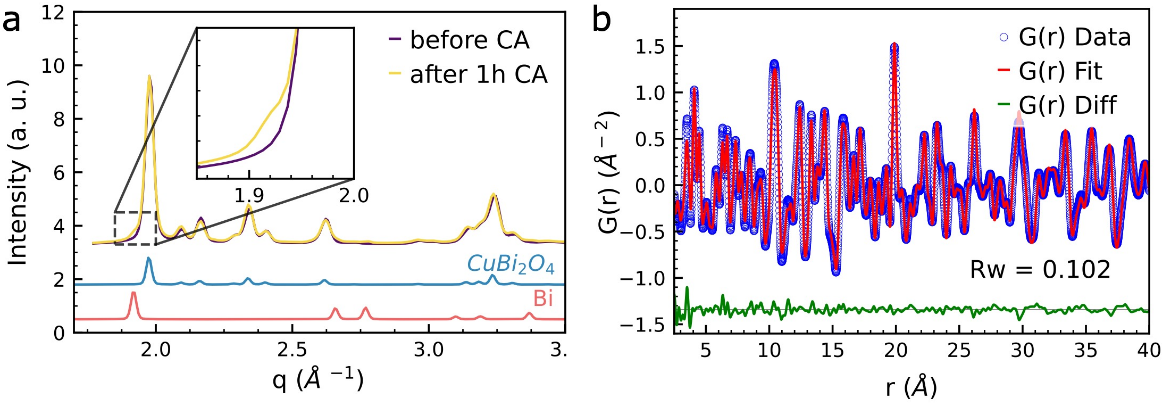

Figure S4.44: Formation of metallic Bi phase during chronoamperometric measurement under solar illumination a) Ex situ X-ray TS patterns of a CuBi$_2$O$_4$ electrode before (purple) and after (yellow) 1h CA performed by use of a solar simulated emission and at an applied bias of 0.5 V vs. RHE. In the inset, a zoomed view of the patterns highlighting the presence of the metallic Bi R-3m (611) reflection after the CA. **b)** PDF fit by two-phase refinement of the yellow pattern in **a** after the Fourier transformation.

$CuBi_2O_4$ phase				Bi phase				
Scale factor (a. u.)	a (Å)	c (Å)	δ_2 (Å^2)	Scale factor (a. u.)	a (Å)	c (Å)	δ_2 (Å^2)	R_w
0.16(7)	8.49(4)	5.81(1)	(4)	0.00(9)	4.55(3)	11.75(0)	1(0)	0.102

Table 4.2: Selected refined structural values from the PDF fit of a $CuBi_2O_4$ electrode after CA measurements under solar illumination. The digits in brackets are in the same order of magnitude as the uncertainty in the refined parameters.

Chapter 5

Summary and perspective

During fabrication and operation, nanomaterials undergo complex transformations that profoundly modify their overall structure, including their chemical composition, size, shape, degree of porosity, and atomic arrangement. Due to the intricacy of these processes, the use of a single characterization technique is generally not sufficient to obtain a comprehensive understanding of the multifaceted phenomena at play. In this thesis, we introduce a multi-modal X-ray analytical approach to determine structural transformation at the nanoscale. We apply the method to investigate two different classes of processes: the synthesis of metallic nanocrystals and nanocrystal assemblies, and the photocorrosion of photo-electrochemically active electrodes.

We establish a dedicated setup for the simultaneous acquisition of TS-PDF and SAXS. We further develop a sample environment which permits to investigate the synthesis of nanoparticles by either X-ray scattering or X-ray spectroscopy. We then apply our multi-modal experimental approach to investigate the model syntheses of both Pd and Cu nanocrystals. We use in situ XAS and complementary PDF to reveal the chemical transformations leading Pd(II) and Cu(II) precursors to convert into the nanocrystal nuclei in the presence of an oleylamine and oleic acid mixture. In the case of Pd nanocrystals, we detect the direct conversion of the initial Pd(II)-amino complex into single-crystalline metal nanocrystals at 190 °C. The formation of the Pd nanocrystals perfectly agrees with the general principles of the classical nucleation theory.

Conversely, we find that the synthesis of Cu nanocrystals follows a multi-step non-classical nucleation pathways. By both XAS and PDF, we detect that the initial Cu(II)-

amino complex presumably transforms into a [Cu(II)$(OAm)_2(OAc)_2 2H_2O$] complex at the intermediate temperature of 100 °C. This result shows that the affinity of the Cu metal center with oleylamine and oleic acid ligands evolves with temperature. At 210 °C we detect the formation of a relatively stable intermediate species, which precedes the nanocrystal nucleation and which we identify as a partially reduced Cu(I)-amino complex.

We investigate the nucleation and post-nucleation transformations during the synthesis of Cu nanocrystals by both PDF and SAXS. We first detect the emergence of small sized Cu_2O nuclei, which then fuse together into larger polycrystalline Cu_2O nanocrystals. The Cu_2O phase eventually reduces into metallic Cu after prolonged heating at 210 °C. We thus conclude that the unoriented attachment of small Cu_2O nuclei plays a crucial role in the non-classical formation mechanism of larger Cu nanocrystals.

We investigate the direct synthesis of CuPd icosahedra supercrystals by in situ X-ray methods. The complementary PDF and XAS data clearly indicates that the presence of the Pd precursor effectively promotes the direct reduction of the Cu(I)-amino intermediate complex into its metallic form without formation of Cu_2O intermediates. We thus propose that small Pd-rich nuclei form at early stages of the nucleation and then act as seeds for the co-reduction of Cu and Pd species.

The simultaneous acquisition of in situ SAXS and TS-PDF permits to follow the one-pot synthesis and assembly of CuPd nanocrystals over multiple length scales in a single experimental setup. We demonstrate by both in situ PDF and ex situ HRTEM that the atomic structure of the CuPd nanocrystals consists of a multi-twinned crystalline domains with an overall icosahedral arrangement. By simultaneous in situ PDF and SAXS, we detect both the growth of the icosahedra and the formation of a soft shell of oleylamine/oleic acid ligands at the nanoparticle surface.

We reveal the supercrystal formation mechanism via a detailed analysis of the in situ SAXS. We show that cooling of the reaction mixture prompts the nanocrystals to assemble into a dense SRO phase, which eventually evolves into a closed-pack fcc arrangement. We then demonstrate that the organization of the oleylamine/oleic acid solvent molecules into lamellae induces the nanocrystals self assembly by reducing the available volume to particle diffusion. The proposed mechanism contrasts with previous examples of one-pot synthesis and assembly of nanocrystals, in which the assembly process was predominantly attributed to van der Waals attraction and short-range steric repulsion.

We investigate the structure of thin films via surface sensitive X-ray scattering. We show that a precise control over the angle of incidence between the X-rays and the film surfaces permits to selectively probe the structure of the thin film deposited on a crystalline support. However, we also observe that the X-ray penetration depth increases for rough films, leading to the formation of additional background signal due to diffraction from the support.

We demonstrate that even a slight misalignment of the films, on the order of fractions of micrometers, introduces aberrations in the measured scattering angles and therefore affects the accuracy of the PDF measurements of films. We therefore implement an aberration correction algorithm that mitigates this issue.

We investigate the photocorrosion of $CuBi_2O_4$ electrodes via fast acquisition of simultaneous TS-PDF and SAXS. To this goal, we develop an operando cell to determine the surface structure of photoactive electrodes while simultaneously testing their PEC response. We find that the fast degradation of the PEC properties of the material under operation correlates with formation of a segregating metallic Bi phase due to a cathodic photocorrosion process. We additionally determine a change in the porosity of the $CuBi_2O_4$ films, which we ascribe to the crystallization of $BiPO_4$ nanostructures at the surface of the electrode. We reveal additional degradation processes via complementary ex situ TS, XANES, ICP-MS, and electron microscopy. Such processes include the release of Cu^{2+} ions in solution and the formation of metallic Cu on the $CuBi_2O_4$ surface.

Our understanding of the complex transformations occurring at the atomic and nano scales greatly benefits from the detailed structural, morphological, and chemical information provided by the complementary analytical methods introduced in this thesis. The combined use of in situ PDF and XAS proves remarkably valuable in detecting organometallic intermediates with short-range order. The PDF further enables to identify small nuclei and twinned nanocrystals that cannot be fully characterized via standard analytical methods in reciprocal space. Changes in the TS intensity clearly indicate phase transformations, while SAXS provides detailed information on nanoscale morphology such as size, shape, polydispersity, and porosity.

By offering a comprehensive elucidation of nanocrystal formation pathways, the combined utilization of in situ PDF, SAXS, and XAS is anticipated to yield significant advancements in the design of novel fabrication routes for nanocrystals. Moreover, the ability to correlate the atomic arrangement of individual nanocrystals with the emergence of periodic organizations at the nanoscale, such as nanocrystal dense phases, superlattices, and lamellar phases, via simultaneous in situ SAXS and PDF offers great opportunities to enhance our understanding of the formation of hierarchically structured materials, with potential impacts in several applications.

The use of highly brilliant 4th generation synchrotron radiation offers the exciting potential of further increasing the time resolution of the in situ X-ray experiments to enable the detection of even shorter leaving intermediates, such as very small nuclei or dense pre-nucleation phases. We expect that the complementary use of in situ XAS and PDF will permit to determine numerous organometallic species and multi-atomic clusters that are not yet known or cannot be isolated for single crystal X-ray diffraction measurements. To this goal, the development of suitable algorithms capable of simulating plausible chemical structures and subsequently verifying them against both the experimental PDF and XAS data would significantly expand our capability to identify potential intermediate species during the nanoparticle synthesis. The ability to detect molecular structures in solution holds the premise to investigate in situ the synthesis of both organometallic and polyatomic compounds, as well as the atomic arrangement of activated homogeneous catalysts, with potential implications in inorganic synthetic chemistry and catalysis.

In the field of green H_2 production, rationalizing the photodegradation mechanisms of PEC materials constitutes a fundamental prerequisite for improving their long-term stability and efficiency by establishment of appropriate mitigation measures. For instance, in the case of $CuBi_2O_4$ films the observation of metallic Bi and Cu at the surface of the electrode advocates for the use of an effective co-catalyst to hinder the reduction of the active film by quickly transferring the photogenerated electrons to the liquid phase. Moreover, improving the hole transport properties of the photocathode would enhance stability of $CuBi_2O_4$ against anodic photocorrosion.[272] Finally, the fabrication of a protective layer on top of the photoactive film would likely prevent the dissolution of Cu^{2+} and Bi^{2+} cations into the electrolyte by screening the electrode surface from the electrolyte.

In addition to photo-electrochemical materials, the combined chemical and morphological information provided by the measurement of SAXS and TS in grazing incidence paves the way to study the operation of a wide range of film-based functional devices, in the field of electrochemistry, photochromism, batteries, and sensing. The possibility to detect short-range ordered or amorphous phases via PDF analysis offers exciting opportunities in the investigation of subtle changes at the solid/liquid or solid/air interfaces of thin films, such as the formation of reaction intermediates at the material surface or restructuring of the solvent. Due to the weak scattering signal expected by such subtle structural modifications, we anticipate that similar X-ray scattering experiments will require optimized experimental conditions and the use of nanometer smooth film samples.

Bibliography

(1) Alivisatos, A. P. Semiconductor clusters, nanocrystals, and quantum dots. *Science* **1996**, *271*, 933–937.

(2) Weller, H. Quantized semiconductor particles: a novel state of matter for materials science. *Advanced Materials* **1993**, *5*, 88–95.

(3) Sun, L.; Wu, G.; Wang, Q.; Lu, J. Nanostructural metallic materials: Structures and mechanical properties. *Materials Today* **2020**, *38*, 114–135.

(4) Zaera, F. Nanostructured materials for applications in heterogeneous catalysis. *Chemical Society Reviews* **2013**, *42*, 2746–2762.

(5) Wang, L.; Hasanzadeh Kafshgari, M.; Meunier, M. Optical properties and applications of plasmonic-metal nanoparticles. *Advanced Functional Materials* **2020**, *30*, 2005400.

(6) Mitchell, M. J.; Billingsley, M. M.; Haley, R. M.; Wechsler, M. E.; Peppas, N. A.; Langer, R. Engineering precision nanoparticles for drug delivery. *Nature reviews drug discovery* **2021**, *20*, 101–124.

(7) Zhang, Q.; Uchaker, E.; Candelaria, S. L.; Cao, G. Nanomaterials for energy conversion and storage. *Chemical Society Reviews* **2013**, *42*, 3127–3171.

(8) Zito, C. A.; Perfecto, T. M.; Dippel, A.-C.; Volanti, D. P.; Koziej, D. Low-temperature carbon dioxide gas sensor based on yolk–shell ceria nanospheres. *ACS applied materials & interfaces* **2020**, *12*, 17745–17751.

(9) Balanta, A.; Godard, C.; Claver, C. Pd nanoparticles for C–C coupling reactions. *Chemical Society Reviews* **2011**, *40*, 4973–4985.

(10) Saldan, I.; Semenyuk, Y.; Marchuk, I.; Reshetnyak, O. Chemical synthesis and application of palladium nanoparticles. *Journal of Materials Science* **2015**, *50*, 2337–2354.

(11) Chen, A.; Ostrom, C. Palladium-based nanomaterials: synthesis and electrochemical applications. *Chemical Reviews* **2015**, *115*, 11999–12044.

(12) Gawande, M. B.; Goswami, A.; Felpin, F.-X.; Asefa, T.; Huang, X.; Silva, R.; Zou, X.; Zboril, R.; Varma, R. S. Cu and Cu-based nanoparticles: synthesis and applications in catalysis. *Chemical Reviews* **2016**, *116*, 3722–3811.

(13) Rossi, K.; Buonsanti, R. Shaping copper nanocatalysts to steer selectivity in the electrochemical CO2 reduction reaction. *Accounts of Chemical Research* **2022**, *55*, 629–637.

(14) Mun, Y.; Lee, S.; Cho, A.; Kim, S.; Han, J. W.; Lee, J. Cu-Pd alloy nanoparticles as highly selective catalysts for efficient electrochemical reduction of CO2 to CO. *Applied Catalysis B: Environmental* **2019**, *246*, 82–88.

(15) Ma, S.; Sadakiyo, M.; Heima, M.; Luo, R.; Haasch, R. T.; Gold, J. I.; Yamauchi, M.; Kenis, P. J. Electroreduction of carbon dioxide to hydrocarbons using bimetallic Cu–Pd catalysts with different mixing patterns. *Journal of the American Chemical Society* **2017**, *139*, 47–50.

(16) Goulas, K. A.; Sreekumar, S.; Song, Y.; Kharidehal, P.; Gunbas, G.; Dietrich, P. J.; Johnson, G. R.; Wang, Y.; Grippo, A. M.; Grabow, L. C., et al. Synergistic effects in bimetallic palladium–copper catalysts improve selectivity in oxygenate coupling reactions. *Journal of the American Chemical Society* **2016**, *138*, 6805–6812.

(17) Walter, M. G.; Warren, E. L.; McKone, J. R.; Boettcher, S. W.; Mi, Q.; Santori, E. A.; Lewis, N. S. Solar water splitting cells. *Chemical Reviews* **2010**, *110*, 6446–6473.

(18) Hisatomi, T.; Kubota, J.; Domen, K. Recent advances in semiconductors for photocatalytic and photoelectrochemical water splitting. *Chemical Society Reviews* **2014**, *43*, 7520–7535.

(19) Spitler, M. T.; Modestino, M. A.; Deutsch, T. G.; Xiang, C. X.; Durrant, J. R.; Esposito, D. V.; Haussener, S.; Maldonado, S.; Sharp, I. D.; Parkinson, B. A., et al. Practical challenges in the development of photoelectrochemical solar fuels production. *Sustainable Energy & Fuels* **2020**, *4*, 985–995.

(20) Chen, S.; Huang, D.; Xu, P.; Xue, W.; Lei, L.; Cheng, M.; Wang, R.; Liu, X.; Deng, R. Semiconductor-based photocatalysts for photocatalytic and photoelectrochemical water splitting: will we stop with photocorrosion? *Journal of Materials Chemistry A* **2020**, *8*, 2286–2322.

(21) Ros, C.; Andreu, T.; Morante, J. R. Photoelectrochemical water splitting: a road from stable metal oxides to protected thin film solar cells. *Journal of Materials Chemistry A* **2020**, *8*, 10625–10669.

(22) Billinge, S. J. The rise of the X-ray atomic pair distribution function method: A series of fortunate events. *Philosophical Transactions of the Royal Society A: Mathematical, Physical and Engineering Sciences* **2019**, *377*, DOI: `10.1098/rsta.018.0413`.

(23) Billinge, S. J.; Levin, I. The problem with determining atomic structure at the nanoscale. *Science* **2007**, *316*, 561–565.

(24) Jehannin, M.; Rao, A.; Cölfen, H. New horizons of nonclassical crystallization. *Journal of the American Chemical Society* **2019**, *141*, 10120–10136.

(25) LaMer, V. K.; Dinegar, R. H. Theory, production and mechanism of formation of monodispersed hydrosols. *Journal of the american chemical society* **1950**, *72*, 4847–4854.

(26) Sugimoto, T. Preparation of monodispersed colloidal particles. *Advances in Colloid and Interface Science* **1987**, *28*, 65–108.

(27) Sugimoto, T., *Monodispersed particles*; Elsevier: 2019.

(28) Leite, E. R.; Ribeiro, C., *Crystallization and growth of colloidal nanocrystals*; Springer Science & Business Media: 2011.

(29) Gibbs, J. W. On the equilibrium of heterogeneous substances. *American journal of science* **1878**, *3*, 441–458.

(30) Grote, L. Imaging nanomaterials in solution – A multimodal approach using in situ X-ray ptychography , spectroscopy and scattering, Ph.D. Thesis, 2022.

(31) Peng, X.; Wickham, J.; Alivisatos, A. Kinetics of II-VI and III-V colloidal semiconductor nanocrystal growth:"focusing" of size distributions. *Journal of the American Chemical Society* **1998**, *120*, 5343–5344.

(32) De Mello Donegá, C.; Liljeroth, P.; Vanmaekelbergh, D. Physicochemical evaluation of the hot-injection method, a synthesis route for monodisperse nanocrystals. *Small* **2005**, *1*, 1152–1162.

(33) Reiss, P.; Protiere, M.; Li, L. Core/shell semiconductor nanocrystals. *Small* **2009**, *5*, 154–168.

(34) Kwon, S. G.; Hyeon, T. Formation mechanisms of uniform nanocrystals via hot-injection and heat-up methods. *Small* **2011**, *7*, 2685–2702.

(35) Murray, C.; Norris, D. J.; Bawendi, M. G. Synthesis and characterization of nearly monodisperse CdE (E= sulfur, selenium, tellurium) semiconductor nanocrystallites. *Journal of the American Chemical Society* **1993**, *115*, 8706–8715.

(36) Talapin, D. V.; Rogach, A. L.; Kornowski, A.; Haase, M.; Weller, H. Highly luminescent monodisperse CdSe and CdSe/ZnS nanocrystals synthesized in a hexadecylamine- trioctylphosphine oxide- trioctylphospine mixture. *Nano Letters* **2001**, *1*, 207–211.

(37) Van de Krol, R. In *Photoelectrochemical hydrogen production*; Springer: 2011, pp 13–67.

(38) Kwon, S. G.; Hyeon, T. Colloidal chemical synthesis and formation kinetics of uniformly sized nanocrystals of metals, oxides, and chalcogenides. *Accounts of Chemical Research* **2008**, *41*, 1696–1709.

(39) Park, J.; An, K.; Hwang, Y.; Park, J.-G.; Noh, H.-J.; Kim, J.-Y.; Park, J.-H.; Hwang, N.-M.; Hyeon, T. Ultra-large-scale syntheses of monodisperse nanocrystals. *Nature Materials* **2004**, *3*, 891–895.

(40) Sun, S.; Murray, C. B.; Weller, D.; Folks, L.; Moser, A. Monodisperse FePt nanoparticles and ferromagnetic FePt nanocrystal superlattices. *Science* **2000**, *287*, 1989–1992.

(41) Timonen, J. V.; Seppälä, E. T.; Ikkala, O.; Ras, R. H. From Hot-Injection Synthesis to Heating-Up Synthesis of Cobalt Nanoparticles: Observation of Kinetically Controllable Nucleation. *Angewandte Chemie* **2011**, *123*, 2128–2132.

(42) Jana, N. R.; Chen, Y.; Peng, X. Size-and shape-controlled magnetic (Cr, Mn, Fe, Co, Ni) oxide nanocrystals via a simple and general approach. *Chemistry of materials* **2004**, *16*, 3931–3935.

(43) Kim, S.-W.; Park, J.; Jang, Y.; Chung, Y.; Hwang, S.; Hyeon, T.; Kim, Y. W. Synthesis of monodisperse palladium nanoparticles. *Nano Letters* **2003**, *3*, 1289–1291.

(44) Kwon, S. G.; Piao, Y.; Park, J.; Angappane, S.; Jo, Y.; Hwang, N.-M.; Park, J.-G.; Hyeon, T. Kinetics of monodisperse iron oxide nanocrystal formation by "heating-up" process. *Journal of the American Chemical Society* **2007**, *129*, 12571–12584.

(45) Gebauer, D.; Wolf, S. E. Designing solid materials from their solute state: a shift in paradigms toward a holistic approach in functional materials chemistry. *Journal of the American Chemical Society* **2019**, *141*, 4490–4504.

(46) Lee, J.; Yang, J.; Kwon, S. G.; Hyeon, T. Nonclassical nucleation and growth of inorganic nanoparticles. *Nature Reviews Materials* **2016**, *1*, 1–16.

(47) Ruiz-Agudo, E.; Burgos-Cara, A.; Ruiz-Agudo, C.; Ibañez-Velasco, A.; Cölfen, H.; Rodriguez-Navarro, C. A non-classical view on calcium oxalate precipitation and the role of citrate. *Nature Communications* **2017**, *8*, 768.

(48) Gary, D. C.; Terban, M. W.; Billinge, S. J.; Cossairt, B. M. Two-step nucleation and growth of InP quantum dots via magic-sized cluster intermediates. *Chemistry of Materials* **2015**, *27*, 1432–1441.

(49) Loiudice, A.; Buonsanti, R. Reaction intermediates in the synthesis of colloidal nanocrystals. *Nature Synthesis* **2022**, *1*, 344–351.

(50) Li, D.; Nielsen, M. H.; Lee, J. R.; Frandsen, C.; Banfield, J. F.; De Yoreo, J. J. Direction-specific interactions control crystal growth by oriented attachment. *Science* **2012**, *336*, 1014–1018.

(51) Simon, P.; Bahrig, L.; Baburin, I. A.; Formanek, P.; Röder, F.; Sickmann, J.; Hickey, S. G.; Eychmüller, A.; Lichte, H.; Kniep, R., et al. Interconnection of nanoparticles within 2D superlattices of PbS/oleic acid thin films. *Advanced Materials* **2014**, *26*, 3042–3049.

(52) Wu, H.; Yang, Y.; Ou, Y.; Lu, B.; Li, J.; Yuan, W.; Wang, Y.; Zhang, Z. Early stage growth of rutile titania mesocrystals. *Crystal Growth & Design* **2018**, *18*, 4209–4214.

(53) Cölfen, H.; Antonietti, M. Mesocrystals: inorganic superstructures made by highly parallel crystallization and controlled alignment. *Angewandte Chemie International Edition* **2005**, *44*, 5576–5591.

(54) Sturm, E. V.; Cölfen, H. Mesocrystals: structural and morphogenetic aspects. *Chemical Society Reviews* **2016**, *45*, 5821–5833.

(55) Sturm, E. V.; Cölfen, H. Mesocrystals: Past, presence, future. *Crystals* **2017**, *7*, 207.

(56) Loh, N. D.; Sen, S.; Bosman, M.; Tan, S. F.; Zhong, J.; Nijhuis, C. A.; Král, P.; Matsudaira, P.; Mirsaidov, U. Multistep nucleation of nanocrystals in aqueous solution. *Nature Chemistry* **2017**, *9*, 77–82.

(57) Gebauer, D.; Kellermeier, M.; Gale, J. D.; Bergström, L.; Cölfen, H. Pre-nucleation clusters as solute precursors in crystallisation. *Chemical Society Reviews* **2014**, *43*, 2348–2371.

(58) Wolf, S. L.; Caballero, L.; Melo, F.; Cölfen, H. Gel-like calcium carbonate precursors observed by in situ AFM. *Langmuir* **2017**, *33*, 158–163.

(59) De Yoreo, J. J.; Gilbert, P. U.; Sommerdijk, N. A.; Penn, R. L.; Whitelam, S.; Joester, D.; Zhang, H.; Rimer, J. D.; Navrotsky, A.; Banfield, J. F., et al. Crystallization by particle attachment in synthetic, biogenic, and geologic environments. *Science* **2015**, *349*, aaa6760.

(60) Niederberger, M. Multiscale nanoparticle assembly: From particulate precise manufacturing to colloidal processing. *Advanced Functional Materials* **2017**, *27*, 1703647.

(61) Bøjesen, E.; Iversen, B. The chemistry of nucleation. *CrystEngComm* **2016**, *18*, 8332–8353.

(62) Mourdikoudis, S.; Liz-Marzán, L. M. Oleylamine in nanoparticle synthesis. *Chemistry of Materials* **2013**, *25*, 1465–1476.

(63) Xu, Z.; Shen, C.; Hou, Y.; Gao, H.; Sun, S. Oleylamine as both reducing agent and stabilizer in a facile synthesis of magnetite nanoparticles. *Chemistry of Materials* **2009**, *21*, 1778–1780.

(64) Seo, W. S.; Shim, J. H.; Oh, S. J.; Lee, E. K.; Hur, N. H.; Park, J. T. Phase-and size-controlled synthesis of hexagonal and cubic CoO nanocrystals. *Journal of the American Chemical Society* **2005**, *127*, 6188–6189.

(65) Son, S. U.; Park, I. K.; Park, J.; Hyeon, T. Synthesis of Cu 2 O coated Cu nanoparticles and their successful applications to Ullmann-type amination coupling reactions of aryl chlorides. *Chemical Communications* **2004**, 778–779.

(66) Mazumder, V.; Sun, S. Oleylamine-mediated synthesis of Pd nanoparticles for catalytic formic acid oxidation. *Journal of the American Chemical Society* **2009**, *131*, 4588–4589.

(67) Niu, Z.; Peng, Q.; Gong, M.; Rong, H.; Li, Y. Oleylamine-mediated shape evolution of palladium nanocrystals. *Angewandte Chemie - International Edition* **2011**, *50*, 6315–6319.

(68) Watt, J.; Young, N.; Haigh, S.; Kirkland, A.; Tilley, R. D. Synthesis and structural characterization of branched palladium nanostructures. *Advanced Materials* **2009**, *21*, 2288–2293.

(69) Lacroix, L.-M.; Gatel, C.; Arenal, R.; Garcia, C.; Lachaize, S.; Blon, T.; Warot-Fonrose, B.; Snoeck, E.; Chaudret, B.; Viau, G. Tuning complex shapes in platinum nanoparticles: from cubic dendrites to fivefold stars. *Angewandte Chemie International Edition* **2012**, *51*, 4690–4694.

(70) Kang, Y.; Ye, X.; Murray, C. B. Size-and Shape-Selective Synthesis of Metal Nanocrystals and Nanowires Using CO as a Reducing Agent. *Angewandte Chemie* **2010**, *122*, 6292–6295.

(71) Yin, X.; Shi, M.; Kwok, K. S.; Zhao, H.; Gray, D. L.; Bertke, J. A.; Yang, H. Dish-like higher-ordered palladium nanostructures through metal ion-ligand complexation. *Nano Research* **2018**, *11*, 3442–3452.

(72) Effenberger, F. B.; Sulca, M. A.; Machini, M. T.; Couto, R. A.; Kiyohara, P. K.; Machado, G.; Rossi, L. M. Copper nanoparticles synthesized by thermal decomposition in liquid phase: the influence of capping ligands on the synthesis and bactericidal activity. *Journal of Nanoparticle Research* **2014**, *16*, 1–10.

(73) Mott, D.; Galkowski, J.; Wang, L.; Luo, J.; Zhong, C. J. Synthesis of size-controlled and shaped copper nanoparticles. *Langmuir* **2007**, *23*, 5740–5745.

(74) Watt, J.; Cheong, S.; Toney, M. F.; Ingham, B.; Cookson, J.; Bishop, P. T.; Tilley, R. D. Ultrafast growth of highly branched palladium nanostructures for catalysis. *ACS Nano* **2010**, *4*, 396–402.

(75) Ishizaki, T.; Watanabe, R. A new one-pot method for the synthesis of Cu nanoparticles for low temperature bonding. *Journal of Materials Chemistry* **2012**, *22*, 25198–25206.

(76) Devaraj, M.; Saravanan, R.; Deivasigamani, R.; Gupta, V. K.; Gracia, F.; Jayadevan, S. Fabrication of novel shape Cu and Cu/Cu2O nanoparticles modified electrode for the determination of dopamine and paracetamol. *Journal of Molecular Liquids* **2016**, *221*, 930–941.

(77) Jin, T.; Guo, S.; Zuo, J.-l.; Sun, S. Synthesis and assembly of Pd nanoparticles on graphene for enhanced electrooxidation of formic acid. *Nanoscale* **2013**, *5*, 160–163.

(78) Diaz-Droguett, D. E.; Espinoza, R.; Fuenzalida, V. Copper nanoparticles grown under hydrogen: study of the surface oxide. *Applied Surface Science* **2011**, *257*, 4597–4602.

(79) Pesesse, A.; Carenco, S. Influence of the copper precursor on the catalytic transformation of oleylamine during Cu nanoparticle synthesis. *Catalysis Science and Technology* **2021**, *11*, 5310–5320.

(80) Zhang, S.; Kang, P.; Bakir, M.; Lapides, A. M.; Dares, C. J.; Meyer, T. J. Polymer-supported CuPd nanoalloy as a synergistic catalyst for electrocatalytic reduction of carbon dioxide to methane. *Proceedings of the National Academy of Sciences* **2015**, *112*, 15809–15814.

(81) Bai, S.; Shao, Q.; Wang, P.; Dai, Q.; Wang, X.; Huang, X. Highly active and selective hydrogenation of CO2 to ethanol by ordered Pd–Cu nanoparticles. *Journal of the American Chemical Society* **2017**, *139*, 6827–6830.

(82) Cai, X.; Wang, A.; Wang, J.; Wang, R.; Zhong, S.; Zhao, Y.; Wu, L.; Chen, J.; Bai, S. Order engineering on the lattice of intermetallic PdCu co-catalysts for boosting the photocatalytic conversion of CO 2 into CH 4. *Journal of Materials Chemistry A* **2018**, *6*, 17444–17456.

(83) Xi, P.; Cao, Y.; Yang, F.; Ma, C.; Chen, F.; Yu, S.; Wang, S.; Zeng, Z.; Zhang, X. Facile synthesis of Pd-based bimetallic nanocrystals and their application as catalysts for methanol oxidation reaction. *Nanoscale* **2013**, *5*, 6124–6130.

(84) Dong, K.; Dai, H.; Pu, H.; Zhang, T.; Wang, Y.; Deng, Y. Enhanced electrocatalytic activity and stability of Pd-based bimetallic icosahedral nanoparticles towards alcohol oxidation reactions. *International Journal of Hydrogen Energy* **2023**, *48*, 12288–12298.

(85) Diyarbakir, S.; Can, H.; Metin, Ö. Reduced graphene oxide-supported CuPd alloy nanoparticles as efficient catalysts for the Sonogashira cross-coupling reactions. *ACS Applied Materials & Interfaces* **2015**, *7*, 3199–3206.

(86) Smith, S. E.; Siamaki, A. R.; Gupton, B. F.; Carpenter, E. E. CuPd nanoparticles as a catalyst in carbon–carbon cross-coupling reactions by a facile oleylamine synthesis. *RSC Advances* **2016**, *6*, 91541–91545.

(87) Zhang, L.; Hou, F.; Tan, Y. Shape-tailoring of CuPd nanocrystals for enhancement of electro-catalytic activity in oxygen reduction reaction. *Chemical Communications* **2012**, *48*, 7152–7154.

(88) Li, P.; Xiao, Z.; Liu, Z.; Huang, J.; Li, Q.; Sun, D. Highly efficient hydrogen generation from methanolysis of ammonia borane on CuPd alloy nanoparticles. *Nanotechnology* **2014**, *26*, 025401.

(89) Marakatti, V. S.; Sarma, S. C.; Joseph, B.; Banerjee, D.; Peter, S. C. Synthetically tuned atomic ordering in PdCu nanoparticles with enhanced catalytic activity toward solvent-free benzylamine oxidation. *ACS Applied Materials & Interfaces* **2017**, *9*, 3602–3615.

(90) Wang, C.; Chen, D. P.; Sang, X.; Unocic, R. R.; Skrabalak, S. E. Size-dependent disorder–order transformation in the synthesis of monodisperse intermetallic PdCu nanocatalysts. *ACS Nano* **2016**, *10*, 6345–6353.

(91) Mathiesen, J. K.; Bøjesen, E. D.; Pedersen, J. K.; Kjær, E. T.; Juelsholt, M.; Cooper, S.; Quinson, J.; Anker, A. S.; Cutts, G.; Keeble, D. S.; Thomsen, M. S.; Rossmeisl, J.; Jensen, K. M. Breaking with the Principles of Coreduction to Form Stoichiometric Intermetallic PdCu Nanoparticles. *Small Methods* **2022**, *6*, DOI: `10.1002/smtd.202200420`.

(92) Tong, W.; Huang, B. L.; Wang, P. T.; Li, L. G.; Shao, Q.; Huang, X. Q. Crystal-Phase-Engineered PdCu Electrocatalyst for Enhanced Ammonia Synthesis. *Angewandte Chemie-International Edition* **2020**, *59*, 2649–2653.

(93) Popov, A.; Shubin, Y. V.; Plyusnin, P.; Sharafutdinov, M.; Korenev, S. Experimental redetermination of the Cu–Pd phase diagram. *Journal of Alloys and Compounds* **2019**, *777*, 204–212.

(94) Jiang, Y.; Duchamp, M.; Ang, S. J.; Yan, H.; Tan, T. L.; Mirsaidov, U. Dynamics of the fcc-to-bcc phase transition in single-crystalline PdCu alloy nanoparticles. *Nature Communications* **2023**, *14*, 104.

(95) Hsu, S.-W.; Rodarte, A. L.; Som, M.; Arya, G.; Tao, A. R. Colloidal plasmonic nanocomposites: from fabrication to optical function. *Chemical Reviews* **2018**, *118*, 3100–3120.

(96) Cherniukh, I.; Rainò, G.; Stöferle, T.; Burian, M.; Travesset, A.; Naumenko, D.; Amenitsch, H.; Erni, R.; Mahrt, R. F.; Bodnarchuk, M. I., et al. Perovskite-type superlattices from lead halide perovskite nanocubes. *Nature* **2021**, *593*, 535–542.

(97) Kagan, C. R.; Lifshitz, E.; Sargent, E. H.; Talapin, D. V. Building devices from colloidal quantum dots. *Science* **2016**, *353*, aac5523.

(98) Hadjimichael, M.; Li, Y.; Zatterin, E.; Chahine, G. A.; Conroy, M.; Moore, K.; Connell, E. N. O.; Ondrejkovic, P.; Marton, P.; Hlinka, J., et al. Metal–ferroelectric supercrystals with periodically curved metallic layers. *Nature Materials* **2021**, *20*, 495–502.

(99) Zhao, H.; Sen, S.; Udayabhaskararao, T.; Sawczyk, M.; Kučanda, K.; Manna, D.; Kundu, P. K.; Lee, J.-W.; Král, P.; Klajn, R. Reversible trapping and reaction acceleration within dynamically self-assembling nanoflasks. *Nature Nanotechnology* **2016**, *11*, 82–88.

(100) Baek, W.; Bootharaju, M. S.; Walsh, K. M.; Lee, S.; Gamelin, D. R.; Hyeon, T. Highly luminescent and catalytically active suprastructures of magic-sized semiconductor nanoclusters. *Nature Materials* **2021**, *20*, 650–657.

(101) Begley, M. R.; Gianola, D. S.; Ray, T. R. Bridging functional nanocomposites to robust macroscale devices. *Science* **2019**, *364*, eaav4299.

(102) Shi, J.; Xiao, Z.; Kamaly, N.; Farokhzad, O. C. Self-assembled targeted nanoparticles: evolution of technologies and bench to bedside translation. *Accounts of Chemical Research* **2011**, *44*, 1123–1134.

(103) Zhou, H.; Guo, M.; Li, J.; Qin, F.; Wang, Y.; Liu, T.; Liu, J.; Sabet, Z. F.; Wang, Y.; Liu, Y., et al. Hypoxia-triggered self-assembly of ultrasmall iron oxide nanoparticles to amplify the imaging signal of a tumor. *Journal of the American Chemical Society* **2021**, *143*, 1846–1853.

(104) Shamay, Y.; Shah, J.; Işık, M.; Mizrachi, A.; Leibold, J.; Tschaharganeh, D. F.; Roxbury, D.; Budhathoki-Uprety, J.; Nawaly, K.; Sugarman, J. L., et al. Quantitative self-assembly prediction yields targeted nanomedicines. *Nature Materials* **2018**, *17*, 361–368.

(105) Kovalenko, M. V.; Manna, L.; Cabot, A.; Hens, Z.; Talapin, D. V.; Kagan, C. R.; Klimov, V. I.; Rogach, A. L.; Reiss, P.; Milliron, D. J., et al. Prospects of nanoscience with nanocrystals. *ACS Nano* **2015**, *9*, 1012–1057.

(106) Sugi, K. S.; Maier, A.; Scheele, M. Emergent properties in supercrystals of atomically precise nanoclusters and colloidal nanocrystals. *Chemical Communications* **2022**, *58*, 6998–7017.

(107) Jenewein, C.; Schupp, S. M.; Ni, B.; Schmidt-Mende, L.; Cölfen, H. Tuning the Electronic Properties of Mesocrystals. *Small Science* **2022**, *2*, 2200014.

(108) Coropceanu, I.; Janke, E. M.; Portner, J.; Haubold, D.; Nguyen, T. D.; Das, A.; Tanner, C. P.; Utterback, J. K.; Teitelbaum, S. W.; Hudson, M. H., et al. Self-assembly of nanocrystals into strongly electronically coupled all-inorganic supercrystals. *Science* **2022**, *375*, 1422–1426.

(109) Boles, M. A.; Engel, M.; Talapin, D. V. Self-assembly of colloidal nanocrystals: From intricate structures to functional materials. *Chemical Reviews* **2016**, *116*, 11220–11289.

(110) Han, H.; Kallakuri, S.; Yao, Y.; Williamson, C. B.; Nevers, D. R.; Savitzky, B. H.; Skye, R. S.; Xu, M.; Voznyy, O.; Dshemuchadse, J., et al. Multiscale hierarchical structures from a nanocluster mesophase. *Nature Materials* **2022**, *21*, 518–525.

(111) Vogel, N.; Retsch, M.; Fustin, C.-A.; Del Campo, A.; Jonas, U. Advances in colloidal assembly: the design of structure and hierarchy in two and three dimensions. *Chemical Reviews* **2015**, *115*, 6265–6311.

(112) Gu, X. W.; Ye, X.; Koshy, D. M.; Vachhani, S.; Hosemann, P.; Alivisatos, A. P. Tolerance to structural disorder and tunable mechanical behavior in self-assembled superlattices of polymer-grafted nanocrystals. *Proceedings of the National Academy of Sciences* **2017**, *114*, 2836–2841.

(113) Rupich, S. M.; Shevchenko, E. V.; Bodnarchuk, M. I.; Lee, B.; Talapin, D. V. Size-dependent multiple twinning in nanocrystal superlattices. *Journal of the American Chemical Society* **2010**, *132*, 289–296.

(114) Zhuang, J.; Wu, H.; Yang, Y.; Cao, Y. C. Supercrystalline colloidal particles from artificial atoms. *Journal of the American Chemical Society* **2007**, *129*, 14166–14167.

(115) Rabani, E.; Reichman, D. R.; Geissler, P. L.; Brus, L. E. Drying-mediated self-assembly of nanoparticles. *Nature* **2003**, *426*, 271–274.

(116) Murray, C. B.; Kagan, C. R.; Bawendi, M. G. Synthesis and characterization of monodisperse nanocrystals and close-packed nanocrystal assemblies. *Annual Review of Materials Science* **2000**, *30*, 545–610.

(117) Pileni, M.-P. Nanocrystal self-assemblies: fabrication and collective properties, 2001.

(118) Shevchenko, E. V.; Talapin, D. V.; Kotov, N. A.; O'Brien, S.; Murray, C. B. Structural diversity in binary nanoparticle superlattices. *Nature* **2006**, *439*, 55–59.

(119) Hanrath, T. Colloidal nanocrystal quantum dot assemblies as artificial solids. *Journal of Vacuum Science & Technology A* **2012**, *30*.

(120) Wilcoxon, J. P.; Martin, J. E.; Provencio, P. Size distributions of gold nanoclusters studied by liquid chromatography. *Langmuir* **2000**, *16*, 9912–9920.

(121) Prasad, B.; Stoeva, S. I.; Sorensen, C. M.; Klabunde, K. J. Digestive ripening of thiolated gold nanoparticles: the effect of alkyl chain length. *Langmuir* **2002**, *18*, 7515–7520.

(122) Abécassis, B.; Testard, F.; Spalla, O. Gold nanoparticle superlattice crystallization probed in situ. *Physical Review Letters* **2008**, *100*, 115504.

(123) Wu, L.; Willis, J. J.; McKay, I. S.; Diroll, B. T.; Qin, J.; Cargnello, M.; Tassone, C. J. High-temperature crystallization of nanocrystals into three-dimensional superlattices. *Nature* **2017**, *548*, 197–201.

(124) Nevers, D. R.; Williamson, C. B.; Savitzky, B. H.; Hadar, I.; Banin, U.; Kourkoutis, L. F.; Hanrath, T.; Robinson, R. D. Mesophase formation stabilizes high-purity magic-sized clusters. *Journal of the American Chemical Society* **2018**, *140*, 3652–3662.

(125) Nakagawa, F.; Saruyama, M.; Takahata, R.; Sato, R.; Matsumoto, K.; Teranishi, T. In Situ Control of Crystallinity of 3D Colloidal Crystals by Tuning the Growth Kinetics of Nanoparticle Building Blocks. *Journal of the American Chemical Society* **2022**, *144*, 5871–5877.

(126) Montanarella, F.; Akkerman, Q. A.; Bonatz, D.; van der Sluijs, M. M.; van der Bok, J. C.; Prins, P. T.; Aebli, M.; Mews, A.; Vanmaekelbergh, D.; Kovalenko, M. V. Growth and Self-Assembly of CsPbBr3 Nanocrystals in the TOPO/PbBr2 Synthesis as Seen with X-ray Scattering. *Nano Letters* **2023**, *23*, 667–676.

(127) Kister, T.; Monego, D.; Mulvaney, P.; Widmer-Cooper, A.; Kraus, T. Colloidal stability of apolar nanoparticles: The role of particle size and ligand shell structure. *ACS Nano* **2018**, *12*, 5969–5977.

(128) Calvin, J. J.; Brewer, A. S.; Alivisatos, A. P. The role of organic ligand shell structures in colloidal nanocrystal synthesis. *Nature Synthesis* **2022**, *1*, 127–137.

(129) Schulz, F.; Lokteva, I.; Parak, W. J.; Lehmkühler, F. Recent Notable Approaches to Study Self-Assembly of Nanoparticles with X-Ray Scattering and Electron Microscopy. *Particle and Particle Systems Characterization* **2021**, *38*, DOI: `10.1002/ppsc.202100087`.

(130) Saxena, V.; Portale, G. Contribution of Ex-Situ and In-Situ X-ray Grazing Incidence Scattering Techniques to the Understanding of Quantum Dot Self-Assembly: A Review. *Nanomaterials* **2020**, *10*, 2240.

(131) Weidman, M. C.; Smilgies, D.-M.; Tisdale, W. A. Kinetics of the self-assembly of nanocrystal superlattices measured by real-time in situ X-ray scattering. *Nature Materials* **2016**, *15*, 775–781.

(132) Lokteva, I.; Koof, M.; Walther, M.; Grübel, G.; Lehmkühler, F. Monitoring Nanocrystal Self-Assembly in Real Time Using In Situ Small-Angle X-Ray Scattering. *Small* **2019**, *15*, 1900438.

(133) Huang, X.; Zhu, J.; Ge, B.; Deng, K.; Wu, X.; Xiao, T.; Jiang, T.; Quan, Z.; Cao, Y. C.; Wang, Z. Understanding Fe3O4 nanocube assembly with reconstruction of a consistent superlattice phase diagram. *Journal of the American Chemical Society* **2019**, *141*, 3198–3206.

(134) Yang, P.-W.; Thoka, S.; Lin, P.-C.; Su, C.-J.; Sheu, H.-S.; Huang, M. H.; Jeng, U.-S. Tracing the surfactant-mediated nucleation, growth, and superpacking of gold supercrystals using time and spatially resolved x-ray scattering. *Langmuir* **2017**, *33*, 3253–3261.

(135) Lee, B.; Littrell, K.; Sha, Y.; Shevchenko, E. V. Revealing the Effects of the Nonsolvent on the Ligand Shell of Nanoparticles and Their Crystallization. *Journal of the American Chemical Society* **2019**, *141*, 16651–16662.

(136) Tan, M. X.; Laibinis, P. E.; Nguyen, S. T.; Kesselman, J. M.; Stanton, C. E.; Lewis, N. S. Principles and applications of semiconductor photoelectrochemistry. *Progress in inorganic chemistry* **1994**, 21–144.

(137) Medicus, S. Ternary metal-oxide CuBi2O4 thin-films for photo-electrochemical (PEC) water splitting, Bachelor's Thesis, University of Hamburg, 2021.

(138) Chen, Z.; Dinh, H. N.; Miller, E., et al., *Photoelectrochemical water splitting*; Springer: 2013; Vol. 344.

(139) Tilley, S. D.; Schreier, M.; Azevedo, J.; Stefik, M.; Graetzel, M. Ruthenium oxide hydrogen evolution catalysis on composite cuprous oxide water-splitting photocathodes. *Advanced Functional Materials* **2014**, *24*, 303–311.

(140) Toma, F. M.; Cooper, J. K.; Kunzelmann, V.; McDowell, M. T.; Yu, J.; Larson, D. M.; Borys, N. J.; Abelyan, C.; Beeman, J. W.; Yu, K. M., et al. Mechanistic insights into chemical and photochemical transformations of bismuth vanadate photoanodes. *Nature Communications* **2016**, *7*, 12012.

(141) Zhong, M.; Hisatomi, T.; Sasaki, Y.; Suzuki, S.; Teshima, K.; Nakabayashi, M.; Shibata, N.; Nishiyama, H.; Katayama, M.; Yamada, T., et al. Highly active GaN-stabilized Ta3N5 thin-film photoanode for solar water oxidation. *Angewandte Chemie* **2017**, *129*, 4817–4821.

(142) He, Y.; Thorne, J. E.; Wu, C. H.; Ma, P.; Du, C.; Dong, Q.; Guo, J.; Wang, D. What limits the performance of Ta3N5 for solar water splitting? *Chem* **2016**, *1*, 640–655.

(143) Seki, K.; Higashi, T.; Kawase, Y.; Takanabe, K.; Domen, K. Exploring the Photocorrosion Mechanism of a Photocatalyst. *The Journal of Physical Chemistry Letters* **2022**, *13*, 10356–10363.

(144) Hahn, N. T.; Holmberg, V. C.; Korgel, B. A.; Mullins, C. B. Electrochemical synthesis and characterization of p-CuBi2O4 thin film photocathodes. *The Journal of Physical Chemistry C* **2012**, *116*, 6459–6466.

(145) Berglund, S. P.; Abdi, F. F.; Bogdanoff, P.; Chemseddine, A.; Friedrich, D.; Van De Krol, R. Comprehensive evaluation of CuBi2O4 as a photocathode material for photoelectrochemical water splitting. *Chemistry of Materials* **2016**, *28*, 4231–4242.

(146) Song, A.; Levine, I.; van de Krol, R.; Dittrich, T.; Berglund, S. P. Revealing the relationship between photoelectrochemical performance and interface hole trapping in CuBi 2 O 4 heterojunction photoelectrodes. *Chemical Science* **2020**, *11*, 11195–11204.

(147) Liu, G.; Zheng, F.; Li, J.; Zeng, G.; Ye, Y.; Larson, D. M.; Yano, J.; Crumlin, E. J.; Ager, J. W.; Wang, L.-w., et al. Investigation and mitigation of degradation mechanisms in Cu2O photoelectrodes for CO2 reduction to ethylene. *Nature Energy* **2021**, *6*, 1124–1132.

(148) Jenewein, C.; Avaro, J.; Appel, C.; Liebi, M.; Cölfen, H. 3D Binary Mesocrystals from Anisotropic Nanoparticles. *Angewandte Chemie International Edition* **2022**, *61*, e202112461.

(149) Zhang, S.; Rohloff, M.; Kasian, O.; Mingers, A. M.; Mayrhofer, K. J.; Fischer, A.; Scheu, C.; Cherevko, S. Dissolution of BiVO4 photoanodes revealed by time-resolved measurements under photoelectrochemical conditions. *The Journal of Physical Chemistry C* **2019**, *123*, 23410–23418.

(150) Pishgar, S.; Strain, J. M.; Gulati, S.; Sumanasekera, G.; Gupta, G.; Spurgeon, J. M. Investigation of the photocorrosion of n-GaP photoanodes in acid with in situ UV-Vis spectroscopy. *Journal of Materials Chemistry A* **2019**, *7*, 25377–25388.

(151) Scott, S. B.; Hogg, T. V.; Landers, A. T.; Maagaard, T.; Bertheussen, E.; Lin, J. C.; Davis, R. C.; Beeman, J. W.; Higgins, D.; Drisdell, W. S., et al. Absence of oxidized phases in Cu under CO reduction conditions. *ACS Energy Letters* **2019**, *4*, 803–804.

(152) Dionigi, F.; Zeng, Z.; Sinev, I.; Merzdorf, T.; Deshpande, S.; Lopez, M. B.; Kunze, S.; Zegkinoglou, I.; Sarodnik, H.; Fan, D., et al. In-situ structure and catalytic mechanism of NiFe and CoFe layered double hydroxides during oxygen evolution. *Nature Communications* **2020**, *11*, 2522.

(153) Als-Nielsen, J.; McMorrow, D., *Elements of modern X-ray physics*; John Wiley & Sons: 2011.

(154) Egami, T.; Billinge, S. J., *Underneath the Bragg peaks: structural analysis of complex materials*; Elsevier: 2003.

(155) Juhás, P.; Davis, T.; Farrow, C. L.; Billinge, S. J. PDFgetX3: A rapid and highly automatable program for processing powder diffraction data into total scattering pair distribution functions. *Journal of Applied Crystallography* **2013**, *46*, 560–566.

(156) Farrow, C. L.; Billinge, S. J. Relationship between the atomic pair distribution function and small-angle scattering: Implications for modeling of nanoparticles. *Acta Crystallographica Section A: Foundations of Crystallography* **2009**, *65*, 232–239.

(157) Chupas, P. J.; Qiu, X.; Hanson, J. C.; Lee, P. L.; Grey, C. P.; Billinge, S. J. Rapid-acquisition pair distribution function (RA-PDF) analysis. *Journal of Applied Crystallography* **2003**, *36*, 1342–1347.

(158) Farrow, C.; Juhas, P.; Liu, J.; Bryndin, D.; Božin, E.; Bloch, J.; Proffen, T.; Billinge, S. PDFfit2 and PDFgui: computer programs for studying nanostructure in crystals. *Journal of Physics: Condensed Matter* **2007**, *19*, 335219.

(159) Qiu, X.; Thompson, J. W.; Billinge, S. J. PDFgetX2: a GUI-driven program to obtain the pair distribution function from X-ray powder diffraction data. *Journal of Applied Crystallography* **2004**, *37*, 678–678.

(160) Juhás, P.; Farrow, C. L.; Yang, X.; Knox, K. R.; Billinge, S. J. Complex modeling: a strategy and software program for combining multiple information sources to solve ill posed structure and nanostructure inverse problems. *Acta Crystallographica Section A* **2015**, *71*, 562–568.

(161) Rietveld, H. M. A profile refinement method for nuclear and magnetic structures. *Journal of Applied Crystallography* **1969**, *2*, 65–71.

(162) Proffen, T.; Billinge, S. PDFFIT, a program for full profile structural refinement of the atomic pair distribution function. *Journal of Applied Crystallography* **1999**, *32*, 572–575.

(163) Jeong, I.-K.; Proffen, T.; Mohiuddin-Jacobs, F.; Billinge, S. J. Measuring correlated atomic motion using X-ray diffraction. *The Journal of Physical Chemistry A* **1999**, *103*, 921–924.

(164) Kodama, K.; Iikubo, S.; Taguchi, T.; Shamoto, S. I. Finite size effects of nanoparticles on the atomic pair distribution functions. *Acta Crystallographica Section A: Foundations of Crystallography* **2006**, *62*, 444–453.

(165) Lei, M.; De Graff, A. M.; Thorpe, M.; Wells, S. A.; Sartbaeva, A. Uncovering the intrinsic geometry from the atomic pair distribution function of nanomaterials. *Physical Review B* **2009**, *80*, 024118.

(166) Billinge, S. Obtaining the PDF from a model. *International Tables for Crystallography* **2019**, *H*, 649–672.

(167) Larsen, A. H.; Mortensen, J. J.; Blomqvist, J.; Castelli, I. E.; Christensen, R.; Dułak, M.; Friis, J.; Groves, M. N.; Hammer, B.; Hargus, C., et al. The atomic simulation environment—a Python library for working with atoms. *Journal of Physics: Condensed Matter* **2017**, *29*, 273002.

(168) Proffen, T.; Neder, R. B. DISCUS: A program for diffuse scattering and defect-structure simulation. *Journal of Applied Crystallography* **1997**, *30*, 171–175.

(169) Thompson, A. P.; Aktulga, H. M.; Berger, R.; Bolintineanu, D. S.; Brown, W. M.; Crozier, P. S.; in't Veld, P. J.; Kohlmeyer, A.; Moore, S. G.; Nguyen, T. D., et al. LAMMPS-a flexible simulation tool for particle-based materials modeling at the atomic, meso, and continuum scales. *Computer Physics Communications* **2022**, *271*, 108171.

(170) Hanwell, M. D.; Curtis, D. E.; Lonie, D. C.; Vandermeersch, T.; Zurek, E.; Hutchison, G. R. Avogadro: an advanced semantic chemical editor, visualization, and analysis platform. *Journal of Cheminformatics* **2012**, *4*, 1–17.

(171) Pedersen, J. S. Analysis of small-angle scattering data from colloids and polymer solutions: modeling and least-squares fitting. *Advances in colloid and interface science* **1997**, *70*, 171–210.

(172) Mildner, D.; Hall, P. Small-angle scattering from porous solids with fractal geometry. *Journal of Physics D: Applied Physics* **1986**, *19*, 1535.

(173) Megens, M.; van Kats, C. M.; Bösecke, P.; Vos, W. L. Synchrotron small-angle X-ray scattering of colloids and photonic colloidal crystals. *Journal of Applied Crystallography* **1997**, *30*, 637–641.

(174) Ballauff, M. SAXS and SANS studies of polymer colloids. *Current Opinion in Colloid & Interface Science* **2001**, *6*, 132–139.

(175) Young, R. A., *The Rietveld method*; International union of crystallography: 1993; Vol. 5.

(176) Van Bokhoven, J. A.; Lamberti, C., *X-ray absorption and X-ray emission spectroscopy: theory and applications*; John Wiley & Sons: 2016; Vol. 1.

(177) Yamamoto, T. Assignment of pre-edge peaks in K-edge x-ray absorption spectra of 3d transition metal compounds: Electric dipole or quadrupole? *X-Ray Spectrometry: An International Journal* **2008**, *37*, 572–584.

(178) Newville, M. EXAFS analysis using FEFF and FEFFIT. *Journal of Synchrotron Radiation* **2001**, *8*, 96–100.

(179) Bunău, O.; Joly, Y. Self-consistent aspects of x-ray absorption calculations. *Journal of Physics: Condensed Matter* **2009**, *21*, 345501.

(180) Bunău, O.; Ramos, A. Y.; Joly, Y. The FDMNES code. **2021**.

(181) Bauer, M. HERFD-XAS and valence-to-core-XES: new tools to push the limits in research with hard X-rays? *Physical Chemistry Chemical Physics* **2014**, *16*, 13827–13837.

(182) Glatzel, P.; Weng, T.-C.; Kvashnina, K.; Swarbrick, J.; Sikora, M.; Gallo, E.; Smolentsev, N.; Mori, R. A. Reflections on hard X-ray photon-in/photon-out spectroscopy for electronic structure studies. *Journal of Electron Spectroscopy and Related Phenomena* **2013**, *188*, 17–25.

(183) Prestipino, C.; Mathon, O.; Hino, R.; Beteva, A.; Pascarelli, S. Quick-EXAFS implementation on the general purpose EXAFS beamline at ESRF. *Journal of Synchrotron Radiation* **2011**, *18*, 176–182.

(184) Müller, O.; Nachtegaal, M.; Just, J.; Lützenkirchen-Hecht, D.; Frahm, R. Quick-EXAFS setup at the SuperXAS beamline for in situ X-ray absorption spectroscopy with 10 ms time resolution. *Journal of synchrotron radiation* **2016**, *23*, 260–266.

(185) Müller, O.; Lützenkirchen-Hecht, D.; Frahm, R. Quick scanning monochromator for millisecond in situ and in operando X-ray absorption spectroscopy. *Review of Scientific Instruments* **2015**, *86.*

(186) Hubbell, J. H.; Seltzer, S. M. *Tables of X-ray mass attenuation coefficients and mass energy-absorption coefficients 1 keV to 20 MeV for elements Z= 1 to 92 and 48 additional substances of dosimetric interest*; tech. rep.; National Inst. of Standards and Technology-PL, Gaithersburg, MD (United ..., 1995.

(187) Dippel, A. C.; Roelsgaard, M.; Boettger, U.; Schneller, T.; Gutowski, O.; Ruett, U. Local atomic structure of thin and ultrathin films via rapid high-energy X-ray total scattering at grazing incidence. *IUCrJ* **2019**, *6*, 290–298.

(188) Jensen, K.; Blichfeld, A. B.; Bauers, S. R.; Wood, S. R.; Dooryhée, E.; Johnson, D. C.; Iversen, B. B.; Billinge, S. J. Demonstration of thin film pair distribution function analysis (tfPDF) for the study of local structure in amorphous and crystalline thin films. *IUCrJ* **2015**, *2*, 481–489.

(189) Nakamura, N.; Terban, M. W.; Billinge, S. J.; Reeja-Jayan, B. Unlocking the structure of mixed amorphous-crystalline ceramic oxide films synthesized under low temperature electromagnetic excitation. *Journal of Materials Chemistry A* **2017**, *5*, 18434–18441.

(190) Shi, C.; Teerakapibal, R.; Yu, L.; Zhang, G. G. Pair distribution functions of amorphous organic thin films from synchrotron X-ray scattering in transmission mode. *IUCrJ* **2017**, *4*, 555–559.

(191) Wood, S. R.; Woods, K. N.; Plassmeyer, P. N.; Marsh, D. A.; Johnson, D. W.; Page, C. J.; Jensen, K. M.; Johnson, D. C. Same Precursor, Two Different Products: Comparing the Structural Evolution of In–Ga–O “Gel-Derived” Powders and Solution-Cast Films Using Pair Distribution Function Analysis. *Journal of the American Chemical Society* **2017**, *139*, 5607–5613.

(192) Vlieg, E.; van der Gon, A. D.; Van der Veen, J.; MacDonald, J. E.; Norris, C. Surface X-ray scattering during crystal growth: Ge on Ge (111). *Physical Review Letters* **1988**, *61*, 2241.

(193) Fuoss, P.; Kisker, D.; Lamelas, F.; Stephenson, G.; Imperatori, P.; Brennan, S. Time-resolved x-ray scattering studies of layer-by-layer epitaxial growth. *Physical Review Letters* **1992**, *69*, 2791.

(194) Richard, M.-I.; Highland, M.; Fister, T.; Munkholm, A.; Mei, J.; Streiffer, S.; Thompson, C.; Fuoss, P.; Stephenson, G. In situ synchrotron x-ray studies of strain and composition evolution during metal-organic chemical vapor deposition of InGaN. *Applied Physics Letters* **2010**, *96*.

(195) Gustafson, J.; Shipilin, M.; Zhang, C.; Stierle, A.; Hejral, U.; Ruett, U.; Gutowski, O.; Carlsson, P.-A.; Skoglundh, M.; Lundgren, E. High-energy surface X-ray diffraction for fast surface structure determination. *Science* **2014**, *343*, 758–761.

(196) Dippel, A. C.; Gutowski, O.; Klemeyer, L.; Boettger, U.; Berg, F.; Schneller, T.; Hardtdegen, A.; Aussen, S.; Hoffmann-Eifert, S.; Zimmermann, M. V. Evolution of short-range order in chemically and physically grown thin film bilayer structures for electronic applications. *Nanoscale* **2020**, *12*, 13103–13112.

(197) Erdem, D.; Bingham, N. S.; Heiligtag, F. J.; Pilet, N.; Warnicke, P.; Heyderman, L. J.; Niederberger, M. CoFe2O4 and CoFe2O4-SiO2 Nanoparticle Thin Films with Perpendicular Magnetic Anisotropy for Magnetic and Magneto-Optical Applications. *Advanced Functional Materials* **2016**, *26*, 1954–1963.

(198) Rebber, M. 3D printing of nanoparticle-based aerogels, Ph.D. Thesis, 2022.

(199) Caliebe, W. A.; Murzin, V.; Kalinko, A.; Görlitz, M. In *AIP Conference Proceedings*, 2019; Vol. 2054.

(200) Gauthier, C.; Solé, V.; Signorato, R.; Goulon, J.; Moguiline, E. The ESRF beamline ID26: X-ray absorption on ultra dilute sample. *Journal of Synchrotron Radiation* **1999**, *6*, 164–166.

(201) Glatzel, P.; Harris, A.; Marion, P.; Sikora, M.; Weng, T.-C.; Guilloud, C.; Lafuerza, S.; Rovezzi, M.; Detlefs, B.; Ducotté, L. The five-analyzer point-to-point scanning crystal spectrometer at ESRF ID26. *Journal of Synchrotron Radiation* **2021**, *28*, 362–371.

(202) Ashiotis, G.; Deschildre, A.; Nawaz, Z.; Wright, J. P.; Karkoulis, D.; Picca, F. E.; Kieffer, J. The fast azimuthal integration Python library: pyFAI. *Journal of Applied Crystallography* **2015**, *48*, 510–519.

(203) Harris, C. R.; Millman, K. J.; Van Der Walt, S. J.; Gommers, R.; Virtanen, P.; Cournapeau, D.; Wieser, E.; Taylor, J.; Berg, S.; Smith, N. J., et al. Array programming with NumPy. *Nature* **2020**, *585*, 357–362.

(204) Yang, X.; Juhas, P.; Farrow, C. L.; Billinge, S. J. xPDFsuite: an end-to-end software solution for high throughput pair distribution function transformation, visualization and analysis. *arXiv preprint arXiv:1402.3163* **2014**.

(205) Juhás, P.; Davis, T.; Farrow, C. L.; Billinge, S. J. PDFgetX3: A rapid and highly automatable program for processing powder diffraction data into total scattering pair distribution functions. *Journal of Applied Crystallography* **2013**, *46*, 560–566.

(206) Billinge, S. Nanometre-scale structure from powder diffraction: total scattering and atomic pair distribution function analysis. *International Tables for Crystallography* **2019**, *H*, 649–672.

(207) Allen, F. H. The Cambridge Structural Database: a quarter of a million crystal structures and rising. *Acta Crystallographica Section B: Structural Science* **2002**, *58*, 380–388.

(208) Gražulis, S.; Daškevič, A.; Merkys, A.; Chateigner, D.; Lutterotti, L.; Quiros, M.; Serebryanaya, N. R.; Moeck, P.; Downs, R. T.; Le Bail, A. Crystallography Open Database (COD): an open-access collection of crystal structures and platform for world-wide collaboration. *Nucleic Acids Research* **2012**, *40*, D420–D427.

(209) Banerjee, S.; Liu, C. H.; Jensen, K. M.; Juhas, P.; Lee, J. D.; Tofanelli, M.; Ackerson, C. J.; Murrayd, C. B.; Billingea, S. J. Cluster-mining: An approach for determining core structures of metallic nanoparticles from atomic pair distribution function data Banerjee Soham. *Acta Crystallographica Section A: Foundations and Advances* **2020**, *76*, 24–31.

(210) Virtanen, P.; Gommers, R.; Oliphant, T. E.; Haberland, M.; Reddy, T.; Cournapeau, D.; Burovski, E.; Peterson, P.; Weckesser, W.; Bright, J., et al. SciPy

1.0: fundamental algorithms for scientific computing in Python. *Nature Methods* **2020**, *17*, 261–272.

(211) Korepanov, V. I.; Sedlovets, D. M. An asymmetric fitting function for condensed-phase Raman spectroscopy. *Analyst* **2018**, *143*, 2674–2679.

(212) Doucet, M. et al. SasView version 5.0.5, 2022.

(213) Vrugt, J. A.; ter Braak, C. J.; Diks, C. G.; Robinson, B. A.; Hyman, J. M.; Higdon, D. Accelerating Markov chain Monte Carlo simulation by differential evolution with self-adaptive randomized subspace sampling. *International Journal of Nonlinear Sciences and Numerical Simulation* **2009**, *10*, 273–290.

(214) Newville, M. et al. lmfit/lmfit-py: 1.2.2, version 1.2.2, 2023.

(215) Percus, J. K.; Yevick, G. J. Analysis of classical statistical mechanics by means of collective coordinates. *Physical Review* **1958**, *110*, 1.

(216) Kotlarchyk, M.; Chen, S.-H. Analysis of small angle neutron scattering spectra from polydisperse interacting colloids. *The Journal of Chemical Physics* **1983**, *79*, 2461–2469.

(217) Förster, S.; Timmann, A.; Konrad, M.; Schellbach, C.; Meyer, A.; Funari, S.; Mulvaney, P.; Knott, R. Scattering curves of ordered mesoscopic materials. *The Journal of Physical Chemistry B* **2005**, *109*, 1347–1360.

(218) Yager, K. G.; Zhang, Y.; Lu, F.; Gang, O. Periodic lattices of arbitrary nano-objects: modeling and applications for self-assembled systems. *Journal of Applied Crystallography* **2014**, *47*, 118–129.

(219) Glatter, O. Small angle X-ray scattering. *(No Title)* **1982**.

(220) Clark, A. H.; Imbao, J.; Frahm, R.; Nachtegaal, M. ProQEXAFS: a highly optimized parallelized rapid processing software for QEXAFS data. *Journal of Synchrotron Radiation* **2020**, *27*, 551–557.

(221) De Juan, A.; Jaumot, J.; Tauler, R. Multivariate Curve Resolution (MCR). Solving the mixture analysis problem. *Analytical Methods* **2014**, *6*, 4964–4976.

(222) Jaumot, J.; Gargallo, R.; De Juan, A.; Tauler, R. A graphical user-friendly interface for MCR-ALS: a new tool for multivariate curve resolution in MATLAB. *Chemometrics and Intelligent Laboratory Systems* **2005**, *76*, 101–110.

(223) Jaumot, J.; de Juan, A.; Tauler, R. MCR-ALS GUI 2.0: New features and applications. *Chemometrics and Intelligent Laboratory Systems* **2015**, *140*, 1–12.

(224) Windig, W.; Stephenson, D. Self-modeling mixture analysis of second-derivative near-infrared spectral data using the SIMPLISMA approach. *Analytical Chemistry* **1992**, *64*, 2735–2742.

(225) Ravel, B.; Newville, M. ATHENA, ARTEMIS, HEPHAESTUS: data analysis for X-ray absorption spectroscopy using IFEFFIT. *Journal of Synchrotron Radiation* **2005**, *12*, 537–541.

(226) Rehr, J. J.; Albers, R. C. Theoretical approaches to x-ray absorption fine structure. *Reviews of Modern Physics* **2000**, *72*, 621.

(227) Solé, V. A.; Papillon, E.; Cotte, M.; Walter, P.; Susini, J. A multiplatform code for the analysis of energy-dispersive X-ray fluorescence spectra. *Spectrochimica Acta Part B: Atomic Spectroscopy* **2007**, *62*, 63–68.

(228) Reuter, J. A.; Menzel, M. SLIX: A Python package for fully automated evaluation of Scattered Light Imaging measurements on brain tissue. *Journal of Open Source Software* **2020**, *5*, 2675.

(229) Eilers, P. H. A perfect smoother. *Analytical Chemistry* **2003**, *75*, 3631–3636.

(230) Hong, X.; Newville, M.; Duffy, T. S. In *Journal of Physics: Conference Series*, 2013; Vol. 430, p 012120.

(231) Kim, J. U.; Matsen, M. W. Interaction between polymer-grafted particles. *Macromolecules* **2008**, *41*, 4435–4443.

(232) Glicksman, M. In *Solid state physics*; Elsevier: 1971; Vol. 26, pp 275–427.

(233) Israelachvili, J. N., *Intermolecular and surface forces*; Academic press: 2011.

(234) Garcia-Munoz, J.; Rodriguez-Carvajal, J.; Sapina, F.; Sanchis, M.; Ibanez, R.; Beltran-Porter, D. Crystal and magnetic structures of Bi2CuO4. *Journal of Physics: Condensed Matter* **1990**, *2*, 2205.

(235) Malecki, J. G. CCDC 864691: Experimental Crystal Structure Determination, Cambridge Crystallographic Data Centre, DOI: 10.5517/ccy0s8z, **2012**.

(236) Dineshkumar, P.; Sahana, R.; Rajmohan, G.; Elangovan, A.; Naganandhini, S.; Sangeetha, T.; Arivazhagan, G. Interaction behaviour of acetonitrile in the presence of acetylacetone: FTIR studies and DFT calculations. *Physics and Chemistry of Liquids* **2022**, *60*, 696–706.

(237) Borges, J.; Ribeiro, J. A.; Pereira, E. M.; Carreira, C. A.; Pereira, C. M.; Silva, F. Preparation and characterization of DNA films using oleylamine modified Au surfaces. *Journal of Colloid and Interface Science* **2011**, *358*, 626–634.

(238) Mazumder, V.; Sun, S. Oleylamine-mediated synthesis of monodisperse Pd-based composite nanoparticles for catalytic formic acid oxidation. *ACS National Meeting Book of Abstracts* **2009**, 4588–4589.

(239) Kurauchi, T.; Matsui, M.; Nakamura, Y.; Ooi, S.; Kawaguchi, S.; Kuroya, H. Six-coordinate Copper (II) Complexes Derived from the Reactions of Bis (acetylacetonato)- and Bis (ethyl acetoacetato)-copper (II) with Some Bidentate Nitrogen Bases. *Bulletin of the Chemical Society of Japan* **1974**, *47*, 3049–3056.

(240) Golchoubian, H.; Moayyedi, G.; Bruno, G.; Rudbari, H. A. Syntheses and characterization of mixed-chelate copper (II) complexes containing different counter ions; spectroscopic studies on solvatochromic properties. *Polyhedron* **2011**, *30*, 1027–1034.

(241) Shukla, N.; Liu, C.; Jones, P. M.; Weller, D. FTIR study of surfactant bonding to FePt nanoparticles. *Journal of Magnetism and Magnetic Materials* **2003**, *266*, 178–184.

(242) Klokkenburg, M.; Hilhorst, J.; Erné, B. H. Surface analysis of magnetite nanoparticles in cyclohexane solutions of oleic acid and oleylamine. *Vibrational Spectroscopy* **2007**, *43*, 243–248.

(243) Yin, X.; Shi, M.; Kwok, K. S.; Zhao, H.; Gray, D. L.; Bertke, J. A.; Yang, H. CCDC 1557612: Experimental Crystal Structure Determination, Cambridge Crystallographic Data Centre, DOI: 10.5517/ccy0s8z, **2018**.

(244) Rancan, M.; Carlotto, A.; Bottaro, G.; Armelao, L. Effect of Coordinating Solvents on the Structure of Cu (II)-4, 4'-bipyridine Coordination Polymers. *Inorganics* **2019**, *7*, 103.

(245) Sánchez-Férez, F.; Guerrero, M.; Ayllón, J. A.; Calvet, T.; Font-Bardia, M.; J Planas, o. G.; Pons, J. CCDC 1851976: Experimental Crystal Structure Determination, Cambridge Crystallographic Data Centre, DOI: 10.5517/ccdc.csd.cc20545j, **2018**.

(246) Sánchez-Férez, F.; Guerrero, M.; Ayllón, J. A.; Calvet, T.; Font-Bardia, M.; Planas, J. G.; Pons, J. Reactivity of homoleptic and heteroleptic core paddle wheel Cu (II) compounds. *Inorganica Chimica Acta* **2019**, *487*, 295–306.

(247) Sánchez-Férez, F.; Guerrero, M.; Ayllón, J. A.; Calvet, T.; Font-Bardia, M.; J Planas, o. G.; Pons, J. CCDC 1851979: Experimental Crystal Structure Determination, Cambridge Crystallographic Data Centre, DOI: 10.5517/ccdc.csd.cc20548m, **2018**.

(248) Rheingold, A. L. CCDC 2105533: Experimental Crystal Structure Determination, Cambridge Crystallographic Data Centre, DOI: 10.5517/ccdc.csd.cc28nzfc, **2021**.

(249) Schneider, W.; Bauer, A.; Schmidbaur, H. Benzophenoneimine Complexes of Copper (1). *Chemische Berichte* **1997**, *130*, 947–950.

(250) Kirfel, A.; Eichhorn, K. Accurate structure analysis with synchrotron radiation. The electron density in Al2O3 and Cu2O. *Acta Crystallographica Section A: Foundations of Crystallography* **1990**, *46*, 271–284.

(251) Zhang, Q.; Xie, J.; Yang, J.; Lee, J. Y. Monodisperse icosahedral Ag, Au, and Pd nanoparticles: size control strategy and superlattice formation. *ACS Nano* **2009**, *3*, 139–148.

(252) Reyes-Gasga, J.; Tehuacanero-Nunez, S.; Montejano-Carrizales, J.; Gao, X.; Jose-Yacaman, M. Analysis of the contrast in icosahedral gold nanoparticles. *Topics in Catalysis* **2007**, *46*, 23–30.

(253) Reyes-Gasga, J.; Tehuacanero-Nuñez, S.; Montejano-Carrizales, J. Simulation of the experimental HRTEM constrast of icosahedral gold nanoparticles of different sizes. *Acta Microscopica* **2009**, *18*.

(254) Mourdikoudis, S.; Menelaou, M.; Fiuza-Maneiro, N.; Zheng, G.; Wei, S.; Pérez-Juste, J.; Polavarapu, L.; Sofer, Z. Oleic acid/oleylamine ligand pair: a versatile combination in the synthesis of colloidal nanoparticles. *Nanoscale Horizons* **2022**, *7*, 941–1015.

(255) Weidman, M. C.; Nguyen, Q.; Smilgies, D.-M.; Tisdale, W. A. Impact of size dispersity, ligand coverage, and ligand length on the structure of PbS nanocrystal superlattices. *Chemistry of Materials* **2018**, *30*, 807–816.

(256) De Nijs, B.; Dussi, S.; Smallenburg, F.; Meeldijk, J. D.; Groenendijk, D. J.; Filion, L.; Imhof, A.; Van Blaaderen, A.; Dijkstra, M. Entropy-driven formation of large icosahedral colloidal clusters by spherical confinement. *Nature Materials* **2015**, *14*, 56–60.

(257) Lesaine, A.; Bonamy, D.; Rountree, C. L.; Gauthier, G.; Impéror-Clerc, M.; Lazarus, V. Role of particle aggregation in the structure of dried colloidal silica layers. *Soft Matter* **2021**, *17*, 1589–1600.

(258) Mondal, R.; Kumaraswamy, G. Materials prepared by Freezing-Induced Self-Assembly of Dispersed Solutes: A Review. *Materials Advances* **2022**, *3*, 3041–3054.

(259) Rajamanickam, R.; Kumari, S.; Kumar, D.; Ghosh, S.; Kim, J. C.; Tae, G.; Sen Gupta, S.; Kumaraswamy, G. Soft colloidal scaffolds capable of elastic recovery after large compressive strains. *Chemistry of Materials* **2014**, *26*, 5161–5168.

(260) Karthika, S.; Radhakrishnan, T.; Kalaichelvi, P. A review of classical and non-classical nucleation theories. *Crystal Growth & Design* **2016**, *16*, 6663–6681.

(261) Alder, B. J.; Wainwright, T. E. Phase transition for a hard sphere system. *The Journal of Chemical Physics* **1957**, *27*, 1208–1209.

(262) Pusey, P. N.; Van Megen, W. Phase behaviour of concentrated suspensions of nearly hard colloidal spheres. *Nature* **1986**, *320*, 340–342.

(263) Rodriguez-Gutierrez, I.; Garcia-Rodriguez, R.; Rodriguez-Perez, M.; Vega-Poot, A.; Rodríguez Gattorno, G.; Parkinson, B. A.; Oskam, G. Charge transfer and recombination dynamics at inkjet-printed CuBi2O4 electrodes for photoelectro-

chemical water splitting. *The Journal of Physical Chemistry C* **2018**, *122*, 27169–27179.

(264) Zhang, Z.; Lindley, S. A.; Dhall, R.; Bustillo, K.; Han, W.; Xie, E.; Cooper, J. K. Beneficial CuO phase segregation in the ternary p-type oxide photocathode CuBi2O4. *ACS Applied Energy Materials* **2019**, *2*, 4111–4117.

(265) Krötzsch, K. An Operando Study on Photo-electrochemically Active, BSc Thesis, 2021.

(266) Luo, J.; Steier, L.; Son, M.-K.; Schreier, M.; Mayer, M. T.; Grätzel, M. Cu2O nanowire photocathodes for efficient and durable solar water splitting. *Nano Letters* **2016**, *16*, 1848–1857.

(267) Pan, L.; Kim, J. H.; Mayer, M. T.; Son, M. K.; Ummadisingu, A.; Lee, J. S.; Hagfeldt, A.; Luo, J.; Grätzel, M. Boosting the performance of Cu2O photocathodes for unassisted solar water splitting devices. *Nature Catalysis* **2018**, *1*, 412–420.

(268) Li, X.; Wang, H. Y.; Yang, H.; Cai, W.; Liu, S.; Liu, B. In Situ/Operando Characterization Techniques to Probe the Electrochemical Reactions for Energy Conversion. *Small Methods* **2018**, *2*, 1–14.

(269) Mooney-Slater, R. C. Polymorphic forms of bismuth phosphate. *Zeitschrift für Kristallographie-Crystalline Materials* **1962**, *117*, 371–385.

(270) Renaud, G.; Lazzari, R.; Leroy, F. Probing surface and interface morphology with grazing incidence small angle X-ray scattering. *Surface Science Reports* **2009**, *64*, 255–380.

(271) Gerischer, H. On the stability of semiconductor electrodes against photodecomposition. *Journal of Electroanalytical Chemistry and Interfacial Electrochemistry* **1977**, *82*, 133–143.

(272) Kang, D.; Hill, J. C.; Park, Y.; Choi, K.-S. Photoelectrochemical properties and photostabilities of high surface area CuBi2O4 and Ag-doped CuBi2O4 photocathodes. *Chemistry of Materials* **2016**, *28*, 4331–4340.

Appendix

Table 5.1: List of hazardous substances used in this thesis according to GHS.

Chemical	**GHS Pictograms**	**H statements**	**P statements**
[2-(2-methoxyethoxy)ethoxy] acetic acid		H314	P260, P264, P280, P301+P330+P331, P302+P361+P354, P304+P340, P305+P354+P338, P316, P321, P363, P405, P501
2-propanol	 	H225, H319, H336	P210, P240, P305+P351+P338, P403+P233
acetic acid	 	H226, H314	P210, P280, P301+P330+P331, P303+P361+P353, P305+P351+P338, P310
benzyl alcohol		H302+H332, H319	P261, P270, P304+P340

Continued on next page

Chemical	**GHS Pictograms**	**H statements**	**P statements**
bismuth(III) nitrate pentahydrate		H272, H315, H319, H335	P210, P261, P280, P302+P352, P305+P351+P338, P312, P370+P378, P403+P233, P501
copper(II) acetylacetonate		H315, H319, H335	P261, P264, P271, P280, P302+P352, P304+P340, P305+P351+P338, P312, P321, P332+P313, P337+P313, P362, P403+P233, P405, P501
copper(II) nitrate trihydrate	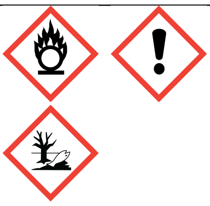	H272, H302, H315, H319, H410	P220, P273, P280, P302+P352, P305+P351+P338
diethyl ether		H224, H302, H319, H333, H336	P210, P261, P305+P351+P338
dioctyl ether	not classifiable	not classifiable	not classifiable
ethanol		H225, H319	P210, P233, P305+P351+P33

Continued on next page

Chemical	**GHS Pictograms**	**H statements**	**P statements**
ethylene glycol		H302, H373	P260, P270, P301+P312
glycerol	no hazards	no hazards	no precautions
hexane	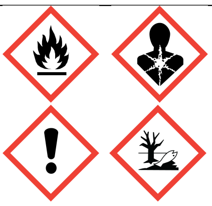	H225, H304, H315, H336, H361f, H373	P202, P210, P273, P301+P310, P303+P361+P353, P331
iron(III) acetylacetonate		H302, H312, H318, H332	P261, P280, P301+P312, P302+P352+P312, P304+P340+P312, P305+P351+P338
oleic acid		H315, H319, H413	P264, P273, P280, P337, P332+P313, P501
oleylamine	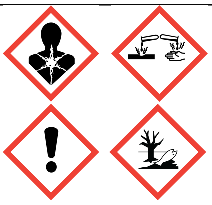	H302, H304, H314, H335, H373, H410	P273, P280, P301+P330+P331, P303+P361+P353, P304+P340+P310, P305+P351+P338
palladium(II) acetylacetonate		H319	P264, P280, P305+P351+P338, P337+P313

Continued on next page

Chemical	**GHS Pictograms**	**H statements**	**P statements**
sodium dihydrogen phosphate		H315, H319, H355	P261, P264, P264+P265, P271, P280, P302+P352, P304+P340, P305+P351+P338, P319, P321, P332+P317, P337+P317, P362+P364, P403+P233, P405, P501
sodium hydroxide		H290, H314	P233, P280, P303+P361+P353, P305+P351+P338 P310
sodium sulphate decahydrate	no hazards	no hazards	no precautions
titanium(IV) tetrachloride	 	H314, H330, H335	P260, P280, P303+P361+P353, P304+P340, P305+P351+P338, P310 P403+P233
toluene	  	H225, H304, H315, H336, H361d, H373, H412	P202, P210, P273, P301+P310, P303+P361+P353, P331

Acknowledgments

The completion of this Ph.D. work would not have been possible without the support of fellow colleagues and scientists. I would like to express my gratitude to all individuals who contributed to this thesis through engaging discussion, assistance in the data acquisition and interpretation, and by fostering a pleasant working environment.

I would like to thank Prof. Dr. Dorota Koziej for giving me the opportunity to work on this exciting and interdisciplinary project, and for her supervision and support throughout my doctoral studies. I am extremely thankful for the autonomy she gave me in shaping my own path toward the goals of the project, for the trust she consistently placed in me, and for her ability to guide me when required by providing invaluable insights and different perspectives. I highly appreciated her commitment to fostering an open and collaborative scientific environment and her efforts in establishing fruitful collaborations with external scientists and research teams. Working in such a dynamic environment has undoubtedly enriched both my personal and academic growth.

I extend my heartfelt thanks to PD Dr. Bert Nickel and Kilian Frank for their tireless effort in our joint X-ray scattering studies. Without their decisive and passionate contribution many of the results presented in this thesis would have not been achieved. Thanks also to Dr. Ann-Christin Dippel and Olof Gutowski for their precious support at the P07 beamline and for the numerous valuable discussions.

I would like to thank Prof. Dr. Tobias Beck for evaluating this thesis and the members of the examination committee, Prof. Dr. Carmen Herrmann and Prof. Dr. Alf Mews, for their interest in my work. I also express my gratitude to Prof. Dr. Robert Blick for serving as the second supervisor of my doctoral studies.

I deeply appreciated the relaxed and cooperative atmosphere of the Center for Hybrid Nanostructure. I am thankful to all present and former members of the Hybrid Nanostructures Group for creating an enjoyable and supporting environment. Special thanks to Francesco Caddeo who first proposed the study of $CuBi_2O_4$ films and who invaluably contributed to the entire project through his deep knowledge of PEC water splitting and photocorrosion processes. My Ph.D. experience was greatly enriched by his long-standing experience and personal touch. I extend my thanks to Sophie Medicus and Marco Krüger, who assisted Francesco in the preparation of $CuBi_2O_4$ thin films with great dedication and attention to details. I also thank Federica Mancini for her efforts in helping me developing the synthesis of CuPd nanocrystals and for her personal support throughout my Ph.D. journey. A special acknowledgment goes to Jagadesh Kopula Kesavan for leading the XAS experiments and analyzing the data with expertise and patience.

I am grateful to Kilian Krötzsch for his tireless efforts in the lab and for his contagious enthusiasm and curiosity. Thanks also to Patrick Ewerhardt for working with me on the operando studies of metal-oxide thin films and for his dedication in the analysis of the data. I would like to extend my thanks to everyone who assisted during the synchrotron measurements for their valuable help and commitment. Thanks to Sani Harouna-Mayer, Lars Klemeyer, and Tjark Gröne for our useful discussion regarding various PDF analysis strategies. I am profoundly grateful to Lukas Grote who first introduced me in the group and greatly helped me at the beginning of my Ph.D. through his deep knowledge on the various X-ray investigation methods, and his experience in the design of in situ reactors. I still regard him as a model colleague.

I thank Marvin Skiba for performing the ICP-MS measurements and Andrea Köppen, Stefan Werner, and Charlotte Ruhmlieb for carrying out the electron microscopy imaging. I acknowledge all the scientific staff of the P07, P21.1, P64, and ID26 beamlines for their assistance in the acquisition of the synchrotron based data and their efforts in continuously improving the capabilities of these facilities. Many thanks to Stephan Fleig and the team of the Mechanical Workshop (Standortwerkstatt Bahrenfeld) of the University of Hamburg for their assistance in realizing the in situ and operando sample environments.

Finally, I thank all my family and friends whose continuous encouragement and wholehearted support have empowered me to pursue my aspirations and become the individual I am today.

Parts of this thesis were proofread by Dorota Koziej, Francesco Caddeo, Cecilia Zito, Sani Harouna-Mayer, Sarah-Alexandra Hussak, and Jagadesh Kopula Kesavan. The translation of the English Abstract into the German Zusammenfassung was handled by Sani Harouna-Mayer and Sarah-Alexandra Hussak.

Declaration of Oath

Hiermit erkläre ich an Eides statt, dass ich die vorliegende Dissertationsschrift selbst verfasst und keine anderen als die angegebenen Quellen und Hilfsmittel benutzt habe.
Ich versichere, dass dieses gebundene Exemplar der Dissertation und das in elektronischer Form eingereichte Dissertationsexemplar (über den Docata-Upload) und das bei der Fakultät (zuständiges Studienbüro bzw. Promotionsbüro Physik) zur Archivierung eingereichte gedruckte gebundene Exemplar der Dissertationsschrift identisch sind.

I hereby declare on oath that this doctoral dissertation is written independently and solely by my own based on the original work of my PhD and has not been used other than the acknowledged resources and aids.
I, the undersigned, declare that this bound copy of the dissertation and the dissertation submitted in electronic form (via the Docata upload) and the printed bound copy of the dissertation submitted to the faculty (responsible Academic Office or the Doctoral Office Physics) for archiving are identical.

Hamburg, 11.04.2024

Davide Derelli